Physics of dissociating clathrates in cyrovolcanic vents: application to Enceladus, Triton and Titan

Physics of dissociating clathrates in cryovolcanic vents: application to Enceladus, Triton and Titan

Gillian Sclater

A thesis submitted for the Degree of Doctor of Philosophy

Department of Earth and Planetary Sciences

School of Science

Birkbeck, University of London

September 2023

Abstract

There is strong evidence for past cryovolcanic resurfacing (eruption of liquid water, aqueous solutions of ammonia and/or other volatiles) on many bodies in the outer solar system. Locations where active cryovolcanism has recently been observed are Saturn's small moon Enceladus, and Triton, the largest moon of Neptune. In 1989, Voyager 2 imaged four active geysers on Triton's south polar region. During a flyby of Enceladus in 2005, Cassini discovered plumes composed of water vapour, solid particles and other volatiles erupting from the fractures on the south polar terrain, and it has been suggested that the abundance of gases observed in the plumes and the explosive nature of the eruptions were the result of the dissociation of clathrate hydrates. It has also been suggested that vigorous explosive activity involving the dissociation of clathrates might be the norm on Titan, and might be responsible for many of the of cryovolcanic landforms observed, as well as providing a plausible explanation for the replenishment of methane in Titan's atmosphere. Results of *in-situ* high-pressure neutron diffraction studies of methane clathrate were used to improve the modelling of clathrate formation and behaviour under the conditions that exist deep in Titan's icy mantle, and thus aid in constraining the origin and evolution of methane in Titan's atmosphere. The model developed in this study and the neutron diffraction experiment results aim to establish a framework in which explosive activity can occur on Enceladus, Triton and Titan, and provide a firm physical basis for future modelling and observation.

Contents

List of figures

List of tables

Abbreviations

Voyager 2 Instruments

ISS - Imaging Science System

UVS - Ultraviolet Spectrometer

IRIS - Infrared Interferometer Spectrometer

RSS - Radio Science System

Cassini Instruments

CAPS - Cassini Plasma Spectrometer

CDA - Cosmic Dust Analyser

CIRS - Composite Infrared Spectrometer

INMS - Ion and Neutral Mass Spectrometer

ISS - Imaging Science Subsystem

MAG - Dual-Technique Magnetometer

MIMI - Magnetospheric Imaging Instrument

RADAR - Cassini Radar

RPWS - Radio and Plasma Wave Spectrometer

RSS - Radio Science Subsystem

UVIS - Ultraviolet Imaging Spectrograph

VIMS - Visible and Infrared Mapping Spectrometer

Huygens Lander Instruments

HASI - Huygens Atmospheric Structure Instrument

DWE - Doppler Wind Experiment

DISR - Descent Imager/Spectral Radiometer

GCMS - Gas Chromatograph Mass Spectrometer

ACP - Aerosol Collector and Pyrolyser

SSP - Surface Science Package

Acknowledgements

I am extremely grateful to both my supervisors, Dr A. Dominic Fortes and Professor Ian Crawford for all their support and feedback during the duration of this process. I am particularly indebted to Dom for all I have learnt from him, and for his continued interest and help even after he joined the ISIS Neutron and Muon source as an instrument scientist at the Science and Technology Facilities Council. It is much appreciated. Gratitude also goes to my friends and work colleagues, who have been unfailingly supportive and encouraging.

This thesis is dedicated to the memory of my Father, Mother and Sister, who are not around to see me finish.

CHAPTER ONE
Introduction

1. Introduction

There is strong evidence for past cryovolcanic resurfacing (eruption of liquid water, aqueous solutions of ammonia, volatiles and/or substances like $MgSO_4$ and H_2SO_4) on many bodies in the outer solar system (Kargel 1995; Brown & Cruikshank, 1997; Hansen et al., 2006; Lopes et al., 2007; Mitri and Showman, 2008; Le Corre et al., 2009; Nelson et al., 2009; Lopes et al., 2013). Locations where cryovolcanism is thought to be recently or currently active are Saturn's small moon Enceladus, Saturn's giant moon Titan, and Triton, the largest moon of Neptune. This project investigates the possible role that clathrate hydrates have in driving explosive cryovolcanism on these icy satellites. Clathrate hydrates are crystalline inclusion compounds of hydrogen-bonded water molecules that trap a non-polar guest molecule (e.g., CH_4, CO_2 and N_2) and are thermodynamically stable at high pressures and low temperatures. Outside the clathrate stability region, dissociation occurs, breaking the host water lattice and releasing the guest molecule. The dissociated or exsolved gas released into a

cryomagma can drive explosive eruption and ice fountaining, comparable to terrestrial basaltic fire fountains caused by volatile exsolution.

This chapter will begin with a summary of the background to the exploration and observations of Titan, Enceladus and Triton (section 1.1), followed by an outline for the rationale behind and justification for this work (section 1.2). The methods employed to satisfy the goals of this thesis will be discussed in section 1.3, and section 1.4 will conclude with a description of the work done towards achieving this.

1.1 Exploration and observations

The Jovian planets, (Jupiter, Saturn, Uranus and Neptune), found beyond the solar system 'frost' line, are each orbited by satellites or moons. These satellites, dubbed 'icy moons', have surfaces mostly covered by ice, where volatile compounds such as water, ammonia, methane, carbon dioxide and nitrogen have condensed to form solid ice surfaces (Brown & Cruikshank, 1997). Analysis of evidence from ground-breaking space missions has indicated so far that the interiors of some of the icy moons might harbour liquid water and that past cryovolcanism might be, in part, responsible for shaping the landscapes of some of the icy bodies orbiting Saturn and Neptune. The focus of this study is two moons of Saturn (Titan and Enceladus) and Neptune's largest moon, Triton and their exploration is discussed next.

1.1.1 Titan

The first probe to visit the Saturnian system was Pioneer 11, launched in 1973, and during its flyby of Saturn in 1979, it sent back images of Titan, revealing an orange

shrouded globe (Coustenis & Taylor, 2008). This was followed by the launch of Voyager 1 and 2 in 1977, with Voyager 2 passing by the surface of Titan at an altitude of ~7,000 km in 1989. The onboard camera returned images of the moon shrouded in orange smog (Lorenz et al. 2002). Further analysis of data collected by onboard instruments determined Titan's bulk atmospheric composition (nitrogen and methane), pressure and density, the vertical temperature profile, and the mean surface temperature and pressure (Coustenis & Taylor, 2008).

Telescopes orbiting Earth, the Hubble Space Telescope (visible and near-IR range) and the Infrared Space Observatory (infrared), took images of regions of the surface and atmosphere in the 1990s, at infrared wavelengths. The Hubble Space telescope imaged Titan in 1990, and subsequently in 1994/5, when the first images of surface features were obtained. In 1997, the Infrared Space Observatory instruments were able to obtain more precise chemical abundance and temperature profiles, identifying molecules not detected before (Coustenis & Taylor, 2008).

Ground-based observatories monitoring Titan are the Mauna Kea Observatory in Hawaii and the European Space Observatory (ESO) in Chile. Also monitoring Titan are radio astronomy telescopes, covering the electromagnetic spectrum from the far infrared (500 μm) wavelengths to kilometre wavelengths; these include the Institut de Radio Millimétrique (IRAM) in France and the Very Large Array (VLA) in New Mexico (Coustenis & Taylor, 2008).

The Cassini-Huygens mission to Saturn arrived in the vicinity of Titan in July 2004 and began imaging and mapping the moon. The twelve onboard instruments included imaging cameras, radar, spectrometers and magnetometers. On the 14th of January 2005, the European Space Agency's Huygens lander was separated from the Cassini

orbiter and proceeded to land on the surface of Titan. The instruments onboard the Huygens probe included the Huygens Atmosphere Structure Instrument (HASI), Gas Chromatograph and Mass Spectrometer (GCMS), Aerosol Collector and Pyrolyser (ACP), Descent Imager/Spectral Radiometer (DISR), Doppler Wind Experiment (DWE) and the Surface Science Package (SSP). The Cassini mission was extended three times after its primary mission was completed in July 2008, first to June 2010 (Cassini Equinox mission) and then to 2016 (Cassini Solstice mission). The end of this mission began in late 2016 (Grand Finale mission) and commenced with its orbit being changed to carry it high above Saturn's north pole where it was plunged into the innermost of its rings, initially to orbit 22 times before being sent into the Saturnian atmosphere to incinerate. Altogether, Cassini spent ~13 years orbiting Saturn and its satellites.

Images obtained of the surface of Titan show it to be geologically young, with relatively few impact craters, suggesting that the resurfacing rate must be considerably higher than the impact cratering rate (Elachi et al., 2005). Mountain chains and labyrinth terrains (highly incised and dissected plateaus) are considered the oldest geological units (Lopes et al., 2019). Seas and lakes are found across Titan's polar regions, one of which, Kraken Mare, at 500,000 km^2 is thought to be the largest body of liquid hydrocarbons (mainly methane) on Titan (Hayes, 2016). Figure 1.1 shows images captured of the Shangri-la dunes, the Sinlap crater, Kraken Mare, the Kaitain Labyrinth (and undifferentiated plains), the surface at the Huygen's landing site and an image of Titan showing the position of the equatorial dune fields and Kraken mare.

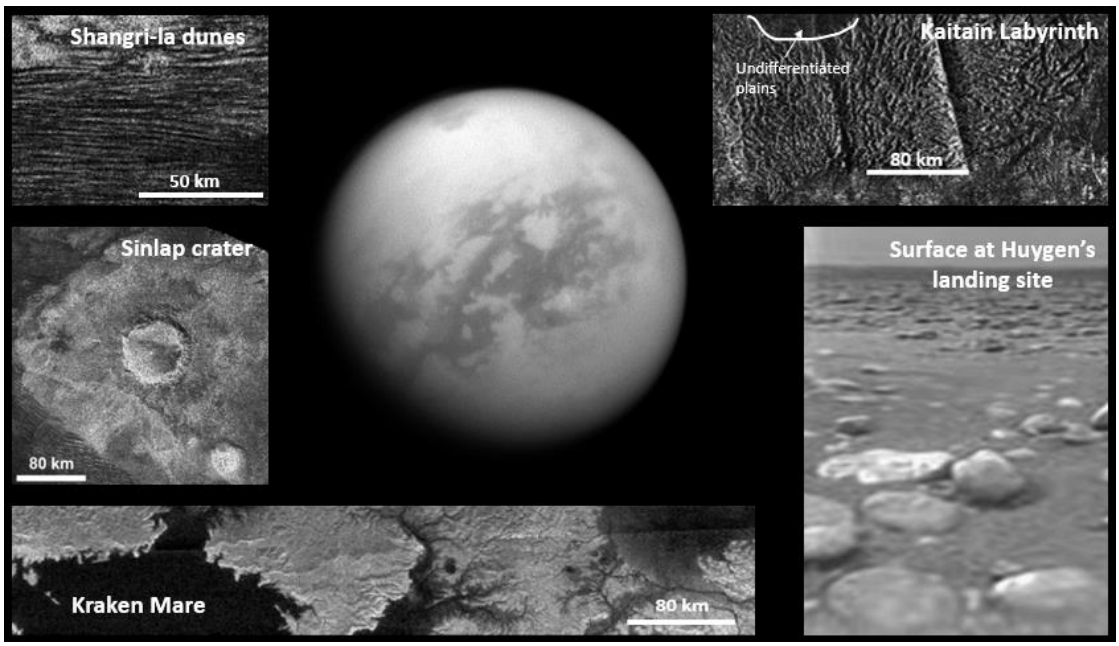

Figure 1.1. Surface terrains of Titan. The top left image is of the Shangri-la dunes (NASA/JPL-Caltech/ASI PIA12037) captured by Cassini Radar mapper from an altitude of 965 km. The middle left image is the Sinlap crater, captured by Cassini Radar mapper (NASA/JPL-Caltech/ASI PIA16638) and the bottom left image is Kraken Mare and associated channel systems also captured by the Cassini radar mapper (NASA/JPL-Caltech/ASI PIA09217). The top right image shows the Kaitain labyrinth showing a section of undifferentiated plain, which are always found downslope and in contact with the Labyrinth terrains (Lopes et al., 2016). The bottom right image is a view from the Descent Image Spectral Radiometer (DISR) carried by Huygens where the cobbles in the foreground are 10-15 cm across (ESA/NASA/JPL/University of Arizona PIA06440). The middle image was captured by Cassini ISS Narrow angle camera and shows the dark equatorial regions of Titan's vast dune fields while Kraken Mare is visible as dark area at the top of the image (NASA/JPL-Caltech/Space Science Institute PIA14584).

Titan has a substantial atmosphere, unlike other similarly large planetary bodies except Earth (Niemann et al., 2005). The thick and layered atmosphere is mainly composed of nitrogen (95-98%) and methane (2-5%), together with molecular hydrogen, and trace species of hydrocarbons, nitriles, oxygen compounds as well as ^{36}Ar and ^{40}Ar (Coustenis, 2005; Niemann et al., 2005). Like Earth, Titan has a well-defined troposphere, stratosphere, mesosphere and thermosphere, although this is more extended due to Titan's lower gravity (Coustenis et al., 2008; Hörst, 2017). Two thick haze regions shroud the moon blocking most visible light from the Sun: the main haze or tholin region

between ~100-210 km, and a detached layer in the stratosphere between ~450-500 km (Coustenis et al., 2008). The thick organic photochemical hazes are thought to be produced from a series of chemically complex processes where sunlight or highly energetic particles from Saturn's magnetosphere hit the layer of Titan's upper atmosphere, breaking up the nitrogen and methane molecules, resulting in the formation of massive positive ions and electrons which trigger a series of chemical reactions that produce a variety of hydrocarbons, including polycyclic aromatic hydrocarbons (PAHs).

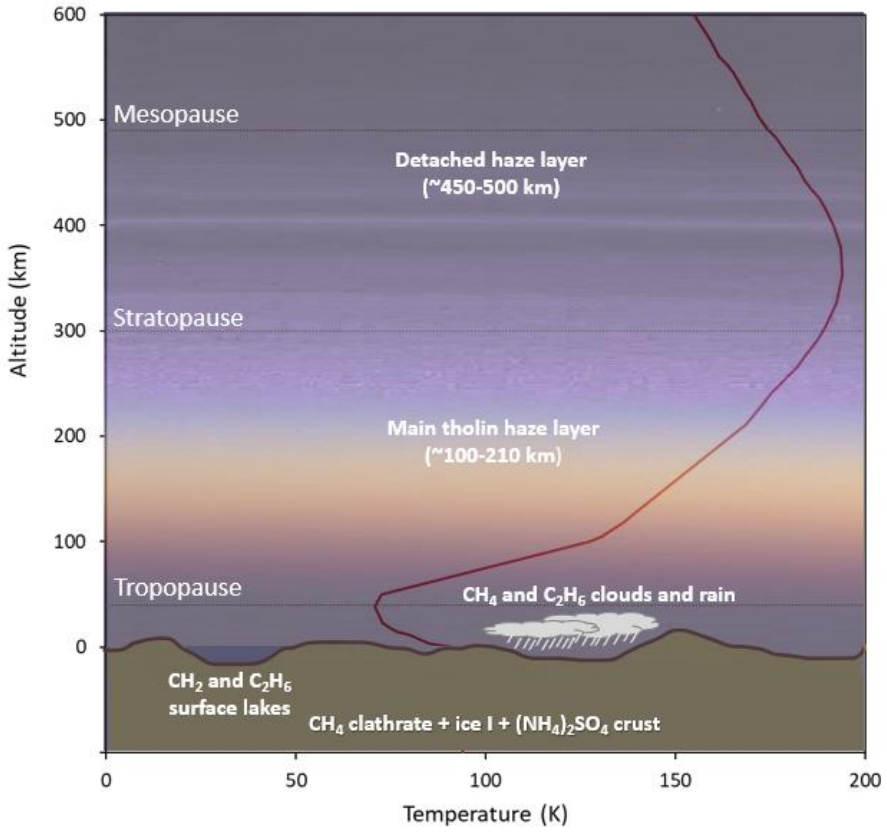

Figure 1.2. A schematic view of Titan's atmosphere up to an altitude of 600 km, showing the temperature profile (K) in red (after Hörst, 2017), CH_4 and C_2H_6 clouds and precipitation, CH_4 and C_2H_6 lakes and the approximate altitude of the tropopause, stratopause, mesopause and haze layers (after Coustenis et al., 2008). The background is an ultraviolet image of Titan's night-side limb, colourized to look like true colour, taken by Cassini's narrow angle camera (http://photojournal.jpl.nasa.gov/catalog/PIA06160).

These large carbon based molecules can coagulate and form larger aggregates which sink into the denser lower atmospheric layers: further growth of the atoms and molecules occurs, resulting in the production of the carbon based aerosols found in the lower layers, and producing the haze that covers Titan (Schulz et al., 2021; Hörst, 2017; Lavvas et al., 2009). As Huygens descended onto the surface of Titan, a temperature profile (figure 1.2) was obtained in the upper atmosphere as a function of altitude from ~1,400 km down to ~150 km (using measured decelerations, inferred pressures, densities and the equation of state for an ideal gas); below an altitude of ~150 km, onboard thermometers measured the temperature directly (Coustenis et al., 2008).

The presence of methane in the atmosphere plays a critical role in sustaining the nitrogen rich atmosphere: CH_4 provides warming in the hydrocarbon haze in the stratosphere by H_2-N_2 and CH_4-N_2 collisions in the troposphere (Atreya et al., 2006). Methane in Titan's atmosphere is irreversibly destroyed by solar UV photolytic reactions because one of the photolysis products, H_2, escapes from the upper atmosphere (Hörst, 2017). At the current depletion rate, methane would disappear over a period of 10-100 million years, thus it is accepted that methane is periodically being replenished in the atmosphere (Niemann et al., 2005).

The surface temperature (~94 K) and surface pressure (~1.5 bar) on Titan are near the triple point of methane, allowing for the liquid phase of methane and ethane (a photolytic by-product of methane) to exist on the surface, and gaseous methane and ethane to be stable in the atmosphere (Hörst, 2017). Methane and ethane condense and produce clouds, haze and surface liquid resulting in a hydrocarbon cycle, analogous to Earth's hydrological cycle (Figure 1.3).

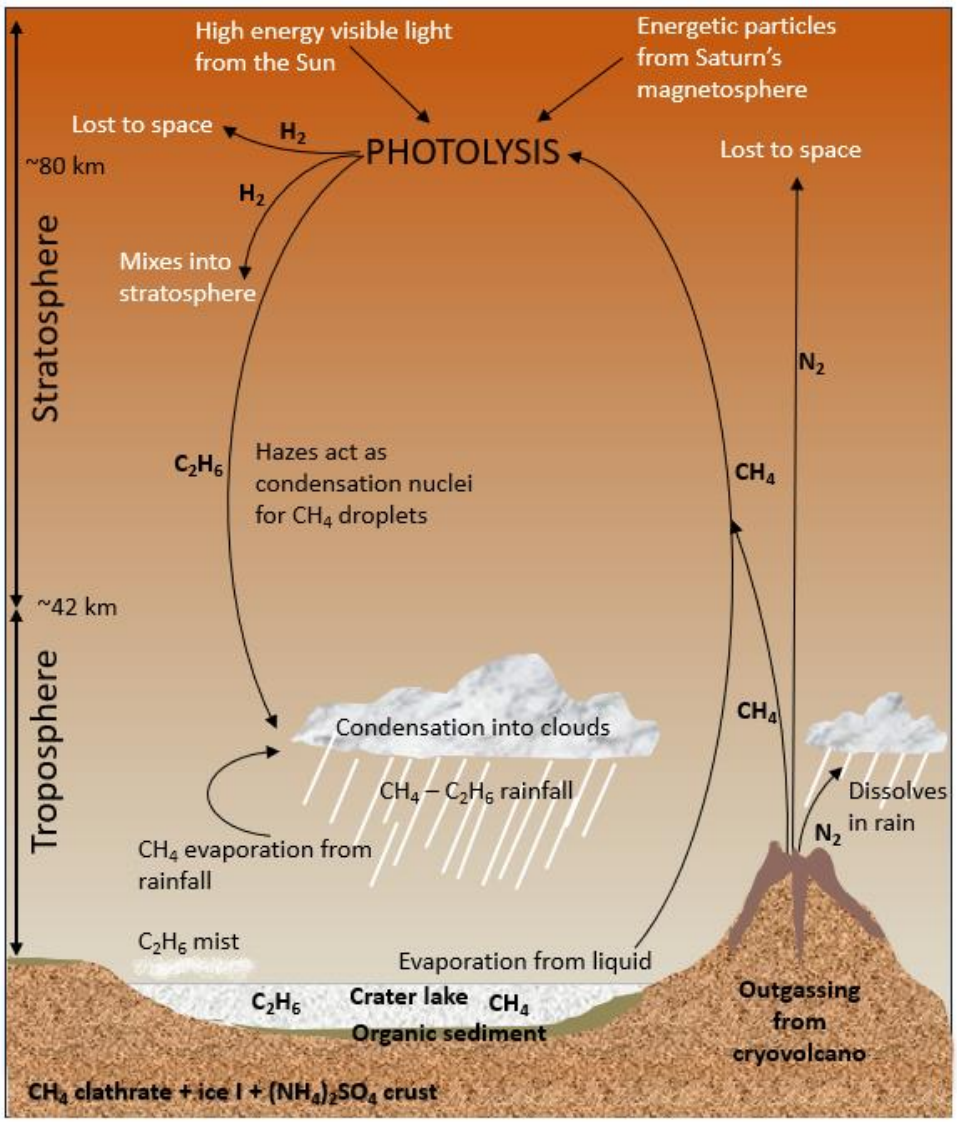

Figure 1.3. A schematic view of the hydrocarbon cycle on Titan (adapted from Coustenis, 2005), showing the cycle of CH_4, C_2H_6, H_2 and N_2 in the Troposphere and Stratosphere. CH_4 is outgassed from cryovolcanoes or evaporated from surface lakes, where it escapes to the Stratosphere where it is irreversibly destroyed by photolytic processes. Products of the photolysis include C_2H_6, which acts as condensation nuclei for CH_4 droplets, which condense into clouds, producing CH_4 and C_2H_6 rain. Evaporation of CH_4 from rainfall can also condense directly into clouds.

Titan experiences seasonal changes, with differences in atmospheric temperatures, chemical composition and circular patterns, particularly at the poles (Mitchell et al., 2016; Hörst, 2017; Dhingra et al, 2019) . Titan's inclination of ~27° results in solar radiation reaching different areas with varying intensity and the direction of incoming

sunlight is driven by Titan's day-night cycle of 15.95 Earth days (Hörst, 2017). It takes Saturn 29.5 Earth years to orbit the Sun, exposing different amounts of sunlight to Titan's northern and southern hemispheres during different parts of the Saturnian year where lower latitudes receive more sunlight than higher latitudes (Mitchell et al., 2016). Dhingra et al. (2019) suggest that the smoothening of previously dry, rough surfaces by a thin layer of fluid are evidence of summer rain at Titan's north pole. Latitudinal and seasonal variations in temperature profiles and methane mixing ratios were also observed by Cassini on Titan (Hörst, 2017). West et al. (2011) report on changes in the vertical structure of Titan's detached haze layer, dropping in altitude from over 500 km to 380 km between 2007 and 2010, and suggest that this is seasonal, since the drop in altitude was most rapid during equinox where meridional stratospheric circulation weakens as solar heating becomes more symmetrical.

1.1.2 Enceladus

NASA's Voyager 1 imaged Enceladus from 624,000 km in November 1980 although images from this distance had poor spatial resolution. Voyager 2 images of Enceladus in August 1981, at 109,000 km, revealed some smooth, surface terrains devoid of craters (therefore considered relatively young), and other older terrains, modified by tectonic processes and cratering.

In 2005, the Cassini spacecraft had three encounters with Enceladus and gathered information about its physical characteristics, magnetic and plasma environment and geological activity. During the first flyby at a distance of 1,259 km in Feb 2005, Cassini's onboard Magnetometer and Visual and Infrared Mapping Spectrometer (VIMS) detected a tenuous atmosphere and a surface dominated by water ice, together with

simple organics and CO_2. Four large, roughly parallel linear depressions or fissures, ('tiger stripes') were detected in the south polar region, each flanked by prominent ridges and littered with house-sized boulders (Porco et al., 2006). The second flyby of the equatorial region at 497 km in March 2005 detected a southerly source of water-ion mass loading of the plasma around Enceladus. During the third flyby of the south polar region at 168 km in July 2005, high resolution images of the south polar terrain were obtained, showing a terrain carved by tectonic features, and almost entirely free of impact craters.

Cassini instruments detected evidence for ongoing endogenic activity in the region: the Cassini Composite Infrared Spectrometer (CIRS) found the south polar region to be anomalously warm (Spencer et al., 2006) and the Ion and Neutral Mass Spectrometer (INMS) detected plumes of water vapour and small icy particles emanating from this region. High resolution images from the Imaging Science Subsystem (ISS) of the surface and plumes emanating from the south polar terrain were obtained on the November 2005 flyover, revealing indications of a youthful surface, and morphological evidence of a change over time in surface stresses in the southern hemisphere (Porco et al., 2006).

The surface of Enceladus is divided into morphologically diverse geological terrains (Porco et al., 2006), where fracturing and tectonic modification of the surface have probably aided in producing its relatively young appearance. The more heavily cratered terrains in the northern hemisphere are shown in figure 1.4, which also indicates the areas of different morphological landscapes. Figure 1.5 shows the south polar terrain, and the position of the four 'tiger stripes' (Alexandria sulcus, Cairo sulcus, Baghdad sulcus and Damascus sulcus) as well as other diverse terrains.

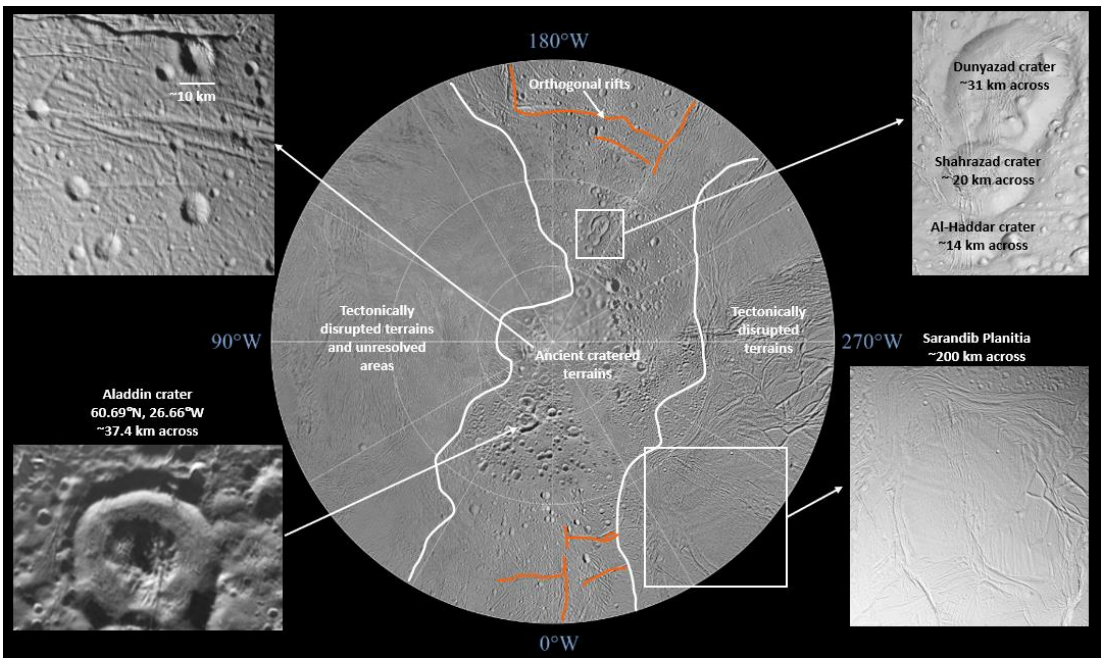

Figure 1.4. Mosaic of Voyager and Cassini images of the northern hemisphere of Enceladus. The centre of the map is the north pole and extends to the equator where gridlines show latitude and longitude in 30-degree increments (NASA/JPL/Space Science Institute PIA14939). Annotated on the image are the areas showing tectonically disrupted terrains and ancient cratered terrains (after Dougherty et al., 2009). The top left image shows an area of the ancient, cratered terrain where the craters have been modified by tectonic forces. The crater near the upper right in this image has a prominent north-south fracturing along its northeastern slope (NASA/JPL/Space Science Institute (PIA06217). The bottom left is the Aladdin crater, a mosaic of images from Cassini and Voyager spacecraft which show a large dome in its interior (NASA/JPL/Space Science Institute). The top right hand image is of a trio of craters named Dunyazad, Shahrazad and Al-Haddar (NASA/JPL-Caltech/Space Science Institute PIA20011) and the bottom right is a mosaic image of the Sarandib Planitia (showing relatively few craters), bounded on the north and west by a band of grooved terrain called Samarkand Sulci (NASA/JPL/Space Science Institute PIA06191). Orthogonal rifts are annotated in orange, showing long, straight rift border faults and intra-rift faults perpendicular to the extension direction (after Dougherty et al., 2009).

Enceladus has an atmosphere, mostly composed of water vapour (Dougherty et al., 2006; Spencer et al., 2006). Cassini's magnetometer instrument (MAG) showed draping of Saturn's magnetic field lines around Enceladus during its February 2005 flyby, which suggested the presence of an atmosphere on Enceladus (Spencer et al., 2006). Two subsequent flybys confirmed that the magnetospheric plasma that corotated with Saturn was slowed and deflected by an obstacle to its flow. Dougherty et al. (2006)

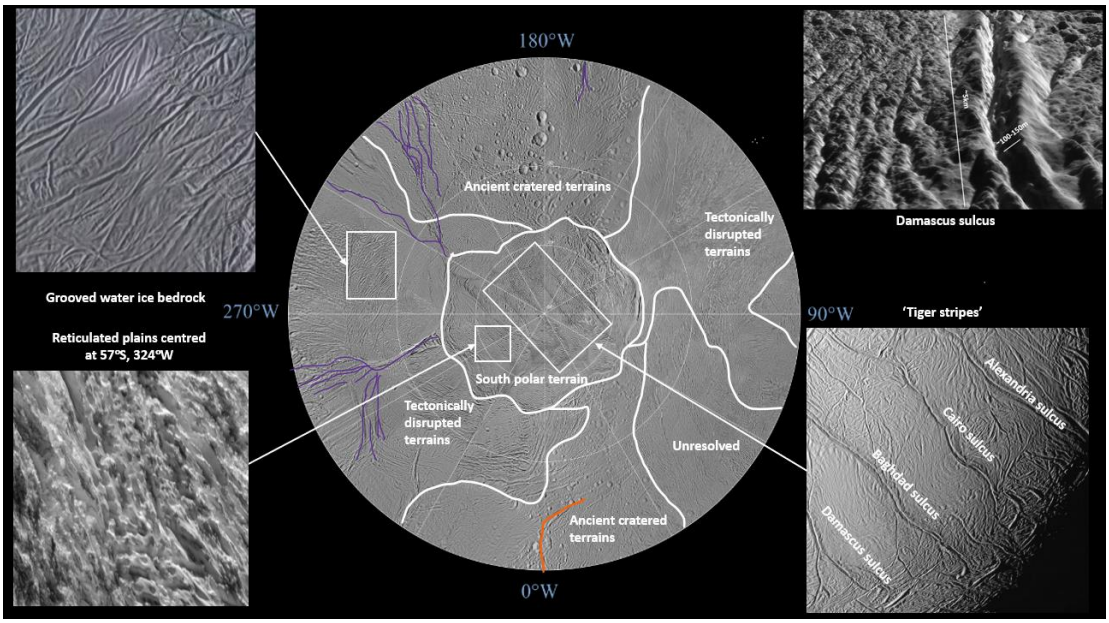

Figure 1.5. Mosaic of Voyager and Cassini images of the southern hemisphere of Enceladus. The centre of the map is the south pole and it extends to the equator where gridlines show latitude and longitude in 30-degree increments (NASA/JPL/Space Science Institute PIA14940). Annotated on the image are the areas showing tectonically disrupted terrains and ancient cratered terrains (after Dougherty et al., 2009). The top left image shows an area of grooved water ice bedrock (NASA/JPL-Caltech/ASI/Space Science Institute PIA15171). The bottom left image shows reticulated plains centred at 57°S, 324°W NASA/JPL-Caltech/Space Science Institute PIA17204). The top right image is of Damascus sulcus, one of the four 'Tiger stripes', where the relief has been exaggerated by a factor of 10 to enhance clarity. The medial trough between the ridges is ~200-250 m deep (NASA/JPL/Space Science Institute/Universities Space Research Association/Lunar & Planetary Institute PIA12207). The bottom right image shows the four 'Tiger stripes', from lower left to upper right, Damascus, Baghdad, Cairo and Alexandria sulci (NASA/JPL/Space Science Institute PIA06247). Orthogonal rifts are annotated in orange (showing long, straight rift border faults and intra-rift faults perpendicular to the extension direction) and North-South trending fan-shaped rift networks are shown in purple (after Dougherty et al., 2009).

suggested that this could be provided by an atmosphere in which ionized water vapour was being vented from the surface or interior of Enceladus, leading to mass loading of the magnetized plasma near Enceladus. The magnetometer data suggest that Enceladus's atmosphere was about the moon's diameter in extent during the period it was detected (Dougherty et al., 2006). Further evidence for the source for an

atmosphere was obtained by Cassini's Ultraviolet Imaging Spectrograph (UVIS) which observed that Enceladus's plume was dominated by water vapour (Hansen et al., 2006).

1.1.3 Triton

Before the Voyager 2 mission encounter with the Neptune System in August 1989, Earth based telescopes detected nitrogen (N_2) and methane (CH_4) in Triton's reflection spectrum (Cruikshank et al., 1984). Six individual absorption bands in the spectral range 0.8-2.5 μm indicated that the ice was not uniform, since the strength of the individual absorption bands varied according to Triton's orbital position, and laboratory experiments suggested that the methane was in the ice phase (Cruikshank & Apt, 1984). An additional absorption band occurred at 2.16 μm and was attributed to a density-induced absorption in molecular nitrogen in the liquid state on the surface of Triton (Cruikshank et al., 1984). However, Lunine and Stevenson (1985) modelled the requirements of phase equilibrium between solid and liquid components and determined that the nitrogen on Triton was mostly solid. Water frost on the surface, argon and carbon monoxide were also identified in the absorption spectra (Cruikshank et al., 1984). The diameter, density, albedo and temperature of Triton were unknown, although it was speculated that if the diameter were large, and the albedo very low, Triton's surface temperature could exceed the triple point temperature of nitrogen (~63 K), allowing for nitrogen rivers, lakes, rain and snow to exist in places (Cruikshank et al., 1993). A chemically produced Titan-like atmospheric haze was also predicted (McKay et al., 1989).

The 1977 Voyager mission, of which Voyager 2 was part, flew past Neptune in August 1989, and a few hours later passed by Triton at a minimum distance of 39,800 km. On-

board instrumentation collected data in the visible, infrared, ultra-violet and centimetre wavelengths as well as probing the magnetic field and radio emissions. Voyager 2 ultraviolet spectroscopic observations confirmed the presence of CH_4 and N_2 (Broadfoot et al., 1989) and a cold surface temperature of about 38 K was revealed from infrared observations (Conrath et al., 1989). Voyager 2 radio and science observations of the mass and density of Triton revealed a surface pressure of 1.6 ± 0.3 pascals and a surface temperature of 38 ± 4 K (Tyler et al., 1989). The surface reflectance of Triton differs depending on the terrain (from dark polar cap to bright polar frost) but the mean albedo was determined to be from 0.6 to 0.9 µm, almost uniformly bright except for areas of dark streaks, whose reflectance was still considered bright compared to most outer planetary bodies (Smith et al., 1989). Triton's radius of 1350 ± 5 km was determined from limb measurement of the Voyager images, and an initial estimate of the mass, obtained from radio tracking data (Tyler et al., 1989) yielded a mean density of about 2.075 g cm^{-3} (Tyler et al., 1989) although this figure was revised by Cruikshank (2005) to 2.06 g cm^{-3}. This density suggests that Triton is composed of a silicate rocky core (~60%) and ice (Cruikshank, 2005).

Forty percent of Triton was imaged, and an array of surface features recorded (Smith et al., 1989). At least four distinct geyser-like eruptions were observed between 55° and 57° S and stereoscopic viewing determined that the dark columns of material rose to an altitude of about 8 km, and were less than 1 km in width (Soderblom et al., 1990; Yelle et al., 1991). Two of these were named Hili and Mahilani, named after a Zulu water sprite and a Tongan sea spirit, respectively. A dense cloud of material formed from the plumes was observed to have been driven westward for more than a 100 km with high-resolution oblique views showing the shadows from this (Stone & Miner, 1989).

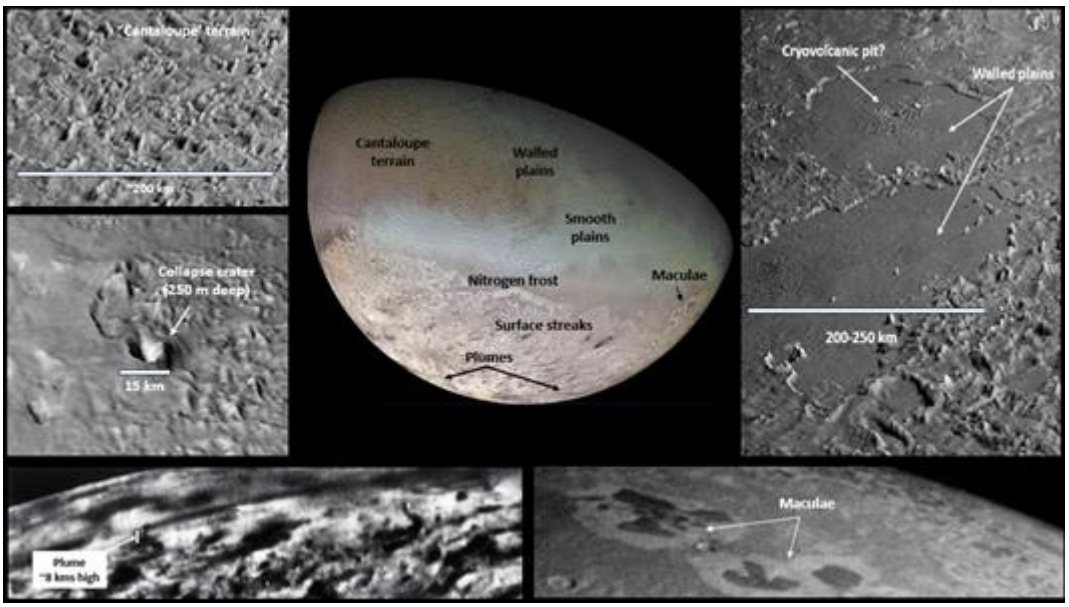

Figure 1.6. Surface terrains on Triton. The top left image shows the rugged 'cantaloupe' terrain (NASA/JPL/Universities Space Research Association/Lunar & Planetary Institute PIA12186). The middle left image shows a possible collapsed crater (NASA/JPL/Universities Space Research Association/Lunar & Planetary Institute PIA12184). The bottom left image is of the Mahilani plume (NASA JPL via Smithsonian Air and Space). The image on the top right shows two walled plains of unknown origin and a possible cryovolcanic pit (NASA/JPL/Universities Space Research Association/Lunar & Planetary Institute PIA12186). The bottom right image shows maculae (or guttae) (NASA/JPL PIA00056). All images were taken by VG ISS Narrow Angle camera. The top middle image is a global colour mosaic taken in 1989 by Voyager 2 where the colour was synthesized by combining high-resolution images taken through filters. The pinkish deposits are the vast south polar cap (possibly methane after reaction with sunlight), the bluish-green band near the equator may be fresh nitrogen deposits and the greenish areas are the 'cantaloupe' terrain (NASA/JPL/USGS PIA00317).

There is relatively little evidence for impact cratering on Triton, but the entire surface shows evidence of endogenic processes and cryovolcanism (Smith et al., 1989; Brown et al., 1990). Past cryovolcanism is evident on Triton where cryovolcanic landscapes are similar to those on Earth, such as volcanic terrains, possible volcanic rifts, calderas, solidified lava lakes, flow fields, stratovolcanoes and viscous lava domes (Kargel, 1995). Figure 1.6 shows images of the surface terrains on Triton, imaged by Voyager 2 in 1989.

The ultraviolet spectrometer instrument on board Voyager 2 detected a thin atmosphere, with an atmospheric pressure in the range of 1.5 – 1.9 Pa, determined by the refraction of Voyager's radio signal through Triton's atmosphere (Hansen et al., 1990; Ingersoll, 1990). The atmosphere is layered and has a troposphere, thermosphere and exosphere. In the troposphere, a negative temperature gradient in the lower atmosphere probably exists, caused by turbulence or eddy mixing, which drives the atmosphere towards the dry adiabat[1] (Yelle et al., 1991). The geyser activity at Triton's surface is thought to sublimate the nitrogen ice cap which initiates moist convective plumes which reach to a level just above the tropopause and which are thought to contribute to the required eddy mixing needed to establish a tropopause at 8-10 km (Yelle et al., 1991). Yelle et al. (1991) also suggest that a thermosphere (a positive temperature gradient) exists at higher altitudes because of the downward conduction of heat produced in the ionosphere, and that there is an exosphere, but no stratosphere. The top of the atmosphere is approximately 800 km above the surface of Triton (Ingersoll, 1990). Figure 1.7 is a schematic diagram of Triton's atmosphere. Voyager 2's images of Triton's limb, taken at its closest approach, show a scattering[2] layer above the surface (Smith et al. 1989). These were thought to be a widespread haze (composed of photochemically generated hydrocarbons and nitriles) extending to an altitude of 30 km, and discrete clouds, believed to be N_2 condensation clouds (Smith et al., 1989; Rages & Pollack, 1992). Winds (between 5 and 10 m s^{-1}) in the southern hemisphere blow in a northeasterly direction at low altitudes (as shown by streaks on the surface) and towards the west at high altitudes (as shown by geyser plume tails): the change in

[1] The Dry adiabat is a line representing the dry adiabatic lapse rate which is defined as the temperature decrease (~10 C per 1000 m) of a rising unsaturated air parcel.

[2] Scattering (Rayleigh) refers to the scattering of light by particles in its path where the size of the particles is up to one-tenth the wavelength of light.

direction being a result of the polar atmospheres being colder than the atmosphere in equatorial regions (Ingersoll, 1990).

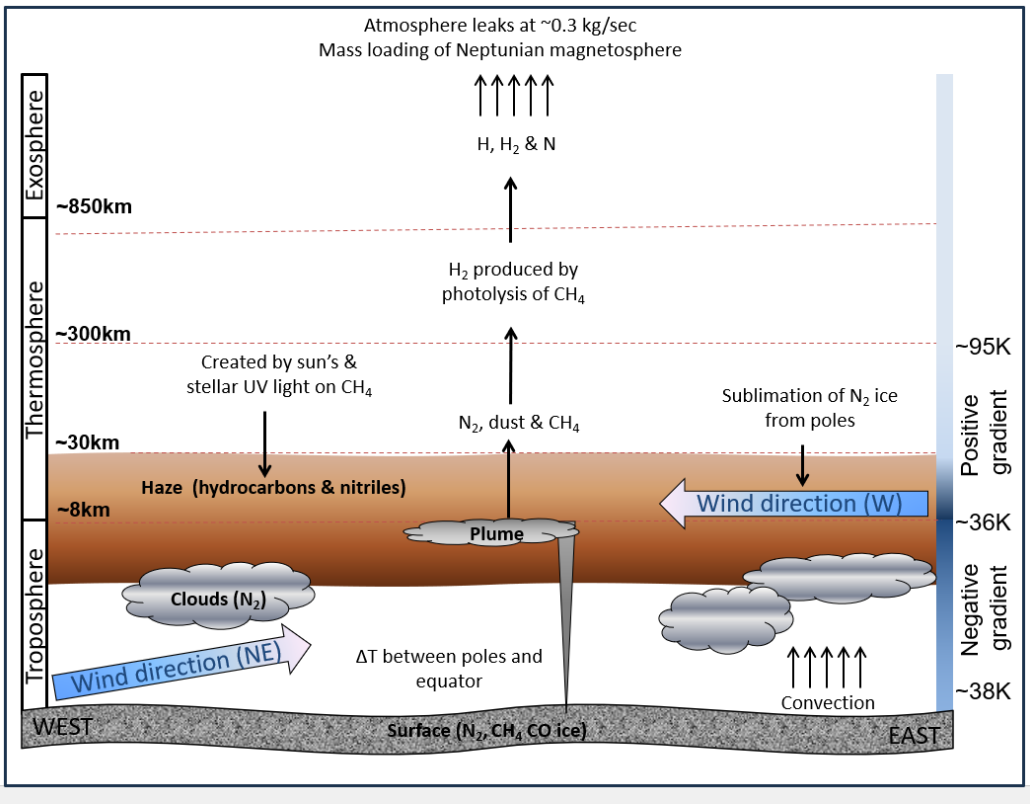

Figure 1.7. Schematic drawing of Triton's atmospheric processes and layers at the time of the 1989 Voyager 2 flyover (not to scale), showing the relative positions of the layers of atmosphere and haze. The wind directions are also indicated.

Based on observational evidence of evolving photometric colours at visible and ultraviolet wavelengths, Triton's atmosphere is thought to undergo large and complex seasonal variations (Trafton et al., 1984; Elliot et al., 2000; Grundy et al., 2010). Triton is partially coated with a layer of volatile ices that support and interact with a seasonally-variable atmosphere where a seasonal cycle is expected to drive large regional variations in solar heating, leading to changes in atmospheric pressure and the seasonal redistribution of the volatile ices (Trafton et al., 1984; Grundy et al., 2010). Comparisons of Hubble telescope observations in 2005 with those of Voyager 2 have detected large-

scale differences in increased and decreased reflectance, thus indicating ongoing seasonal volatile transport (Bauer et al., 2010).

Spectroscopic analysis from ground-based telescopes shows the presence of absorption bands of solid N_2, CH_4, CO_2, CO, and H_2O, all in the region 1.5-2.5 μm (Cruikshank et al., 1988, Cruikshank et al., 2000; Quirico et al., 1999). Measurements from Voyager 2, the International Ultraviolet Explorer (IUE), and Hubble Space Telescope Faint Object Spectrograph (FOS) were used to infer the existence of a spatially variant UV-absorbing material on Triton (Stern, 1999). The absorption bands of CH_4 are all shifted to wavelengths shorter than the laboratory values, indicating that the methane is dissolved in the nitrogen ice (Cruikshank et al. 1993). Studies in 2000 reveal evidence for the presence of solid H_2O on the surface (Cruikshank et al., 2000). A high geometric albedo at visible wavelengths (typically ~80% in the V-band) is consistent with widespread, fresh frost deposits of methane and nitrogen (Cruikshank et al., 1988). DeMeo et al. (2010) have presented evidence for the presence of solid ethane (C_2H_6) on the surface of Triton, based on near-infrared spectral observations using the Very Large Telescope (VLT) and the United Kingdom Infrared Telescope (UKIRT). Burgdorf et al. (2010) suggested that 2006 data from the AKARI satellite's onboard infrared camera might indicate the presence of solid hydrogen cyanide (HCN) dissolved in the frozen nitrogen surface of Triton. The presence of HCN is of interest as a potential precursor of life: HCN is known to polymerize spontaneously to complex heterogeneous polymers that yield amino acids and nucleobases on contact with water and it has been hypothesized that primitive proteins on early Earth originated directly from the hydrolysis of hydrogen cyanide polymers (Mathews & Minard, 2006). During the period of late heavy bombardment of primitive Earth, HCN and hydrocarbon polymers deposited by comets, meteorites and

interplanetary dust may have covered the Earth and with later contact with terrestrial water might have provided the components for establishing primitive proteins/nucleic acid life on Earth (Mathews & Minard, 2006). Hydrogen cyanide has been observed in comets and the atmospheres of Jupiter and Saturn's moon Titan. Hydrogen cyanide polymers range in colour from yellow to red to black (Mathews & Minard, 2006) and it is possible that brown polymers of HCN can account for the low-albedo particulate material emanating from the active geyser-like vents revealed in Voyager 2 images of Triton's surface. (Burgdorf et al., 2010, Mathews & Minard, 2006).

1.2 Aims and Objectives of this study

There are two objectives for carrying out a study of the role clathrate hydrates play in explosive cryovolcanism on Enceladus, Titan and Triton. The first is to improve and extend the current models of cryovolcanism on icy moons and advance the understanding of the role clathrate hydrate dissociation plays in explosive eruptions, developing a more complete physical model of the process (section 1.2.1) . The second objective is to improve modelling of clathrate formation and behaviour under the Pressure-Temperature conditions that exist deep in Titan's icy mantle by performing *in-situ* high-pressure neutron diffraction studies which will investigate methane clathrate close to its dissociation point and will aid in constraining the origin and evolution of methane in Titan's atmosphere, thus informing the modelling effort (section 1.2.2).

1.2.1 Cryovolcanic models of relevance to this study

Several different theories and models have been proposed concerning the source and nature of the plumes on Enceladus (Porco et al., 2006; Kieffer et al., 2006; Halevy & Stewart, 2008a and 2008b; Nimmo et al., 2007; Hurford et al., 2007, Fortes, 2007) and the geysers on Triton (Smith et al., 1989; Brown et al., 1990; Ingersoll & Tryka, 1990; Kargel, 1995). Models have also been developed to explain the observed evidence of past cryovolcanic activity on Titan (Tobie, et al., 2005; Tobie et al., 2006, Fortes et al., 2007; Mitri et al., 2008; Mitri & Showman, 2008; Czechowski & Kossacki, 2009). This thesis is concerned with those models that attribute the explosive activity to clathrate dissociation in the cryolava, with particular emphasis on the models proposed by Fortes (2007) and Fortes et al. (2007) and these are discussed in chapter 2. Other models formulated to account for the plumes on Enceladus and Triton and to explain the evidence of cryovolcanism on Titan are reviewed in chapter two.

The models reviewed to account for cryovolcanic activity on Titan, Enceladus and Triton all propose explanations for the composition of the plumes, the interior structure of the satellites and various mechanisms responsible for bringing cryolava to the surface. Despite this, no model reviewed has explicitly addressed the size and geometries of the vents erupting the plumes on Enceladus and Triton (and possibly Titan), nor the kinetics of clathrate dissociation, viscosity changes in the rising cryomagma, the flow velocity regime and thermodynamic energy balance. The clathrate hydrate model developed in this thesis redresses these limitations.

1.2.2 High pressure behaviour of clathrate hydrates

Clathrate hydrates are common on the Earth and are also thought to be abundant in the outer Solar System (Fortes & Choukroun, 2010; Mousis et al., 2015). Although clathrates have been extensively studied in the 0 – 0.5 GPa range, principally at ambient temperatures (Loveday & Nelmes, 2008), the behaviour of methane clathrate at pressures (0.6 – 1.6 GPa) and temperatures thought to reflect the interior of the larger icy satellites (i.e., close to their dissociation point) have not been examined in detail and there are some outstanding questions. High-pressure behaviour underpins planetary modelling efforts; for example, the behaviour of methane hydrate in the ranges 0 – 5 GPa and 100 – 500 K is crucial to models of Titan, where clathrates are hypothesised to be the source of the dense N_2, CH_4 atmosphere (Loveday et al., 2003).

Existing neutron-scattering crystallography studies of high pressure clathrate hydrates, and in particular, methane hydrate, which is thought to exist in the ice shell of Titan, do not provide adequate evidence for the phase behaviour of methane clathrate near to its high-pressure dissociation temperature in the 0.6 – 1.6 GPa pressure region (Lunine & Stevenson, 1985; Dyadin et al., 1997; Kuhs et al., 1997; Chazallon et al., 2002; Liu et al., 2015). Additional data from such studies could inform and constrain the modelling of clathrate dissociation as a mechanism for explosive cryovolcanism on Titan.

1.3 Methods used to satisfy the goals of this thesis

Two methods were used to investigate the role of clathrate hydrate dissociation in explosive cryovolcanism on icy satellites in the solar system with specific application to Enceladus, Titan and Triton. These are computer simulation in the form of a numeric model, and neutron diffraction experiments, each of which is described below.

1.3.1 Computer simulation

Numerical or computer simulations are widely used in the Earth and planetary sciences to describe physical and chemical behaviours that govern systems, using mathematical models to describe and interpret the processes under consideration, using numbers and equations. To represent a particular physical or chemical process, a set of algorithms and equations, describing physical and thermodynamic relationships, need to be constructed. The equations, solved according to initial and boundary conditions, are adapted or developed based on the constraints of the model assumptions (Kavanagh et al., 2018). Dimensional analysis allows for variables of interest to be grouped to form a set of dimensionless variables, allowing for the identification of different physical regimes. An example of this is the dimensionless Reynolds number (Re) which describes the ratio of inertial and viscous forces in a plume, thus defining laminar ($Re < 2000$), transient ($2000 < Re < 4000$) and turbulent flow ($Re > 4000$). Mach numbers are also dimensionless, and are derived from the relationship between the local flow velocity and sound speed in a plume and indicate the transfer from subsonic ($Mach < 1$) to supersonic flow ($Mach > 1$). Both Reynolds numbers and Mach numbers are used in the model developed for this work.

Where a model aims to reproduce the underlying physical behaviour of a process and is controlled by the model parameters and initial conditions, models are considered deterministic, whereas stochastic models possess some inherent randomness. Steady-state models provide a first approximation of the physical behaviour and a simplified view of the processes involved, requiring assumptions and simplifications to be made. However, for every approximation and simplification made in constructing a model

implementation, errors and uncertainty accumulate; errors in given input data, simplification errors, rounding errors during computation and discretization errors where continuous functions and equations are transformed into discrete parts. Results of models can be evaluated or confirmed only to a partial degree, even if the predicted data set outcome in a numerical model matches the observational data (Oreskes et al., 1994). Reasons for this might include input parameters which are best estimates (e.g., vent geometries on an icy moon) or that the observational data has a degree of uncertainty (e.g., plume abundances on Enceladus).

Modelling is arguably the only method to analyse and understand the complex processes and nature of the cryovolcanic mechanisms on distant icy moons. Eruptive plumes and flows are controlled by a range of physical subsurface processes and regimes, which are not insignificant due to their multiphase nature; cryomagmas comprise melt, crystals, and volatiles, while eruptive plumes and flows commonly comprise many different particles sizes and gas phases. There is a wide range of data available as input for analysis and modelling from spacecraft instruments (e.g., images across the infrared and ultraviolet spectra, detection of dust particles): the Cassini mission has gathered an unprecedented amount of data for analysis of Enceladus and Titan, and to a lesser degree, Voyager 2 has provided data for Triton. The deterministic, steady-state model developed in this work uses data directly from these missions, and builds on the current analysis of the icy moons under investigation (Enceladus, Titan, Triton), utilising Earth based volcanic models and processes. The models studied in this thesis compare outcomes with data observations obtained from space missions, and evaluate the results in terms of the extent to which clathrate hydrates play a role in the mechanism of explosive cryovolcanism on icy moons.

1.3.2 Neutron diffraction experiments

Neutron diffraction experiments can determine the unit cell dimensions and atomic structure of a material. This technique can be applied to study crystalline solids, gasses, liquids or amorphous materials. A sample to be examined is placed in a beam of cold or hot neutrons[3] for high resolution single-crystal studies and the intensity pattern around the sample gives information of the structure of the material. Neutrons are produced for research purposes in one of two ways, by nuclear fission, or by spallation. The ISIS facility, Rutherford Appleton Laboratory, Oxfordshire, UK is a spallation source which consists of a powerful synchrotron and two target stations where neutrons are channelled through beam lines to several instruments, each individually optimised for the study of different types of interactions between the neutron beam and matter. Protons are accelerated to high velocities in the synchrotron and periodically (10-50 times a second) 'fired' at a target. This target is typically a heavy metal; depleted uranium was commonly used, but currently, the target core is made of tungsten and clad in tantalum. Illuminating the target with a high-energy proton beam produces a spray of neutrons, which are passed through a moderator (water, liquid methane or liquid hydrogen) to slow them down; this process takes advantage of the large scattering cross-section of hydrogen. At ISIS, the total power delivered to the target station is ~ 160 kW, from a proton beam current of ~ 180 μA (2.3×10^{13} protons per pulse). The PEARL instrument at ISIS (figure 1.8) is optimised for *in situ* studies of the structural changes and phase behaviour of materials like methane clathrate that occur under the high pressures that exist in Titan's interior.

[3] The temperature of a neutron, also called the neutron energy, describes the neutron's kinetic energy in electron volts

The diffraction pattern produced will show changes in the size of the unit cell, and positions of the atoms at different pressures and temperatures, if a pressure cell and temperature controller (furnace or cryostat) are introduced into the path of the radiation beam. This yields important material properties such as the incompressibility and thermal expansivity. When a beam of radiation is incident on a crystalline sample, interference effects between wavefronts scattered from the regular array of atoms in the material produce a diffraction pattern characteristic of that material.

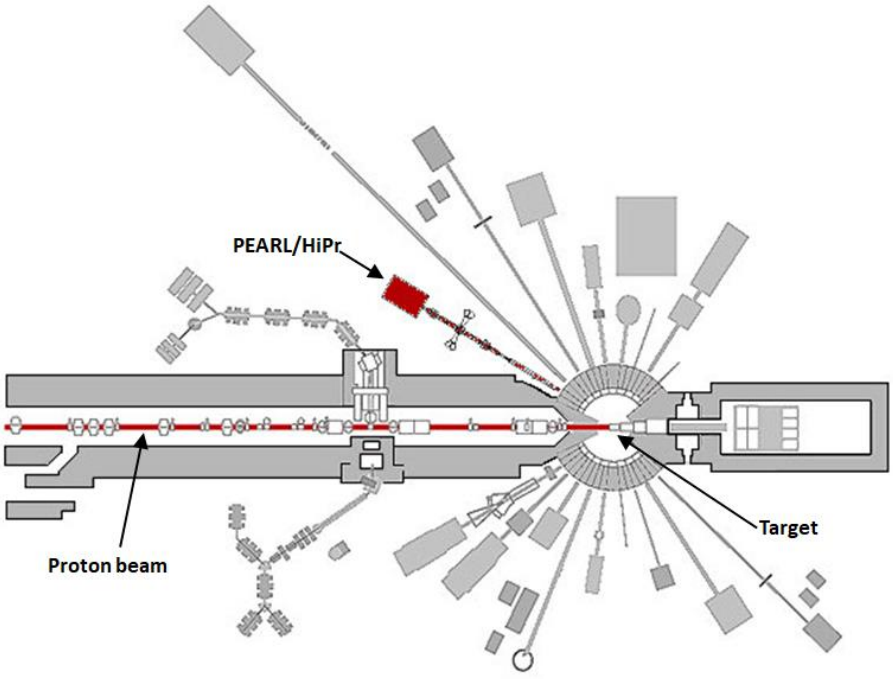

Figure 1.8. Schematic of the arrangement of the beamlines around target station 1 at the ISIS facility, Rutherford Appleton Laboratory, Oxfordshire, UK, showing the position of the PEARL instrument used for experimental work in this thesis (after Bennington, 2004).

Bragg's law, $n\lambda = 2d\sin\theta$ (see Fig. 1.9 for definition of terms), is used to determine the structure of an unknown solid. Since crystals have repeating unit patterns, diffraction can be seen in terms of reflection from the planes of the crystals. The angle at which an incident beam hits a plane of the crystal (2θ) is reflected at the same angle 2θ. If two

beams with identical wavelength (λ) and phase are scattered off different atoms, separated by a crystal plane (d), the lower beam traverses an extra length of 2dsinθ.

In an X-ray or electron diffraction experiment, radiation is scattered by the electrons surrounding the nuclei and an electron density map is obtained from which positions of the nuclei can be deduced. Neutrons, however, are scattered by the atomic nuclei themselves, which present a small cross-section to the incoming neutron, thus allowing the neutrons to penetrate the sample. The wavelengths of X-rays and cold neutrons are in the region of 1 Å, and are therefore comparable to the distances between atoms in solids, rendering them suitable for the study of materials on an atomic scale.

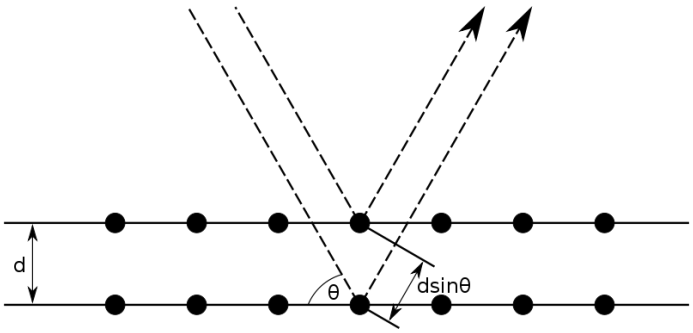

Figure 1.9. Schematic representation of Bragg's law. Two beams with identical wavelength and phase approach a crystalline solid and are scattered off two different atoms within it. The lower beam traverses an extra length of 2dsinθ. Constructive interference occurs when this length is equal to an integer multiple of the wavelength of the radiation.

1.4 Work done to achieve the goals of this thesis

The work done to realise the stated goals of this thesis is outlined in the following section. Chapter 1 serves as background to the justification and motivation and methods employed for investigating the potential role that clathrate hydrate

dissociation has in explosive cryovolcanism on Titan, Enceladus and Triton. A comprehensive background and literature review makes up chapter 2 of this study and begins with a general description of the behaviour of clathrate hydrates both on Earth and in the planetary bodies under investigation. Cryovolcanism on Titan, Enceladus and Triton is discussed in detail, focusing on the evidence for cryovolcanism, and chapter two includes a critical analysis of models developed to explain cryovolcanic activity, and how they differ from the model developed for this study. This work has involved the development of a clathrate hydrate model, called Xenolith II, to describe the physical processes of the explosive plume activity on Enceladus, the geysers on Triton and the evidence for cryovolcanic activity on Titan. Chapter 3 outlines the theory and computational method behind the development of this model, and includes the rationale behind the selection of algorithms and equations used to describe the physical and thermodynamic behaviour under investigation, as well as justification for the boundary conditions and assumptions made. Chapters 4, 5 and 6 present the results of the Xenolith II model for Enceladus, Triton and Titan, relating each moon's internal structure and evidence for a subsurface ocean to the modelling effort. The results obtained are evaluated against the observed data from the Cassini and Voyager 2 missions. Chapter 7 includes a summary of the literature on high pressure clathrate hydrate as well as the presentation of **t**wo separate neutron powder diffraction experiments and results that were carried out on the HiPr/PEARL instrument at the ISIS facility at the Rutherford Appleton Laboratory in Oxfordshire, UK. The samples of deuterated methane clathrate for these experiments were grown in the UCL Earth Sciences Cold Rooms at temperatures of -12°C over a period of five months, and then transported to ISIS for analysis. Chapter 8 presents a synopsis of the results of the Xenolith II model developed in chapter 3 and applied in chapters 4, 5 and 6, with a

discussion of the how the results compare to the observations from space missions and other workers' models. The assumptions and estimations made in constructing the Xenolith II model are evaluated in terms of the uncertainty inherent in a steady state numerical model. The extent to which the Xenolith II models extends current models of clathrate dissociation on icy moons are also discussed. Finally, proposals for future studies and analysis which build on this thesis will be presented.

CHAPTER TWO

Background and literature review

2 Background and literature review

This chapter first provides a general introduction to clathrate hydrates, which, from the evidence in the literature, are likely to be an important constituent of icy satellite interiors. The release of gases trapped in clathrate hydrates is a potential mechanism for the outgassing of volatiles in the cryovolcanic activity observed on Enceladus and Triton, and in the case of Titan, a source of methane in its atmosphere. The current inventory of volatiles, as a source of the gases observed in the plumes of Enceladus, the geysers on Triton and in Titan's atmosphere, is related to the evolution and formation of the icy moons under investigation, and this is discussed in section 2.2. The evidence for cryovolcanism is discussed for each moon, followed by a literature review of the current models formulated to explain cryovolcanic activity (section 2.3).

2.1 Introduction to Clathrate hydrates

Gas hydrates or clathrate hydrates[4] are crystalline compounds which form polyhedral structures under suitable temperature and pressure conditions, combining frozen water molecules and small (<10 Å) non-polar gas molecules (such as CO_2, CH_4, N_2, O_2) which are trapped inside but not reactive with their hydrogen bonded 'cages' (Fig. 2.1). They are formed when water and gas come into contact (at ~6-15 MPa at 277K) and are composed of ~ 85 mol% water and ~15 mol% gas species. The equilibrium structure is mainly determined by the size of the 'guest' molecule and the Pressure-Temperature (P-T) curve depends on the nature of the gas and mixture. Under conditions which destabilize their equilibrium structure, clathrate hydrates dissociate, melting the ice structure and releasing the encaged gas molecules.

Clathrate hydrates were first created in a laboratory in 1778 by Joseph Priestley and remained an academic curiosity until 1934, when Hammerschmidt published results after an inspection of the US gas transmission pipelines. He detected solid 'ice' plugs which were causing blockages, and which were determined to be hydrates formed from the transported gas. Makogan (2010) showed that hydrates represented a potential energy resource, as a means of storing natural gases. Gas hydrates are of enormous commercial and scientific interest, both in terms of the flow assurance in gas pipelines (preventing hydrate deposits from forming in pipelines) as well as exploiting their potential for meeting the world's energy demands. Large amounts of natural gas hydrates have been discovered buried in the permafrost and deep in the ocean floor, where global estimates of methane gas trapped in hydrates represent one of the largest

[4] These terms are used interchangeably. When a hydrate or clathrate hydrate hosts a gas of a particular species, for instance methane, they are often described as 'methane hydrate' or 'methane clathrate'.

sources of hydrocarbon on Earth (Makogan, 2010). Research continues into the role that clathrate hydrates play in carbon dioxide storage and sequestration, reducing carbon emissions (Adeyemo et al., 2010; Eslamimanesh et al., 2013) and their use for storage and transportation of natural gas (Taheri et al., 2014).

The guest molecule-cage interaction stability of the hydrate structure is maintained by an interaction between the van der Waals forces and the hydrogen bonds between the water molecules. Mostly, the host structure is only thermodynamically stable when the guest molecules are present; when they are removed, the host cage structure collapses since the empty cage structure is energetically unfavourable relative to more compact forms of water ice (Lunine & Stevenson, 1985). Water molecules tend to arrange themselves in ring structures, typically preferring 5- or 6-sided rings, forming sheets which stack to create a three-dimensional crystal structure. In the presence of a suitable guest species ('hydrate-former'), and under the right thermodynamic conditions, rings of water molecules can instead join to form a variety of polyhedral cages; these polyhedra are bonded together to create a regular three-dimensional array.

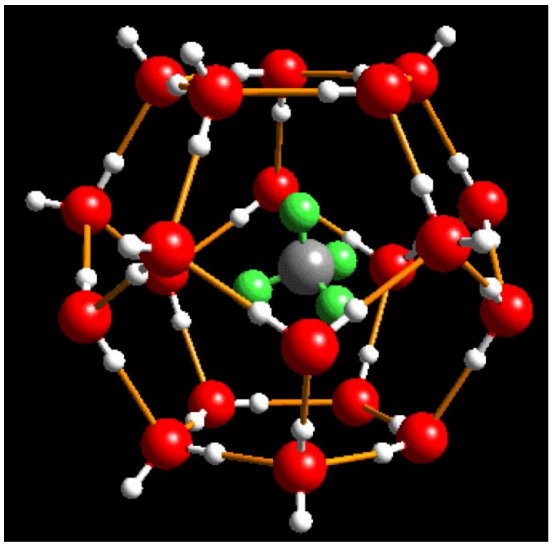

Figure 2.1. Representation of a structure I (sI) methane clathrate pentagonal dodecahedron cavity (5^{12}) showing 12 pentagonal faces. The red and white balls represent the oxygen and hydrogen atoms respectively, and the grey and green balls represents the methane molecule. Reprinted with permission of Janda labs.

The three common types of clathrate hydrate structures are known as sI, sII and sH. The type of polyhedral structure that forms depend mostly on the size of the 'hydrate former' or guest molecule, and typically, each cavity is occupied by only one guest molecule. Structure I (sI) can have one of two types of structures, a small pentagonal dodecahedron denoted 5^{12} (12 pentagonal faces) and a large tetrakaidecahedral cavity, denoted $5^{12}6^2$ (12 pentagonal faces and 2 hexagonal faces).

Structure II (sII) can also have two types of cavities, a small pentagonal dodecahedron 5^{12} cavity and a large hexakaidecahedral cavity denoted $5^{12}6^4$ (12 pentagonal faces and 4 hexagonal faces). Structure H or (sH) has three types of cavities, the small 5^{12} cavity, a midsized $4^35^66^3$ cavity, and a large icosahedral cavity, $5^{12}6^8$ (Koh et al., 2009). The small cages do not touch each other, but bond to the larger cages, forming a cube-like structure. Figures 2.2 and 2.3 show the sI and sII structures respectively. Each vertex is the site of an oxygen atom and each edge an O-H….O hydrogen bond. Smaller molecules such as N_2 or O_2 occupy the smaller cages, whereas larger molecules, such as propane, are restricted to the larger polyhedral structures. However, there are exceptions, for instance, methane normally forms structure I (sI) clathrate, but in the presence of ethane, can form structure II (sII) and hydrogen and helium form 'exotic' structures based on ice, rather than the hydrate structure (Loveday & Nelmes, 2008). Structures I and II are composed mostly of light hydrocarbons, including methane, ethane, propane, and isobutane, as well as many nonpolar molecules (such as carbon dioxide, nitrogen, argon, krypton, and xenon). Larger molecules (e.g., 2,2-dimethylbutane, cycloheptane) can also stabilize the hydrate structure (fitting into the $5^{12}6^8$ cavities of structure H) in the presence of a smaller guest molecule (e.g., methane, xenon) that occupies the smaller cavities ($4^35^66^3$ and 5^{12}) (Sum et al., 2009).

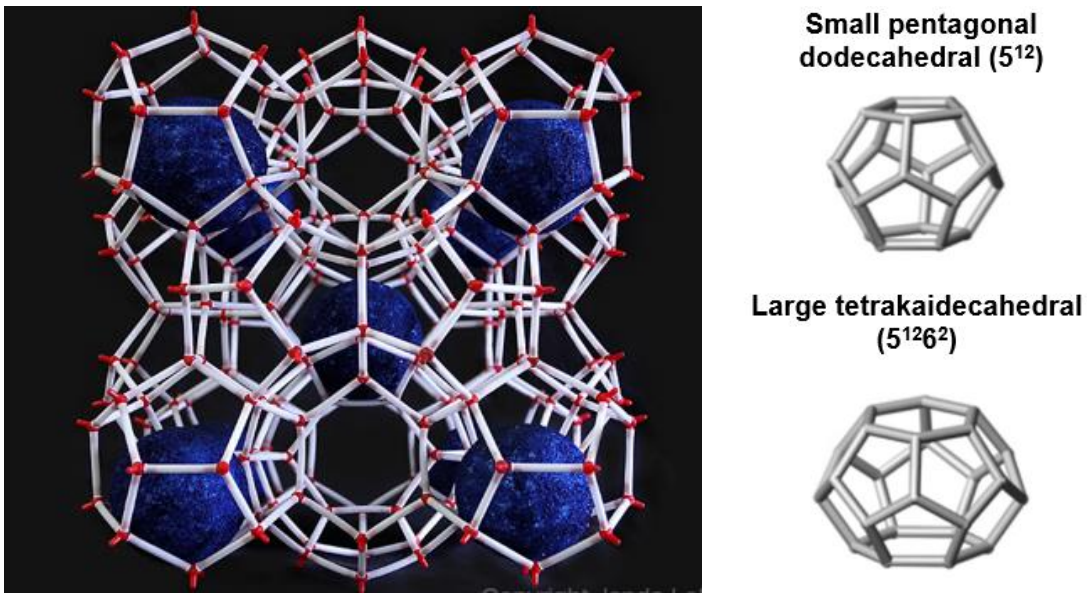

Figure 2.2. Model of structure I methane hydrate (sI structure) on the left-hand side, where the two polyhedral structures shown on the right-hand side form an 3D array; a small pentagonal dodecahedron (5^{12}) and a large tetrakaidecahedral cavity ($5^{12}6^2$). CH_4, CO_2, H_2S, and Xe can form sI hydrates, where the gases have a molecular diameter of 4.3 to 5.3 Å. (After Marvin, 2010; Koh et al., 2009).

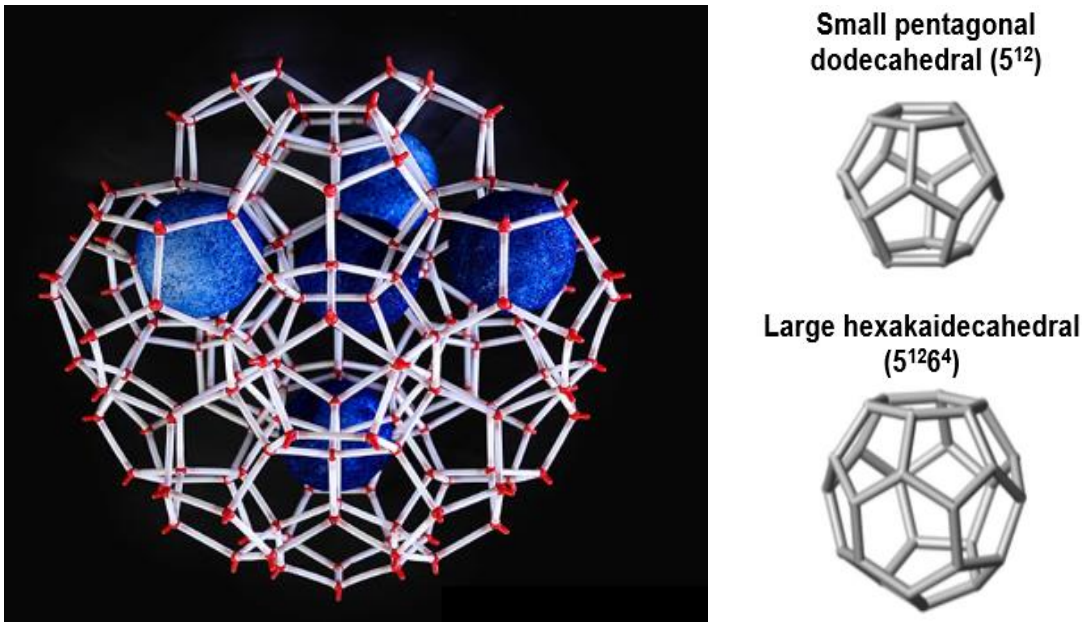

Figure 2.3. Model of structure II methane hydrate (sII structure) on the left-hand side, where the two polyhedral structures shown on the right-hand side form an 3D array; a small pentagonal dodecahedron (5^{12}) and a large hexakaidecahedral cavity ($5^{12}6^4$). Gases with a molecular diameter of 3.8 to 4.3 Å (Ar, Kr, N_2 and O_2) and those with a molecular diameter >6 Å can form sII hydrates. (After Martin, 2010; Koh et al., 2009).

Because most hydrate structures are 85% water on a molecular basis, many of their properties are like those of ice. The oxygen coordination is close to a tetrahedral structure, with three angles at 108° and three at 110.9°, very like the structure of hexagonal or cubic ice[5] (Koh et al, 2009). Despite the similarity of hydrates' physical appearance and refractive index to ice, there are distinct mechanical and thermophysical differences. The high-pressure (between 0.6-1.6 GPa) behaviour of methane hydrate is of importance in planetary modelling conditions by indicating what conditions could exist within planetary bodies. As an example, an understanding of clathrate formation and behaviour under the pressure and temperature conditions that exist deep in Titan's mantle could constrain the origin and evolution of methane in Titan's atmosphere.

Methane hydrate is thought to transform with increasing pressure as follows:

$$sI \rightarrow sII \rightarrow sH \rightarrow sO$$

where sO is 'filled ice' (sometimes called sIII), with molecules of CH_4 penetrating the interstices of ice phases at around 2.1. GPa to form an orthorhombic structure with a H-bond network related to ice Ih (Koh et al., 2009). These high pressure clathrate hydrates will be discussed in chapter 7, together with the results of experiments carried out at the ISIS facility of the STFC Rutherford Appleton Laboratory where the first *in-situ* diffraction-based evidence was obtained for the phase behaviour of methane clathrate near to its high-pressure dissociation temperature in the 0.6 – 1.6 GPa region.

[5] Ice 1h (hexagonal crystal ice) is the hexagonal crystal form of ordinary water ice. Ice I_c is a metastable cubic variant of ice Ih.

2.2 Evolution and volatile inventory

The Jovian planets, (Jupiter, Saturn, Uranus and Neptune), found beyond the solar system 'frost' line, are each orbited by satellites or moons. These satellites, dubbed 'icy moons', have surfaces mostly covered by ice, where volatile compounds such as water, ammonia, methane, carbon dioxide and nitrogen have condensed to form solid ice surfaces (Brown & Cruikshank, 1997). The three icy moons of Titan, Enceladus and Triton, are thought to be differentiated into rocky cores and ice shells and possibly contain subsurface oceans, and all have atmospheres.

The evolution conditions of giant planets constrain processes and events in the origin of each of its satellites, since the initial conditions of the gas and dust in the circumplanetary disk influence the processes governing the formation of moons. During the late stages of the formation of Saturn in a its own circumplanetary disk (CPD), Titan and Enceladus were thought to have formed together with other bodies in a regular system of prograde low-inclination satellites (Rufu et al., 2017; Szulágyi et al., 2018; Anderson et al., 2021). Similarly, Neptune could have formed a gaseous disk at the end of its formation, allowing for the formation of satellites, although these might have been destroyed during the capture of Triton from the Kuiper belt (Rufu et al., 2017). The formation times of satellites are very short compared with those of their parent planets, thus it is possible for several satellites to have existed before their present configuration, each formed under different circumstances (Coradini et al., 2010). This complicates the determination of the origin of chemical and physical properties of each satellite. However, pressure and temperature profiles in the circumplanetary disks shape the chemical gradients of the forming satellites, allowing for the condensation of ices and noble gases which determine, to some extent, the chemical composition of the regular

satellites. Gautier and Hersant (2005) argue that in some regions in the protosolar nebula, volatiles where initially trapped in the form of clathrate hydrates, depending on the temperature and pressure required for the stability of the clathrate species, and the amount of water ice available locally.

Mousis et al., (2009a) propose that Enceladus formed from icy planetesimals, initially produced in the protosolar nebula (PSN), and became part of the circumplanetary nebula of Saturn. Due to increasing gas temperature and pressure conditions during their inward migration within the Saturnian subnebula, these planetesimals became partly devolatized, losing Ar, CO and N_2. The building blocks of Enceladus would therefore not contain CO and N_2, although Anderson et al., (2021) argue that the transport due to gas diffusion and drift of solid particles of key volatiles around the location of their respective icelines[6] was not factored into this assessment.

CH_4 could be trapped in planetesimals during their formation in the solar nebula, or produced via serpentinization[7] reactions in the moon's interior (Mousis et al., 2009a). Deuterium is a sensitive indicator of the origin and evolution of planetary atmospheres and the deuterium-to-hydrogen (D/H) ratio measured by the Cassini Ion and Mass Spectrometer in the plumes of Enceladus constrains the origin of CH_4 in the interior. If Enceladus' methane originates from the solar nebula, then its D/H ratio should range between $\sim 4.7 \times 10^{-5}$ and 1.5×10^{-4}, but if the methane of Enceladus results from serpentinization reactions then its D/H ratio should range between $\sim 2.1 \times 10^{-4}$ and 4.5

[6] An iceline is defined as the distance from the Sun at which the disk temperature is equal to the sublimation or condensation temperature of water ice or any other species in the PSN or CPD (Anderson et al., 2021)

[7] Serpentinization is the process of hydration and metamorphic transformation of ferromagnesian minerals (e.g., olivine, pyroxene) in mafic and ultramafic rocks producing serpentinite (e.g., antigorite and magnetite).

× 10^{-4} according to Mousis et al. (2009a). The D/H ratio of ~2.9 x 10^{-4} determined by Waite et al. (2009a) supports the suggestion that some of the building blocks of Enceladus are primordial in origin, however the specific measurement of D/H in CH_4 could not be made with INMS due to overlapping signals of several species in this portion of the mass spectrum (Mousis et al., 2009a). Waite et al. (2009) suggest that H_2O, NH_3, H_2S, and CO_2 are expected to be primordial in origin on Enceladus.

Mousis et al. (2009b) propose a formation scenario for Titan in which the satellite accreted from solids and planetesimals initially produced in the solar nebula. They postulate that these solids encountered gas temperature and pressure conditions high enough to generate a loss via sublimation of most of their CO and Ar, but low enough to retain the incorporated CH_4, NH_3, Kr and Xe. However, the model predicts that even if most of the CO and Ar volatiles where devolatilized from planetesimals ultimately accreted by Titan, small amounts of these species could have been trapped in CH_4-dominated clathrates, and subsequently in the satellite. This is in good agreement with the abundances of CO and ^{36}Ar observed in Titan's atmosphere. It has also been suggested that during accretion, a large amount of ammonia was trapped in the interior of Titan (Prinn & Fegley, 1981), and a proportion of this is thought to have been converted to N_2 by photolysis[8], radiolysis (damage caused by ionizing radiation) and thermolytic destruction (chemical decomposition caused by heat) in meteorite impacts (Fortes et al., 2007).

Triton is thought to have accreted beyond 30 AU in the Kuiper belt region of the solar nebula, making it possibly the only large moon in the solar system not formed around

[8] Photolysis is a chemical reaction in which molecules are broken down by photons. On Titan, CH_4 is irreversibly destroyed and converted to heavier hydrocarbons (e.g., C_2H_6) on a relatively short timescale compared to its lifetime (10-100 million years). Without CH_4, Titan's stratosphere and troposphere may become too cold for N_2 to remain in the gas phase, thus reducing the atmospheric pressure.

its host planet (Cruikshank, 2005; Masters et al., 2014; McKinnon & Kirk, 2014). Other Kuiper belt objects (KBO) of which Triton was probably a member, include the icy dwarf planets and primitive bodies such as Eris, Pluto, Makemake, Haumea, Sedna, Orcus, and Quaoar. During the early stages of the evolution of the solar system, and during the final stages of its accretion, Neptune's orbit expanded, perturbing Triton's orbit in the Kuiper belt, and eventually permanently capturing it in its own orbit. Triton would have needed to lose sufficient energy to allow for its capture by colliding with another object in the vicinity, or with one of the planet's already formed regular satellites (Cruikshank, 2005; McKinnon & Kirk, 2014). Triton is thought to have experienced an episode of runaway melting within a few hundred million years of its capture (McKinnon & Kirk, 2014). During this period, large chemical exchanges probably occurred between the mantle (which contained dissolved volatiles) and the hot rocky core. Tidal energy produced more than sufficient heat to completely melt Triton, the rate of which depended on the evolution of the orbit and dissipative qualities of its interior structure where liquid is more dissipative than solid rock. As a layer of ice melted, heat released in that region through dissipation would drive volatile material to the surface (Cruikshank, 2005). Many of these volatiles were likely forced into Triton's atmosphere where CO, CH_4, CO_2, NH_3 and even H_2 have been observed. H_2 could be a product of photolysis of methane or ammonia in the atmosphere, but could also be a minor component in Triton's original ice (Cruikshank, 2005; McKinnon & Kirk, 2014). Triton's possible formation in the Kuiper belt, capture into the Neptunian system and subsequent evolution imposes constraints on its volatile inventory.

2.3 Cryovolcanism: evidence and models

The surface of the icy planets can contain both endogenic and exogenic materials. Endogenic materials can include materials remaining from the original formation processes of the satellite, as well as materials created from exchange processes between the surface, subsurface and any atmospheres, and emplaced on the surface through cryovolcanism or extensional tectonics. Geologic and morphological surface features and chemical composition constrain models of how these exchange processes might operate (Prockter et al., 2010). Exogenic material can be brought to the surface by comets, meteorites and micrometeorites. A convecting ice layer might transport hydrated salts, clathrates and aqueous minerals from the interior to the surface, and exchange exogenically emplaced materials with the interior. In addition, ultraviolet photolysis and radiolysis, driven by charged particle bombardment may also chemically alter the surface (Dalton, 2010).

The process of cryovolcanism on icy planetary bodies requires an internal heat source sufficient to partially melt material at depth. If the resultant melt is buoyant with respect to its surroundings, it will attempt to rise to the surface. If unsuccessful, it will be emplaced in the subsurface as a plutonic body where it could later erupt, either effusively or explosively, at the surface. Either manifestation may produce geological structures that are observable by imaging cameras on spacecraft. It is thought that most of the ice-dominated bodies in the solar system contain naturally radioactive elements from the time of their formation and the decay process of these could serve as a heat source (Wilson, 2009). Additionally, satellites can be subject to tidal friction processes where orbital or rotational energy from the primary planet, or other local satellites, is dissipated as heat energy in the interior of a satellite. It has also been suggested that

translucent deposits of frozen materials could create a solid-state greenhouse effect where light and heat are trapped in a specific location, thus accumulating the required heat for cryovolcanism (Brown et al., 1990). Evidence of past cryovolcanic activity has been detected on many of the icy satellites; volcanic rifts, calderas and solidified lava lakes, flow fields, stratovolcanoes, viscous lava domes and sinuous rilles (Kargel, 1995). The evidence that cryovolcanism is still active on Enceladus and Triton, and possibly Titan, will be discussed in the following sections, examining evidence for cryovolcanic activity. This will be followed by a review of some of the current models proposing the mechanisms for this.

2.3.1 Titan

Titan is the largest moon in the Saturnian system of more than 146 known moons and is bigger that the planet Mercury making it the second largest moon in the solar system, after Ganymede. Titan is covered in a dense, predominantly nitrogen atmosphere, containing photochemical hazes which shroud the surface to direct observations (Elachi et al., 2005; Atreya et al., 2006). It is also the only known object on the solar system where evidence of stable liquid phases of methane and ethane in the form of lakes, rivers and seas, is found on the surface (Hörst, 2017). Titan's internal structure, relevant to cryovolcanism, is discussed in chapter 6.

Cassini radar observations of Titan have revealed surface morphological landforms on Titan which have been interpreted as comparable to volcanic terrains on Earth (Wood & Radebaugh., 2020; Mitri & Showman, 2008; Le Corre et al., 2009; Nelson et al., 2009; Lopes et al., 2007; Lopes et al., 2013), although no active plumes or geysers were detected. Features consistent with volcanic landforms formed by explosion, excavation

and collapse in the north polar region, have also been interpreted as being fresh, indicating that cryovolcanism might have been recently active on Titan (Wood & Radebaugh., 2020). Analysis of spectrophotometric variability detected in two separate locations on the surface of Titan, observed between October 2005 and March 2006 by Cassini's Visual and Infrared Mapping Spectrometer (VIMS) and Synthetic Aperture RADAR (SAR) instruments onboard the Cassini Saturn Orbiter have led Nelson et al., (2009) to propose that cryovolcanism is still active on Titan. They determined that the surface morphology at both locations (7°S, 138°W and 26°S 78°W) observed at different times was different, and therefore consistent with surface flows resulting from cryovolcanic activity; material having been extruded or effused from Titan's interior and deposited on the surface.

Further evidence for past eruptions and outgassing from Titan's interior was detected by the Gas Chromatograph Mass spectrometer (GCMS) onboard the Cassini Huygens lander where significant amounts of radiogenic ^{40}Ar were found in the atmosphere. ^{40}Ar is the decay product of ^{40}K, proposed to have been sourced from the rocky core (Tobie et al., 2010). The carbon isotopic ratio $^{13}C/^{12}C$ detected by the GCMS instrument in the atmosphere is only slightly smaller than the value detected on the surface, and suggests that methane is unlikely to have been formed during Titan's early formation and must periodically be replenished from cryovolcanic processes, since it is irreversibly destroyed in a relatively short period of 10-100 Myr by photolysis (Niemann et al., 2005).

About 1% of Titan's surface was mapped by the Cassini Titan Radar Mapper at a resolution of ~0.5 km, and larger areas of the moon in lower resolution modes (Elachi et al., 2005). Interpreting and comparing images obtained from SAR or VIMS infrared images of potential cryovolcanic terrains on Titan with volcanic morphological features on Earth or other planetary bodies has resulted in several candidate cryovolcanoes being

proposed (Kirk et al., 2010). RADAR images, at a higher resolution, serve to constrain or refine VIMS images. The stereo analysis of RADAR images, which produce 3D visualizations (Digital topographic models), has provided further refinement of images, although only a few percent of Titan has benefited from the use of this method (Kirk et al., 2010). Since applying this analysis, several previously proposed cryovolcanic terrains, Ganesa Macula, Tortola Facula and Winia Fluctus, have been re-evaluated and based on the results of these refining techniques, and are no longer considered cryovolcanic in nature (Lopes et al., 2013). Ganesa Macula (50° N, 87° W) was initially interpreted as a cryovolcanic shield or dome, based on its appearance in SAR data, and is a large circular feature with associated lobate flow-like deposits and distinct flows (Lopes et al., 2007; Elachi et al., 2005). Further analysis with SAR stereo and overlapping SAR beams showed that Ganesa Macula's current shape is more likely a heavily dissected and eroded region of Titan or an eroded shield or dome that has suffered deflation or collapse (Lopez et al., 2010; Lopez et al., 2013; Kirk et al., 2010). Similarly, Tortola Facula (8.8° N, 143.1° W), was initially proposed as a cryovolcanic dome or thick cryolava flow, based on VIMS data (Sotin et al., 2005), but later SAR data analysis showed it to be morphologically like other hummocky and mountainous terrains on Titan and not cryovolcanic in origin (Lopes et al., 2010). Winia Fluctus (~30° W, 45° W) was interpreted to be a large cryovolcanic flow field or of fluvial origin, based on SAR data (Elachi et al. 2005; Lopes et al., 2007) but data from SAR topographical data showed that the features imaged were more likely to be depressed features and inconsistent with either cryovolcanic or fluvial origins (Lopes et al., 2013).

Table 2.1 lists a summary of those terrains on Titan thought to be candidate cryovolcanoes or cryovolcanic in origin. Figure 2.4 shows the positions of some of these candidate cryovolcanic features on a global mosaic map of VIMS data.

Table 2.1. Candidate cryovolcanic terrains on Titan. The methods of detection are listed with each feature: Visible and Infrared Mapping Spectrometer (VIMS) and Synthetic Aperture radar (SAR).

Candidate cryovolcanic terrain	**Observed Cryovolcanic features**	**Literature source**
Sotra Patera (40.0° W, 14.5° S)	Pit or caldera adjacent to Doom Mons; 1,700 m deep and diameter of ~30 km (SAR and VIMS).	Lopes et al., 2007 Lopes et al., 2013
Doom Mons (40.4° W, 14.7° S)	Cryovolcano; ~1,245 m high and ~70 km and diameter of (VIMS and SAR)	Lopes et al., 2007 Lopes et al., 2013
Mohini Fluctus (38.5° W, 11.8° S)	Finger-like flows and lobate flow-like features from Sotra Patera caldera and Doom Mons (VIMS and SAR)	Lopes et al., 2007 Lopes et al., 2013
Erebor Mons (36.2° W, 5.0° S)	Cryovolcano; ~ 1,000 m high with a diameter of ~40 km with associated flows (SAR and topographic analysis)	Lopes et al., 2007 Lopes et al., 2013
Hotei Regio flows (~78° W, 26° S)	Two possible calderas with numerous overlapping lobate features and flows (SAR, VIMS and topographic analysis)	Barnes et al., 2006 Lopes et al., 2013 Soderblom et al., 2009
Tui Regio flows (~125° W, 24° S)	Numerous lobate deposits not associated with a specific candidate vent area (SAT and VIMS)	Lopes et al., 2013 Solomonidou et al., 2014
Ara Fluctus (118.4° W, 39.8° N)	Flow-like features not associated with a specific candidate vent area (SAR)	Lopes et al., 2007 Lopes et al., 2013 Wood et al., 2020
Western Xanadu (~140° W, 10° S)	Flow-like features, possibly recent (variable infrared brightness) (SAR and VIMS)	Lopes et al., 2013 Wall et al., 2009
Hotei Arcus (79° W, 26° S)	Flow-like features (SAR and VIMS)	Lopes et al., 2013 Wall et al., 2009
Rohe Fluctus (37.8° W, 47.3° N)	Flow-like features associated with caldera-like feature (SAR and VIMS)	Lopes et al., 2007 Lopes et al., 2013 Wood et al., 2020
"T3" flow (~70° W, 20° N)	Flow-like features associated with a caldera-like feature (SAR and VIMS)	Lopes et al., 2007 Lopes et al., 2013 Le Corre et al., 2009
North Polar region	Raised rampart craters and overlapping sharp-edged depressions with lobate flows and flowing channels, consistent with explosive cryovolcanism (average ~ 10 km in diameter) (SAR and topographic analysis)	Birch et al., 2017 Birch et al., 2018 Wood et al., 2020

Surface manifestations of cryovolcanism on Titan are well documented and several models of the erupting mechanisms responsible for cryovolcanic activity and the outgassing of volatiles from the interior have been proposed to explain this activity on Titan. Some accretion and evolution models predict that the subsurface and upper crust

of Titan could contain clathrate hydrates, and that episodic outgassing of methane stored as clathrate hydrates within an ice Ih layer above an ammonia-rich water ocean is a likely explanation for the methane replenishment in Titan's atmosphere (Tobie et all., 2006; Fortes et al., 2007; Mousis et al., 2015).

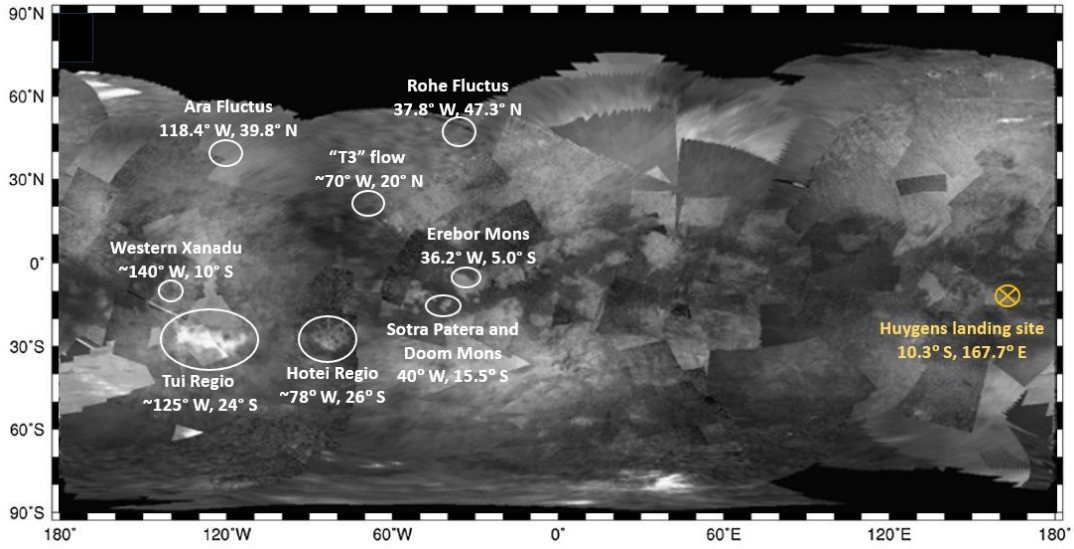

Figure 2.4. Map of Titan from Visual and Infrared Mapping Spectrometer (VIMS) data (after Solomonidou et al., 2014) showing the positions of some of the candidate cryovolcanic terrains mentions in table 2.1: Ara Fluctus, Rohe Fluctus, "T3" flow, Western Xanadu, Erebor Mons, Tui Regio, Hotei Regio and the Sotra Patera Region which includes Doom Mons and the Mohini Fluctus flows. Also shown is the reference area of the Huygens landing site (NASA/JPL/Cassini-ISS/Space Science Institute and ESO/NACO-SDI/VLT). The background image is a global mosaic of VIMS data acquired between 2004 and 2010 (Le Mouélic et al., 2012).

Mechanisms for clathrate dissociation that are related to thermal convection in the ice Ih shell are also proposed in several studies (Tobie et al., 2005; Tobie et al., 2006, Mitri et al., 2008; Czechowski & Kossacki, 2009). Other models propose that melt pockets of ammonia-water moving through an unstable ice Ih shell could ascend buoyantly through the shell, either erupting effusively (Mitri et al., 2008) or explosively at the clathrate

decomposition depth (Fortes et al., 2007). Thermal convection could dissociate clathrates embedded in the ice-I shell.

In a thermal-orbital evolution model of Titan, (Tobie et al. 2005; Tobie et al., 2006) it was proposed that the ice-I shell could have transitioned only recently from a conductive state to a convective state, and that a late onset of convection (within the past ~1 Gyr) in the ice Ih shell could dissociate the methane clathrates trapped in the ice and produce episodic events of methane outgassing from the interior of the satellite. Mitri and Showman (2008) hypothesize that in the presence of an internal ocean, conductive–convective transition of the ice Ih shell can produce geological activity, and induce the formation of numerous surface structures and result in cryovolcanic activity. If ammonia is present in the ocean, changes in the ice shell thickness cause changes in the temperature and viscosity at the base of the shell and because of the high viscosity contrast between the surface and the bottom of the ice-I shells on Titan, convection is likely to occur. Czechowski and Kossacki (2009) also investigated the possibility of thermal convection in Titan's ice shell and proposed that it is saturated with liquid methane and heated from below by geothermal heat sources. Convection could lead to changes in the heat flow and temperature in the regolith which could in turn be distributed to geysers on the surface.

Mitri and Showman (2008) proposed a model of cryovolcanism on Titan that involves the cracking at the base of the ice shell and the formation of ammonia-water pockets in the ice, where large scale tectonic stress (tides, non-synchronous rotation, satellite volume changes, solid state convection, or subsurface pressure gradients associated with topography) may help overcome the negative buoyancy of the ammonia-water pockets as partial freezing occurs. This increase, and any addition of silicates delivered

by impacts to the ice shell would reduce the liquid-solid density, and would enable the ammonia to erupt effusively onto the surface.

Serpentinization reactions in the interior of Titan could lead to the formation of methane (Atreya et al., 2006) and Fortes et al. (2007) proposed that Titan's core density is consistent with serpentinite mineralogy. In their model of both effusive and explosive cryovolcanism on Titan, Fortes et al. (2007) proposed that the cooling of a subsurface ocean could result in the underplating of the outer ice shell with ice Ih, resulting in a gravitationally unstable system where compositional plumes could be produced and ascend buoyantly. These ice plumes might move melt pockets through the shell, creating pressure gradients sufficient to drive such melts to the surface, where contact between the cryomagma and wall rock (clathrate shell) could cause a portion of the frozen volatile species (CH_4, N_2, CO) to dissolve into the melt, as well as eroding fragments of wall rock that can be transported as Xenoliths. At the clathrate decomposition depth, the entrained xenoliths could break down to ice and gas, powering explosive cryovolcanism as the gas in the partial melt fragments.

2.3.2 Enceladus

Enceladus is the sixth largest moon of Saturn and about 500 km in diameter. It is mostly covered by water ice which reflects more than 90% of incident sunlight, and is therefore considered one of the most reflective bodies in the solar system. Its mean surface temperature is ~75 K. Enceladus orbits Saturn between the orbits of Mimas and Tethys and is tidally locked with its parent planet, keeping the same face towards Saturn.

Enceladus completes an orbit of Saturn within its E-ring every 32.9 hours and is trapped in orbital resonance with Dione where the two moons line up at regular intervals,

interacting gravitationally. The effects of Dione's gravity cause Enceladus's orbit to be pulled into an elliptical shape, ensuring that Enceladus is not at an equal distance from Saturn during its orbit and results in tidal heating within the moon. Enceladus's internal structure, relevant to cryovolcanism, is discussed in chapter 4.

In a July 2005 flyby of Enceladus, the Composite Infrared Spectrometer (CIRS) onboard Cassini detected spatially varying temperature anomalies in the 'tiger stripes' region, where the mean temperature was a few kelvin higher than the background (Nimmo et al., 2007). Cassini's Ion and Neutral Mass spectrometer (INMS) instrument detected substantial plumes or geysers emanating from the region of the 'tiger stripes' (Waite et al., 2006). The gas composition of the plume was detected by Cassini's Ultraviolet Imaging Spectrograph (UVIS) and analysis of these data revealed that the plumes were dominated by water (Hansen et al., 2006). Further analysis of the plumes was revealed from data obtained by Cassini's INMS instrument and showed the presence of CO_2, NH_3, H_2, CH_4 and various other hydrocarbons (Waite et al., 2009; Waite et al., 2017). Data from Cassini's Cosmic Dust Analyser (CDA) has determined the particle size and compositional profile of the water ice particles in the plume, imaged by the Imaging Science Subsystem (ISS) (Postberg et al., 2009; Postberg et al., 2011). Figure 2.5 shows a mosaic of the plumes of Enceladus taken by Cassini's Imaging Science Subsystem (ISS) narrow angle camera in November 2010, showing the eruption of the geysers from the fractures in the south polar terrain. The mechanism driving the ongoing geyser-like eruptions from sources along the fissures is the subject of many theories and proposals, including the model presented in chapter three of this work.

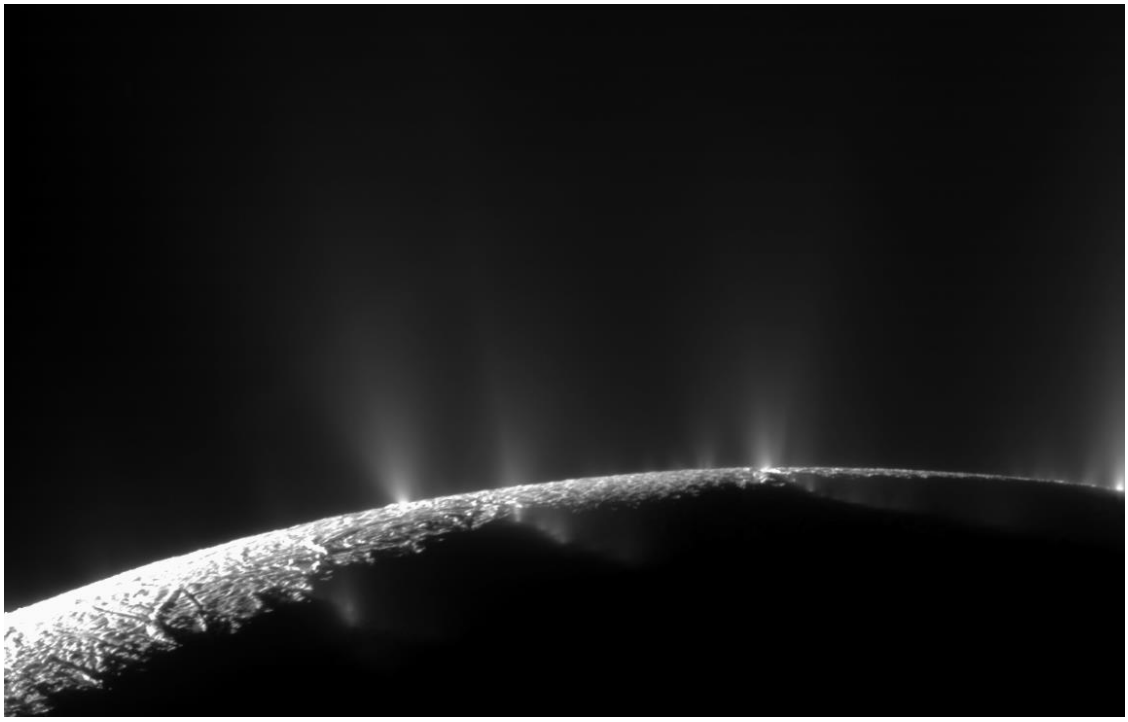

Figure 2.5. Two-image mosaic of the plumes of Enceladus taken by Cassini's Imaging Science Subsystem (ISS) narrow angle camera in November 2010, showing the eruption of the geysers from the fractures in the south polar terrain. From left to right, the fractures are Alexandria, Cairo, Baghdad, and Damascus (NASA/JPL/Space Science Institute PIA11688).

The models can be categorized into two groups where the first involves the low-pressure boiling of water near the surface in shallow reservoirs of warm (~273 K) water (Porco et al., 2006). The second group of models propose that the dissociation of clathrates hydrates in depressurised fractures is responsible for the plumes (Kieffer et al., 2006; Halevy & Stewart, 2008a and 2008b; Nimmo et al., 2007; Hurford et al., 2007, Fortes, 2007).

Porco et al. (2006) proposed the 'Cold Faithful' model and hypothesised that the plumes were the result of low-pressure boiling of liquid water in reservoirs as close as 7m from the surface, where near freezing water erupted in giant geysers. They suggested that ~1% of upward-moving particles in the plumes escaped to supply Saturn's E ring and are its primary source. In this model, heating sufficient to raise the temperature to 273K

(triple point of water) is required to bring the liquid water close to the surface where small fractures may form, erupting as plumes at any time, driven by tectonic disturbances. They proposed that the heat source could be provided by localised near-surface tidal forces operating on or within the 'tiger stripe' fractures. Although Enceladus' subsurface structure may be globally heterogeneous, the south polar region might have been the only region where liquid could be close to the surface at the time of observation. The plumes would erupt where small fractures decompressed the pockets of liquid water, causing the liquid water to boil at a temperature of at least 273K. The plumes of the Cold Faithful model might remain active over long periods of time. However, this model did not consider the composition of the volatiles and water in the plumes as measured by Cassini INMS (H_2O = 91 ± 3%, N_2 = 4 ± 1%, CO_2 = 3.2 ± 0.6%, and CH_4 = 1.6 ± 0.4%), which were (except for CO_2), at least an order of magnitude larger than the plausible solubility of these species in cold water (Waite et al., 2006). It was hypothesised that the only way to incorporate these gases into the plume was by the breakdown of clathrate hydrates (Fortes et al., 2007, Keiffer et al., 2006).

To take the measured gas composition into account, Kieffer et al. (2006) proposed that the south pole of Enceladus is a colder world with a 'Frigid Faithful' plume emanating from the decomposition of clathrates. They hypothesised that active tectonic processes in the SPT create fractures that cause degassing of clathrates which would occur wherever tensional fractures penetrated to an underlying clathrate reservoir. The model also explains the variability of fluxes over space and time by providing an advective heat transfer mechanism: heat is absorbed as latent heat of decomposition of clathrate and re-deposited near the surface as latent heat of condensation of ice. Keiffer et al. (2006) assume that the composition of the plumes observed by Cassini give an

indication of the composition of the shell from where the plumes originate. The model proposes that Enceladus has a shell of water ice and clathrate hydrates (containing CO_2, CH_4, N_2) covered by a layer of H_2O–CO_2 ice. Large fissures expose and decompress clathrates in the shell. The clathrates could absorb heat from a source at depth, resulting in the explosive eruption of plumes. The model proposes that underground reservoirs of pressurized liquid water above 273 K could fuel geysers that send jets of icy material above the moon's south pole. The plumes represent numerous relatively small leaks tapping a system of advecting gases, ice and vapour. The Keiffer et al. (2006) model does not provide an explanation for the thermal anomaly in the south polar terrain, the numerous fresh large-scale tension fractures observed in the mid-latitudes which were not venting, nor the origin of the subsurface clathrate reservoir.

Hurford et al. (2007) reported that the south polar terrain rifts were under tension for only about half the diurnal cycle, implying that the eruption of the plumes was periodic, rather than continuous. They reported a mechanism in which temporal variations in tidal stress opened and closed the rifts, which in turn governed the timing of the eruptions. Keiffer et al. (2006) suggested two possibilities to account for the observed temporal variance of the plumes. First, they proposed that over time, some H_2O and CO_2 may re-condense on the walls of the fissures and near the surface to form the low ridges of H_2O with trapped O_2. Secondly, they suggested that as the clathrates degassed, the calculated fluxes could be reduced, thus coating surfaces with water ice and slowing or terminating the reaction. Nimmo et al. (2007) however, postulated that vapour production occurs because of tidal shear heating along fractures in the SPT where there is a large thermal anomaly due to condensation of ~90% of this vapour around the south polar terrain.

This tidally forced periodic eruption of the plumes mentioned by Hurford et al. (2007) implies that the dissociation of clathrates might not be under equilibrium conditions. To account for this, Halevy and Stewart (2008a and 2008b) proposed a numerical, non-equilibrium clathrate dissociation model where clathrate hydrate dissociation might explain the temporal variability of the plumes and the geometry of the faults on the south polar region. The model assumes that the dissociation of clathrate hydrates on Enceladus is not an equilibrium process: the rifts are under tensional stress for only about half of the diurnal cycle. The model predicts that the exposure of clathrates to low pressure destabilizes them, which results in their dissociation to water ice and a mixture of gases along a 'dissociation front'. A fraction of the ice produced by clathrate dissociation becomes entrained in the gas flow and jets out of the rifts together with the gas. The rest of the ice is deposited on the fault walls as a porous coating. This ice coating may sublimate from its outer boundary ('sublimation front') at a rate dependent on its temperature. The water vapour produced by sublimation is also entrained in the gas flow, adding to the water content of the escaping plume. The faults may widen or seal, depending on the relative rates of ice sublimation and deposition. This implies periodic, short-term exposure of clathrates to low pressure, alternating with closure of the rifts and an increase in pressure and temperature. Thus, over the course of a diurnal cycle, the temperature slowly approaches the equilibrium temperature of clathrate dissociation or ice sublimation at the local pressure, rather than being arbitrarily set to it.

Fortes (2007) proposed a cryomagmatic model for Enceladus which describes an internal structure for Enceladus: a two-layer differentiated body with a rocky core overlain by an ice-rich mantle. This model also proposed that clathrates may have been

formed in situ from volatiles generated by hydrothermal activity at the rock–ice interface. These enriched aqueous fluids could be capable of percolating throughout the ice shell, along fractures and grain boundaries, and result in extensive modal metasomatism[9] of the mantle. Gas-saturated liquid at pressures exceeding the clathrate stability pressure and could react with exposed ice to form clathrate hydrates, thus the mantle of Enceladus need not contain primitive clathrate hydrates. If the clathrates were primordial in origin, having condensed *ex-situ* from the proto-saturnian nebula, the plumes would be venting an abundance of noble gases, which is not evident from Cassini data (Fortes, 2007). Fortes (2007) suggests that the passage of younger melts through altered mantle will entrain fragments of metasomatic clathrates (as xenoliths) to higher levels, where decompression of clathrate grains during ascent could result in their dissociation at a critical pressure, releasing a considerable quantity of gas into the melt. The model, incorporating the dissociation curve and other physical properties of the clathrate xenolith phase, describes a plausible explanation for the release of gas from the clathrate host: a certain amount is dissolved in the cryomagma and the rest forms gas bubbles. Ascent and continued decompression lead to the growth of the gas bubbles as well as further gas exsolution. Since most gases are poorly soluble in cold water, the excess gas would form bubbles which would expand, and eventually coalesce to create a highly unstable foam that would expand upwards through the vent at high velocity, resulting in an explosive eruption. Once the volume fraction of gas bubbles exceeds approximately 75%, the magma is said to be fragmented. The fragmentation of magma, containing abundant gas bubbles, is thought to be a defining characteristic

[9] Metasomatism is the process whereby igneous, sedimentary or metamorphic rock undergoes compositional and mineralogical transformations associated with chemical reactions of the fluids which invade the original rock.

of explosive eruptions. Because the transit of the foam up the last few kilometres of the magma conduit is rapid, the model predicts that extremely turbulent flow will be generated which would result in significant mechanical erosion of the vent walls. Additional xenolith material eroded from the conduit walls could be incorporated in the flow. The Titan model of Fortes et al. (2007) describes a similar process to explain the explosive cryovolcanism that is predicted to have occurred, or is still possibly occurring on Titan.

The clathrate dissociation mechanism, of direct relevance to this study, could also explain the geysers on Triton, where observed eruptions of nitrogen gas and entrained dust may be the result of the dissociation of nitrogen clathrates, resulting in plumes up to 8 km high (Kargel, 1995).

2.3.3 Triton

Triton, the largest satellite of the Neptune system, is the seventh largest moon in the solar system. Triton is covered with a surface layer of frozen nitrogen, and has a tenuous nitrogen atmosphere, with trace amounts of carbon monoxide and methane near its surface (Broadfoot et al., 1989). The area of Triton observed by Voyager 2 exhibits active geological processes (Smith et al., 1989), a time-variable atmosphere (Elliot et al., 1998), high wind speeds and a visible haze layer (Buratti et el., 2011). Triton's orbit is retrograde, and the plane of its orbit (orbital inclination) is tilted 157° to Neptune's equator (Jacobson, 2009). Triton rotates once on its axis every 5.9 days and takes the same time to revolve around Neptune (synchronous rotation) which results in one face being orientated towards Neptune throughout its orbit. Triton's axial tilt with respect to Neptune's axis combines in such a way that results in both polar regions taking turns

to face the sun, ensuring seasonal changes in each pole, as one, then another, moves into sunlight. Triton's internal structure, relevant to cryovolcanism, is discussed in chapter 5.

Images of Triton's surface from Voyager 2 suggest two types of cryovolcanism. First, there are large craters that appear to be extensively flooded by flows of some type, examples of liquid water or 'slurry' volcanism (Smith et al., 1989) and secondly, current geyser activity on the south polar region between 50° and 57° S, the part of Triton's surface close to the subsolar point, where the sun was directly overhead during the 1989 Voyager 2 flyover (Hansen et al., 1990). Voyager 2 was only able to image regions in high resolution located between 50° and 57° S, and there may have been activity elsewhere. Streaks across Triton's surface are believed to be remnants of eruptive material from these and other, perhaps inactive geysers (Smith et al., 1989). Rubincam (2003) suggested that the eruption of volatiles from Triton's equatorial region, and its deposition at the poles, may redistribute enough mass over the course of 10 000 years to cause polar wander (migration of the magnetic poles over time). Each eruption of a Triton geyser may last up to a year, and during this time about 100 million cubic metres of material may be deposited up to 150 km downwind (Kirk, 1990). The position of the geysers indicates that solar heating, although very weak at Triton's great distance from the Sun, plays a crucial role. Figure 2.6 is an image of the active geysers and plumes on Triton. The surface of Triton absorbs only 20% of the incident sunlight at 30 AU (Hillier et al, 1990).

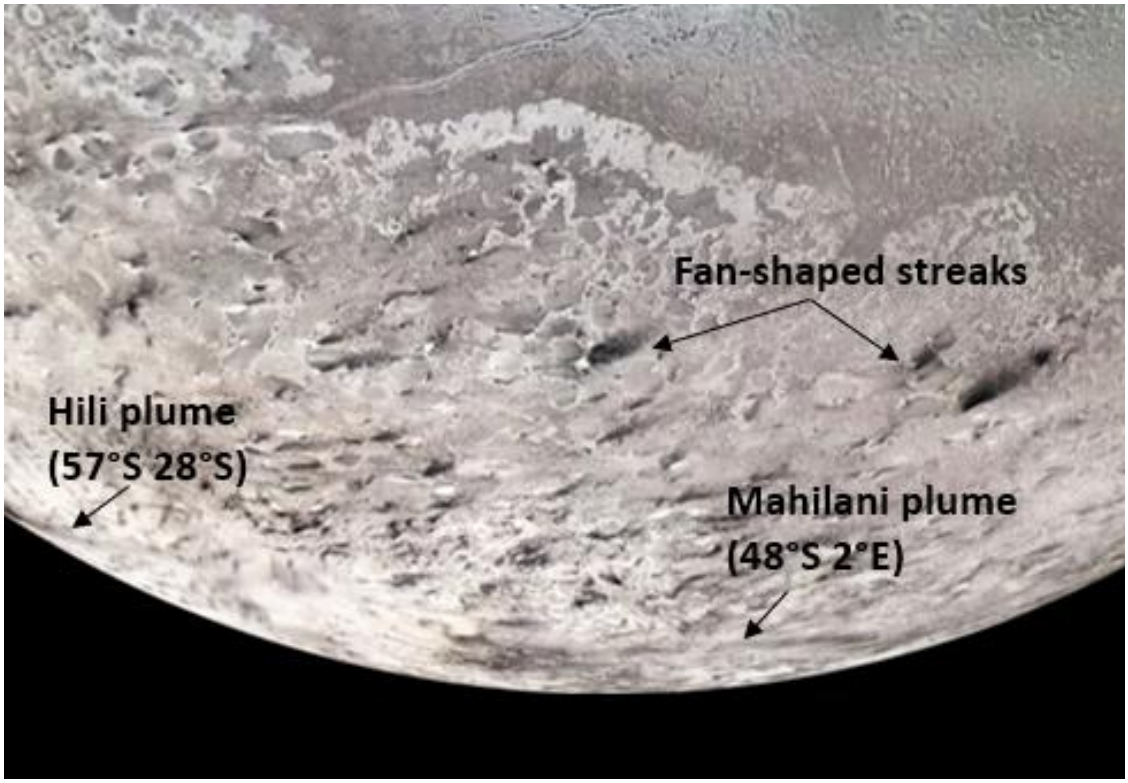

Figure 2.6. Global mosaic image of Triton, taken by Voyager 2 in 1989. The Mahilani (~100 km long) and Hili plumes are annotated, as well two of the numerous fan-shaped streaks, possibly dust remnants of previous eruptions. Image *NASA/JPL/USGS (https://photojournal.jpl.nasa.gov/catalog/PIA00317.*

Several models have been proposed to explain the origin of the plumes or geysers on Triton as observed by Voyager 2. The active plumes observed at mid to high latitude, during a season on Triton when the sun was almost directly overhead, suggested that they could be solar powered (Smith et al., 1989; Brown et al., 1990; Kargel, 1995).

It has also been proposed that the plumes are an atmospheric phenomenon (Ingersoll & Tryka, 1990). Finally, the heat driving the geysers could be transported in the solid-nitrogen polar caps through a process of thermal convection and conduction (Duxbury & Brown, 1997).

The gas-clathrate model of Kargel (1995) proposed that nonpolar and weakly polar molecular liquids (mainly N_2, CH_4, CO, CO_2, and Ar) may have originated by the

decomposition of gas-clathrate hydrates. Triton's plumes could be volcanogenic fumaroles or geyser-like emissions, powered by deep internal heating, indicating an interior that is still cryomagmatically active. Kargel (1995) suggests though, that the geysers on Triton could also be solar powered.

Smith et al. (1989) proposed that because the surface of Triton consists of a translucent, low-conductivity layer of frozen nitrogen overlying a darker substrate, solar radiation passing through the surface ice would slowly heat and vaporize subsurface nitrogen until sufficient gas pressure accumulates for it to erupt through the crust (a 'solid greenhouse effect'). Two basic types of greenhouse models exist that could supply the thermodynamic temperature differences required for this (Brown et al., 1990). The first is a classical solid-state greenhouse mechanism where insolation is absorbed exponentially with depth in a visually translucent layer of solid nitrogen by trace impurities dissolved in or dispersed throughout (for example, methane, ethane, ethylene, acetylene and polycyclic, aromatic hydrocarbons). Because the nitrogen layer is relatively opaque to thermal radiation in the 30 to 300μm spectral region, sufficient energy could be trapped in the subsurface layer and stored as specific heat, and create a thermal gradient.

The dominant heat-transport mechanism within this layer is by diffusion of stored subsurface heat to the surface which is released as latent heat of sublimation by the venting of nitrogen gas through fissures and/or radiated to space. Figure 2.7 is a schematic representation of classic solid-state greenhouse model after Brown et al. (1990).

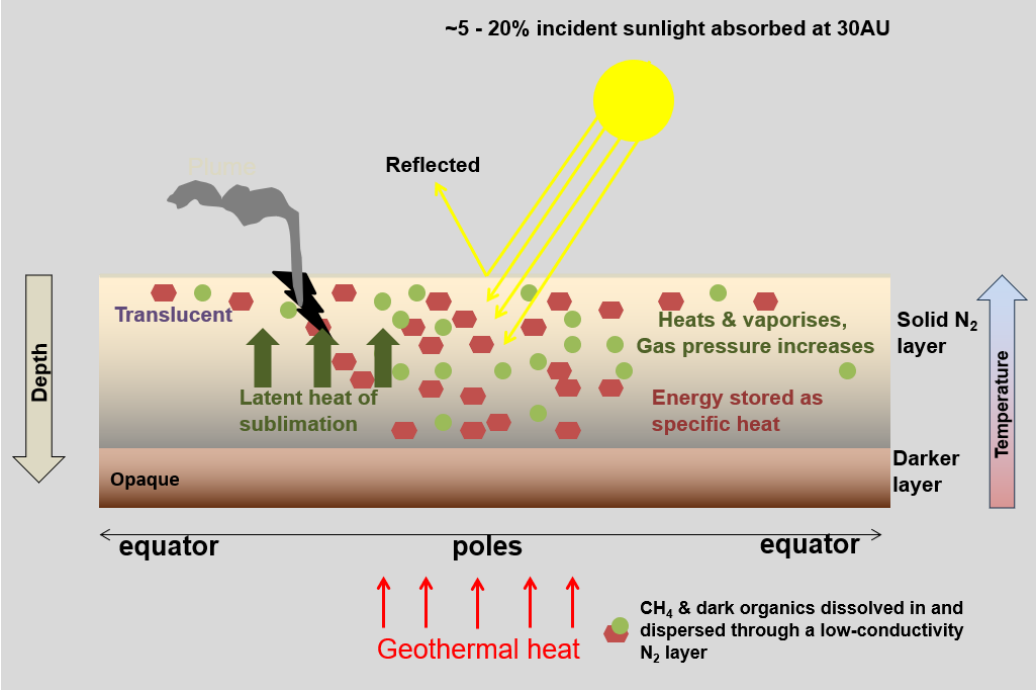

Figure 2.7. Schematic representation of classical solid-state greenhouse model after Brown et al. (1990) showing the absorption of sunlight into a low-conductivity translucent layer of solid nitrogen, the trace impurities dissolved in and dispersed throughout. Heat trapped in the subsurface layer creates a thermal gradient and energy stored as specific heat can be released as latent heat of sublimation by venting of nitrogen gas through fissures (not to scale).

The second greenhouse model of Brown et al., (1990) is a variation on the classical greenhouse and is termed a "super" greenhouse. The major difference between it and the classical greenhouse model is that insolation is not absorbed by a layer of solid nitrogen and remains largely unattenuated, and is absorbed in a dark, opaque layer at the base of the nitrogen ice. Thus, the thermal gradients can be somewhat larger, and the nitrogen ice layer equivalently thinner for a given amount of absorbed insolation to support the thermodynamic temperature differences required for the venting of nitrogen gas.

The role of the internal heat source due to radioactive decay in Triton's core was investigated with respect to geyser-like plumes (Duxbury & Brown, 1997). They described a model that is based on heat transport in the solid-nitrogen polar caps due

to thermal convection and conduction. They show that an increase of just 1 K of the temperature of N_2 in the subsurface ice above that of the surface temperature would be sufficient to at least double the vapour pressure which would drive the plumes to the observed height of 8 Km. Solid-state convection would occur should the nitrogen ice layer be thick enough and the average solid N_2 grain size small enough. The model assumes that Triton is completely differentiated, with a core being approximately 70% of the satellite's mass (density, determined as 2.054 g cm^{-3} from Voyager 2 data). Because of the small thermal conductivity of solid nitrogen, this translates into a large thermal gradient. Figure 2.8 is a schematic representation of this process after Duxbury and Brown (1997).

Because Triton's plumes are narrow columns ~8 km in height, with tails extending horizontally for distances over 100 km, Ingersoll & Tryka, (1990) have suggested that the plumes are an atmospheric rather than a surface phenomenon. The closest terrestrial analogues may be dust devils, which are atmospheric vortices originating in the unstable layer close to the ground. Since Triton has such a low surface pressure, extremely unstable layers could develop during the day. Patches of unfrosted ground near the subsolar point could act as sites for dust devil formation because they heat up relative to the surrounding nitrogen frost.

The resulting convection would warm the atmosphere to temperatures of 48 K or higher, as observed by the Voyager radio science team (Tyler et al., 1989). The atmosphere above these hot spots would rise adiabatically, possibly carrying dust particles upwards at a derived rate of 20 m s^{-1}.

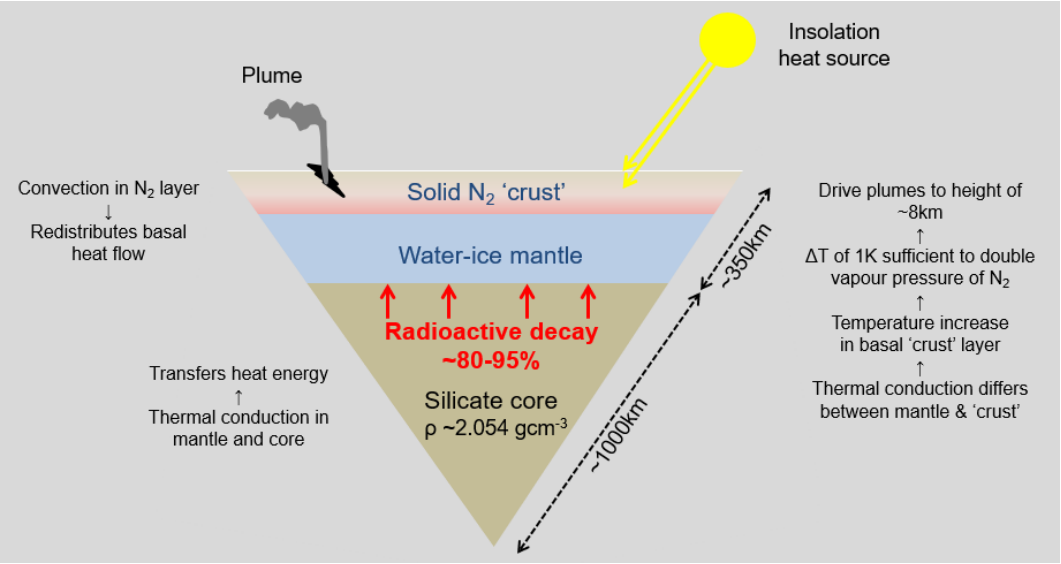

Figure 2.8. Schematic representation of conductive-convective model after Duxbury and Brown (1997), showing thermal convection in the N_2 ice crust and the conduction of radioactive heat from Triton's silicate core (not to scale).

2.4 Discussion

The models reviewed to account for cryovolcanic activity on Titan, Enceladus and Triton all propose explanations for the composition of the plumes, the interior structure of the satellites and various mechanisms responsible for bringing cryolava to the surface. Despite this, no model reviewed has explicitly addressed the vent geometries of the observed plumes on Enceladus and Triton (and possibly Titan), nor the kinetics of clathrate dissociation, viscosity changes in the rising cryomagma, the flow velocity regime and thermodynamic energy balance.

CHAPTER THREE

Clathrate dissociation model: Computational method

3. Clathrate dissociation model: Computational method

As stated in chapter one, the primary goal of this study is to examine the potential role that clathrate hydrate dissociation has in explosive cryovolcanism on icy satellites of Saturn and Neptune, specifically Enceladus, Triton and Titan. The primary objective towards realising this goal is to improve and extend the current models of cryovolcanism on icy moons, developed by Fortes (2007) and Fortes et al. (2007), hereafter collectively dubbed Xenolith I. The numerical model developed for this study, henceforth called Xenolith II, satisfies this requirement, and redresses some of the limitations of the Xenolith I model. The Xenolith II model is a computer simulation representing the physical, chemical and thermodynamic processes considered likely to prevail on icy moons in the outer solar system, where clathrate dissociation is proposed as the mechanism for explosive cryovolcanism. The model is designed to calculate the fragmentation pressure and depth, the local velocity and sound speed in the plume, the height of the of the plume, the effect of bubbles and the crystallisation of ice on the viscosity of the plume, and the kinetic energy of the eruption. These computed variables

are used to determine the plume dynamics: laminar to turbulent flow (Reynolds number), and transition from subsonic to supersonic flow velocities (Mach number). Finally, the latent heats of clathrate dissociation, sublimation and crystallisation are obtained and used to estimate the thermodynamic energy balance associated with the eruption. Applications of this model to Enceladus, Triton and Titan are presented in chapter 4, 5 and 6 respectively, each section beginning with a discussion of specific assumptions made in respect of each moon, followed by a description of the results of each model application. The physics of clathrate hydrates is presented in the following section, as a background to the central premise of the Xenolith II model, that clathrate dissociation is a mechanism for explosive cryovolcanism.

3.1 Clathrate hydrates

A general description of clathrate hydrates is outlined in chapter two. However, central to the formulation of the Xenolith II model and other clathrate dissociation models (Keiffer et al., 2006, Fortes, 2007 and Fortes et al., 2007) is the dissociation of clathrate hydrates as a mechanism for generating explosive cryovolcanism. The physics of the formation and dissociation of a single guest clathrate (e.g., methane) under different equilibrium conditions is outlined in the following section (3.1.1) and the complex phase relationships of mixed guest clathrates (as observed in the plume of Enceladus, Triton and Titan) are discussed in section 3.1.2.

3.1.1 Physics of clathrate hydrates

The equilibrium state of a system under a given set of conditions provides a means of classifying clathrates hydrates, and phase diagrams are a graphical representation of the

values of the thermodynamic variables when equilibrium is established among the phases of a system. In thermodynamic terms, the state of a system is defined by *intensive* properties, such as pressure and temperature which are independent of the mass of a system, and by *extensive* properties, such as volume and internal energy. These properties are used to mathematically describe changes in energy and entropy in a system that is subject to mechanical, thermal or chemical action. Thermodynamic laws describe the conditions that lead to the minimization of free energy, or Gibbs[10] energy, in a system, thereby predicting the equilibrium state of the material (in this case, the clathrate hydrate phase). For phase transformations that occur at constant temperature and pressure, the relative stability of a system is determined by the change in Gibbs free energy (G) where:

$$dG = dH - TdS \qquad \text{(Eq. 3.1)}$$

where dS is the change in entropy, a measure of the randomness of a system, T is temperature and dH is the change in enthalpy, which is a measure of the heat content of the system and can be represented as:

$$dH = dE + d(PV) \qquad \text{(Eq. 3.2)}$$

where E is the sum of total kinetic and potential energy of the atoms in the system and P and V are pressure and volume respectively. Internal energy changes during hydrate phase transformation, and heat is either absorbed (endothermic) or given off (exothermic). The internal energy is dependent on changes in the volume of the system where $dE = TdS - PdV$. A system is in stable equilibrium if it has the lowest possible value of the Gibbs free energy, where $dG = 0$ and thus a highly stable state will have the

[10] Gibbs free energy is the thermodynamic potential energy that is minimized when a system reaches chemical equilibrium at constant pressure and temperature.

lowest enthalpy and highest entropy. Any transformation that results in a decrease in Gibbs free energy is possible, but the reverse cannot occur, therefore, for any phase transformation:

$$\Delta G = G_{final} - G_{initial} < 0 \qquad \text{(Eq. 3.3)}$$

where $G_{initial}$ and G_{final} are the free energies of the initial and final states, respectively. The kinetic behaviour of clathrate formation and dissociation is not as well understood as that of the P-T conditions of thermodynamic equilibrium (Yin et al., 2016). During the formation of sI and sII structures, intermediate metastable crystalline phases can occur, which are thermodynamically unstable, or different from the stable structures. These structures can persist sufficiently long enough to be detected (either by Raman and NMR spectroscopy, or neutron and x-ray diffraction). These metastable states might maintain a stable structure for up to a month, even after the clathrate is removed from its thermodynamic P-T conditions (Koh et al., 2009).

During the formation of clathrates, as gas pressure increases, the Gibbs free energy of the gas is increased by decreasing its entropy; the clathrate's Gibbs free energy is minimally affected by pressure, since the pressure is much less than the bulk modulus[11], thus an increase in pressure favours clathrate formation. Volume and entropy changes during clathrate formation are negative and the Clausius-Clapeyron relation[12] predicts a positive value for dT/dP for the line separating two coexistent phases on a pressure-temperature phase diagram. This phase boundary pressure is the dissociation pressure.

[11] The bulk modulus K is the measure of how incompressible a substance is and is the ratio of an infinitesimal increase in pressure P to the resulting decrease in volume V where $K = -V(dP/dV)$.

[12] The Clausius-Clapeyron relation specifies the temperature dependence of pressure, most importantly vapor pressure, at a discontinuous phase transition between two phases of matter of a single constituent.

Figure 3.1 illustrates the stability fields of a clathrate hydrate occupied by guest molecule X. As pressure increases, the compression of the guest molecule increases, resulting in a decreasing volume difference (ΔV) between the gas + liquid phase and the clathrate phase, and a decreasing dT/dP value. As the volume change between these phases becomes zero, ($dT/dP = 0$) the maximum temperature at which the clathrate phase is stable is indicated (Lunine & Stevenson, 1985).

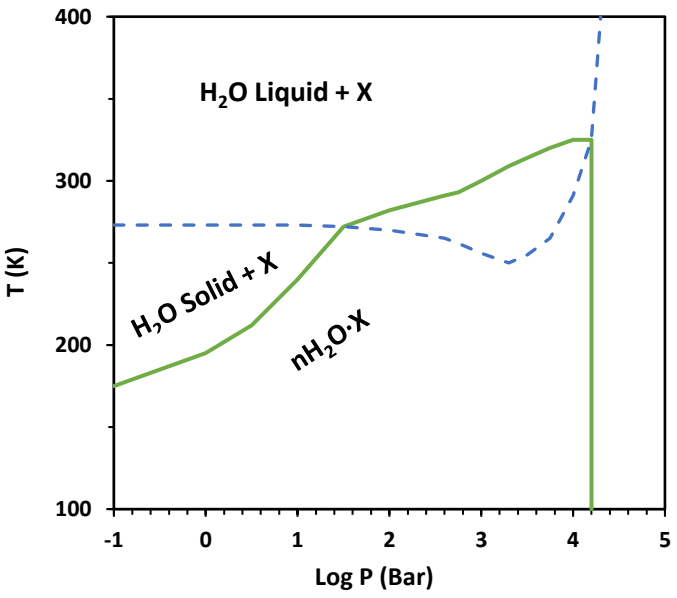

Figure 3.1. Schematic diagram of stability fields of clathrate hydrate occupied by guest X. The solid green line indicates the region in which the clathrate is thermodynamically preferred relative to H_2O liquid or H_2O solid plus coexisting component X. The dashed blue line is the H_2O liquid-solid boundary. The clathrate stability slope changes after crossing the H_2O liquid-solid boundary (after Lunine & Stevenson, 1985).

A significant amount of research has been conducted into clathrate stability, resulting in a comprehensive knowledge base for the phase boundaries and stability regions of gas hydrate systems (Fortes et al., 2010 and references therein). These data, obtained through experiments (e.g., calorimetric studies, neutron diffraction, Raman spectroscopy) have been incorporated into predictive programs and these include CSMGem (Colorado School of Mines Hydrate Prediction Program, 2007) and the clathrate modelling package developed by Bakker and colleagues (Bakker et al., 1996,

Bakker, 1997 and Bakker, 1998) of which the programs NOSALT and CURVES are part (see below). These programs can derive quantitative phase diagrams of the behaviour of fluid systems at variable temperature and pressure and can be used to predict equilibrium conditions and phase changes.

The NOSALT program was developed to obtain clathrate stability conditions in a salt free multi-component system (H_2O, CO_2, CH_4 and N_2). NOSALT calculates bulk densities and compositions and uses clathrate melting temperatures in combinations with liquid vapour equilibria, data from Raman spectroscopic analysis of non-aqueous phases, and volume fraction estimates of the phases present. The equation of state (EOS) for fugacity calculations in the equilibrium calculations is from Duan et al., (1996) and uses a mixing rule for combining the potential parameters of the unlike end members. The CURVES program calculates clathrate stability for a known fluid composition and salinity. Similarly, the equation of state (EOS) for fugacity calculations in the equilibrium calculations is from Duan et al. (1996).

The CSMGem model is based on the van der Waals and Platteeuw solid solution theory for hydrates which was developed in 1958 and, assuming a constant volume, predicted hydrate formation temperatures near the ice point at low pressures (van der Waals, J. H., and Platteeuw, J. C. (1958). The current CSMGem statistical thermodynamic model has been adapted and changed, removing the constant volume assumption, and incorporates more up-to-date models for aqueous, vapour, liquid hydrocarbon, ice and solid salt phases. The model, tailored specifically for the hydrocarbon industry, calculates multi-phase equilibria at any given temperature and pressure using an algorithm based on Gibbs energy minimization (after Gordon & McBride, 1994).

3.1.2 Mixed clathrate

Mixed guest clathrates have a more complex phase relationship (P, T) with several degrees of freedom, compared with that of a single-guest clathrate. Variables include the dissociation temperature and pressure at formation, equilibrium and dissociation, as well as the composition ratios, types of the individual gas species in the mixture and cage occupancy preferences. Dissociation data for binary clathrate systems have been extensively reported in the literature (Sloan & Koh, 2008), although experimental data for ternary systems (such as H_2O+CO_2 with either CH_4 or N_2) are limited, and for a quaternary system (H_2O+CO_2+CH_4+N_2) even more so. Differences in equilibria data vary considerably, depending on what system is under investigation. For instance, CO_2 and N_2 form sI and sII respectively where N_2 occupies the small cage structure of sII (Sloan & Koh, 2008). Bouchafaa and Dalmazzone (2011), in a study of mixed clathrates containing CO_2 and N_2, H_2 or CH_4 using differential scanning calorimetry, found that mixed hydrates of CO_2+ N_2 have a thermodynamic behaviour which is closer to the pure CO_2 hydrate at low pressures and that CO_2 + CH_4 mixed hydrate dissociation temperatures as a function of the pressure are quite close when the gas proportion varies. Bruusgaard et al., (2008) studied equilibrium conditions for the N_2 + CO_2 + H_2O system, experimentally determining vapour-liquid-hydrate equilibrium, and found that the equilibrium pressure increased with the increasing mole fraction of nitrogen in the gas phase. In a study predicting the equilibrium pressures of mixtures of CH_4, C_2H_6, C_3H_8, N_2, H_2, and CO_2 as a function of temperature, Klauda and Sandler (2003) found evidence of the double occupancy of nitrogen in the sII large $5^{12}6^4$ cavities (notation explained in section 2.1) at high pressure in a mixed clathrate. The phase equilibrium behaviours of CH_4-N_2-CO_2 gas mixtures were analysed with differing CH_4 concentrations

and N_2/CO_2 ratios, and the resultant occupancies of guests in hydrate cavities evaluated by Sun et al., (2017). Their results indicated that CO_2 molecules were mostly trapped in large cavities ($5^{12}6^2$), while N_2 and CH_4 competed for the occupation of small (5^{12}) cavities (Figure 3.2).

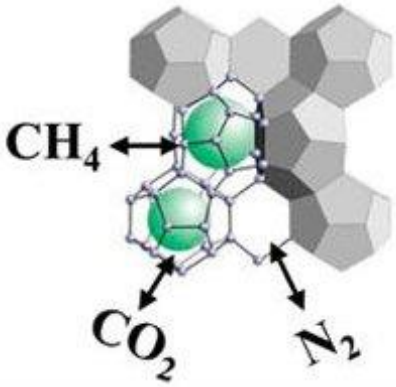

Figure 3.2. Schematic diagram of a mixed clathrate hydrate structure of a CH_4-N_2-CO_2 gas mixture (image used with permission from Sun et al., 2017).

3.2 Xenolith II model input and assumptions

Initial and boundary conditions of the Xenolith II model are set from data obtained from space missions, ground-based spectrometry and analysis of these data. Input parameters include observed data for each moon (mass, density, surface temperature, surface gravity and surface pressure) and physical characteristics of the volatiles assumed to be in the cryomagma (molecular mass, density, solubility and viscosity). The ratio of the entrained volatile component, vent geometries and vapour mass flow rates are determined from analyses by various workers. The cryomagma is assumed to be liquid water at its ambient pressure liquidus, and the density of the cryomagma is presumed to be the same as that of the surrounding ice crust on Enceladus. The ice shell on Triton is 937 kg m^{-3} (Hu et al.,2019) and 1,065 kg m^{-3} on Titan (Fortes et al., 2007) Conditions for explosive cryovolcanism resulting from the dissociation of clathrates

include the probability that each moon has a subsurface body of water, and a heat source.

Because water is denser than ice, the buoyancy-driven ascent of cryomagma should not be possible. However, this 'buoyancy crisis' (Kargel, 1995) or negative buoyancy has been overcome, not only on Enceladus, but in other examples of cryovolcanism in the outer Solar System (Triton, and possible Europa). An increase in the pressure on a liquid reservoir (e.g., caused by tectonic stresses, tidal flexing or volume changes) could result in the eruption of water on smaller icy satellites, as argued by Manga and Wang (2007). The addition of volatiles (such as CO_2, SO_2, CO, N_2, CH_4, NH_3) which reduce the density of aqueous cryomagma, formed in-situ from hydrothermal activity at the rock-ice interface, might overcome the bouyancy issue, and recent studies have proposed that the detection of molecular hydrogen in the plume could be evidence for this (Waite et al., 2017, Tobie, 2015). The density of the ice shell could be modified by the addition of high density silicates, increasing the density of the ice (e.g., Showman et al., 2004; Fortes et al., 2007). Finally, the density of the liquid cryomagma will be lowered by the presence of exsolved volatiles in the cryomagma.

3.3 Xenolith II Model description

The model is implemented using Microsoft Excel which allows for data input, computation using visual basic for applications, and graphing tools. The graphing capabilities are useful to obtain the slopes of graphs for certain relationships such as solubilities and Mach numbers (see appendix I and II). Additionally, analytical tools such

as trendlines (best fit or regression lines) form part of Excel, allowing for the graphical illustration of any trends in a data series.

The Xenolith II model begins with the construction of a static pressure profile of selected pressure points, incrementally increasing the pressure, starting at the surface pressure. At each pressure point the depth at which the pressure occurs is calculated, based on the input values associated with the moon being modelled (crust density and surface gravity). At each fixed pressure point, the mass fraction and exsolved gas fraction of each gas component in the plume is determined (after Fortes, 2007). Thereafter a set of equations is developed and employed to describe the physical and chemical behaviour or thermodynamic state at each pressure point in the plume for each of the different vent geometries (circular conduits and/or fissures) of varying areas. These equations are then solved according to a set of initial and boundary conditions (input parameters), and are modified or developed based on the model assumptions. The results of these computations are then used to predict different plume and flow dynamics in each of the different vent geometries being modelled. The following sections outline the set of equations and processes applied to simulate and describe both the cryomagma plumes of Enceladus where clathrate dissociation is proposed as the eruptive mechanism and the plumes observed on Triton. Figure 3.4 is a process flow diagram for the Xenolith II model.

3.3.1 Fragmentation pressure and depth

In volcanic eruptions on Earth, magmatic volatiles are dissolved in the melt, and upon ascent, their pressure-dependent solubility leads to exsolution by the formation of

bubbles and their diffusion into existing bubbles. As the magma ascends, existing bubbles expand rapidly and shear stresses act on the thinning walls of the bubbles. As the resulting total gas bubble volume fraction becomes large enough, the bubbles begin to coalesce. Closer to the surface, the bubbles increase in number and size so that the gas volume may exceed the melt volume in the magma, creating an unstable foam, where gases are released into the rising magma. The accelerating, expanding foam becomes unstable and is said to fragment when the total bubble volume reaches ~75%, producing an explosive eruption (Sparks, 1978, Pinkerton et al., 2002; Gonnermann, 2015). At the point of fragmentation, the magma changes from a liquid containing gas bubbles to a continuous gas containing droplets and clots of liquid, which may still contain bubbles (Pinkerton et al., 2002).

In the Xenolith II model, it is assumed that the cryomagma is a water-based fluid containing entrained clathrates, as on Enceladus, Triton and Titan. Gas is released from the clathrate host and a certain amount is dissolved in the cryomagma, the rest forming gas bubbles, in process similar to that of silicate-based volcanism on Earth. Fortes et al. (2007) predict that fragmentation occurs on Titan when the total gas bubble volume is between ~60-85%, and Fortes (2007) predicts that the plumes on Enceladus fragment when the volume fraction of gas bubbles exceeds approximately 75%. In a recent model of briny cryomagma eruptions on Ceres (Yumoto et al., 2023), fragmentation is predicted to occur when the bubble volume fraction is 80%. For the purposes of this model, fragmentation is therefore reasonably assumed to occur when the bubble volume fraction reaches approximately 75%. It should be noted that the cryomagma is assumed to be liquid H_2O at depth, and as pressure decreases on ascent, the triple point of water is reached. This is very near the surface on Enceladus (5.3 m), Triton (0.8 m) and Titan (0.4 m). At the triple point, three phases (ice, solid and liquid) can exist

together, and it is conceivable that some bubbles can remain in the liquid component of the cryomagma, although it is likely that most of the bubbles will have released their gas into the cryomagma. Thus, at any point from depth (when the entrained clathrates begin to exsolve) to the surface, the cryomagma is assumed to contain exsolved gas from the dissociation of entrained clathrates, (directly into the cryomagma and formed into bubbles) and liquid cryomagma. Since the ratio of bubbles and exsolved gases is unknown (even after fragmentation), the total mass fraction of exsolved volatiles (CO_2, N_2 and CH_4) in the cryomagma is termed 'exsolved gas fraction' and refers to both bubbles, and/or the fraction of gas released from bubbles.

The eruption dynamics of the plume depend, in part, on the total mass fractions of the exsolved gas components and their solubility as a function of pressure. The Xenolith II model determines the solubilities of CO_2, N_2 and CH_4 as a function of pressure on Enceladus (in pure water and 3.5% NaCl and water), Triton (in pure water) and Titan (10.6 wt% $(NH_4)_2SO_4$ and water, and 40% wt% $(NH_4)_2SO_4$ and water), using the CLATHRATES software (version 1) package (Bakker et al. 1996, Bakker 1997, 1998). An example of the different solubilities of CH_4 at various pressures and salinities, showing the increase in solubility with decreasing pressure, and the effects of varying concentrations of NaCl in water is shown in Figure 3.3.

Fortes (2007) developed a version of the bubble growth model of Pinkerton et al. (2002) and Head and Wilson (2003), modified to account for each of the three exsolved gas species in the plume, which was used to determine the pressure at which fragmentation occurs. These entrained volatiles and cryomagma compositions are different for Triton and Titan.

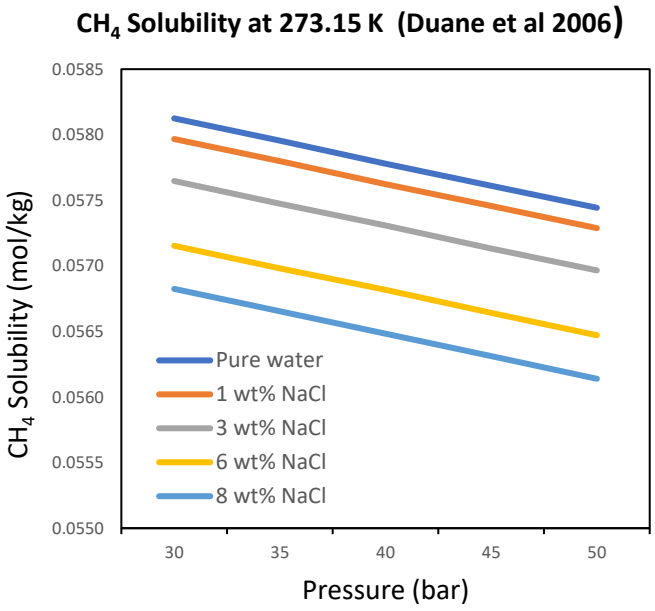

Figure 3.3: Derived solubilities of CH_4 at various pressures and salinities, showing the increase in solubility with decreasing pressure, and the effects of varying concentrations of NaCl in water. Calculated from programs for determining the solubilities of CO_2, N_2 and CH_4 (Duan & Mao, 2006). *www.geochem-model.org /programs.htm*

Initially, increasing pressure increments (arbitrarily selected) from the surface, beginning with a pressure of zero, the depth (in km) at each pressure *P* increment is calculated as follows:

$$D = ((P/\rho_{crust})(g_{surface}))/1000 \qquad \text{(Eq. 3.4)}$$

where *P* is pressure, ρ_{crust} is the density of the crust and $g_{surface}$ the surface gravity. Although gravity changes with depth in any planetary body, $g_{surface}$ is used in these calculations since the changes in gravity at increasing depths has minimal influence on the results; most of the high velocity of the plume is developed at shallow depths close to the surface.

At each pressure *P*, the mass fraction (Ø) for each gas identified in the plume is determined, beginning at the surface:

$$\emptyset_0 = ((X_{mf}/100) \cdot X_{fit}) \cdot (Gas_{content}/100) \quad \text{(Eq. 3.5)}$$

where $\emptyset_0$ is the gas mass fraction at the surface and X_{mf} is the xenolith mass fraction, set at a minimum xenolith abundance of ~16.5 wt%[13] for the nominal atmosphere and nominal clathrate composition in pure water (Fortes, 2007). The minimum xenolith load is dictated by the need to be consistent with the amount and composition of the gases in the plumes. Fortes (2007) and Fortes et al., (2007) examine the effects of incorporating variable mass fractions of entrained clathrate xenoliths, and calculate that the critical minimum load to achieve realistic plume velocities may be achieved at a xenolith abundance of ~16.5 wt% (on Enceladus) and ~10 wt% (on Titan). A minimum xenolith load of 16.5% is also assumed on Triton since both Enceladus and Triton are predicted to have ice I shells. Fortes (2007) points out that terrestrial igneous rocks can contain up to 60% foreign material. X_{fit} is the xenolith load multiplied by the water mass fraction in the clathrate[14]. The $Gas_{content}$ is the wt% of each of the gases obtained from literature values.

The gas mass fraction of each of the constituent gases in the plume will decrease as the pressure and depth from the surface increase (assuming that all the clathrates have dissociated at the surface). The gas mass fraction value ($\emptyset_0$) is then used to determine the exsolved gas fraction ($\emptyset_x$) for each gas species at each increasing pressure value *P* as follows:

[13] A 16.5wt% xenolith load was proposed by Fortes (2007) since the clathrate occupancy is assumed to be one part gas to 7.5% parts water and corresponds to a bulk occupancy of 75%.

[14] As an example, the nominal methane clathrate composition is 1 mole of methane for every 5.75 moles of water, corresponding to 13.4% methane by mass.

$$\emptyset_x = \begin{cases} 0 \quad , (\emptyset_\circ - (-a\left(\frac{P}{10}\right)^2 + b\left(\frac{P}{10}\right) - c)) < 0 \\ (\emptyset_\circ - (a\left(\frac{P}{10}\right)^2 + b\left(\frac{P}{10}\right) - c)), \ otherwise \end{cases} \quad \text{(Eq. 3.6)}$$

where $\emptyset_\circ$ is initial mass fraction (eq. 3.5) at the surface, *P* is pressure, and *a*, *b* and *c* are solubility fitting parameters obtained from the graph of mass fraction against pressure (Appendix I). Each constituent gas has a different solubility in the liquid cryomagma (water for example) and this needs to be factored into the above equation. For example, the very low solubility of N_2 in water means the melt becomes supersaturated in N_2 even when dissociation takes place at 20 km depth, where N_2 bubbles begin to form. CO_2 has a much higher solubility, and does not contribute to the exsolved gas fraction until the cryomagma is near the surface. For the purposes of this model, the solubilities of each gas species in the cryomagma are treated independently in equation 3.6. and as such, do not account for the increase or reduction in solubility of the same species when co-existing in a mixed gas in the same solution. For example, Liu et al, (2021) report that when CO_2 is paired with lower solubility gases (e.g., CH_4, H_2, O_2, etc.), CO_2 increases the solubility of the other component, while lowering its own solubility. Similarly, when pairing CO_2 with higher solubility gases (e.g., SO_2 and H_2S), the other gases can enhance CO_2 solubility. Solubility data for the quaternary system H_2O–CO_2–CH_4–N_2 would need to be obtained experimentally and is beyond the scope of this thesis, thus it is assumed that the discrepancies resulting from treating the solubilities independently is negligible.

By modifying the bubble growth model (Pinkerton et al., 2002; Head & Wilson, 2003) to account for each of the exsolved gas species, the bulk magma density (β) at each pressure *P* can now be determined. Here, *R* is the gas constant (8.314 kg mol^{-1}), *P* is the pressure, *ρ* is the density of the gas-free cryomagma and *T* is the cryomagma

temperature. In the following equation (after Fortes, 2007), n_i is the exsolved mass fraction of the volatile species *i*, and m_i is the molar mass of the *i*th species:

$$\beta^{-1} = [\sum_i (n_i RT)/m_i P] + [(1\text{-}n_{tot})/\rho] \quad \text{(Eq. 3.7)}$$

The bulk magma density equation described does not consider that the plume might contain solid crystals.

The exsolved gas fraction (V_b) can now be calculated at each pressure *P*, where:

$$V_b = 1 - \beta\,[(1 - n_{tot})/\rho] \quad \text{(Eq. 3.8)}$$

and β is the bulk magma density, n_{tot} is the sum of the mass fractions of all exsolved species, ρ is the gas-free magma density.

The pressure (P_F) at which magma is said to fragment occurs when the volume fraction of gas bubbles exceeds ~75% and becomes unstable, analogous to volatile exsolution in a magma flow on Earth, which results in an explosive eruption (Sparks, 1978).

3.3.2 Plume velocity

The vent geometries and magma flow rate are used to estimate the local magma flow velocity (*u*) at each pressure *P* of the model (Woods, 1995):

$$u = \frac{Q}{A\beta} \quad \text{(Eq. 3.9)}$$

where *Q* is the estimated flow rate or mass flux, β is the bulk density, and A is the estimated area of the vent, using π $(w/2)^2$ for a circular vent and *wl* for a fissure where *w* and *l* are the width and horizontal lengths, respectively. If the mass flux *Q* remains constant throughout the conduit, conservation of mass dictates that *Q* = β A *u*. As the bulk density decreases, the velocity must increase for *Q* to remain constant.

The height of the plume can be estimated using the following equation:

$$H = u^2/2g \quad \text{(Eq. 3.10)}$$

where H is the cryolava plume height, u is the velocity calculated at the vent pressure and g, the acceleration due to gravity.

The concept of sound speed (i.e., the velocity at which small disturbances in pressure or density are propagated through a multicomponent, multiphase liquid-gas system) is, together with the local flow velocity, fundamental to constraining, and thus estimating the behaviour of a magma flow regime (Lu & Keiffer, 2009). Sound speed (c) in a system is a partial derivative of pressure and density [15] and is related to the bulk modulus, K, and K = 1/β, where β is the compressibility, and to the density, ρ. In a multi component

[15] $c^2 = \left(\frac{\partial P}{\partial \rho}\right)_s$ where P is the pressure, and ρ the density and the derivative are taken for constant entropy (s) conditions. Sound wave propagation involves infinitesimally small and rapid amplitude changes and can be approximated as adiabatic and reversible, i.e., constant entropy (Lu & Keiffer, 2009). This is an isentropic process.

mixed gas and liquid system, the sound speed also depends on the mass fraction of gas and vapour in a system (Lu & Keiffer, 2009). An increase in exsolved gases in the Enceladus plume will have the effect of lowering the sound speed, as gases are more compressible than either liquids or solids; most of the volume of a gas is composed of large amounts of empty space between the gas particles.

The sound speed of a two-phase cryomagma (liquid water and volatile gases) will be very different from the sound speed in either pure component (Kieffer, 1977). The model assumes that before exsolution of the entrained clathrates begins, the liquid cryomagma is imcompressible and independent of pressure and temperature and a constant value for the sound speed in the gas-free cryomagma is adopted, assumed to be pure water in all instances where the sound speed is 1402.4 m s^{-1} (Haynes, 2011). Once exsolution begins, the sound speed in two-phase cryomagma is highly dependent on pressure (Keiffer, 1977). To determine this relationship, an equation for sound speed (u_s) is adapted (after Pinkerton et al., 2002) to account for the gas species incorporated into a bulk magmatic fluid:

$$u_s = \left[RT / \sum_i (m_i n_i)\right]^{\frac{1}{2}} \cdot \left[\sum_i \left(n_i + \left[\frac{(1 - n_i) m_i P}{\rho RT}\right]\right)\right] \qquad \text{(Eq. 3.11)}$$

where the variables R, T, m_i and n_i have the same meanings as in the preceding equations. To account for the sound speed in a two-phase fluid, equation 3.11 includes a term for the gas-free cryomagma density (ρ) which is set as a constant in the model. This is related to the sound speed (c) in water (cryomagma) by $c = (K/\rho)^{½}$ where K is the bulk modulus of water (Keiffer, 1977). A limitation of equation 3.11 is that when the

gas fraction (n_i) is very low, the equation breaks down and the calculated sound speed is greater than the sound speed of the gas free cryomagma, which is unrealistic. Equation 3.11 is designed to calculate the sound speed of a cryomagma containing exsolved gases, but when the exsolved gas fraction is extremely low (tending to zero), the first term in the equation becomes very large, thus producing a result that is physically impossible.

The Mach number (M) can be determined where M = (u/u_s) and together with the values for pressure P, magma bulk density β, gas mass fraction $\emptyset$, sound speed u_s, and magma rise speed u, as a function of pressure P will be used to present an analysis of the flow regime in circular conduits and fissures and show the transition from subsonic to supersonic conditions. When flow velocities are lower than the sound speed, flow is considered subsonic and is nearly incompressible, whereas flow velocities greater than the sound speed result in supersonic flow. In circumstance were flow velocity equals sound speed, the resultant condition is known as 'choking' (choked to the sound speed where Mach = 1) and this condition plays a major role in controlling the mass flux from a depressurizing system where low sound speed would choke at relatively low velocities and consequently lower mass flux from a system (Lu et al., 2009; Rowell et al., 2022). At the point of choking, the flow cannot adjust to the pressure changes in a parallel-sided conduit (Bercovici & Michaut, 2010). Here, an increase in the driving pressure causes no change in flow rate, and is associated with possible vent flaring, wall failure and the development of an acoustic shock or discontinuity in the gas pressure and density (Wilson et al., 1980, Mitchell, 2005). The Xenolith II model incorporates a parallel-sided geometry as well as a constant flow rate, and therefore does not include the effects of choking (vent flaring or wall failure for example). However, the choking

point is determined under these constraints to indicate the depth at which choking occurs (Mach 1). Supersonic flow occurs when the sound speed is less than the velocity and the Mach number is > 1.

3.3.3 Viscosity

The viscosity of a fluid is a measure of its resistance to flow, relating the stress applied to a fluid and the fluid's response. Viscosity controls the rate of magma flow in response to a given pressure change and the rate at which gas bubbles and solids (rock fragments and crystals) move through a magma. For a mixed component cryomagma, the viscosity can be estimated using the following equation (independent of temperature in the Xenolith II model) adapted from Herning and Zipperer (1936) which sums the partial viscosities, weighted by the square root of the molecular weight of each species in the mix :

$$\eta_{mix} = \frac{\sum_i x_i \eta_i (m_i)^{\frac{1}{2}}}{\sum_i x_i (m_i)^{\frac{1}{2}}} \qquad \text{(Eq. 3.12)}$$

where x_i is the mole fraction of component *i* of viscosity η_i and m_i is the molecular weight of component *i*. The equation is applied to all phases of the cryomagma at different depths, beginning where the cryomagma is a gas free liquid water, where the viscosity is 1791.1 µPa·s (Haynes, 2011). As the fluid rises to the surface, the viscosity is calculated

as gases are exsolved into the cryomagma and includes the viscosities of each of the exsolved gases, determined at different depths. The cryomagma is assumed to be liquid water and entrained gases up to the triple point of water, where it is then predicted that the water is in the vapour phase where the viscosity is 8.9 µPa·s (Haynes, 2011).

Before fragmentation, the motion in the plume is assumed to be laminar and is thought to become turbulent after gas exsolution where bubbles formed cause the rising magma to accelerate. The dimensionless Reynolds number (*Re*) is used to predict the transition from laminar to turbulent flow; it is related to the density and velocity of the fluid and is inversely proportional to the viscosity. The Reynolds number represents the ratio of inertial forces (force due to the momentum of the fluid) to viscous forces in a fluid, subject to movement due to velocity. The inertial force, in the direction of the flow, is countered by the viscous force which is in the reverse direction of the flow. Where viscous flow dominates, flow is laminar (smooth, constant fluid motion) and Reynolds numbers are small (Re < 2000), whereas at higher Reynolds numbers, inertial forces dominate, and flow is said to be turbulent ('chaotic' changes in pressure and flow velocity). A large Reynolds number (Re > 4000) indicates that viscous forces are negligible, and large scale fluid motion dominates where there is no viscous resistance to fluid motion. A transition period, where flow is unstable, is defined by Reynolds numbers between 2000 and 4000. The Reynolds number can be determined (Mitchell, 2005) for a fissure conduit by:

$$Re = \frac{4ru\beta}{\eta} \qquad \text{(Eq. 3.13)}$$

And for a circular conduit by:

$$Re = \frac{2ru\beta}{\eta} \quad \text{(Eq. 3.14)}$$

where *r* is the conduit radius or fissure half width, *u*, the local magma flow velocity, β, the bulk density and η, the viscosity of the mixed component plume.

3.3.4 Dissociation kinetics

In this model, rising cryomagma is treated isothermally and since the velocities of the rising cryomagma will likely ensure that any thermal contact with the walls is minimal, the ascent is treated adiabatically. Energy needs to be conserved so as not to contravene the first law of thermodynamics, and gains in kinetic and potential energy need to be offset by other losses in energy, specifically by enthalpy (Mitchell, 2005). Gas bubbles resulting from the dissociation of entrained clathrates that are released into the plume increase the kinetic energy of the plume. The work done by the system during these phase transitions is the sum of the kinetic energy (K_E) of the plume which moves with velocity u, and the potential energy due to the shift of the centre mass of the plume in the Enceladus gravity (Brilliantov et al., 2008).

Since *u* is the upward velocity in a plume, the total kinetic energy in joules ($kg \cdot m^2 \cdot s^{-2}$) can be approximated by:

$$K_E = 0.5mu^2 \quad \text{(Eq. 3.15)}$$

where m is the mass in kg. Using the relationship where bulk density (β) = mass (m)/volume (v), the mass can be obtained, where the volume of a cubic metre is 1000 litres. Kinetic energy changes resulting from the dissociation of the mixed clathrates into the plume will be analysed from the values determined at each pressure *P* for each of the calculated velocity profiles of the conduits and fissures defined in the model.

3.3.5 Thermodynamic energy balance

The first law of thermodynamics states that the change in the internal energy of a system is equal to the amount of heat supplied to the system, minus the amount of work done by the system on its surroundings, where the internal energy excludes the kinetic energy of motion and the potential energy of the system as a whole, keeping account of the gains and losses of energy of the system that are due to changes in its internal state.

The Xenolith II model addresses the dissociation of the clathrate entrained in the xenolith load in the plume, and the expansion of the exsolved gas bubbles which contribute to the cooling of the cryomagma as it ascends. The dissociation enthalpy (ΔH_{diss}) or latent heat[16] of a mixed gas clathrate hydrate is defined as the heat needed to decompose the clathrate structure and release 1 mol of the guest gas mixture. Enthalpy is determined by the number of hydrogen bonds per guest molecule and the interactions between guest molecules. In a mixed clathrate hydrate, calculating the number of

[16] During a change of state at constant pressure the increase or decrease of enthalpy is equal to the latent heat of transformation.

hydrogen bonds per guest molecule is complicated by the structural type of the cage, the cage occupancy and the relative sizes of the guest molecules and cavities (Kwon et al., 2011). The enthalpy of a mixed clathrate can be estimated based on the mole fractions of N_2, CH_4, and CO_2 in the plumes, and the values of enthalpies of dissociation obtained from calorimetric studies. Both Lu and Keiffer (2009) and Fortes (2007) used this method to determine the enthalpy of dissociation of the mixed hydrate from Kang et al. (2001) for pure N_2, CH_4, and CO_2 clathrates. Sloan & Koh (2008) however, have adopted an indirect method to determine the enthalpy of dissociation from the univariant slope of the phase equilibrium line (ln *P* versus 1/*T*) using the Clausius-Clapeyron equation[17].

For the energy balance of the system such as that of Enceladus, where there is a heat source and a reservoir, the clathrate decomposition process and energy required to explosively expel material from the system, the following relationship can be defined (after the method used by Lu and Keiffer, 2009):

$$Q_{\mathrm{net}} = m_{\mathrm{out,g}} L_{\mathrm{dis}} + m_{\mathrm{out,v}} L_{\mathrm{sub}} + m_{\mathrm{out,l}} L_{cry} + m_{\mathrm{out}} \frac{\mathrm{P_r}}{\rho_{\mathrm{r}}} \qquad \text{(Eq. 3.16)}$$

where the left-hand side of the equation, Q_{net} is the net heat gained by the system and $Q_{net} = Q_{in} + Q_{source} - Q_{out}$. The heat supplied by the liquid reservoir is Q_{in} (from the reservoir) and Q_{source} (the endogenic heat described in section 3.2.2). Q_{out} is the total

[17] $\frac{dln(P)}{d(1/T)} = -\frac{\Delta H_{diss}}{zR}$ where *P* is the pressure, *T*, the temperature, ΔH_{diss}, the enthalpy of dissociation, *R*, the universal gas constant and *z*, the compressibility factor ($z = z^0 + \omega z^1$). Values of z^0 and z^1 can be obtained from tables (Smith et al., 2001) and ω, the acentric factor (a measure of the non-sphericity of molecules), from the DIPPR database (2000).

power radiated from the SPT terrain. The right-hand side of this relationship indicates the heat required for clathrate dissociation and the acceleration of the outgoing plume and includes terms for the latent heat of dissociation (L_{dis}), the latent heat of sublimation (L_{sub}) and the latent heat of crystallisation (L_{cry}). The mass flow rate of the plume, mass flow rate of the gas component, the mass rate of the sublimated water vapour and the mass rate of the liquid water are m_{out}, $m_{out,g}$, $m_{out,v}$ and $m_{out,l}$ respectively. P_r is the reservoir pressure, and ρ_r is the plume density.

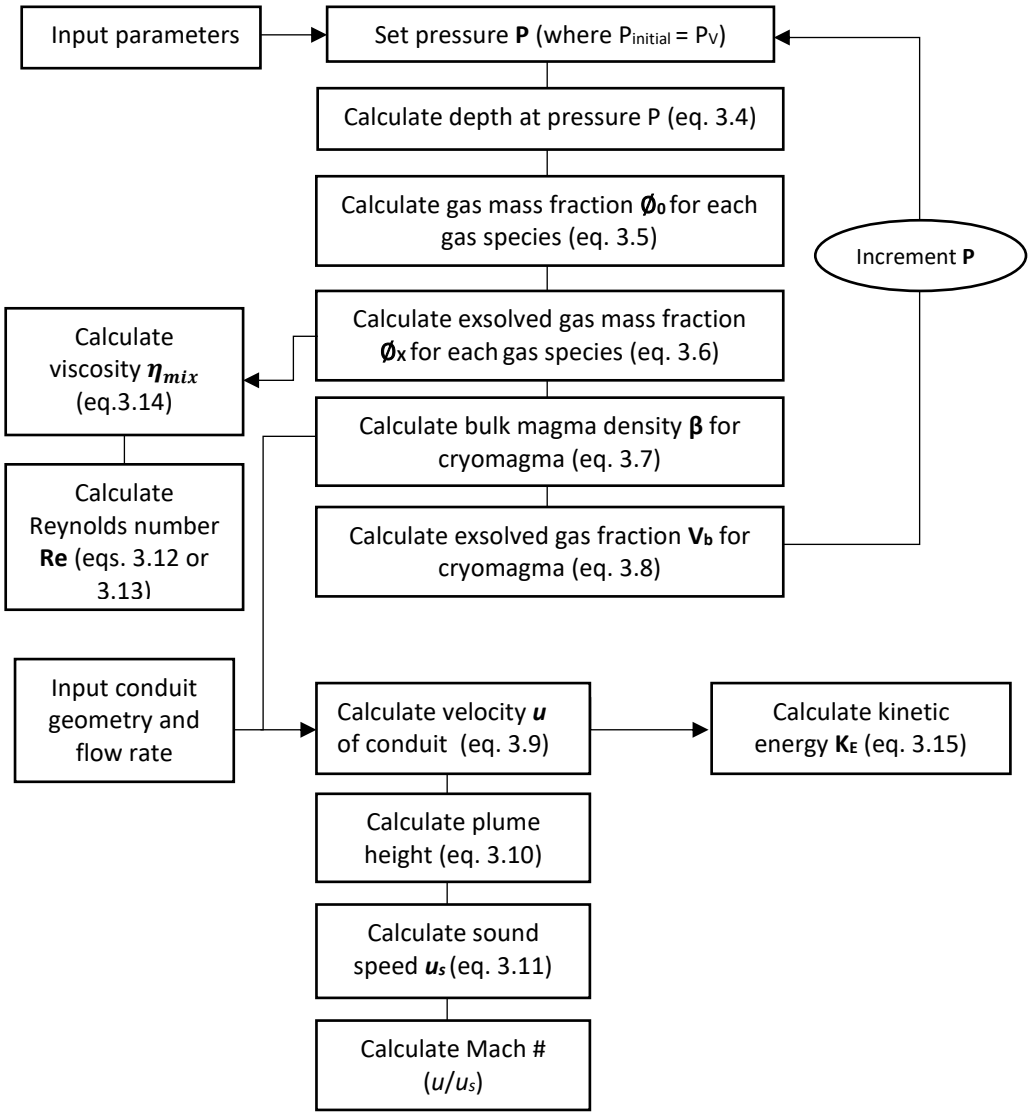

Figure 3.4. Xenolith II model process flow diagram where $P_{initial}$ is the starting pressure of the model and P_V is the vent pressure.

3.4 Discussion and conclusions

The numerical model described in this chapter presents an improvement of the current models of cryovolcanism on icy moons where clathrate hydrate dissociation is proposed as a mechanism for explosive eruption. Both pure water and saline cryomagmas are considered for Enceladus, as well as a selection of vent geometries (circular conduits and fissures) of varying areas. The application of the model to Triton considers two separate volatile content scenarios, three different vapour mass flow rates, and varying circular vent areas. Two cryomagma compositions, three mass flow rates and varying circular vent areas were investigated for Titan.

The Xenolith II model investigates the plume and flow regimes from the determination of flow velocity, sound speed and viscosity. The kinetic energy of the erupting plume is determined, as well as the extent to which the latent heats of clathrate dissociation, sublimation and crystallisation contribute to the thermodynamic energy balance of the plume. The application and results of this model will be presented and evaluated for Enceladus, Triton and Titan in the next three chapters, examining the potential role that clathrate hydrate dissociation might have in explosive cryovolcanism on these icy moons.

CHAPTER FOUR

Cryovolcanism model results and discussion - Enceladus

4. Cryovolcanism model results and discussion - Enceladus

The results of the Xenolith II model described in chapter 3 are presented in this chapter, as applied to Enceladus and serve to contribute to this study's primary goal of examining the potential role that clathrate hydrate dissociation has in explosive cryovolcanism on the icy satellites of the outer solar system. Model assumptions and input for Enceladus are presented in section 4.1, and the results of the modelling in section 4.2. The computed outcomes of the model will be compared with mission data observations and analysis from other workers and then evaluated in terms of the primary goal of this thesis (section 4.3).

4.1 Xenolith II assumptions and input

To approximate the physical behaviour of the plumes of Enceladus, several assumptions need to be made, based on observation and measurement from Cassini and informed judgement based on available analysis and literature. The assumptions made serve to constrain the boundaries of the Xenolith II model and are outlined in the following

sections which describe model input parameters, current data for Enceladus (mass, surface gravity, internal structure) and physical constants (table 4.3).

4.1.1 Internal structure of Enceladus

From observations of the mean radius and density of Enceladus, the moon is assumed to be differentiated with a rocky core ~169 km in diameter (ρ_{core} = 3000 kg m^{-3}) overlain by an ice-rich mantle (ρ_{mantle} = 1000 kg m^{-3}) ~82 km deep (Fortes, 2007).

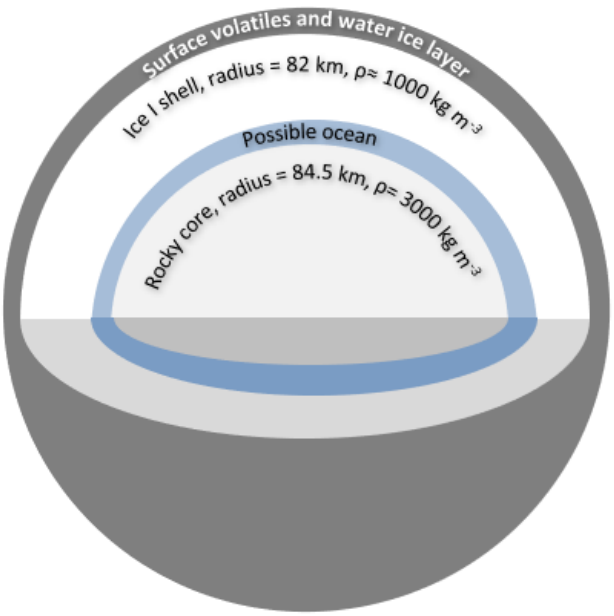

Figure 4.1. Internal structure model of Enceladus (not to scale), after Fortes, 2007. showing the possible location of an ocean (discussed in section 4.1.2).

The Xenolith II model assumes an equal density for the ice crust and the aqueous cryomagma.

4.1.2 The case for a salty subsurface ocean on Enceladus

Evidence suggests that a body of water exists beneath the icy crust of the south polar region (SPT) of Enceladus; gravity measurements taken by Cassini between 2010 and

2012 indicate a negative mass anomaly at the SPT, where there was less mass than would be expected in the case of a uniform spherical body (Fig. 4.1). The absence of material at the surface was therefore thought to be compensated for at depth by a material denser than ice, most probably a body of water at depth (a positive anomaly). The two anomalies account for the measurements (Iess et al., 2014). Other workers (Schmidt et al., 2008; Ingersoll & Pankine, 2010) analysed the ratio of the mass flux in the solid to the total vapour mass flux and suggested that this would be much larger if the geyser jet particles were only produced entirely by the expansion, adiabatic cooling and direct condensation of vapour to solids thus proposing a liquid reservoir source. Porco et al., (2014) proposes that the solid/vapour ratio in the jets indicates that the source of most of the jets is liquid water. Enceladus has a slightly eccentric orbit and somewhat elongated shape, and is subject to periodic torques that force harmonic oscillations (called physical librations) in its orientation, on top of an overall synchronous rotation. Thomas et al. (2016) argue that these physical librations of Enceladus is too large for there to be a rigid connection between the core and crust, and deduce that this confirms that the subsurface liquid feeding the plumes emanating from the south polar region is part of a global subsurface ocean.

There is speculation however concerning the compositional nature of reservoir, and the internal processes associated with a sub-surface body of water which has resulted in the observed plume composition. In-situ spectrometry, and data from Cassini's CDS and INMS, have provided data to inform this debate. The chemical composition of the plumes is of great interest because it provides a direct insight into the make-up of the interior of the moon. The plume contains gas components (H_2O, CO_2, N_2 and CH_4), organic matter (alcohols, aldehydes and hydrocarbons) and solid components (H_2O ice,

sodium salts, silicates, organic materials, and carbonates). The presence of sodium could be considered evidence for liquid ocean since it is highly soluble in water and it is assumed that a subsurface ocean that has prolonged contact with a silicate core would be rich in sodium salts, and easy to detect when dispersed in its atomic form (Spencer, 2009). Schneider et al. (2009) used ground-based spectroscopic analysis of emissions in Enceladus's plumes and found a low sodium content, 30 times lower than the sodium-poor ocean model described by Zolotov (2007). Schneider et al. (2009) conclude that vapour in the plume could result from the evaporation of a low-salinity ocean, either through warm ice sublimation or clathration. In an analysis of the ice grains from the plume using results from Cassini's onboard cosmic dust analyser, Postberg et al. (2009) found that although the grains are dominated by water ice, ~6% are saline, containing ~1.5% of a mixture of sodium chloride, sodium carbonate and sodium bicarbonate. They conclude that these ice grains are a result of direct freezing of salty water from the ocean. In later studies, Postberg et al. (2011) found from analysis of Cassini's cosmic dust analyser (CDA) that salt-rich ice particles are found to dominate the total mass flux of ejected solids (>99% - note that ~70% of ejected grains are salt-rich, but salt rich grains are larger, therefore 99% of total mass flux) but are depleted in the population escaping into Saturn's E-ring. They proposed that if 6% of salt-rich grains detected in the E-ring (which is fed by Enceladus's plumes) is typical of the proportion of salt-rich grains in the plume, then contributions from clathrate decomposition would be viable. During clathrate decomposition, a substantial part of the water in the plume forms from the sublimation of ice grains entrained in the flow of the released volatile gases (CO_2, N_2, CH_4), but sublimation of sodium-rich grains would result in the release of sodium into the plume's gas phase and E-ring, and this was not observed. The general observation though, is that the reservoir is salty and provides nearly all the matter for the plume.

Hsu et al., (2015) suggest that sodium grains are formed as frozen droplets formed from rock-water interactions in regions surrounding the core of Enceladus. In results from a model formulated by Glein et al., (2015), Enceladus' Ocean is thought to be a Na–Cl–CO_3 solution with an alkaline pH of ~11–12. In a later study, Glein and Waite (2020), analyse the plume composition to estimate the concentration of dissolved carbon dioxide in the ocean. Fortes (2007) argues that in a saline cryomagma with a water activity comparable to a 4 % NaCl solution, the dissociation pressure of mixed clathrate would drop to 0.50 MPa (compared to 0.20 MPa in the salt-free system), equivalent to a depth of ∼4.5 km. The Xenolith II model will include a comparison of the effects on the dissociation pressure of a liquid reservoir containing pure water and that of a 3.5% NaCl content which is the average salinity of Earth's oceans.

4.1.3 Volatile component of entrained clathrates

The Xenolith II model assumes that the volatile component of entrained clathrates is the same as that of the plume abundances measured by Cassini INMS: H_2O = 91±3%, N_2 = 4±1%, CO_2 = 3.2±0.6% and CH_4 = 1.6±0.4% (Waite et al., 2006), although it is probable that the vapour phase composition observed by Cassini is not identical to that on the surface (Fortes, 2007). INMS measure the percentage of other volatile species (e.g., acetylene and propane) to be <1% and ammonia at <0.5%. The major gas phases (CO_2, N_2, CH_4) could be sourced in part from these minor phases; substituting propane for methane in the source clathrate crystal would lower the dissociation pressure whereas reducing the proportion of CO_2 relative to CH_4 would shift the dissociation to higher pressures (Sloan & Fleyfel, 1992). Fortes (2007) argues that changes at source in the chemistry of the clathrate are unlikely to vary the critical dissociation pressure below

1.5MPa or above 3.0MPa at 273K. Ammonia, coexisting with the clathrate, would lower the water activity in the aqueous solution, as dissolved salts would, and would shift the dissociation to higher pressures. The effect of the small ammonia abundance (<0.5%) would be less than the uncertainty due to the gas phase abundances measured by Cassini INMS. Xenolith II examines two scenarios: first, that the cryomagma is pure H_2O at an ambient pressure liquidus (273.15K) and secondly, that the cryomagma is saline with a content of 3.5% NaCl at 273.15K.

4.1.4 Vent geometries, mass flow rates and plume velocity

The fissures or Tiger Stripes in the south-polar region of Enceladus are each approximately 130 km in length, 2 km wide and 500 m deep (Helfenstein & Porco, 2015; Porco et al., 2014). The Cassini Ultraviolet Imaging Spectrograph (UVIS) observations show that gas is ejected along the length of the fissures, making up a broad diffuse plume. Within this plume, collimated jets of high density gas, being accelerated at velocities exceeding $1000ms^{-1}$ (Mach numbers between 5 to 8) have been detected, (Hansen et al., 2011). The gas jets have been associated with local 'hot spot' regions less than $1km^2$ (Hansen et al., 2011). Detected by the Cassini Infrared Spectrometer (CIRS), these regions are significantly warmer that the surrounding surface (Spitale & Porco, 2007, Porco et al., 2014). Further detection by the high resolution Cassini Visible and Infrared Mapping spectrometer (VIMS) shows the hot spots to be relatively small, approximately 10m in size (Porco et al., 2014).

Initial observations identified eight discrete jets (Spitale & Porco, 2007), shown in figure 4.2. By 2014, ~100 gas jets had been identified in the fissures (Porco et al., 2014), although this was later disputed by Spitale et al., (2015) who suggested that on analysis

of newer data sets from Cassini, much of the eruptive activity from the plumes could be explained by broad curtain-like distributed eruptions, and that optical illusion was responsible for most of the features being interpreted as discrete jets. The interpretation of the spectra obtained reveal the widths and temperatures of several vents in the vicinity of Baghdad Sulcus.

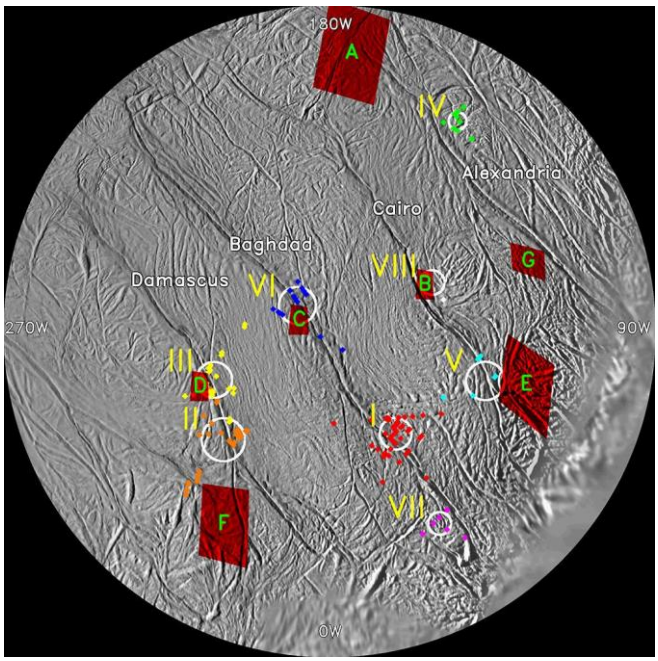

Figure 4.2. Map of stereographic projection of Cassini imaging data of the Enceladus south polar region, showing the correlation between jet sources identified in imaging data and hot spots on the surface located by Cassini's CIRS (Composite Infrared Spectrometer) instrument. Eight identified jet source locations are labelled with yellow roman numerals and CIRS hot spots are red boxes identified with green capital letters. The four tiger stripe fractures, or sulci, are annotated and the south pole is at the centre on the map. Key longitudes are also labelled around the perimeter of the map. https://www.jpl.nasa.gov/images/enceladus-jet-sources.

The horizontal and vertical geometries of the ~100 discrete jets and fissures will affect the mass flow rate and the velocity of the plumes, which are in part linked to the subsurface shape and physical nature of the vents. Truly uniform parallel-sided vents

are unlikely to exist, and in situ observations of vent geometry at depth were not carried out by Cassini at Enceladus. Yeoh et al. (2015) suggest that the observed high Mach numbers at the surface of the vents on Enceladus are due in part to subsurface channels that vary largely in width, allowing the gas to undergo sufficient expansion. However, it is assumed that the walls of the vent are likely to be rapidly eroded and deformed, but the extent of this process is difficult to quantify; the observed velocity of the plumes at the surface suggests that the flow of the cryomagma is extremely turbulent, causing significant mechanical erosion of the vent walls.

The Xenolith II model will account for and evaluate two eruption vent scenarios: portions of the fissures, and discrete jets. For the purposes of constraining the Xenolith II model, a realistic vent geometry has been selected for analysis: a parallel-sided, axis-symmetric shape, which employs a simple circular or fissure shape with no variation of cross-sectional area where magma pressure does not equal the hydrostatic pressure[18] at all depths, as utilised in eruption models by Wilson (1980) and Wilson and Head (1981). Shown in table 4.1 are the five discrete jets and five fissures of differing geometries and mass flow rates that have been selected for the purposes of this model and are extrapolated from data acquired by Cassini VIMS (Visual and Infrared Spectrometer) and analysed by Goguen et al. (2013).

The mass flow rate from the eruptions of the entire vicinity of the region of the stripes in the SPT is not well constrained and a wide range of modelled estimates of the total inferred H_2O production rate from the plumes using observations from UVIS and INMS has emerged (table 4.2). Most of these data were obtained from separate Cassini flyby

[18] The pressure exerted by a fluid at equilibrium at a given point within the fluid, due to the force of gravity; increases in proportion to the depth measured from the surface because of the increasing weight of fluid exerting downward force from above.

trajectories, which could explain some of the variance in the range of results. Additionally, differences could be attributed to the observed temporal variability of the plume over the orbital period of Enceladus (Hedman et al., 2013) and the differences in which data sets were used (INMS, UVIS, VIMS). Total production flow rates from each of these scenarios are based on the values determined in the current literature. The total flux of eruption materials from all sources along continuous sections of the fissures is assumed to come from the discrete geysers and non-discrete sources.

There is also uncertainty as to what proportion of the plume material is sourced from the individual jets and what proportion is from the distributed sources along the Tiger stripes (Yeoh et al., 2017). Tenishev et al. (2014), using INMS and UVIS data sets determined that the Tiger Stripe sources only account for 23–32% of the total H_2O production rate whereas Hansen et al. (2011) estimated that the jets made up 15–25% of the total H_2O production rate from the plume (30-50 kgs^{-1}).

Table 4.1. Summary of conduit and fissure geometries used in Xenolith II, showing estimated flow rates for each (extrapolated from Goguen et al. (2013)

Conduit geometry and flow rates				
	Diameter (m)	**Radius (m)**	**Area (m^2)**	**Flow rate ($kg\ s^{-1}$)**
C1	3	1.5	7.07	68.68
C2	4	2.0	12.57	68.63
C3	5	2.5	19.63	68.57
C4	6	3.0	28.27	68.50
C5	7	3.5	38.48	68.41

Fissure geometry and flow rates				
	Width (m)	**Length (m)**	**Area (m^2)**	**Flow rate ($kg\ s^{-1}$)**
F1	1	1000	1000	60.44
F2	3	1000	3000	44.44
F3	5	1000	5000	29.24
F4	7	1000	7000	14.84
F5	9	1000	9000	1.24

Collimated jets detected in the Enceladus plumes have a greater velocity than the calculated Enceladus escape velocity of 240 ms^{-1} (Hansen et al., 2011). Various

observations of supersonic velocities between 300 ms^{-1} and 1800 ms^{-1} (Hansen et al., 2011; Yeoh et al., 2015; Yeoh et al., 2017; Tucker et al., 2015; Portyankina et al., 2020) have been inferred.

Table 4.2. Summary of Enceladus' modelled mass flow rates from selected workers.

Observations***	Mass flow rate (kg s^{-1})	Reference
INMS E2	~5-14	*Waite et al., 2006*
INMS E2: UVIS 2005	~300	*Burger et al., 2007*
UVIS 2005	~120 - 180	*Tian et al., 2007*
E0, E1, E2	~200 - 1600	*Saur et al., 2008*
UVIS 2007	~150 - 200	*Hansen et al., 2008*
MIMI, CAPS, INMS E2, E3, E5	~36 - 750	*Smith et al., 2010*
INMS E3, E5: UVIS 2005	~780	*Tenishev et al., 2010*
INMS E3, E5, E7	∼500 - 1000	*Dong et al., 2011*
UVIS 2005, 2007, 2010	~170 - 220	*Hansen et al., 2011*
UVIS, INMS E3, E5	~190-870	*Tenishev et al., 2014*
INMS, UVIS E3, E5, E7	~400 – 900	*Yeoh et al., 2017*
UVIS, INMS, MAG	~100-1500	*Goldstein et al., 2018*
UVIS 2005-2017	~240-338	*Portyankina et al., 2020*

******* Cassini instruments are INMS (Ion and Neutral Mass Spectrometer), UVIS (Ultraviolet Imaging Spectrograph), MIMI (Magnetospheric Imaging Instrument), CAPS (Cassini Plasma Spectrometer) and MAG (Dual-Technique Magnetometer). E0, E1, E2, E3, E5 and E7 refer to the equatorial south Enceladus flybys of Cassini.

Fortes (2007) determines the vent pressure P_V on Enceladus to be the vapour pressure of water ice in the vicinity of the Tiger stripes as observed by Cassini's CIRS instrument (Spenser et al., 2006) and extrapolated down to 150K (Mauersberger & Krankowsky, 2003).

4.1.5 Heat sources for the plumes

Thermal scans of the SPT by high resolution observations made by CIRS and VIMS have yielded estimates of the total power radiated from the SPT from between 3 to 6 GW (Spencer et al., 2006) to 15.8 ± 3.1 GW (Howett et al., 2011). Spencer et al. (2013) however, revised this estimate down to radiated heat of ~4.2 GW; and added to this figure a further ~0.5 GW, resulting from latent heat generated from the plume. Heat

may also be generated from endogenic heat from the regions between the tiger stripes. Schubert et al., (2007) suggest that during its formation, radiogenic heating from the radioactive decay of ^{26}Al and ^{60}Fe could have heated Enceladus to the point that eventually resulted in a differentiated structure. The heat in the core, which continues to the present time, would have been retained if surrounded by a porous surface shell of ice acting as an insulator. Choblet et al (2017) show that heat generated by tidal friction inside the unconsolidated rocky core of Enceladus results in water being transported in the tidally heated permeable core resulting in the hot narrow upwellings, characterized by powerful hotspots at the seafloor, particularly at the south pole. This release of heat in narrow regions favours intense interaction between water and rock, and the transport of hydrothermal products from the core to the plume sources.

Another possible source of energy could be from heat generated from exothermic reactions such as serpentinization, a reaction which releases per mole, more than 11 times the energy needed to melt one mole of ice (Travis & Schubert., 2015). Tidal dissipative heating is also a potential source of energy as is convection and shearing of the ice shell. Goguen et al. (2013) discovered small-scale (tens of metres) hot spots on Baghdad Sulcus and modelled temperatures to be as high as 200K. It is also thought that the anomalously high temperatures are a result of Enceladus' eccentric orbit which is maintained by a 2:1 orbital resonance between Enceladus and Dione, and permits the tidal distortion raised on Enceladus by Saturn to vary in magnitude and direction over an orbital period of 1.3 days. Diurnal variations produce cyclical patterns of stress on its surface and horizontal stresses on the fractures will alternate from compressive to shear to tensile, and back again, opening and closing the fractures and producing shear heating in between (Porco et al., 2014). The Xenolith II model will determine to what

extent the clathrate dissociation process accounts for the latent heat supplied to the plumes.

4.1.6 Input parameters

Table 4.3. Xenolith II input parameters for Enceladus

System parameters	Values	Reference
Mantle density (ρ_{mantle})	1000 kg m^{-3}	*Fortes, 2007*
Cryomagma density	1000 kg m^{-3}	*Fortes, 2007*
CH_4 molecular mass	0.016 kg mol^{-1}	*Xenolith II input*
N_2 molecular mass	0.028 kg mol^{-1}	*Xenolith II input*
CO_2 molecular mass	0.044 kg mol^{-1}	*Xenolith II input*
Gas constant	8.314 kg mol^{-1}	*Xenolith II input*
Cryomagma temperature	273.15 K	*Ambient pressure liquidus H_2O*
Enceladus mass	1.079400 X 10^{20} kg	*Solar System Exploration. NASA. 2013*
Enceladus surface gravity	0.113 m s^{-2}	*Solar System Exploration. NASA. 2013*
Vent pressure	3 X 10^{-6} Pa	*Fortes, 2007*
Xenolith mass fraction	16.54 wt%	*Fortes, 2007*
CH_4 plume abundance	1.6%	*Waite et al., 2006*
N_2 plume abundance	4%	*Waite et al., 2006*
CO_2 plume abundance	3.2%	*Waite et al., 2006*

4.2 Model results

The dissociation curves of mixed clathrates in the cryomagma have been calculated using the percentages of each volatile in the mix (N_2, CH_4 and CO_2) in both pure H_2O and 3.5% NaCl. Additionally, the equilibrium curves of individual gas clathrates (N_2, CH_4 and CO_2) have been determined, using the NOSALT and CURVES programs of Bakker (1996, 1997 and 1998) and the CSMGem hydrate prediction program from the Colorado School of Mines (2007). Figure 4.3 shows the pressure-temperature phase diagram for clathrate stability and decomposition (Appendix I). The phases involved are hydrate (H),

ice (I) and gas (G) where the decomposition reaction is H = G + I (after Lu & Keiffer, 2009) The phase equilibria for N_2, CH_4, CO_2 and mixed gas clathrates are shown at temperatures between 245 K and 295 K.

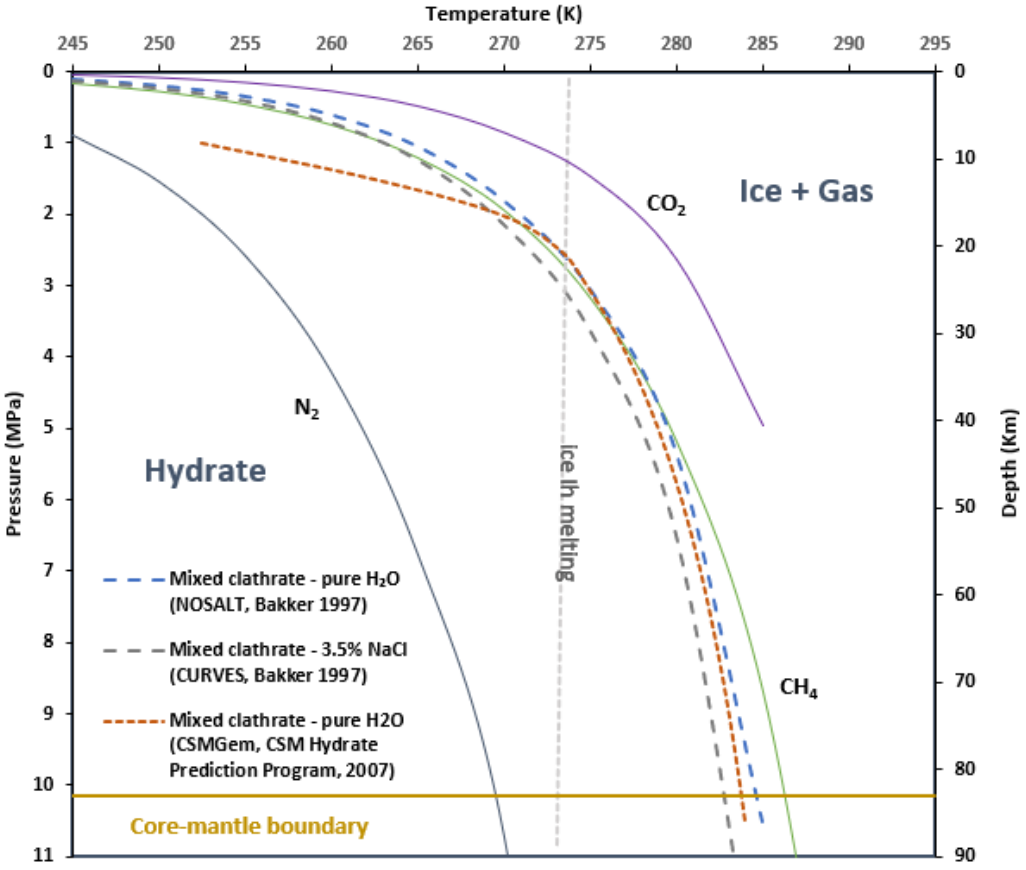

Figure 4.3. Calculated dissociation curve of mixed clathrate hydrate in pure water with CO_2 = 3.2%, CH_4 = 1.6%, N_2 = 4%, where the composition is assumed to be the same as the plume abundances measured by the Cassini INMS instrument at an altitude of 168km and reported by Waite et al. 2006. Shown is the pressure dependent melting curve of ice Ih (Fortes, 2007) and the core-mantle boundary at 83 km depth, for a fully differentiated Enceladus, as described by Fortes (2007). The NOSALT and CURVES components of the CLATHRATES computer package (Bakker, 1997) with the phase equilibria data of Duan et al. (1996) were used to generate the mixed clathrate curves (pure H_2O and 3.5% NaCl) as well as the dissociation curves for N_2, CH_4 and CO_2 in pure H_2O. A mixed clathrate curve was also generated using the CSMGem hydrate prediction program (2007).

4.2.1 Fragmentation pressure and depth

The solubilities of CO_2, CH_4 and N_2 in pure H_2O and in saline H_2O (3.5% NaCl) as a function of pressure at 273.15K were determined (Appendix I) and used to model bubble growth

as rising cryomagma decompressed. Results show that the extremely low solubility of N_2 in water means that the melt becomes supersaturated in N_2 even when dissociation takes place at depth, and N_2 bubbles begin to form. CO_2 has a much higher solubility, and does not contribute to the exsolved gas fraction until the magma is within a few hundred metres of the surface. Fragmentation of the mixed clathrate occurs at an approximate pressure and depth of 3.3 km and 0.375 MPa in both pure water, and saline water (3.5% NaCl). Table 4.4 shows the effect of salinity on the exsolution of each clathrate species in the cryomagma and is most evident in the results for N_2 where the starting dissociation pressure is approximately 11 MPa lower in salty cryomagma than that of pure water. The difference is less pronounced for CH_4 and minimal for CO_2. The calculated exsolved gas fraction of Enceladus's cryomagma as a function of pressure and depth at 273.15K is shown in figure 4.4 showing the modelled depth and pressure at which exsolution begins for each clathrate species (N_2, CH_4, CO_2).

Table 4.4**.** Modelled depth, pressure, percentage exsolved gas fraction and bulk density at which dissociation begins for each clathrate species in pure H_2O cryomagma (Fortes, 2007) and 3.5% NaCl cryomagma (this work) at 273.15K.

	Pure H_2O				**3.5% NaCl**			
	Depth (km)	**Pressure (MPa)**	**Exsolved gas fraction (%)**	**Bulk density (kg m^{-3})**	**Depth (km)**	**Pressure (MPa)**	**Exsolved gas fraction (%)**	**Bulk density (kg m^{-3})**
CO_2	0.18	0.02	98.65	13.75	0.18	0.02	98.69	13.27
CH_4	8.85	1.00	38.11	623.50	11.50	1.30	31.05	694.45
N_2	31.86	3.60	0.57	994.56	41.59	4.70	0.06	999.41

The calculated bulk magma density of Enceladus's cryomagma as a function of pressure and depth at 273.15K is shown in figure 4.5 showing the modelled depth and pressure at which exsolution begins for each clathrate species (N_2, CH_4, CO_2).

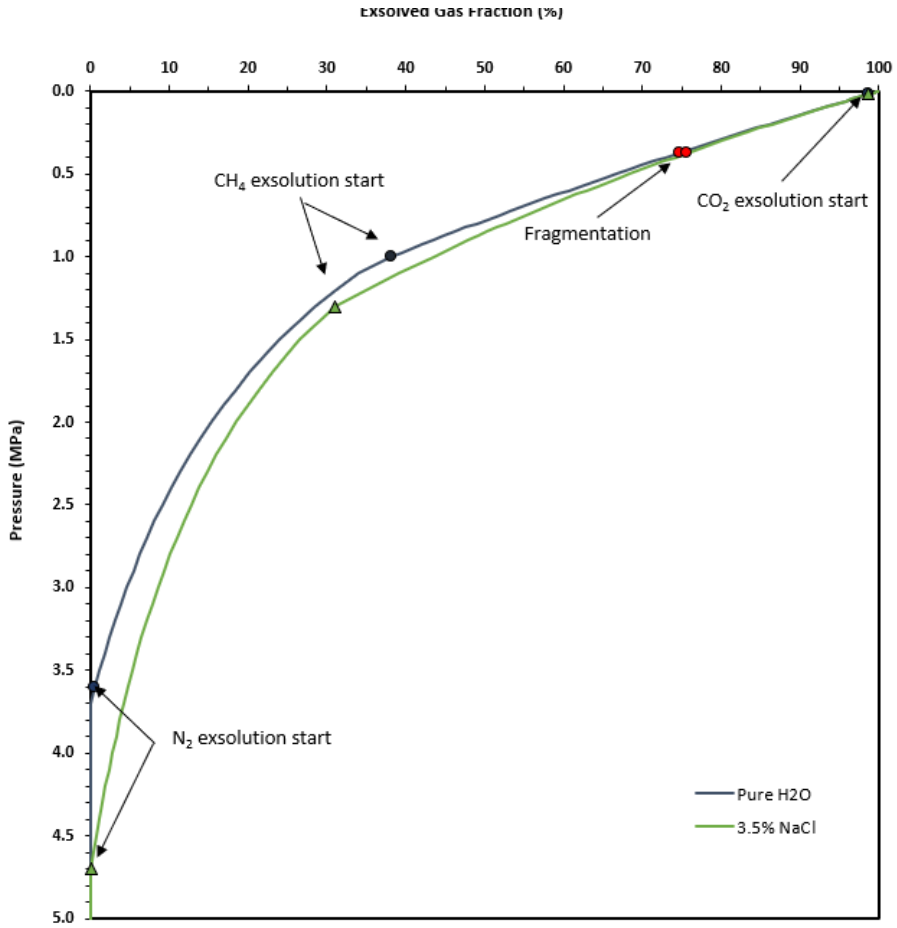

Figure 4.4. Calculated exsolved gas fraction of the Enceladus cryomagma as a function of pressure and depth at 273.15K; pure water cryomagma is shown in blue, and the 3.5% NaCl cryomagma in green. The modelled depth and pressure at which exsolution begins for each clathrate species (N_2, CH_4, CO_2) is shown as blue dots along the pure water cryomagma curve, and green triangles along the 3.5% NaCl cryomagma curve. The approximate point at which fragmentation occurs in the mixed clathrate is shown as a red dot.

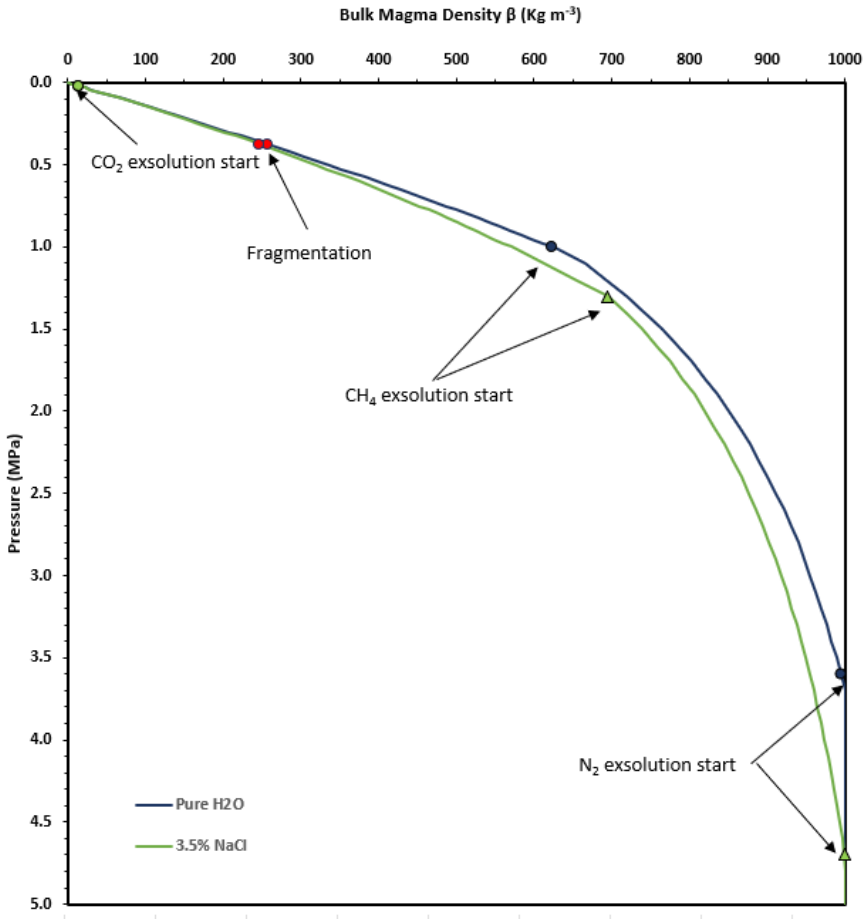

Figure 4.5. Calculated bulk magma density of the Enceladus cryomagma as a function of pressure and depth at 273.15K; pure water cryomagma is shown in blue, and the 3.5% NaCl cryomagma in green. The modelled depth and pressure at which exsolution begins for each clathrate species (N_2, CH_4, CO_2) is shown as blue dots along the pure water cryomagma curve, and green triangles along the 3.5% NaCl cryomagma curve. The approximate point at which fragmentation occurs in the mixed clathrate is shown as a red dot.

4.2.2 Cryomagma flow regime

To evaluate the cryomagma flow regime and plume dynamics, the local magma velocity was calculated (equation 3.9) and then the sound speed of the cryomagma, estimated at each point of the modelled pressure and depth. The sound speed in the plume before the entrained clathrate begins to dissociate is assumed to be 1402.4 ms^{-1} for pure water, and 1449.1 ms^{-1} for 3.5% NaCl salinity at 273.15 K (Haynes, 2011). Equation 3.11 was used to determine the sound speed, showing the effects of the increase of the gas

component in the plume as each of the clathrate species begin, and continue to exsolve. Figure 4.6 shows the calculated sound speed as a function of the exsolved gas fraction, to illustrate that sound travels more slowly through a gas than in a liquid. These data indicate an overall reduction in sound speed from the initial 1402.4 ms^{-1} (pure H_2O) and 1449 ms^{-1} (3.5% NaCl) at depths of 32.8 Km and 41.6 Km respectively to 39.8 ms^{-1} (both pure H_2O and 3.5% NaCl) near the surface, where all the clathrate species are assumed to have dissociated. As discussed in section 3.3.2, equation 3.11 breaks down if the gas fraction of the exsolving gas is very low. This occurs for the first few data points as N_2 starts to exsolve in the 3.5% NaCl cryomagma and to ameliorate this, the sound speed is capped to the gas free sound speed (1449 ms^{-1}). This does not occur when calculating the sound speed in the pure H_2O cryomagma.

The difference in sound speed between the pure water cryomagma, and the 3.5% NaCl cryomagma is most notable before the commencement of exsolution, since 3.5% NaCl cryomagma will have a greater bulk modulus than the pure water cryomagma. In the liquid gas-free cryomagma, the sound speed decreases with increasing density, but increases with increasing bulk modulus, and for saline water, the percentage increase in bulk modulus is greater than the percentage increase in density, so at the same density, sound speed increases with salinity. However, as the bulk magma density decreases with an increasing exsolved gas fraction, the difference in salinity has less effect on the sound speed.

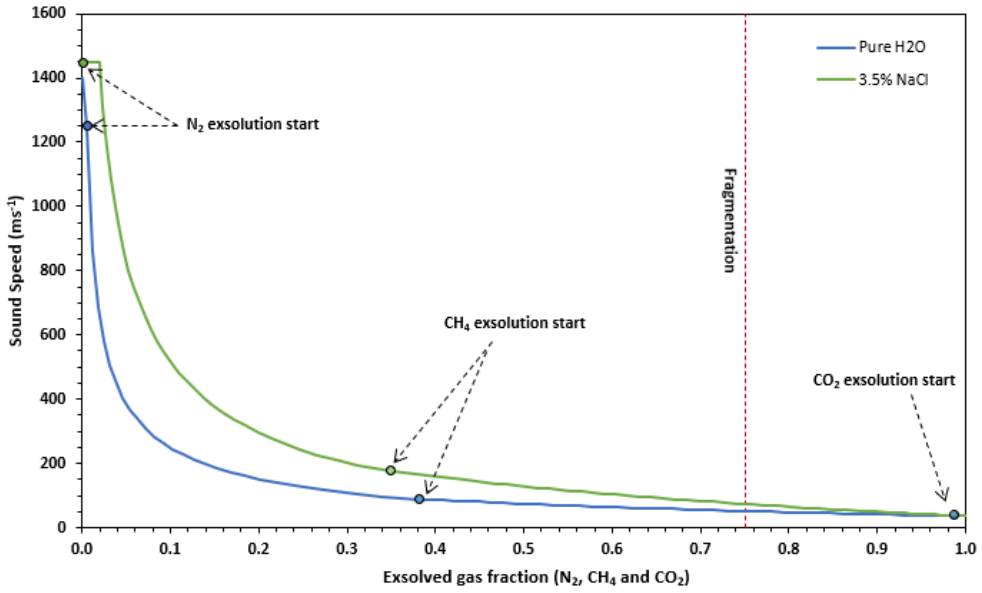

Figure 4.6. Calculated sound speed as a function of the exsolved gas fraction, as modelled in both pure H_2O cryomagma and 3.5% NaCl cryomagma. The points at which each species (N_2, CH_4 and CO_2 clathrate) begin to exsolve are annotated on the graph. The point at which fragmentation (~75% bubble volume fraction) occurs is shown as a red dotted line.

Figure 4.7 shows local flow velocities for pure H_2O and 3.5% NaCl cryomagma, calculated at each point of the modelled pressure and depth for each of the extrapolated conduit and fissure geometries (Table 4.1) using equation 3.9, which incorporates the calculated bulk density at each pressure point. Differences in bulk density between pure H_2O and 3.5% NaCl have been determined to differ by 0.004% at the surface, and 0.026% at 100 m and thus, the differences in flow velocity are negligible.

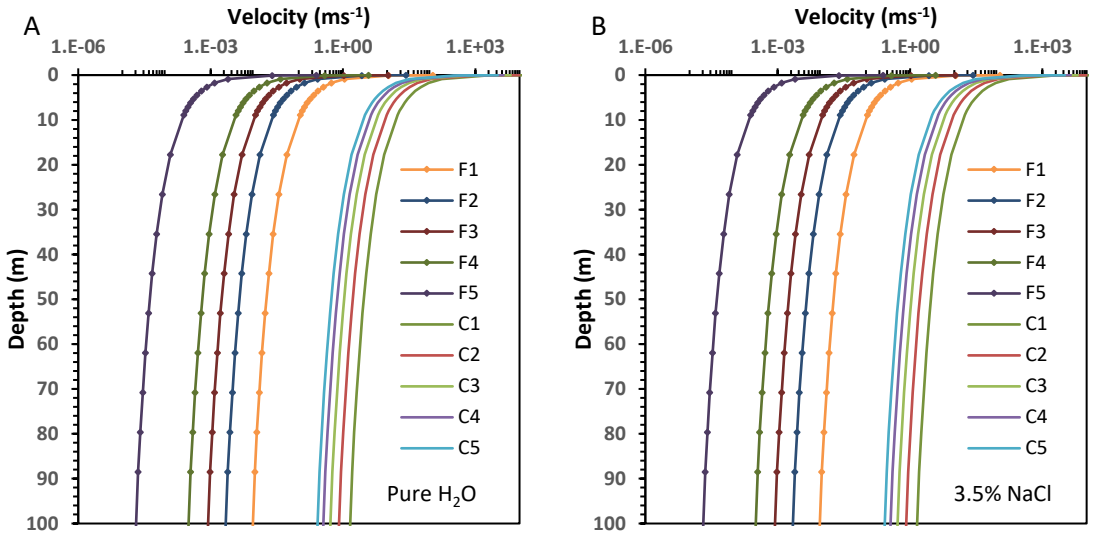

Figure 4.7. Calculated local flow velocities as a function of depth in pure H_2O (A) and 3.5% NaCl (B) up to a depth of 100 m for each of the extrapolated conduit and fissure geometries (conduits C1 to C5, and fissures F1 to F5).

To assess the nature of the plume eruption and the transition from subsonic to supersonic velocities, the ratio of the local flow velocity to the local sound speed (Mach number) was calculated. Figure 4.8 illustrates the points at which the flow velocities of each of the extrapolated conduits reach a Mach 1 condition, where the flow velocity is equal to the sound speed and the flow chokes near the surface. Before this state, flow is said to be subsonic (nearly incompressible) and after, supersonic, reaching Mach 11 in the C1 conduit. The Xenolith II model assumes a parallel-sided geometry and although the modelled results show choking near the surface, with the accompanying transition of the plume flow to supersonic velocities, Mitchell (2005) argues that this is only likely to occur if the conduit is flaring slightly outwards at the surface, with a gradient as little as 1 in 20 from the vertical; a feasible proposition close to the surface, but not considered in this model. None of the fissures modelled reached Mach 1 and are therefore not plotted in figure 4.8 which illustrates the flow dynamics of pure H_2O cryomagma. There is also no significant difference between the velocities of pure H_2O

cryomagma and 3.5% NaCl cryomagma, as observed in figure 4.7, thus there is no significant difference in the modelled points at which Mach conditions occur.

The height of the plume in each of the selected conduit and fissures geometries was estimated using equation 3.10, which relates the velocity to the surface gravity of Enceladus (0.113 kg m^{-3}). Since the velocities of the NaCl plumes are slightly higher than the pure H_2O plume velocities, the predicted heights for the NaCl plumes are higher. The calculated velocity for each conduit and fissure geometry (table 4.1) were selected at the near-surface depth of 0.09 m below the vent opening, where the calculated pressure was 10 Pa. Figure 4.9 shows predicted plume heights from the selected conduit and fissure geometries, for both pure H_2O and 3.5% NaCl.

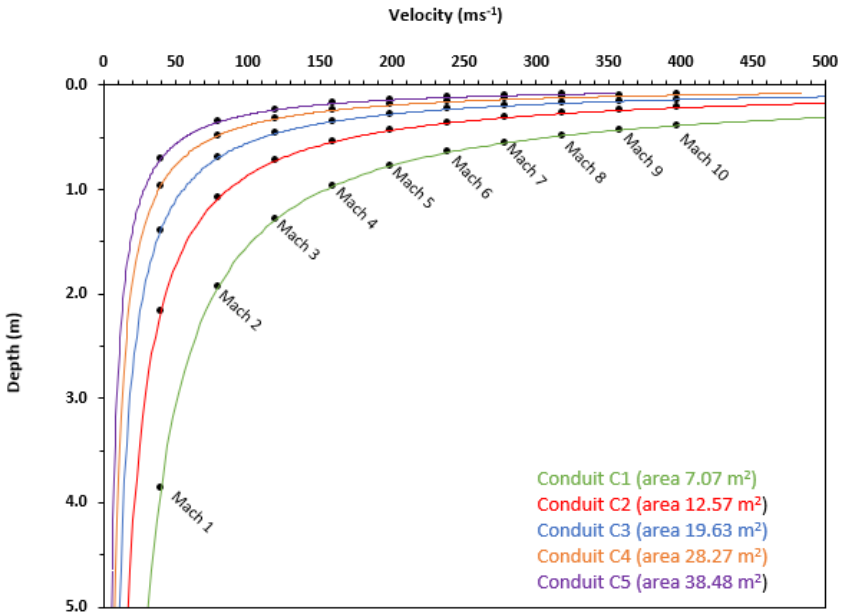

Figure 4.8. Calculated flow velocities in pure water of the extrapolated conduits (Table 4.1), illustrating choking conditions (Mach 1) for each conduit, and supersonic flow conditions up to Mach 10 (from 5 metres below the surface). Best-fit power trendlines were used for each conduit, and the points calculated at which each Mach condition occurred, and annotated with black dots on the graph. (Appendix II describes the method used to achieve this).

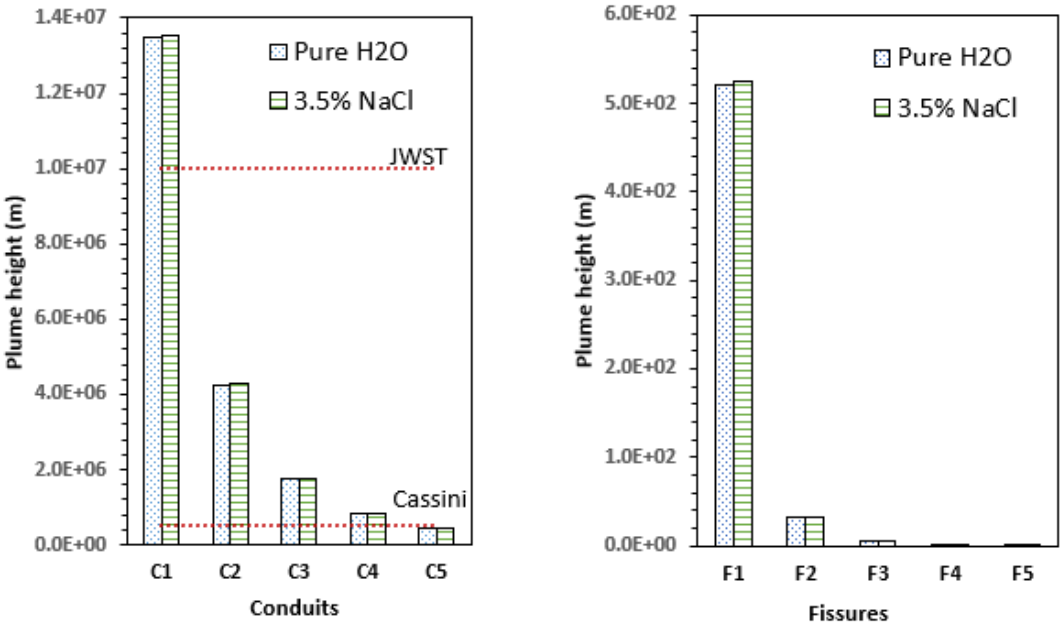

Figure 4.9. Estimates of the plume heights from the selected conduit and fissure geometries, for both pure H_2O and 3.5% NaCl. Cassini images obtained using the narrow-angle camera in 2005 show plumes extending at least 500 km (NASA/JPL/Space Science Institute). The NIRSpec instrument onboard the James Webb Space Telescope (JWST), observed a plume extending up to 10,000 km in 2023 (Villanueva et al., 2023). The observed plume heights from both Cassini and JWST are marked on the plot of conduits. The observed heights are greater than the values obtained for plume heights from fissures, and are not shown on the graph.

4.2.3 Viscosity

To determine the viscosity of the mixed plume, from depth to the surface, the ratio of liquid water to water ice, and water ice to water vapour first need to be estimated, using the phase diagram for water, since the Xenolith II model is constrained by the assumption that the plume is pure water at its ambient pressure liquidus (273.15 K). The Xenolith II model assumes a water vapour to ice ratio of ≈60:40 at the surface vent (Fortes, 2007) where the vapour phase is made up of 91 ± 3% H_2O vapour, 4 ± 1% N_2, 3.2 ± 0.6% CO_2 and 1.6 ± 0.4% CH_4 (Waite et al., 2006). The triple point of water, where the temperature and pressure at which the solid, liquid and vapour phases can coexist in equilibrium, is at a temperature of 273.15 K and pressure of ≈612 Pa at ≈5 metres

below the surface. Table 4.5 illustrates the phases of water that can exists at critical pressure and depths of the model.

Table 4.5. Modelled pressures and depths at critical points in plume eruption showing possible phases of H_2O at 273.15 K.

	Pure H_2O		3.5% NaCl		
	Pressure (MPa)	Depth (m)	Pressure (MPa)	Depth (m)	H_2O phases at 273.15 K
Surface	0.000000	0.0000	0.000000	0.0000	vapour
~Triple point of H_2O*	0.000600	5.3097	-	-	vapour, solid, liquid
CO_2 exsolution start	0.020000	176.9912	0.020000	176.9912	vapour, solid, liquid
Fragmentation	0.375000	3,318.5841	0.375000	3318.5841	vapour, solid, liquid
CH_4 exsolution start	1.000000	8,849.5575	1.300000	11504.4248	vapour, solid, liquid
N_2 exsolution start	3.600000	31,858.4071	4.700000	41592.9204	solid, liquid
Core-mantle boundary	9.300000	82,300.8850	9.300000	82300.8850	solid, liquid

** The addition of NaCl to water increases the boiling point and decreases the specific heat capacity*

The Xenolith II model predicts that as pressure decreases, clathrates entrained in the plume respond to pressure changes, and exsolve, releasing gas into the plume, the fractions of which impact the bulk viscosity of the plume. Additionally, as the pressure drops, water changes phase from liquid to vapour. Viscosity is temperature dependent, but the model temperature of the plume is kept constant at 273.15 K so that the main impact on the bulk viscosity is the addition of the exsolved gases. The ice and xenolith phases of the plume are not taken into consideration when determining the viscosity of the mixed component plume. To constrain the model and determine of the viscosity of the plume, the following assumption has been made: The gas exsolved from the clathrate dissociation process is added to the magma as it erupts, first to the liquid phase of water, then at the triple point, to the vapour phase, where at the surface water is in a ratio of 91 : 4 : 3.2 : 1.6 (H_2O : N_2 : CO_2 : CH_4) with the exsolved gas species. Before N_2 begins to exsolve, the Xenolith II model assumes that 100% of the plume is liquid

water, and as the clathrate continue to exsolve as the cryomagma rises to the surface, the percentage of water (in liquid, then vapour phase) changes from 100% to 91% at the surface. The viscosity for each scenario is modelled for pure H_2O cryomagma (equation 3:12) with individual gas viscosities obtained from Haynes, W.M. (Ed.), 2011 (Appendix III). Table 4.6 tabulates these results for both pure H_2O and 3.5% NaCl cryomagma.

The viscosity of liquid water is much higher than that of water vapour (1791.1 µPa·s compared to 8.95 µPa·s) and will impact the mixed viscosity of the plume. The point at which the water phase is expected to change from liquid to vapour is taken to be at the triple point (table 4.5).

Table 4.6. Modelled pressures and depths at critical points in plume eruption showing calculated viscosity for the mixed plume (H_2O_{LIQUID}, H_2O_{VAPOUR}, CH_4, N_2 and CO_2). The different pressures and depths of the start of the exsolution points of CO_2, CH_4, N_2, fragmentation and the triple point of H_2O are shown for both pure H_2O and 3.5% NaCl.

	Pure H_2O			3.5% NaCl		
	Pressure (MPa)	Depth (m)	$Viscosity_{mix}$ µPa·s	Pressure (MPa)	Depth (m)	$Viscosity_{mix}$ µPa·s
Surface	0.000000	0.0000	9.3350	0.000000	0.0000	9.3350
~Triple point of H_2O*	0.000600	5.3097	9.2476	-	-	-
CO_2 exsolution start	0.020000	176.9912	1736.6750	0.020000	176.9912	1734.1012
Fragmentation	0.375000	3,318.5841	1762.7202	0.375000	3318.5841	1758.6825
CH_4 exsolution start	1.000000	8,849.5575	1783.5870	1.300000	11504.4248	1782.4033
N_2 exsolution start	3.600000	31,858.4071	1791.0998	4.700000	41592.9204	1791.1000
Core-manrle boundary	9.300000	82,300.8850	1791.1000	9.300000	82300.8850	1791.1000

** The addition of NaCl to water increases the boiling point and decreases the specific heat capacity*

The Xenolith model examines the scenario that assumes that up to the triple point of water (273.15 K at 611.657 Pa), the magma is a mixture of liquid water and exsolved gases. At the triple point, the water phase changes from the liquid to the vapour phase. The ice phase is not considered in the viscosity calculations. The equations to calculate the Reynolds number (3.12 and 3.13) define viscosity as being inversely proportional to

the product of the area, density and a factor of 4 or 2 (fissure or conduit respectively). Larger areas such as those defined for fissures will contribute to lowering the Reynolds number, as shown in table 4.7. Figure 4.10 shows the flow velocities of the extrapolated conduits and fissures (Table 4.1), and indicates at which depth and velocity the flow is laminar (Re < 2000) and turbulent (Re > 4000). Reynolds numbers between 2000 and 4000 indicate the flow is transitional, between laminar and turbulent, although there is no indication of this state in the modelled data.

Table 4.7. Modelled Reynolds numbers (Re) at critical depths in pure H_2O from the core-mantle boundary to the surface. The points at which flow is laminar (Re < 2000) are shown in bold.

Conduit/ Fissure	Mantle 83185.84 m	Start of N_2 exsolution 31858.41 m	Start of CH_4 exsolution 8849.32 m	Fragmentation 3318.58 m	Start of CO_2 exsolution 176.99 m	Triple Point of H_2O 5.31 m	Surface 0.00 m
C1	16274.19	16274.19	16342.74	16536.20	16784.20	3152035.12	3122525.20
C2	12196.75	12196.75	12248.13	12393.12	12578.98	2362305.30	2340188.97
C3	9748.87	9748.87	9789.94	9905.83	10054.39	1888192.04	1870514.44
C4	8115.77	8115.77	8149.95	8246.43	8370.10	1571887.05	1557170.77
C5	6947.23	6947.23	6976.50	7059.08	7164.95	1345561.54	1332964.16
F1	**67.49**	**67.49**	**67.77**	**68.58**	**69.60**	13071.53	12949.15
F2	**49.62**	**49.62**	**49.83**	**50.42**	**51.18**	9611.16	9521.18
F3	**32.65**	**32.65**	**32.79**	**33.18**	**33.67**	6323.82	6264.61
F4	**1.08**	**1.08**	**32.79**	**33.18**	**33.67**	**208.58**	**206.63**
F5	**1.38**	**1.38**	**1.39**	**1.41**	**1.43**	**268.18**	**265.67**

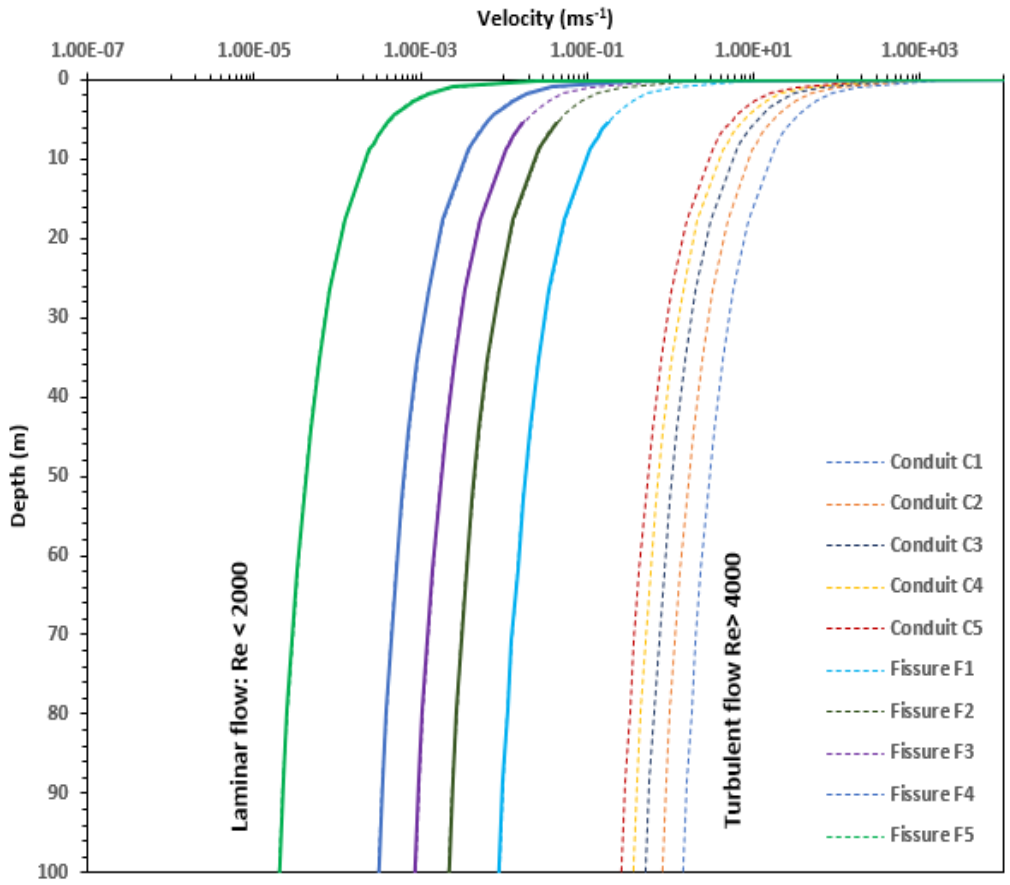

Figure 4.10. Calculated flow velocities of the extrapolated conduits and fissures (table 4.1), showing the velocity at which flow is laminar (Re < 2000) and turbulent (Re > 4000). Laminar flow is illustrated with a thick solid line, and turbulent flow with a dotted line.

4.2.4 Kinetic energy

The upward velocity of the plume was used to model the kinetic energy in each of the conduit and fissures whose geometries are defined in table 4.1. Figure 4.11 illustrates that the increase of gas bubbles in the plume is related to the rise of kinetic energy in the plumes. The geometry of the conduits and fissures is also related to the kinetic energy: the smaller the area of the conduit or fissure, the higher the kinetic energy.

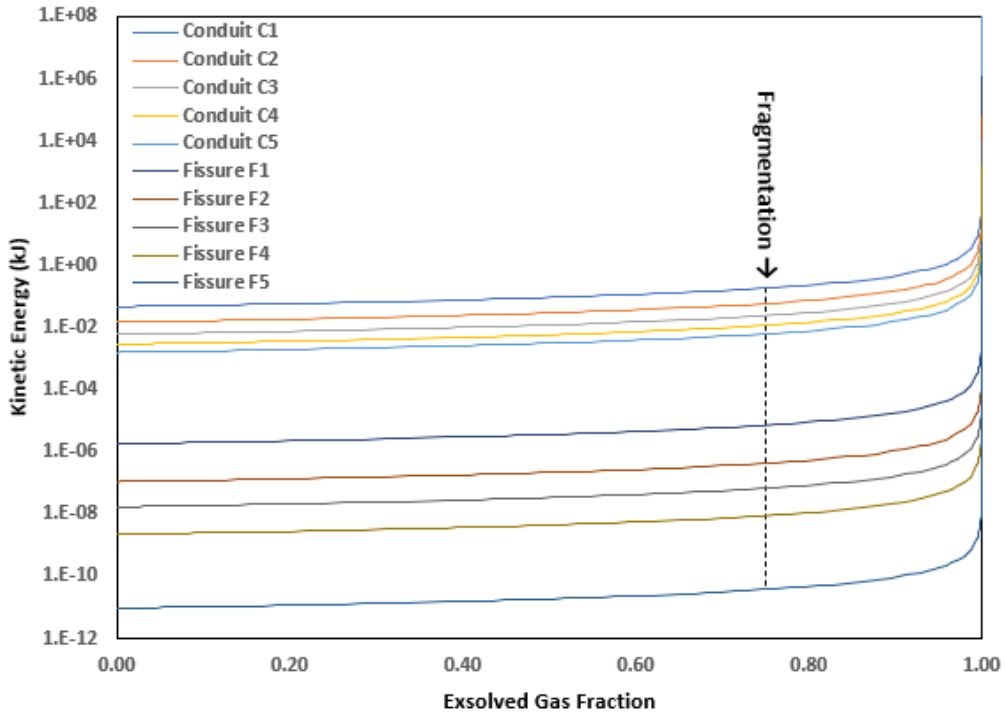

Figure 4.11. Calculated kinetic energy of the extrapolated conduits and fissure geometries (conduits C1 to C5, and fissures F1 to F5) as a function of exsolved gas fraction in a pure water cryomagma. The point at which fragmentation (75% bubble volume fraction) occurs is annotated on the graph.

4.2.5 Thermodynamic energy balance

The average total power radiated from the SPT terrain (Q_{out} in equation 3.16) has been variously estimated to be between 3 to 15.8 GW. Ingersoll and Pankine (2010) average the total power radiated of 5.8 ± 1.9 GW (Spencer et al., 2006) as 11.6 ± 3.8 kW m^{-1} along the 500 km length of the tiger stripes. An estimate of the total mass flux of the plumes (m_{out}) observed by UVIS in 2005, 2007 and 2010 is ~200 kg s^{-1} ± 30 kg s^{-1} (Hansen et al., 2011). Since the molar ratio of the gas mixture (CO_2, CH_4 and N_2) to water vapour is 1:10 (Waite et al., 2006), the mass ratio for the given molar fractions is 1:7 and the mass flow rate of the gas mixture from clathrate dissociation ($m_{out,g}$) is ≈25 kg s^{-1}. The latent heat of clathrate dissociation (L_{dis}) is estimated at ≈465 kJ kg^{-1} (Kang and Lee, 2001) although Lu and Keiffer (2009) estimate a much larger figure (≈890 kJ kg^{-1}). The mass rate of the

sublimated H_2O vapour, $m_{out,v}$, is 350 kg s^{-1}, and the latent heat for the sublimation of ice is (L_{sub}) is 2800 kJ kg^{-1} (Lu and Keiffer, 2009). The latent heat of crystallisation (L_{cry}) is 334 kJ kg^{-1} (Giauque and Stout, 1936) and dissociation will result in a percentage of the liquid water crystallising (Fortes, 2007). Since the mass flow rate of the liquid water phase is unknown, an approximation must be made where the mass flow rate is 40% of the total flow rate: 80 kg s^{-1} since the water vapour to ice ratio predicted by the Fortes (2007) is ≈60:40. The value for the reservoir pressure (P_r) is approximated as 5 bar and the reservoir density (ρ_r), 1000 kg m^{-3} (Lu and Keiffer, 2009).

Table 4.8. Estimated values for the heat required to dissociate clathrate, sublimation of ice and crystallisation of ice.

$m_{out,g}H_{dis}$ (GW)	$m_{out,v}L_{sub}$ (GW)	$m_{out}L_{cry}$ (GW)	$m_{out}(P_r/p_r)$ (GW)	Total (GW)	Literature source
0.011625	0.98	0.00334	6.60E-12	0.99	Lu & Keiffer (2009)
0.017438	0.98	0.00501	6.60E-12	1.00	Fortes (2007) & this work

Table 4.8 shows the results of the calculated values of the terms in the right hand side of the equation 3.16. The various inferred values for the power radiated from the SPT on Enceladus are much larger than the total heat estimated in the table (≈ 1GW for both sources). Section 4.1.5 examines the possible heat sources for the plume, some of which could account for this difference.

4.3 Evaluation and discussion

The Xenolith II model predicts that fragmentation in the plumes occurs at 3.3 kilometres below the surface at 0.375 MPa which is consistent with inferred surface temperatures in the vent areas of the south polar region of Enceladus which are lower than the ice-liquidus temperature (Abramov & Spencer, 2007). At the fragmentation point, ~75% of

the clathrate hydrates have dissociated and released gas into the low density, low viscosity plume and flow is predicted to be turbulent from this point. However, modelled results show that the flow in the conduits (C1 to C5) is turbulent from the core-mantle boundary, and that in all the five selected conduit geometries, the Reynolds numbers approximately double to >> 10^7 at the triple point of H_2O, indicating that upward inertial forces overwhelm the downward viscous forces in the plumes. This extreme turbulence could result in considerable mechanical erosion of the walls of the conduit, incorporating additional xenolith material and entraining and erupting the massive blocks of ice as seen in high resolution images from Cassini (Porco et al., 2006). Smaller material will be erupted in this manner, with the coarsest ice grains being ballistically emplaced closest to the vents, as observed in Cassini images (Porco et al., 2006). The flow in the fissures (F1 to F3) is predicted to be laminar up to the triple point (5 m below the surface), at which point, flow becomes turbulent for the last few metres before the surface. Flow is shown to be laminar from the core-mantle boundary to the surface in fissures F4 and F5.

At 0.1 m below the surface, the predicted results obtained for the velocities of the modelled conduits (C1 to C5) are in good agreement with various observations of supersonic velocities ranging from 300 m s^{-1} to 1800 m s^{-1} (Hansen et al., 2011; Yeoh et al., 2015; Yeoh et al., 2017; Tucker et al., 2015; Portyankina et al., 2020). The predicted Mach numbers for conduits C1 to C5 are higher than those reported by Hansen et al. (2011).

The relationship between the selected conduit and fissure areas has a direct bearing on the predicted plume heights, where conduit C1, which has the smallest area (7.07 m^2) has the highest predicted plume, which is related to its high velocity near the surface.

The estimations made regarding the thermodynamic energy balance of the plumes was an attempt to quantify how much the latent heat of dissociation contributed to the observed power being radiated from the Tiger Stripes on Enceladus. The outcome of this assessment was that a large portion of the radiated power is unaccounted for by the latent heats of dissociation, crystallisation and sublimation and that additional heat sources are contributing to the total power being radiated.

The modelled results have several possible limitations, namely that assumptions made in the Xenolith II model are based on the results of different workers' analyses and observations of data from the Cassini flybys. An attempt has been made to use those values which are either the 'latest' (e.g., as in the power radiated from the SPT) or those which represent an average from the range of possible values available (e.g., the mass flow rates from the plumes). Additionally, many of the reported data have some uncertainty. On evaluation through, Xenolith II has provided a more complete physical model where the dissociation of clathrate hydrates generates explosive cryovolcanism in the south polar region of Enceladus; evidenced by strong matches with observational data from Cassini.

CHAPTER FIVE

Cryovolcanism model results and discussion - Triton

5. Cryovolcanism model results and discussion - Triton

The numerical model described in chapter 3 is presented in this chapter, as applied to Triton. Input parameters are from the observations made by Voyager 2 in 1989, satellite and ground based measurements as well as the available analysis and literature on Triton. The aim is to contribute to this study's primary goal of examining the potential role that clathrate hydrate dissociation has in explosive cryovolcanism on the icy satellites of the outer solar system. Model assumptions and input for Triton are presented in section 5.1, and the results of the modelling in section 5.2. The computed outcomes of the model will be compared with mission data observations and analysis from other workers and then evaluated in terms of the primary goal of this thesis (section 5.3).

5.1 Xenolith II assumptions and input

The input parameters and assumptions made for Xenolith II's application to Triton include current data for Triton (mass, surface gravity, internal structure) and physical

constants (table 5.3). A description of the structure of the model is outlined in chapter 3. The assumptions made are outlined and discussed in the following sections.

5.1.1 Internal structure of Triton

From observations of the mean radius and density of Triton, the moon is assumed to be fully differentiated (where a layered internal structure is sorted by the densities of the different components). Triton's radius is 1352.6 ± 2.4 km (Conrad et al., 2018), and with its mass, yields a density of 2.075 ± 0.0019 g cm^{-3}. Archinal et al., (2018) modelled different interior structure scenarios, in which Triton was differentiated (silicate core and ice mantle) or homogeneous (uniform mix of silicate and ice or clathrates). Because Triton is large enough to have undergone radiogenic and accretional heating, differentiation is the more likely scenario, and Smith et al., (1989) proposed a differentiated interior structure where a silicate core would have been formed (1000 km radius) overlain by an Ice I mantle, which could have developed an ice II layer beneath the Ice I layer, due to the extreme low surface temperatures. Smith et al. (1989) caution though that the existence of an ice II layer would depend on the details of the ice-I/ice-II boundary, poorly constrained at these low temperatures. Subsequent modelling by other workers has suggested that Triton has a metallic core overlain by a silicate mantle, surrounded by an ice II and ice I shell. Figure 5.1 shows a modelled internal structure of Triton (after McKinnon & Kirk, 2014). The case for a subsurface ocean and its predicted depth is discussed in section 5.1.2. The Xenolith II model assumes that the cryomagma is pure H_2O at an ambient pressure liquidus (273.15 K).

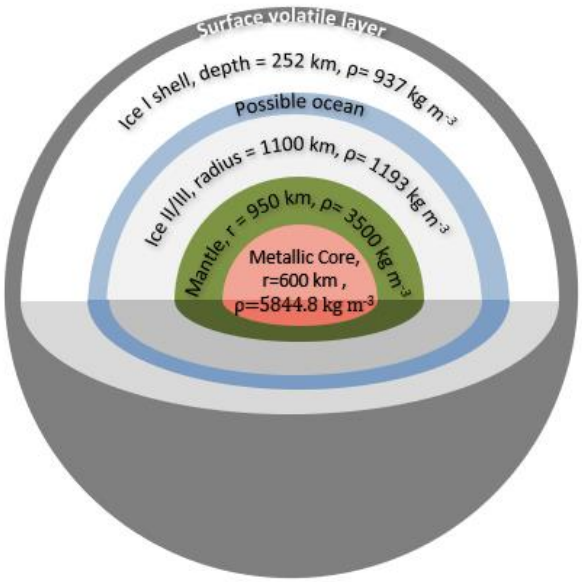

Figure 5.1. Internal structure model for Triton (not to scale), after McKinnon and Kirk (2014), showing the possible location of an ocean (discussed in section 5.1.2). **T**he moon is thought to be made up of a metallic core (Fe, Ni, S) with a 600 km radius and density of ρ = 5844.8 kg m^{-3}. The core is overlain by a silicate mantle with a density of ρ = 3500 kg m^{-3}, surrounded by a deep ice (H_2O) shell approximately 400 km deep. The outer radius of the ice shell is 1352 km.

5.1.2 The case for a subsurface ocean on Triton

Triton's circular orbit is inclined to Neptune's equator by 157° and its motion is retrograde (McKinnon & Kirk, 2014). Through its evolution, Triton's orbit has been reduced to near zero eccentricity with Neptune where its rotation is tidally locked, with one face orientated towards the planet: Triton's orbital period matches its rotational period around Neptune. Based on this, it has been suggested that Triton formed in the Kuiper belt in a heliocentric orbit (McKinnon & Kirk, 2014), and was subsequently captured into Neptune's orbit (Agnor & Hamilton, 2006). After capture, it is thought that through tidal circularization, tidal heating of Triton's interior and surface would have occurred, during which a large amount of heat in Triton's interior would have been dissipated, transforming the icy layers into a global ocean (McKinnon & Kirk, 2014). Speculation exists as to whether this ocean could be sustained until the present day within Triton's interior, particularly since it is unlikely that heat from the initial primordial capture event has any effect on the present day energy budget (Nimmo & Spencer, 2015). As Triton cools, the ice shell will likely grow to engulf the underlying

ocean, but several theoretical models predict that a subsurface liquid layer could be present today, thus potentially linking the complex surface composition to ocean chemistry (Hansen et al., 2021).

Nimmo and Spencer (2015) argued that the interior of Triton consists of a thick convecting ice shell overlying a long-lived ocean maintained by radiogenic heat transferred from the core. Their model further suggests that an ocean temperature of approximately 240 K can be maintained by the presence of an antifreeze such as NH_3. Subsurface oceans can exist in the outer solar system if small amounts of ammonia are present (Hussmann et al., 2006).

In their model for the compaction and thermal evolution of partially molten, ammonia rich ice shells, as applied to Triton, Hammond et al. (2018) find that as Triton's ice shell thickens, there is a slow increase in the concentration of ammonia in the subsurface ocean reducing the rate of freezing. Their model predicts an ocean thickness of up to 50 km. It should be noted that no evidence for NH_3 has been found in the spectral data of Triton ices (Cruikshank et al., 1993). However, Hammond et al. (2018) argue that ammonia is abundant in the outer solar system and that frozen ammonia solutions could be present but not detected, since as the ice shell thickening rate decreases, ammonia-rich melt is excluded from the ice shell and the bulk of the ice shell is pure water ice.

In a study of the rate of the ice shell growth as a function of different orbital eccentricities, Gaeman et al. (2012) conclude that as the orbital eccentricity decreases to the present value, a NH_3-rich ocean exists beneath Triton's icy shell. As the ice shell continues to form, the NH_3 fraction in the ocean increases, becoming denser than the crystallizing H_2O ice, and less viscous (Hogenboom et al., 1997). Consequently, a layer of NH_3-rich fluid could become stable beneath the ice shell.

Triton is thought to be geologically active with few obvious impact craters and a relatively young (<100 to <10 million years old), dynamic surface modified by endogenic processes (Hansen et al., 2021; Stern & McKinnon, 1999). An internal ocean could be a source of cryomagmas for resurfacing (Schenk & Sobieszczyk, 1999; Stern & McKinnon, 1999). Ruiz (2003) argues that it is feasible that Triton could sustain an internal ocean at a depth of 20 to 30 Km below the surface, which could in turn be a source of magmas for resurfacing.

As with dissolved salts coexisting with the clathrate (see 4.1.2), ammonia would shift the dissociation to a higher pressure, although there are insufficient data to quantify how much ammonia potentially exists with water ($NH_3.H_2O$) in a subsurface ocean on Triton.

5.1.3 Volatile component of entrained clathrates

Ground based observations and modelling of absorption features have detected a global surface layer of volatiles of between tens of centimetres to hundreds of metres thick (Brown et al., 1990; Soderblom et al., 1990) on Triton. This layer is optically translucent in the visible region of the solar spectrum, and relatively opaque in the thermal infrared (Brown et al., 1990). Ground based telescopes (United Kingdom Infrared Telescope, Mauna Kea, Hawaii) have identified that the surface of Triton is dominated by N_2 ice, in which small quantities of CH_4 (highly soluble in N_2) and other species (CO_2 and CO) may be dissolved. These species, in their pure form, may also be found in isolated pockets. Table 5.1 summarises the ground based observations and modelling results of three separate studies. Triton is one of the few solid bodies in the solar system where the major component of the atmosphere (nitrogen) also condenses on the surface. Due to ongoing volcanism, N_2 and CH_4 in the atmosphere and on the surface are likely

endogenic and an assumption is made that gases emitted into the atmosphere from the geyser-like eruptions (mentioned in section 1.1.2) will condense on the surface in approximately the same ratio as the plume abundances. For the purposes of the Xenolith II model, the ratio of the volatile components of the entrained clathrates in the plumes is therefore assumed to be the same as that of the ratio of volatiles identified on the surface of Triton. Since debate exists about the exact volatile composition of the surface ices, two scenarios are investigated based on an amalgamation of the ground based observations and modelling of volatile surface ices (table 5.1) : Scenario I, where N_2 = 69%, CH_4 5% and CO_2 = 10%, and Scenario II, where N_2 = 85%, CH_4 = 5% and CO_2 = 10%. Recent studies reveal evidence for solid H_2O on the surface of Triton, but that its spectral signature is masked by other more volatile surface components where models show that H_2O grains are mixed at a granular level with CO_2 (Geissler, 2015; Cruikshank et al., 2000). In the absence of compositional data for the observed geysers on Triton, the Xenolith II model assumes that the percentage of H_2O in the plumes is 91%, the same as that of the plumes on Enceladus.

Table 5.1. Summary of ground based observations and modelling of volatile surface ices (N_2, CH_4, CO_2) on Triton

Volatile	**Cruikshank et al., 1993**	**Quirico et al., 1999**	**McKinnon & Kirk, 2014**
N_2	Surface dominated by N_2 ice	Surface imaged predominantly N_2 ice	Polar cap region predominantly N_2 ice
CH_4	Minor component of the surface ice relative to N_2 and incorporated into N_2 on the surface. Less than 0.05% CH_4 relative to N_2	Not distinguished in the spectra, but ~11% pure CH_4 in isolated pockets (relative to N_2) could be present, explaining the high atmospheric CH_4 abundance observed by Voyager 2	CH_4 abundance relative to N_2 could be as great as 5% Isolated patches of CH_4 detected
CO_2	Less volatile than N_2 and not mixed with N_2. ~10% pure CO_2 outcrops on surface	No data in study	Pure CO_2 ice patches between 10-20%

5.1.4 Vent geometries, vapour mass flow and plume velocity

On the August 25th and 26th 1989, Voyager 2 obtained a series of high resolution images of more than 120 dark surface streaks (Hansen et al., 1990). The streaks, many fan-shaped (between latitudes of 15° and 45° S), varied in length between ~5 to ~100 km and were interpreted to be wind created deposits from eruptions that were no longer active, or ongoing activity at altitudes too low (< 1 km) to measure (Hansen et al., 1990; Kirk et al., 1990). Stereoscopic images from varying angles revealed at least two erupting geyser-like plumes at an altitude of ~8 km on the Neptune-facing southern hemisphere of Triton (figure 2.6). The dark narrow cloud observed from the Mahilani plume (48°S 2°E) was determined to be 90-150 km long, and the Hili plume (57°S 28°S) seemingly a cluster of several plumes with narrowing clouds was up to 100 km long (McKinnon & Kirk, 2014).

The mass flow rate and velocity of the erupting plumes on Triton will be in part linked by the horizontal and vertical geometries of the vents themselves. The dimensions of these vents are unknown, but estimates vary from tens of metres to a kilometre (Soderblom et al., 1990), and up to 2 or 3 kilometres (McKinnon & Kirk, 2014; Hansen et al., 2021).

As was applied to Enceladus, a realistic vent geometry has been selected for analysis on Triton: a parallel-sided, axisymmetric shape, which employs a simple circular with no variation of cross-sectional area. For the purposes of constraining the Xenolith II model, ten different circular eruption vent sizes will be modelled, thus evaluating the consequences of the differences in the vent size estimates in the current literature and in this work.

The estimated vapour flow rate, as mentioned by various workers, does not include the vent area over which this flow is erupted, and therefore is estimated for the purposes of Xenolith II from current studies (McKinnon & Kirk, 2014; Hansen et al., 2021; Yelle et al., 1991; Soderblom et al., 1990; Hofgartner et al., 2022). Table 5.2 shows the estimated figures for a range of circular conduit vent geometries used in the Xenolith II model, ranging from diameters of 5 m to 3000m.

Table 5.2. Summary of conduit geometries used in Xenolith II, showing estimated flow rates for each selected vent diameter. Each vent geometry will be modelled, each with vapour mass flows of 200 kg s^{-1}, 300 kg s^{-1} and 400 kg s^{-1}.

Estimation of circular vent geometry and flow rates						
Vent	**Diameter (m)**	**Radius (m)**	**Area (km^2)**	**Vapour mass flow ($kg\ s^{-1}$)**		
C1	5	2.5	0.02	200	300	400
C2	10	5	0.08	200	300	400
C3	50	25	1.96	200	300	400
C4	75	37.5	4.42	200	300	400
C5	100	50	7.85	200	300	400
C6	250	125	49.09	200	300	400
C7	500	250	196.35	200	300	400
C8	1000	500	785.40	200	300	400
C9	2000	1000	3141.59	200	300	400
C10	3000	1500	7068.58	200	300	400

5.1.5 Heat sources for the plume

The position of the geysers on Triton suggests that solar heating, although very weak at Triton's great distance from the Sun (30 AU), plays a crucial role. The surface of Triton absorbs only 20% of the incident sunlight (Hillier et al., 1990). Triton's southern hemisphere at the time of the Voyager 2 encounter was nearing a summer solstice, and thus insolation as a driver or a trigger for Triton's geyser-like plumes is a plausible

hypothesis. Trapping of solar radiation in a translucent, low-conductivity surface layer (in a solid-state greenhouse), which is subsequently released in the form of latent heat of sublimation, could provide the required energy (Brown et al., 1990).

Geothermal heat may also play a part if assisted by the added energy input of seasonal cycles of insolation. Triton experiences complex seasonal variations in its subsolar latitude due to the combination of Neptune's obliquity and Triton's inclined orbit. Because Triton's N_2-dominated atmosphere is in vapour-pressure equilibrium with its N_2 surface ice, small changes in ice temperature cause extreme changes in surface pressure. As changes in subsolar latitude alter insolation patterns, Triton's surface pressure is expected to vary by one to two orders of magnitude with corresponding seasonal changes in the distributions of volatile N_2, CO, and CH_4 ices on Triton's surface (Grundy et al., 2010). There is observational evidence for this from changing photometric colours at visible and ultraviolet wavelengths (long-term blueing trends and occasional reddening episodes (Buratti et al., 1999).

Triton's bulk density of 2.06 g cm^{-3} (Cruikshank, 2005) suggests a relatively high rock content (figure 5.1). The internal heat produced by the radioactive decay of elements in the rock will produce energy for a rocky satellite for most of its history, often sufficient to raise the internal temperature to levels above the melting point of ice (Johnson, 2005).

Another major source of energy is tidal heating, resulting from Triton's orbital configuration where tidal heating of the crust occurs through tidal friction processes (Johnson, 2005). Triton's orbital configuration with respect to Neptune places it 23° above the planet's equator, an "effective obliquity'' of 51° when combined with Neptune's obliquity of 28° (Buratti et al., 2011).

5.1.6 Input parameters

Table 5.3. Xenolith II input parameters for Triton

System parameters	Values	Reference
Ice shell density (ρ_{mantle})	937 kg m^{-3}	*Hu et al., 2019*
Aqueous cryomagma density	1000 kg m^{-3}	*Xenolith II input*
CH_4 molecular mass	0.016 kg mol^{-1}	*Xenolith II input*
N_2 molecular mass	0.028 kg mol^{-1}	*Xenolith II input*
CO_2 molecular mass	0.044 kg mol^{-1}	*Xenolith II input*
Gas constant	8.314 kg mol^{-1}	*Xenolith II input*
Cryomagma temperature	273.15 K	*Ambient pressure liquidus H_2O*
Triton mass	2.140 X 10^{22} kg	*McKinnon and Kirk, 2014.*
Triton surface gravity	0.78 m s^{-2}	*McKinnon and Kirk, 2014.*
Xenolith mass fraction	16.54 wt%	*F*ortes, *2007*
Triton surface pressure/Vent pressure	1.5 Pa	*Brown et al. 1990*
Triton surface temperature	38±3 K	*Ingersoll and Pankine, 2010*
CH_4 plume abundance Scenario I	11%	*Section 5.1.3*
N_2 plume abundance Scenario I	69%	*Section 5.1.3*
CO_2 plume abundance Scenario I	20%	*Section 5.1.3*
CH_4 plume abundance Scenario II	5%	*Section 5.1.3*
N_2 plume abundance Scenario II	85%	*Section 5.1.3*
CO_2 plume abundance Scenario II	10%	*Section 5.1.3*

5.2 Model results

The dissociation curve of mixed clathrates has been calculated, comparing the equilibrium curves of individual gas clathrates (N_2, CH_4 and CO_2) and mixed clathrates in pure H_2O using the NOSALT and CLATHRATES programs of Bakker (1996, 1997 and 1998). Figure 5.2 shows the pressure-temperature phase diagram for clathrate stability and decomposition. The phases involved are hydrate (H), ice (I) and gas (G) where the decomposition reaction is H = G + I (after Lu & Keiffer, 2009) The phase equilibria for N_2,

CH_4, CO_2 and mixed gas clathrates are shown at temperatures between 240 K and 295 K.

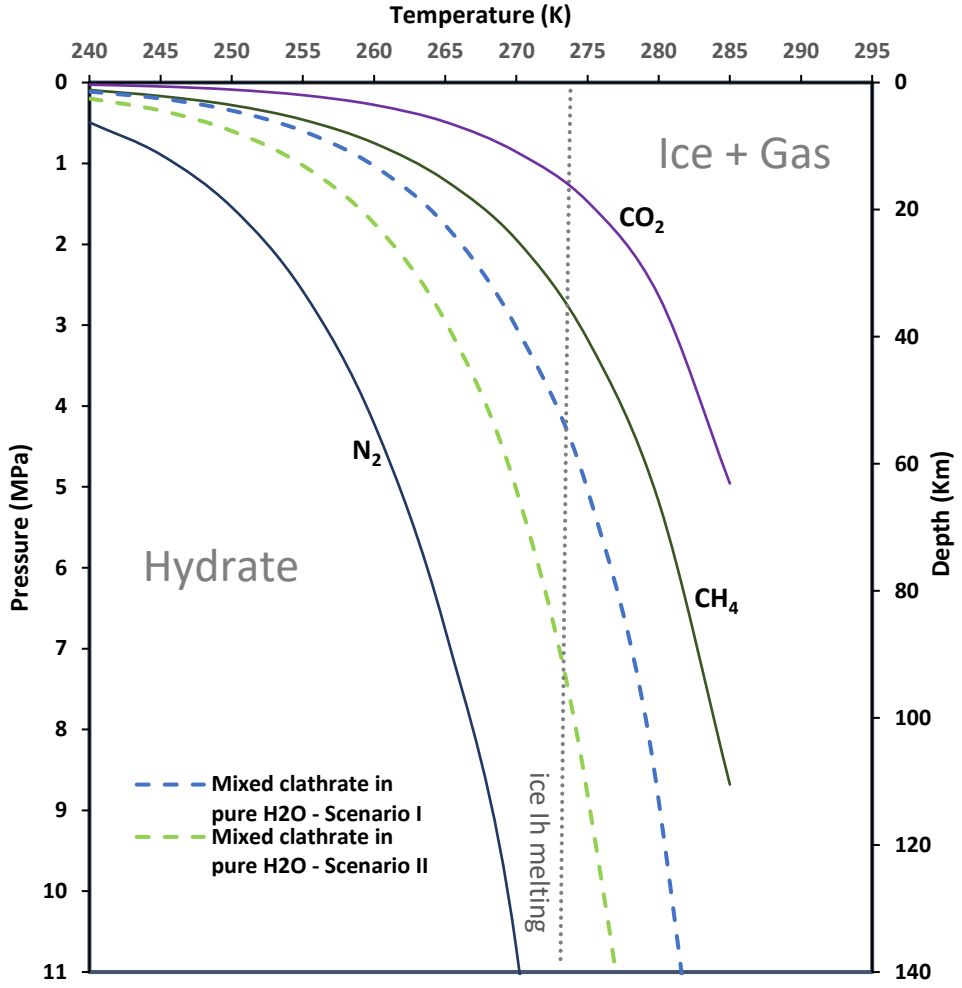

Figure 5.2. Calculated dissociation curve of mixed clathrate hydrate in pure water with CO_2 = 20%, CH_4 = 11%, N_2 = 69% (Scenario I) and CO_2 = 10%, CH_4 = 5%, N_2 = 85% (Scenario II), where the compositions are taken from table 3.2. Also shown is the pressure dependent melting curve of ice Ih (Fortes, 2007). The NOSALT component of the CLATHRATES computer package (Bakker, 1997) with the phase equilibria data of Duan et al. (1996) were used to generate the mixed clathrate curves for both scenarios as well as the dissociation curves for N_2, CH_4 and CO_2 in pure H_2O.

5.2.1 Fragmentation pressure and depth

The solubilities of CO_2, CH_4 and N_2 in pure H_2O as a function of pressure at 273.15K were determined (Appendix I) and used to model bubble growth as rising cryomagma decompressed.

The extremely low solubility of N_2 in water means that the melt becomes supersaturated in N_2 even when dissociation takes place at depth, and N_2 bubbles begin to form. CO_2 has a much higher solubility, and does not contribute to the exsolved gas fraction until the magma is within a few metres of the surface. Fragmentation of the mixed clathrate occurs at an approximate pressure and depth of 0.55 km and 0.40 MPa for volatile content scenario I (CO_2 = 20%, CH_4 = 11%, N_2 = 69%) and at a pressure and depth of 0.62 km and 0.45 MPa for volatile content scenario II (CO_2 = 10%, CH_4 = 5%, N_2 = 85%).

The point at which exsolution starts for each of the clathrate species is shown in table 5.4, showing the calculated depth, pressure, bubble volume fraction and bulk density of the whole cryomagma plume at that instance. Both volatile content scenarios have been modelled, where the most evident difference is shown in the points at which N_2 begins to dissociate: the starting dissociation pressure of N_2 is approximately 1.7 MPa lower in the cryomagma modelled with a smaller N_2 component in scenario I (N_2 = 68%) than that of scenario II (N_2 = 85%).

The calculated exsolved gas fraction of Triton's cryomagma as a function of pressure and depth at 273.15 K is shown in figure 5.3 showing the modelled depth and pressure at which exsolution begins for each clathrate species (N_2, CH_4, CO_2). The calculated bulk magma density of Triton's cryomagma as a function of pressure and depth at 273.15K is shown in figure 5.4 showing the modelled depth and pressure at which exsolution begins for each clathrate species (N_2, CH_4, CO_2).

Table 5.4. Modelled depth, pressure, percentage exsolved gas fraction and bulk density at which dissociation begins for each clathrate species in water showing two scenarios where volatile content is first modelled as CO_2 = 20%, CH_4 = 11%, N_2 = 69%, and secondly as CO_2 = 10%, CH_4 = 5%, N_2 = 85%.

	Volatile content scenario I: CO_2 = 20%, CH_4 = 11%, N_2 = 69%				Volatile content scenario II: CO_2 = 10%, xCH_4 = 5%, xN_2 = 85%			
	Depth (Km)	Pressure (MPa)	Exsolved Gas (%)	Bulk Density (kg m^{-3})	Depth (Km)	Pressure (MPa)	Exsolved Gas (%)	Bulk Density (kg m^{-3})
CO_2	0.014	0.01000	99.40	6.12	0.008	0.00600	99.65	3.56
CH_4	0.855	0.62500	63.96	365.34	0.376	0.27500	84.45	158.40
N_2	7.936	5.80000	0.25	997.64	10.262	7.50000	0.01	999.93

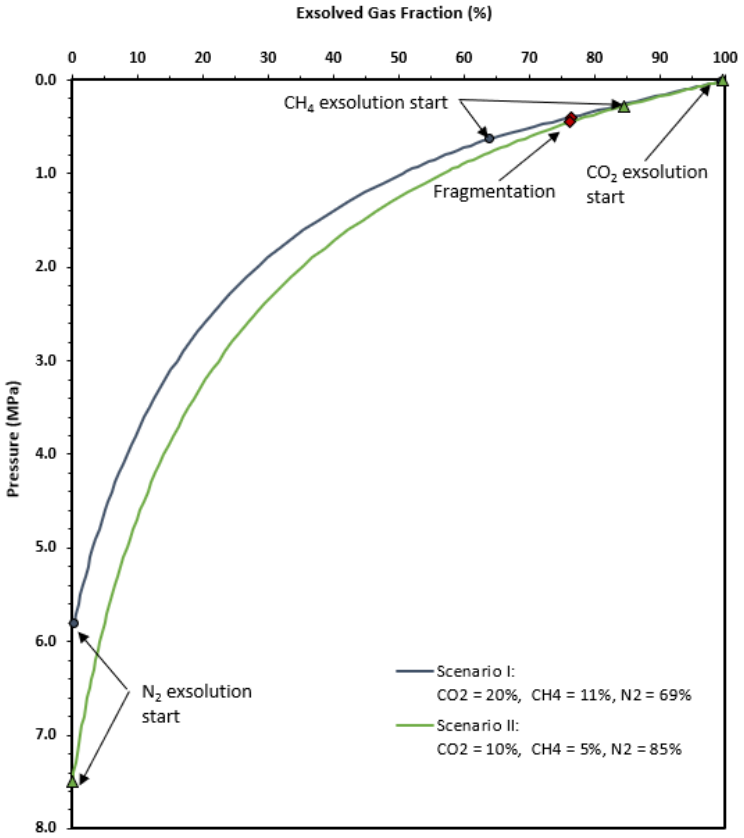

Figure 5.3. Calculated exsolved gas fraction of Triton's cryomagma as a function of pressure at 273.15K; Scenario I (CO_2 = 20%, CH_4 = 11%, N_2 = 69%) in blue , and Scenario II (CO_2 = 10%, CH_4 = 5%, N_2 = 85%) in green. The modelled pressure at which exsolution begins for each clathrate species (N_2, CH_4, CO_2) is shown as blue dots along the Scenario I curve, and green triangles along the Scenario II cryomagma curve. The approximate point at which fragmentation occurs (75% bubble volume fraction) is shown as red diamond for each curve.

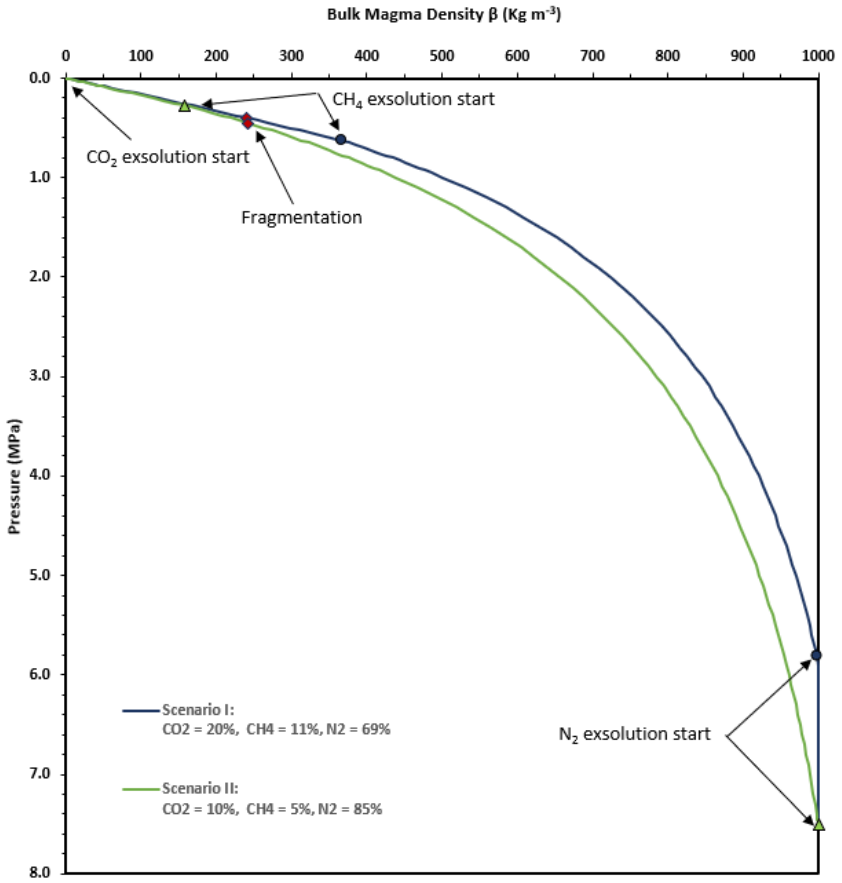

Figure 5.4. Calculated bulk magma density of Triton's cryomagma as a function of pressure at 273.15K; Scenario I (CO_2 = 20%, CH_4 = 11%, N_2 = 69%) in blue , and Scenario II (CO_2 = 10%, CH_4 = 5%, N_2 = 85%) in green. The modelled pressure at which exsolution begins for each clathrate species (N_2, CH_4, CO_2) is shown as blue dots along the Scenario I curve, and green triangles along the Scenario II cryomagma curve. The approximate point at which fragmentation occurs (75% bubble volume fraction) is shown as red diamond for each curve.

5.2.2 Cryomagma flow regime

To assess the cryomagma flow regime and plume dynamics, the local magma velocity and sound speed were calculated (equation 3.9), determined at each point of the modelled pressure and depth. The sound speed in the plume before the entrained clathrate begins to dissociate is assumed to be 1402.4 m s^{-1} for pure H_2O at 273.15 K

(Haynes, W.M., 2011). Equation 3.11 was used to determine the sound speed, showing the effects of the increase of the gas component in the plume as each of the clathrate species begins, and continues to exsolve. Figure 5.5 shows the calculated sound speed as a function of the exsolved gas fraction, and illustrates that as more gas is exsolved into the plume, the sound speed travels more slowly through a gas. Calculated data indicate an overall reduction in sound speed from the initial 1402.40 m s^{-1} (pure H_2O) before exsolution begins for scenario I and scenario II to 40.9 m s^{-1} and 41.6 m s^{-1} near the surface respectively, where all the clathrate species have dissociated.

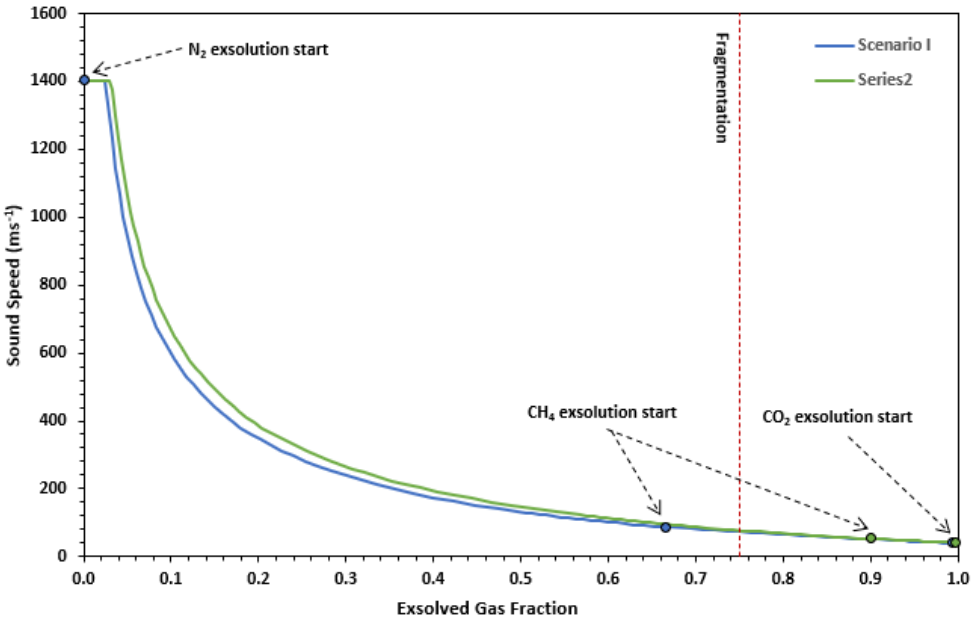

Figure 5.5. Calculated sound speed as a function of the exsolved gas fraction at 273.15 K where Scenario I (CO_2 = 20%, CH_4 = 11%, N_2 = 69% is in blue, and Scenario II (CO_2 = 10%, CH_4 = 50%, N_2 = 85% in green. The points at which each species (N_2, CH_4 and CO_2 clathrate) begin to exsolve are annotated on the graph. The point at which fragmentation (~75% bubble volume fraction) occurs is shown as a red dotted line.

As discussed in section 3.3.2, equation 3.11 breaks down if the gas fraction of the exsolving gas is very low. This occurs for the first few data points as N_2 starts to

exsolve in both scenario I and II and the sound speed is capped to the gas free sound speed in pure H_2O (1402 ms^{-1}).

Local cryomagma flow velocities (for volatile scenarios I and II) were calculated (equation 3.9) at each point of the modelled pressure and depth for all the extrapolated conduit geometries (table 5.2) utilising the three vapour mass flows of 200 m s^{-1}, 300 m s^{-1} and 400 m s^{-1}. Equation 3.9 incorporates the calculated bulk densities at each pressure point, which are shown in table 5.4. The results of the calculations to establish local flow velocities are shown in table 5.5, showing that there is no significant difference between the volatile content scenarios I and II within each of the modelled vapour mass flows. Data were plotted for a vapour mass flow of 200 kg s^{-1} (figure 5.6) and show decreasing velocity with increasing diameter of the conduits. Additionally, the flow velocities of five conduit geometries (C1 = 5 m diameter, C3 = 50 m diameter, C5 = 100 m diameter, C7 = 500 m diameter and C10 = 3000 m diameter) were plotted as a function of depth for scenario I (volatile content: CO_2 = 20%, CH_4 = 11%, N_2 = 69%) and show the increasing velocity with decreasing size (figure 5.7). Also evident is the increase in velocity with vapour mass flow, for each individual conduit plotted.

The transition from subsonic to supersonic velocities was determined by calculating the ratio of the local flow velocity to the local sound speed. A Mach 1 condition, where the flow velocity is equal to the sound speed, is reached near the surface for conduits C1, C2 and C3. Figure 5.8 illustrates the points at which the flow velocities for scenario I conduits (C1, C2 and C3) reach a Mach 1 condition at different vapour mass flow rates (200 kg s^{-1}, 300 kg s^{-1} and 400 kg s^{-1}). Before this state, flow is said to be subsonic

(nearly incompressible) and after that, supersonic (graph shows up to Mach 8), where conduits C4 to C10 did not reach Mach 1 and are therefore not plotted in figure 5.8.

Table 5.5. Modelled velocity (m s^{-1}) at the surface vent pressure (1.5 Pa) for two scenarios where volatile content is first modelled as CO_2 = 20%, CH_4 = 11%, N_2 = 69% (Scenario I), and secondly as CO_2 = 10%, CH_4 = 5%, N_2 = 85% (Scenario II). Each scenario is shown at three different vapour mass flow values: 200 kg s^{-1}, 300 kg s^{-1} and 400 kg s^{-1}.

	Vapour mass flow 200 kg s^{-1}		Vapour mass flow 300 kg s^{-1}		Vapour mass flow 400 kg s^{-1}	
Conduit Diameter (m)	Volatile content scenario I	Volatile content scenario II	Volatile content scenario I	Volatile content scenario II	Volatile content scenario I	Volatile content scenario II
C1 (5)	12262.14	12156.90	18393.21	18235.35	24524.28	24313.81
C2 (10)	3065.54	3039.23	4598.30	4558.84	6131.07	6078.45
C3 (50)	122.62	121.57	183.93	182.35	245.24	243.14
C4 (75)	54.50	54.03	81.75	81.05	109.00	108.06
C5 (100)	30.66	30.39	45.98	45.59	61.31	60.78
C6 (250)	4.90	4.86	7.36	7.29	9.81	9.73
C7 (500)	1.23	1.22	1.84	1.82	2.45	2.43
C8 (1000)	0.31	0.30	0.46	0.46	0.61	0.61
C9 (2000)	0.08	0.08	0.11	0.11	0.15	0.15
C10 (3000)	0.03	0.03	0.03	0.03	0.07	0.07

The height of the plume in each of the selected conduits was determined using equation 3.10, which relates the velocity to the surface acceleration due to gravity on Triton (0.78 m s^{-2}). The calculated velocities for each conduit (table 5.5) were selected at the surface, where the pressure is determined to be 1.5 Pa (Brown et al., 1990). Figure 5.9 shows predicted plume heights from the selected conduit geometries, for both volatile content scenarios. Conduit C1 (1 m diameter) is the only conduit whose plume height reaches or exceeds the height of ~8 km, observed by Voyager 2 in 1989 (Soderblom et al., 1990).

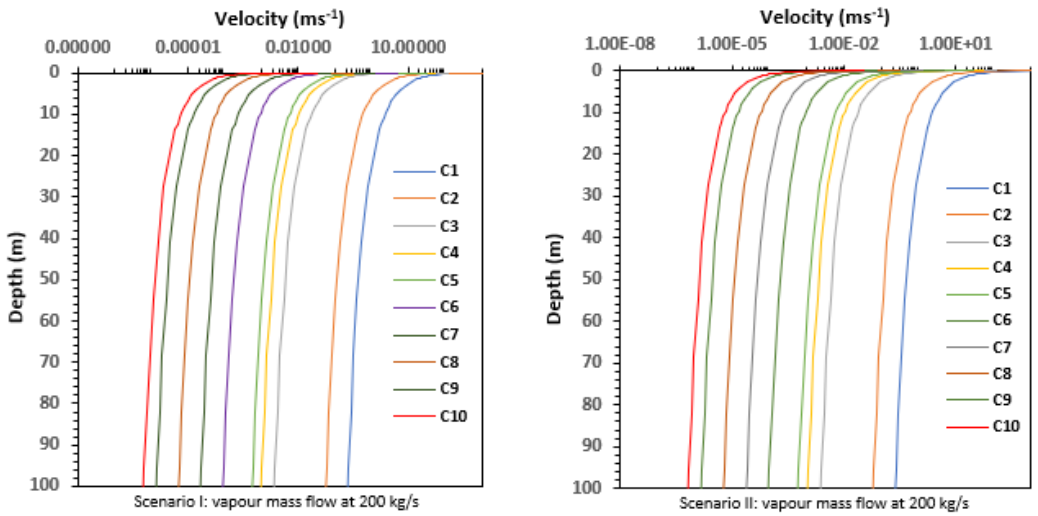

Figure 5.6. Calculated local flow velocities (at vapour mass flow of 200 kg s^{-1}) as a function of depth for scenario I (volatile content: CO_2 = 20%, CH_4 = 11%, N_2 = 69%) and scenario II (CO_2 = 10%, CH_4 = 5%, N_2 = 85%) up to a depth of 100 m (y axis) for each of the extrapolated vent geometries where C1 = 5 m diameter, C2 = 10 m diameter, C3 = 50 m diameter, C4 = 75 m diameter, C5 = 100 m diameter, C6 = 250 m diameter, C7 = 500 m diameter, C8 = 1000 m diameter, C9 = 2000 m diameter, and C10 = 3000 m diameter.

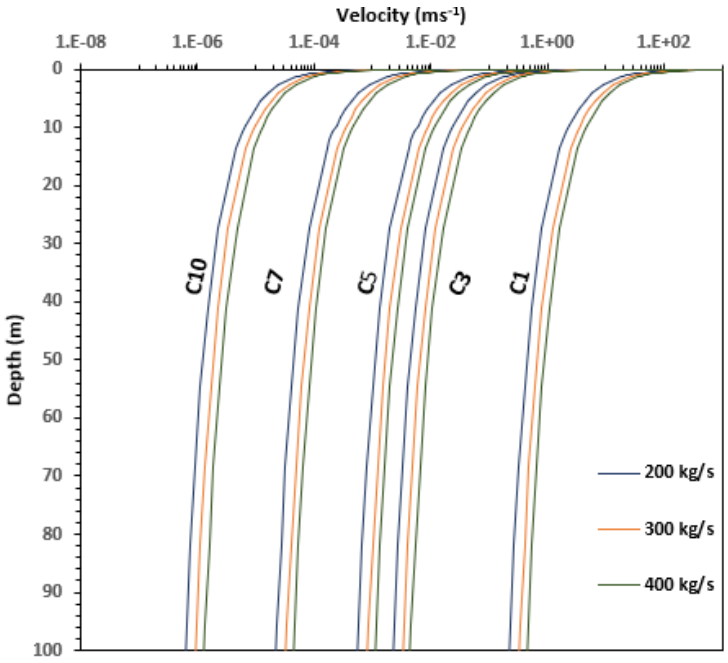

Figure 5.7. Calculated local flow velocities as a function of depth for scenario I (volatile content: CO_2 = 20%, CH_4 = 11%, N_2 = 69%) up to a depth of 100 m for each of five of the extrapolated vent geometries where C1 = 5m diameter, C3 = 50m diameter, C5 = 100m diameter, C7 = 500m diameter and C10 = 3000m diameter. Different vapour mass flow rates are shown for each of these vent diameters.

The plume heights for C2 (10 m diameter) reach about half this height. The exit velocities of the plume from conduit C1 and C2 are shown in table 5.5. However, N_2 gas, by far the largest volatile component in the modelled scenarios reacts to changes in temperature. Since N_2 expands freely at the surface (no change in entropy) even if the initial velocity of the plume is insufficient to drive the plume to the observed height, several factors could ensure the plume rises to the observed 8 km height. A rise of a minimum of 1 K over the surface temperature of Triton (~38 K) is sufficient to at least double the N_2 vapour pressure (Duxbury & Brown, 1997) and this increase in pressure is enough to drive the plumes to the observed height of 8 km (Soderblom et al., 1990). The dissociation pressures and temperatures of the mixed clathrates (scenario I and II) and individual clathrates (N_2, CH_4 and CO_2) in figure 5.2 show that these volatiles exist below the surface in their gaseous forms, mixed with ice, at temperatures far exceeding the surface temperature of Triton, so it feasible that N_2 is warmer than the observed surface temperature of Triton.

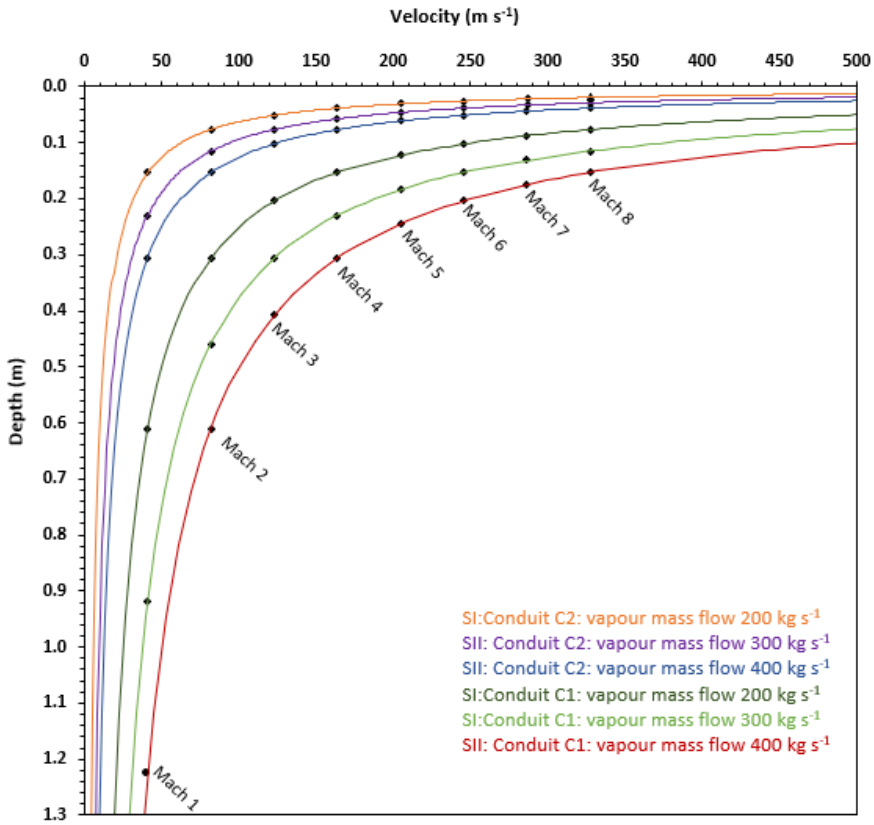

Figure 5.8. Calculated local flow velocities as a function of depth for scenario I (volatile content: CO_2 = 20%, CH_4 = 11%, N_2 = 69%) vent geometries (C1 = 5m diameter, C2 = 10m diameter and C3 diameter = 50m) with different vapour mass flow rates are shown for each of these vent diameters: 200 kg s^{-1}, 300 kg s^{-1} and 400 kg s^{-1} (colours shown in the legend). Choking conditions (Mach 1) are illustrated for each conduit and well as supersonic flow conditions (up to Mach 8) which occur in the last 1.3 metres before the surface. Best-fit power trendlines were used for each conduit, and the points calculated at which each Mach condition occurred, annotated on the graph as black dots (Appendix II describes the method used to achieve this).

Yelle et al., (1991) considered that an increase of N_2 vapour pressure and the positive buoyancy of the plumes, at an initial velocity of 125 m s^{-1}, could drive the plume to the observed height of 8 km. This value falls in the range of 122 m s^{-1} to 245 m s^{-1}, the surface velocities determined by Xenolith II for Conduit C3 (50 m diameter).

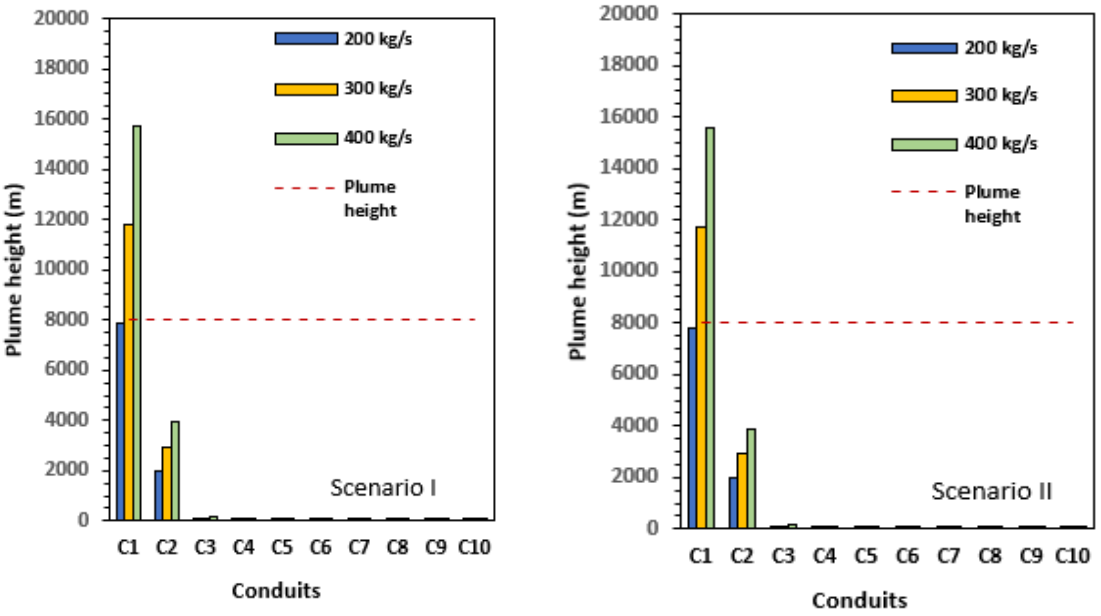

Figure 5.9. Calculated plume heights from the conduits, for both scenario I (volatile content: CO_2 = 20%, CH_4 = 11%, N_2 = 69%) and scenario II (CO_2 = 10%, CH_4 = 5%, N_2 = 85%) for each of the extrapolated vent geometries. The red dotted line represents the observed height (8 km) of the two active plumes on Triton at the time of the Voyager 2 flyby in 1989.

5.2.3 Viscosity

The viscosity of the mixed plume, from the start of the dissociation of N_2 at 8 km depth to the surface is determined by estimating the ratios of liquid water to water ice, and water ice to water vapour using the phase diagram for water, since the Xenolith II model is constrained by the assumption that the plume is pure water at its ambient pressure liquidus (273.15 K).

The Xenolith II model assumes the vapour phase is made up of 91% H_2O vapour at the surface, similar to that of the plumes on Enceladus. The triple point of water, where the temperature and pressure at which the solid, liquid and vapour phases can coexist in equilibrium, is at a temperature of 273.15 K and pressure of ≈612 Pa at ≈0.82 m below the surface. Table 5.6 illustrates the phases of water that can exist at critical pressure and depths of the model.

Table 5.6. Modelled pressures and depths at critical points in plume eruption showing possible phases of H_2O at 273.15 K, based on the phase diagram for water*. The different pressures and depths of the start of the exsolution points of CO_2, CH_4, N_2 and fragmentation are shown at a vapour mass flow of 300 kg s^{-1} for each selected volatile content scenario, where scenario I is CO_2 = 20%, CH_4 = 11%, N_2 = 69% and scenario II is CO_2 = 10%, CH_4 = 5%, N_2 = 85%.

	Volatile content scenario I		Volatile content scenario II		
	Pressure (MPa)	Depth (m)	Pressure (MPa)	Depth (m)	H_2O phases at 273.15 K
Surface	0.000002	0.0021	0.000002	0.00	vapour
~Triple point of H_2O*	0.006000	0.8210	0.000600	0.82	vapour, solid, liquid
CO_2 exsolution start	0.010000	13.6825	0.006000	8.21	vapour, solid, liquid
Fragmentation	0.400000	547.3004	0.450000	615.71	vapour, solid, liquid
CH_4 exsolution start	0.625000	855.1569	0.275000	376.27	vapour, solid, liquid
N_2 exsolution start	5.800000	7935.8564	7.500000	10261.88	solid, liquid

**Phase diagram source: Bore et al. 2023*

As pressure decreases, clathrates entrained in the plume respond to pressure changes, and exsolve, releasing gas into the plume, the fractions of which impact the bulk viscosity of the plume. Furthermore, as the pressure drops, water changes phase from liquid to vapour. Viscosity is temperature dependent, but since Xenolith II constrains the temperature of the plume to a constant 273.15 K, the main impact on the bulk viscosity is the addition of the exsolved gases. The ice and xenolith phases of the plume are not taken into consideration when determining the viscosity of the mixed component plume. To further constrain the model and estimate the viscosity of the plume, the following assumption has been made: The gas exsolved from the clathrate dissociation process is added to the cryomagma as it erupts, first to the liquid phase of water, then at the triple point, to the vapour phase, where at the surface water is in a ratio of 91 : 6.21 : 1.8 : 0.99 (H_2O : N_2 : CO_2 : CH_4) for scenario I and 91 : 7.65 : 0.9 : 0.45 (H_2O : N_2 : CO_2 : CH_4) for scenario II. Before N_2 begins to exsolve, the Xenolith II model

assumes that 100% of the plume is liquid water, and as the clathrates continue to exsolve as the cryomagma rises to the surface, the ratio of liquid to vapour phase of the water changes. The viscosity for each scenario is modelled at a vapour mass flow of 300 kg s^{-1} (equation 3:12) with individual gas viscosities obtained from Haynes, W.M. (Ed.), 2011 (Appendix III). Table 5.7 tabulates these results for volatile content scenario I and II at a vapour mass flow of 300 kg s^{-1}.

Table 5.7. Modelled pressures and depths at critical points in plume eruption showing calculated viscosity for the mixed plume (H_20_{LIQUID}, H_2O_{VAPOUR}, CH_4, N_2 and CO_2). The different pressures and depths of the start of the exsolution points of CO_2, CH_4, N_2 and the triple point of H_2O are shown for each selected volatile content scenario at a vapour mass flow of 300 kg s^{-1}, where scenario I is CO_2 = 20%, CH_4 = 11%, N_2 = 69% and scenario II is CO_2 = 10%, CH_4 = 5%, N_2 = 85%.

	Volatile content scenario I			Volatile content scenario II		
	Pressure (MPa)	Depth (m)	$Viscosity_{mix}$ µPa·s	Pressure (MPa)	Depth (m)	$Viscosity_{mix}$ µPa·s
Surface	0.000002	0.002	9.42	0.000002	0.00	9.48
~Triple point of H_2O*	0.000600	0.821	9.35	0.000600	0.00	9.48
CO_2 exsolution start	0.010000	13.683	1718.12	0.006000	8.21	1661.18
CH_4 exsolution start	0.625000	855.157	1756.64	0.275000	376.27	1671.99
N_2 exsolution start	5.800000	7935.856	1791.10	7.500000	10261.88	1680.55

** Phase diagram source: Bore et al. 2023*

The viscosity of liquid water is much higher than that of water vapour (1791.1 µPa·s compared to 8.95 µPa·s) and will impact the mixed viscosity of the plume. The point at which the water phase is expected to change from liquid to vapour is taken to be at the triple point (table 5.6). The Xenolith model examines the scenario that assumes that up to the triple point (273.15 K at 611.657 Pa), the magma is a mixture of liquid water and exsolved gases. At the triple point, the water phase changes from the liquid to the vapour phase. The ice phase is not considered in the viscosity calculations.

Table 5.8. Modelled Reynolds numbers (Re) at critical depths from 10 km-to the surface shown for a vapour mass flow of 300 kg s^{-1}, where the volatile content CO_2 = 20%, CH_4 = 11%, N_2 = 69% (scenario I). The points at which flow is laminar (Re < 2000) are in bold, and those that are in transitional flow are in red (2000 > Re < 4000).

Conduit	Mantle 10125.06 m	Start of N_2 exsolution 7935.86 m	Start of CH_4 exsolution 855.16 m	Fragmentation 547.30 m	Start of CO_2 exsolution 136.86 m	Triple Point of H_2O 8.21 m	Surface 0.002 m
C1	42652.21	42774.13	50247.71	53313.44	59719.64	72618.33	6305798.81
C2	21326.10	21387.06	25123.86	26656.72	29859.82	36309.16	3152899.40
C3	4265.22	4277.41	5024.77	5331.34	5971.96	7261.83	630579.88
C4	2843.48	2851.61	3349.85	3554.23	3981.31	4841.22	420386.59
C5	2132.61	2138.71	2512.39	2665.67	2985.98	3630.92	315289.94
C6	**853.04**	**855.48**	**1004.95**	**1066.27**	**1194.39**	**1452.37**	126115.98
C7	**426.52**	**427.74**	**502.48**	**533.13**	**597.20**	**726.18**	63057.99
C8	**213.26**	**213.87**	**251.24**	**266.57**	**298.60**	**363.09**	31528.99
C9	**106.63**	**106.94**	**125.62**	**133.28**	**149.30**	**181.55**	15764.50
C10	**71.09**	**71.29**	**83.75**	**88.86**	**99.53**	**121.03**	7006.44

Viscosity is used to determine the Reynolds number (equation 3.13) for each individual conduit, where viscosity is inversely proportional to the product of the area, density and a factor of 2 (for circular conduits). Table 5.8 shows that as the conduit diameter increases, the Reynolds number decreases. Figure 5.10 shows the flow velocities of the extrapolated conduits and indicates at which depth and velocity the flow is laminar (Re < 2000), in transition (2000 > Re < 4000) and turbulent (Re > 4000).

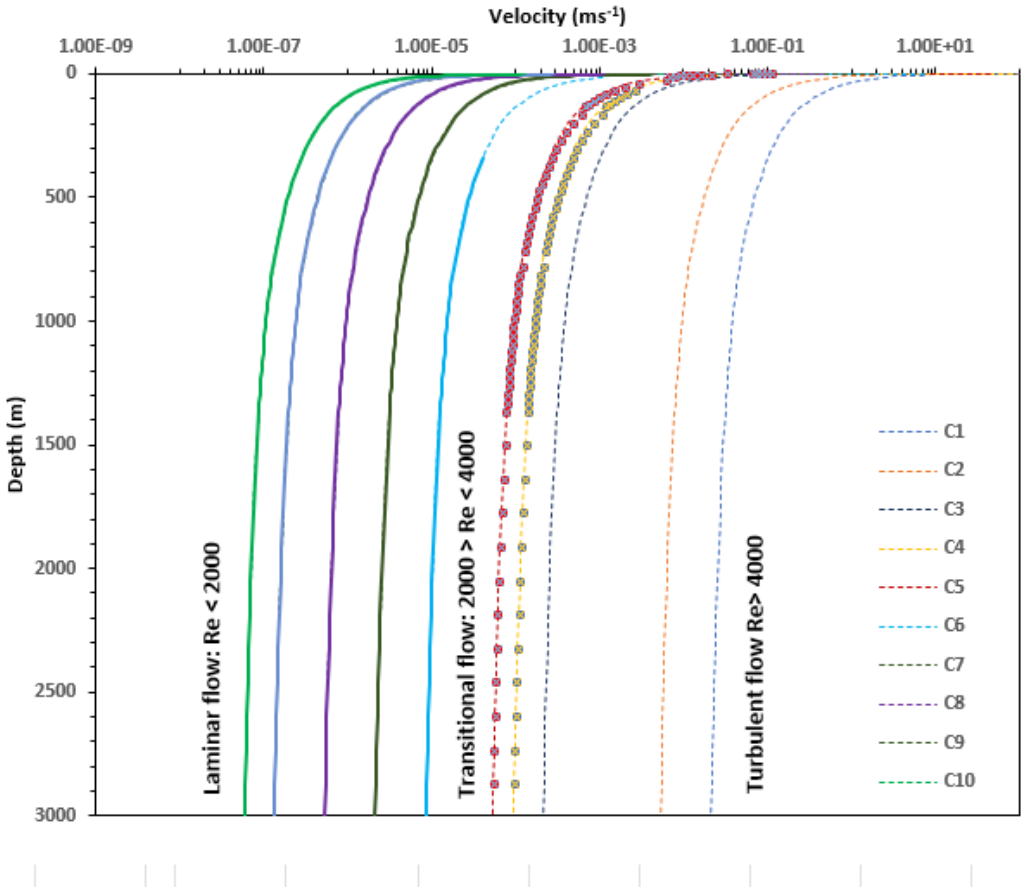

Figure 5.10. Calculated flow velocities of the extrapolated conduits (table 5.2) for vapour mass flow of 300 kg s^{-1}, where the volatile content is CO_2 = 20%, CH_4 = 11%, N_2 = 69% (Scenario I) showing the velocity at which flow is laminar (Re < 2000), in transition (2000 > Re < 4000) and turbulent (Re > 4000). Laminar flow is illustrated with a thick solid line, transitional flow with circles and turbulent flow with a dotted line.

5.2.4 Kinetic energy

Using the calculated upward velocity of the plume at each pressure point (equation 3.15), the kinetic energy per unit volume was determined for each of the circular conduits (C1 to C10) whose geometries are defined in table 5.2. Figure 5.11 illustrates that as clathrate dissociation increases the percentage of gas bubbles in the cryomagma the kinetic energy increases. The geometry of the conduits is also related to the kinetic energy: the smaller the area of the conduit, the higher the kinetic energy.

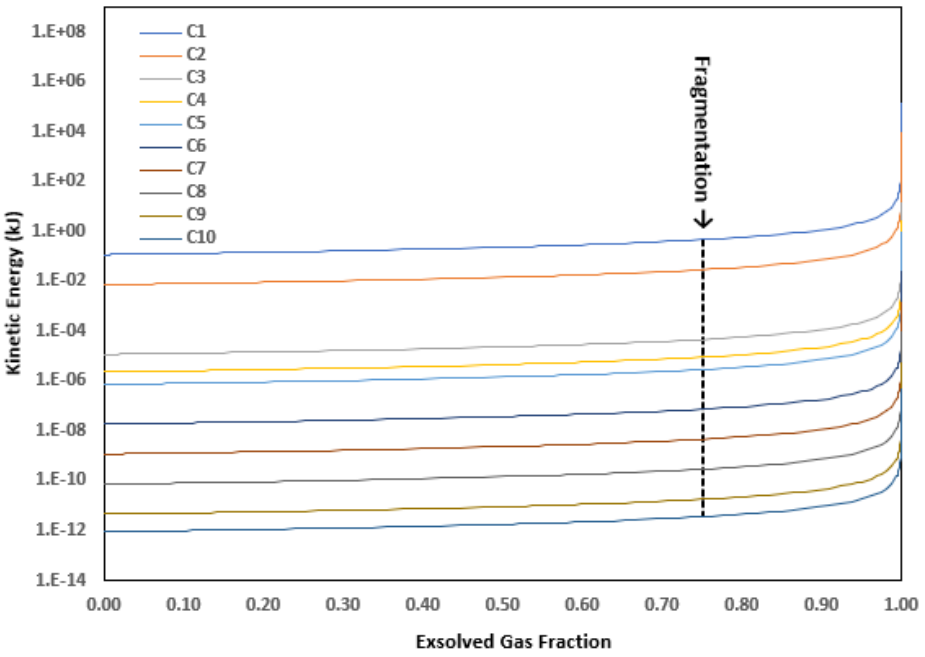

Figure 5.11. Calculated kinetic energy of the extrapolated conduit geometries (conduits C1 to C10) as a function of the exsolved gas fraction for a vapour mass flow of 300 kg s^{-1}, where the volatile content is CO_2 = 20%, CH_4 = 11%, N_2 = 69% (Scenario I). The point at which fragmentation occurs (75% bubble volume fraction) is annotated on the graph.

5.2.5 Thermodynamic energy balance

The average total power radiated from the region of the of the area observed by Voyager 2 in 1989 (between latitudes of 15° and 45° S) is unknown (Q_{out} in equation 3.16). However, an attempt has been made to estimated values for the heat required to dissociate clathrate, and the sublimation and crystallisation of ice. An estimate of the total mass flux of the plume (m_{out}) is 410 kg s^{-1} which includes mass vapour flux and mass particles flux (Hansen et al., 2021). The molar ratio of the gas mixture (CO_2, CH_4 and N_2) to water vapour is taken to be ~1:10, the same as on Enceladus. In the absence of compositional data for the plumes on Triton, this is an assumption, given that both Enceladus and Triton are predicted to have ice I shells and a liquid water ocean (sections

5.1.1 and 5.1.2). The mass ratio for the given molar fractions is 1:7 and the mass flow rate of the gas mixture from clathrate dissociation ($m_{out,g}$) is ≈25 kg s^{-1} for a mass vapour flow of 200 Kg s^{-1}, is ≈37.5 kg s^{-1} for a mass vapour flow of 300 kg s^{-1} and is ≈50 kg s^{-1} for a mass vapour flow of 400 kg s^{-1}. The latent heat of clathrate dissociation (L_{dis}) is estimated at ≈465 kJ kg^{-1} (Kang and Lee, 2001). The mass rate of the sublimated H_2O vapour, $m_{out,v}$, is 350 kg s^{-1}, the latent heat for the sublimation of ice is (L_{sub}) is 2800 kJ kg^{-1} (Lu and Keiffer, 2009) and the latent heat of crystallisation (L_{cry}) is 334 kJ kg^{-1} (Giauque and Stout, 1936) as dissociation will result in a percentage of the liquid water crystallising (Fortes, 2007). The mass flow rate of the liquid water phase is unknown, and an approximation is made where the mass flow rate is 40% of the total flow rate; 80 kg s^{-1} since the water vapour to ice ratio predicted by the Fortes (2007) is ≈60:40. The value for the reservoir pressure (P_r) is taken as the vent pressure at the surface (1.5 Pa) and the reservoir density (ρ_r), 937 kg m^{-3} (Brown et al., 1990). Table 5.9 shows the results of the calculated values of the terms in the right hand side of the equation 3.16 where the estimated total heat required to dissociate the mixed clathrate and the sublimation and crystallisation of ice is estimated for the mass flow rates of 200 kg s^{-1}, 300 kg s^{-1} and 400 kg s^{-1}.

Table 5.9. Estimated values for the heat required to dissociate clathrate, sublimation of ice and crystallisation of ice.

Mass flow rate Kg s^{-1}	$m_{out,g}H_{dis}$ (GW)	$m_{out,v}L_{sub}$ (GW)	$m_{out}L_{cry}$ (GW)	$m_{out}(P_r/p_r)$ (GW)	Total (GW)
200	0.011625	0.98	0.00334	$6.6X10^{-12}$	0.99
300	0.017438	0.98	0.00501	$6.6X10^{-12}$	1.00
400	0.026250	0.98	0.00668	$6.6X10^{-12}$	1.01

5.3 Evaluation and discussion

The aim of this application of the Xenolith II model to Triton is to examine the potential role that clathrate hydrate dissociation may have in explaining the source of the active plumes observed by the Voyager 2 flyby in 1989.

Voyager 2 images are of too low a resolution to show the exact size of the vents, and available instruments on board did not provide data for the compositional nature of the plumes, or the power radiated from the area of the plumes. Input parameters and the modelled results therefore have limitations, namely that assumptions made in the Xenolith II model as applied to Triton are based on the results of different workers' analyses and observations of data from Voyager 2 and satellite and ground-based observations. An informed attempt has been made to use those values which are the most recent (e.g., as in updated spectroscopic analysis of the surface volatiles) or those which represent an average from the range of possible values available from different studies (e.g., the vapour flow rates from the plumes and vapour mass flow rates). The volatile component of the entrained clathrates in the plumes examines two different scenarios (section 5.1.3), the selection of which are based on a range of the available data for the observed volatiles detected on the surface, assuming that a similar ratio is present on the plume.

The model assumes that there is 91% H_2O in the plume (as on Enceladus), in the absence of any compositional data for the plume on Triton. However, this assumption is based on the similarity to some of the conditions on Enceladus (probable presence of a subsurface liquid water body and an ice I shell). Different percentages of H_2O were investigated however, and it was predicted that dropping the percentage to half of 91% (45.5% H_2O) in the plume results in an increase in the viscosity at the surface of

approximately 20% (from 9.4 µPa·s to 11.8 µPa·s for volatile content scenario I), which would in turn affect the Reynolds number.

The vent diameters are estimated, as are the vapour mass flow rates, as tabulated in table 5.2, where a range of possible combinations are modelled.

The Xenolith II model predicts the depth (0.55 km for scenario I and 0.62 km for scenario II) at which fragmentation of the mixed clathrate in the plumes occurs, and at this point, ~75% of the clathrate hydrates have dissociated and released gas into the low density, low viscosity plume. The vapour mass flow is predicted to be turbulent from the start of fragmentation.

However, modelled results for scenario I (volatile content is CO_2 = 20%, CH_4 = 11%, N_2 = 69%) and a vapour mass flow of 300 kg s^{-1} show that the flow in the conduits (C1 to C3) is turbulent from a depth of ~8 km (at the start of N_2 exsolution) whereas conduits C4 and C5 are in transitional flow, and the flow in conduits C6 to C10 remains laminar up to the triple point of H_2O from where all conduits are calculated to have turbulent flow. Turbulent flow would likely result in significant mechanical erosion of the vent walls (Fortes., 2007). The Reynolds numbers (calculated to determine the nature of the flow) increase by 99% at the triple point of H_2O, indicating that upward inertial forces overwhelm the downward viscous forces in the plumes. Before the triple point of H_2O, size of the conduits is related to the nature of the flow where the smaller diameters are determined to be more turbulent than the larger diameter conduits.

At 0.1 m below the surface, the predicted results obtained for the velocities of the modelled conduits (C1 to C10) range from 184 m s^{-1} (C1) to 0.005 m s^{-1} (C10). Clearly, the model results showing extremely low velocities are not improbable, but other workers' estimated velocities (ranging from 20 m s^{-1} to 125 m s^{-1}) fall within the

calculated range (Hansen et al., 2021; Yelle et al., 1991). No predictions for Mach numbers were found in the available literature, so comparisons cannot be made with the Xenolith II results although the velocity of 184 ms^{-1} is described as supersonic by Yelle et al. (1991). The diameters of the selected conduit areas have a direct bearing on the predicted plume heights, where conduit C1, which has the smallest area (19.63 m^2) has the highest predicted plume for modelled scenarios and is related to its high velocity near the surface. It is possible also that the observed plumes are made up of small closely packed vents rather than a much large diameter vent (Kirk, R.L., 1990), which would then account for the heights predicted by the Xenolith II model.

As discussed in detail in section 5.1.5, it is feasible that that N_2 gas rising from the plume is warmer that the surface temperature of Triton and even a small increase in temperature ($\geq$ 1 K) would be sufficient to at least double the vapour pressure which would drive the plumes to the observed height of 8 km.

The estimations made regarding the thermodynamic energy balance of the plumes was an attempt to quantify how much the latent heat of dissociation, crystallisation and sublimation contributed to any observed power being radiated from the region of the plumes on Triton. There are no estimates for the radiated power found in the literature, which does not allow for an assessment of what proportion the heat produced by the clathrate dissociation process contributes to the total power output on the surface of Triton in the region of the plumes.

Despite the limitations of the data available for more accurate modelling, it is feasible that the plumes observed may be generated from the dissociation of clathrates hydrates at depth, resulting in explosive cryovolcanism. A combination of various sources supplying the necessary heat required (section 5.1.5), a large H_2O ice shell (section 5.1.1)

and the possible existence of a subsurface ocean on Triton (section 5.1.2) together with evidence of endogenic surface and atmospheric volatiles point to the possibility that the plumes are generated by the process described by the Xenolith II model. The modelled results show that only the plume from conduit C1 (5 m diameter) reached a height of 8 km, however, a sudden increase of N_2 vapour pressure at the surface could drive the plumes from larger diameter conduits (C2 to C10) to the observed height (5.2.2).

CHAPTER SIX

Cryovolcanism model results and discussion - Titan

6. Cryovolcanism model results and discussion - Titan

Cassini radar observations of Titan have revealed surface morphological landforms on Titan which have been interpreted as comparable to volcanic terrains on Earth (Wood & Radebaugh., 2020.; Mitri et al., 2008; Le Corre et al., 2009; Nelson et al., 2009; Lopes et al., 2007; Lopes et al., 2013), although no active plumes or geysers were detected. Features consistent with volcanic landforms formed by explosion, excavation and collapse in the north polar region, have also been interpreted as being fresh, indicating that cryovolcanism might have been recently active on Titan (Wood & Radebaugh., 2020). Nelson et al. (2009) report on spectrophotometric variability detected in images from Cassini's Visual and Infrared Mapping Spectrometer (VIMS) in two separate locations, suggesting surface flows that were consistent with ongoing cryovolcanic activity. Further evidence for past eruptions and outgassing from Titan's interior was detected by the Gas Chromatograph Mass spectrometer (GCMS) onboard the Cassini Huygens lander where significant amounts of radiogenic ^{40}Ar were found in the atmosphere. ^{40}Ar is the decay product of ^{40}K, contained in and interpreted as being

sourced from the rocky core (Tobie et al., 2010). The carbon isotopic ratio $^{13}C/^{12}C$ detected by the GCMS instrument in the atmosphere is only slightly smaller than the value detected on the surface, and suggests that methane is unlikely to have been formed during Titan's early formation and must periodically be replenished from cryovolcanic processes, since it is irreversibly destroyed in a relatively short period of 10-100 Myr by photolysis (Niemann et al., 2005). Photolysis Is a reaction with light which sets off a chain of chemical reactions in which molecules are broken down by photons. Photolysis fragments are reactive and quickly react with each other, and with other atmospheric constituents to form heavier hydrocarbons (e.g., C_2H_6), nitriles and some oxygen-containing species that condense as hazes and precipitate out of the atmosphere. CH_4 is a greenhouse gas, and its total depletion would rob the atmosphere of near-IR opacity, leading to cooling, where the atmosphere would cool enough for nitrogen to freeze out onto the surface leaving a very thin atmosphere not unlike Triton or Pluto. Without CH_4, Titan's stratosphere and troposphere may become too cold for N_2 to remain in the gas phase, thus reducing the atmospheric pressure.

Thus, based on the evidence that both past and possibly recent cryovolcanism exists, the numerical model described in chapter 3 is here applied to Titan. Input parameters are from the observations made by the instruments on board Cassini and the Huygens lander, as well as the available analysis and literature on Titan. The aim is to contribute to this study's primary goal of examining the potential role that clathrate hydrate dissociation may have in explosive cryovolcanism on the icy satellites of the outer solar system. Model assumptions and input for Titan are presented in section 6.1, and the results of the modelling in section 6.2. The computed outcomes of the model will be

compared to mission data observations and analysis from other workers and then evaluated in terms of the primary goal of this thesis (section 6.3).

6.1 Xenolith II assumptions and input

The input parameters and assumptions made for Xenolith II's application to Titan include current data for Titan (mass, surface gravity, internal structure) and physical constants (table 6.2). A description of the structure of the model is given in chapter 3. The assumptions made are outlined and discussed in the following sections.

6.1.1 Internal structure of Titan

Several models of Titan's interior, based on existing observational constraints (from Huygens and Cassini instruments and ground-based telescopes) have been formulated (Tobie et al., 2005; Fortes et al., 2007; Fortes, 2012). Titan's density (1.88 g cm^{-3}) implies that it is a solid body with a rocky core (silicate), overlain by a thick mantle of impure water ice, some of which might be liquid (Coustenis & Taylor, 2008). Various formation scenarios exist for Titan: one such formation scenario describes three outgassing episodes providing sufficient CH_4 to offset the predicted methane loss rate by photolysis in the upper atmosphere, and resulting in the cryovolcanic terrains observed on the surface by Cassini's October 2004 flybys (Tobie et al., 2005). More complex interior models exist where layers in the ice mantle are predicted, which depend on different pressure and temperature profiles, and where NH_3 and CH_4 molecules are trapped in water ice. Additionally, some models predict that the core may differentiated, with iron and sulfur compounds overlain by a silicate mantle (Coustenis and Taylor, 2008). A

model by Fortes et al. (2007) describes an early Titan, which differentiated as the interior became hot enough due to accretional heating and radiogenic decay, and formed a rocky core (carbonaceous chondritic material) and mantle (water ice, ammonia hydrate and methane clathrate). In this environment, the ice and hydrate component were melted, resulting in the total degassing of methane clathrate and where the water fraction of the rock was yielded up and the rocky component subsequently serpentinized to form the hydrous silicate mineral antigorite. In this model, magnesium sulfate in the aqueous solution reacted with ammonia to form soluble ammonium sulfate and insoluble magnesium hydroxide.

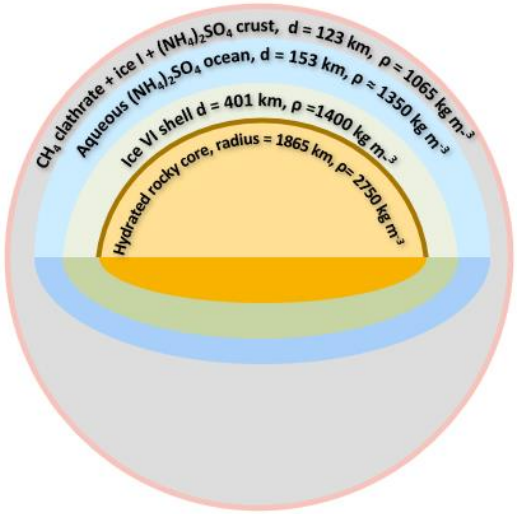

Figure 6.1**.** An internal structure model of Titan (not to scale), after Fortes et al. (2007), showing the relative possible positions of a hydrated rock core (antigorite), an ice VI shell, an aqueous $(NH_4)_2SO_4$ ocean, and a H_2O ice crust containing CH_4 clathrate and $(NH_4)_2SO_4$. At the base of the ice VI shell is a 33 km layer of hydroxide 'mud' shown as a thick line (ρ = 2400 kg m^{-3}).

The degassing of methane (accreted as CH_4 clathrate) and nitrogen (formed by the dissociation of ammonia) formed the dense atmosphere of Titan (Fortes et al., 2007). Figure 6.1 illustrates this model of the interior structure of Titan after Fortes et al. (2007). In a later work, Fortes (2012) argued that Titan's moment of Inertia is consistent with a possible internal structure of a hydrous silicate core (radius between 1980 to

2120 km and density between 2570 to 2460 kg m^{-3}) overlain by a high pressure ice VI shell, a global subsurface ocean and a decoupled water ice/clathrate shell.

6.1.2 The case for a subsurface ocean on Titan

Current models of Titan's interior predict that an aqueous ammonia-rich ocean, several tens of kilometres thick, exists under the ice shell (Fortes et al., 2007; Fortes, 2012; Tobie et al., 2005; Baland et al., 2014; Sotin & Tobie., 2008; Sohl, 2010; Grindrod et al., 2008). Cassini's radar observations over a period between October 2005 and May 2007 (19 flybys) indicated that Titan's rotation period was different from its orbital period, leading to a shift of ~0.36° per year in apparent longitude (Lorenz et al., 2008). Initial radar observations were able to see through the dense haze and image the locations of landmarks on Titan's surface (lakes, dunes, cryovolcanic features, canyons and mountains), and later flybys revealed that these had shifted from their initial positions by up to 30 km. Lorenz et al. (2008) interpreted this to be the result of a decoupling of the surface from the interior, the result of a liquid layer of water and ammonia between the ice crust and an internal mantle and core. However, Sotin & Tobie. (2008) cautioned that these differences could the result of seasonal atmospheric cycles and/or gravitational interaction of the deep interior with the gravitational field of Saturn. As another explanation for the observed movement of surface morphological features, Tokano (2009) argued that Titan's atmospheric circulation resulted in a wind generated torque which could modify the surface in various ways and transfer angular momentum between the atmosphere and surface, leading to seasonal variations in Titan's spin rate and /or length of day. More recent estimates of the spin rate and obliquity of Titan were obtained by tracking surface landmark features in time using Cassini SAR images

acquired from both the Cassini Prime and Extended Mission up until 2009 (Meriggiola et al., 2016).

Accepting the presence of an aqueous layer, the predicted existence of an ice shell above an aqueous layer would provide an insulating layer from the cold surface, ensuring that the aqueous layer remained mostly in the liquid phase (Grindrod et al., 2008). Further to sustaining the fluid state, the amount of heat released from the interior of Titan need not be large for maintaining the aqueous layer, if sufficiently protected from the surface (Coustenis & Taylor, 2008). Additionally, the predicted impurities in the ocean would help toward keeping the water layer liquid: the addition of ammonia, and possibly methane, nitrogen and hydrated salts, lowers the freezing temperature and inhibits crystallisation in the liquid layer (Grasset et al., 1996; Grasset et al., 2000). Grindrod et al. (2008) modelled the thermal evolution of a subsurface ocean of aqueous ammonia sulfate, which predicts the thickness of the ocean throughout the evolution and Titan, and concluded that the ocean could remain liquid to the present day, under a wide range of conditions. They suggest that as the ocean cools, crystallisation at its boundaries results in a thickening of the crust under the ice I layer and above the ice VI layer. The ice I underplating can lead to the formation of buoyant ice diapirs which could be one of the driving forces for the cryovolcanism described in the Xenolith II model (Grindrod et al., 2008).

6.1.3 Volatile component of entrained clathrates

The composition of Titan's lower atmosphere (from ~140 km to the surface) was measured by the gas chromatograph mass spectrometer (GCMS) instrument on the Cassini-Huygens lander, which although not designed to survive the impact, continued

to communicate with the Cassini orbiter for 72 minutes before losing contact. Results from data captured during the descent to the surface were calibrated and analysed by Niemann et al. (2010) who determined altitude profiles of N_2, CH_4, H_2 and ^{40}Ar. N_2 and CH_4 were confirmed to be the major constituents of Titan's lower atmosphere. After landing, CH_4, C_2H_6, C_2H_2, C_2N_2 and CO_2 were also detected on the surface below the Huygens lander (Niemann et al., 2010). For the purposes of the Xenolith II model, the volatile component of entrained clathrates in a possible cryovolcanic plume is assumed to be the same as that of the ratio of CH_4 and N_2 detected in the atmosphere near the surface where CH_4 = 5.65% and N_2 = 94.2%. Although detected on the surface, CO_2 was not present in any detectable abundance in the lower atmosphere and was not included as a modelled volatile component for Titan (Niemann et al., 2010).

Two cryomagma compositions are investigated: Scenario I is based on a composition of 10.6 wt% $(NH_4)_2SO_4$ (density ρ = 1065 kg m^{-3}) and Scenario II has a composition of 40% wt% $(NH_4)_2SO_4$ (density ρ = 1235 kg m^{-3}) where the liquidus temperatures are 270.7 K and 253.8 K respectively (Fortes et al., 2007). Since NaCl aqueous solutions have water activities comparable to the two magma compositions (Fortes et al., 2007), the solubilities of CH_4 and N_2 in 1M NaCl at 270.7 K and 4M NaCl at 253.8 K are treated as an analogue for the solubilities of the volatiles in 10.6 wt% $(NH_4)_2SO_4$ and 40% wt% $(NH_4)_2SO_4$ compositions respectively. These were determined using the CLATHRATES suite of programs by Bakker (1996, 1997 and 1998).

6.1.4 Vent geometries, vapour mass flow and plume velocity

Although there is speculation about the nature and extent of cryovolcanic constructs on Titan, there is evidence from images obtained from Cassini's targeted fly-bys of Titan

that support the existence of calderas, flow-like features and mountains (shields or domes). Shown in figure 6.2 is the Sotra Patera region, containing one of the tallest peaks on Titan, Doom Mons (named after Mount Doom, a volcano in J.R.R. Tolkien's fictional world of Middle earth in The Lord of the Rings). Lying adjacent to this is one of the deepest depressions or pits on Titan, Sotra Patera. Morphological changes were observed in surface images at 7°S 138°W and 26°S 78°W during several fly-bys, and thought to be consistent with surface flows possibly resulting from cryovolcanic activity (either effusive or explosive) where material from Titan's interior was being brought to the surface by some means (Nelson et al., 2009). Flow-like landscapes around them (Mohini Fluctus), have been in interpreted as cryovolcanic structures (Lopes et al., 2013). Calderas have also been identified north of the central Hotei Regio area (Lopes et al., 2013; Soderblom et al., 2009), and Erebor Mons, located near Titan's equator (named after the "Lonely Mountains" in J.R.R Tolkien's Lord of the Rings), is also considered cryovolcanic in origin (Lopes et al., 2013). In a recent study, Wood & Radebaugh. (2020) contend that morphological evidence (nested collapses, elevated ramparts and subsidence craters) revealed by Cassini Radar observations of Titan's north polar region is indicative of cryovolcanic collapse craters. They argue that the abundant small features, approximately round and with raised rims, are relatively fresh, indicating recent or even current cryovolcanic activity. They further propose that these features (maars or calderas, sometimes overlapping) are related to the predicted warmer and thinner crust at Titan's low-elevation poles. The shape of these vents is unknown, but a simple circular vent geometry has been assumed, for analysis: a parallel-sided, axis-symmetric shape, with no variation in cross-sectional area with depth. Although the caldera sizes are known from observational data, they do not represent

the size of the actual cryovolcanic conduits, and these are therefore estimated and shown in table 6.1 which lists the diameters of the conduits considered in this study.

Three mass flow rates in increasing order of magnitude have been selected for this study, (300 kg s^{-1}, 400 kg s^{-1} and 500 kg s^{-1}) and have been applied to each of the conduits in turn, for both cryomagma compositions.

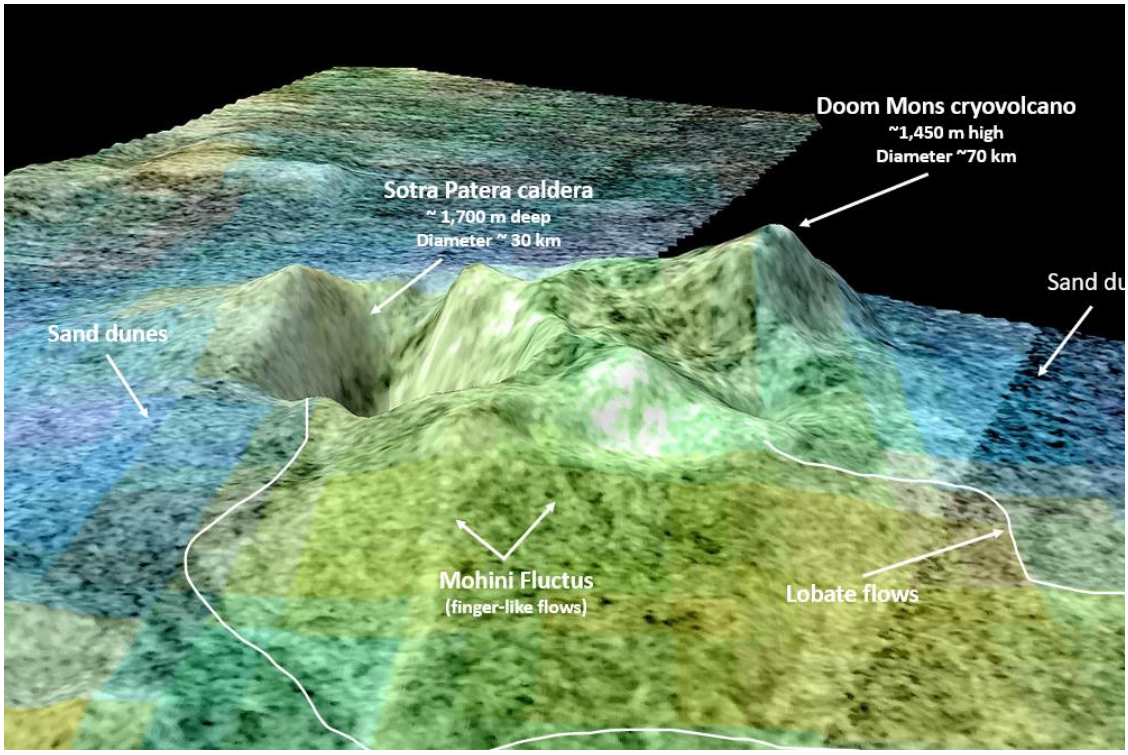

Figure 6.2. Composite image of Titan's Sotra Patera region (known as Sotra Facula before December 2012), combining a digital topographic model (DTM) with a vertical exaggeration of 10:1, from Cassini's SARS instrument, and VIMS data showing compositional differences in false colour which show dune fields in blue, which are of a different composition from the candidate cryovolcanic materials in green and yellow. Doom Mons, the highest peak in the image, is estimated to stand about 1,450 metres high, with a diameter of about 70 km. Multiple craters can also be seen, including Sotra Patera, which is about 1,700 metres deep and 30 km wide. The region also features finger-like flows, named Mohini Fluctus and lobate flow-like features. *Image credit: NASA/JPL-Caltech/USGS/University of Arizona*

Table 6.1. Summary of conduit diameters used in Xenolith II.

Estimated conduit diameters			
Conduit	**Diameter (m)**	**Radius (m)**	**Area (m^2)**
C1	5	2.5	19.63
C2	7	3.5	38.48
C3	10	5	78.54
C4	12	6	113.10
C5	15	7.5	176.71
C6	20	10	314.16
C7	25	12.5	490.87
C8	30	15	706.86

6.1.5 Heat sources for cryovolcanic activity

On Titan, the primary heat source supplying thermal energy for cryovolcanic activity is radiogenic decay in the core (Grasset et al., 2000), with further heat generated from tidal heating and dissipation, cooling of the different shells, and possible freezing of the liquid layer.

Radiogenic heat from long lived radioisotopes (^{40}K, ^{235}U, ^{238}U, and ^{232}Th) has been produced during the entire history of the solar system, and would likely have been present in the core of Titan as it was accreted. The heat generated by the decay of these isotopes would have increased the interior temperature of Titan by several hundreds of Kelvins or more, and supported the differentiation of the moon into a silicate core and aqueous ammonia mantle during the early part of its evolution (Dorofeeva et al., 2010). The heat released by radioactive decay in the core continues today (Grasset et al., 2000).

Another source of energy is tidal heating (the repeated deformation of Titan due to tides raised by Saturn), although the heat that this produces is at least ten times lower than that of radiogenic heating (Sohl et al., 1995). Titan orbits Saturn at a mean distance of 1.22 million km, with an orbital period of 15 days and 22 hours and is locked in synchronous rotation with its planet, permanently showing one face to Saturn. Its orbital eccentricity is 0.0288 and the orbital plane is inclined at 0.348 degrees relative to Saturn's equator (Sohl et al., 1995, Hörst, 2017). This results in a changing gravitational potential, triggering mechanical work on the moon, a portion of which is converted to thermal energy. This tidal dissipation affects both solid and fluid regions of the moon (Hay & Matsuyama., 2017).

In a model of convective heat transfer in Titan's subsurface ocean, Kvorka and Čadek (2022) argue that the evolution of Titan's ice shell is primarily controlled by the heat transferred from the core to the surface and that the heat produced in the deep interior is redistributed by ocean circulation.

Other sources of heat could be generated from the cooling of the mantle from ~300 K to 100 K (approximately a tenth of the present power produced by the core), and the crystallization of ice I at the top of the crust, increasing the internal heating by less than 3% (Grasset et al., 2000).

Titan is ~ 9.5 AU from the Sun, and receives approximately 1% of the sunlight received on Earth. Tomasko et al. (2008) evaluated the solar heating rate with altitude in Titan's atmosphere using measurements from the thermal emission spectrum of the Cassini Composite Infrared Spectrometer (CIRS) around the latitude of the Huygens site. Their findings showed ~90% of the sunlight was absorbed by Titan's thick atmosphere and that only ~10% reached the surface. However, haze in Titan's atmosphere reflects sunlight back into space, making the surface much colder than its upper atmosphere,

reducing the surface temperature by 9 K (anti-greenhouse effect). Balancing this is greenhouse warming, which increases the surface temperature by 21 K: the net effect of which is to increase the effective temperature from 82 K (the temperature of the moon's surface in the absence of an atmosphere) to the 94 K measured on the surface by the Huygens lander (McKay et al., 1991).

6.1.6 Input parameters

Table 6.2. Xenolith II input parameters for Titan

System parameters	**Values**	**Reference**
Ice shell density (ρ_{mantle})	1065 kg m^{-3}	*Fortes et al., 2007*
Aqueous cryomagma density	1065/1235 kg m^{-3}	*Xenolith II Scenario I/II*
CH_4 molecular mass	0.016 kg mol^{-1}	*Xenolith II input*
N_2 molecular mass	0.028 kg mol^{-1}	*Xenolith II input*
Gas constant	8.314 kg mol^{-1}	*Xenolith II input*
Cryomagma temperature	270.7/253.8 K	*Xenolith II Scenario I/II*
Titan mass	1.346 X 10^{23} kg	*Coustenis & Taylor, 2008.*
Titan surface gravity	1.354 m s^{-2}	*Fulchignoni et al., 2006*
Xenolith mass fraction	10.00 wt%	*F*ortes et al., *2007*
Titan surface pressure	~1.5 bar	*Fulchignoni et al., 2006*
Titan surface temperature	~94 K	*Coustenis & Taylor, 2008*
CH_4 plume abundance	5.65%	*Section 6*.1.3
N_2 plume abundance	94.2%	*Section 6*.1.3

6.2 Model results

The dissociation curve of mixed clathrates has been calculated for each modelled cryomagma composition (10.6 wt% $(NH_4)_2SO_4$-H_2O cryomagma with CH_4 = 5.65%, N_2 = 94.2% (Scenario I) and 40.0 wt% $(NH_4)_2SO_4$-H_2O cryomagma with CH_4 = 5.65%, N_2 = 94.2% (Scenario II).

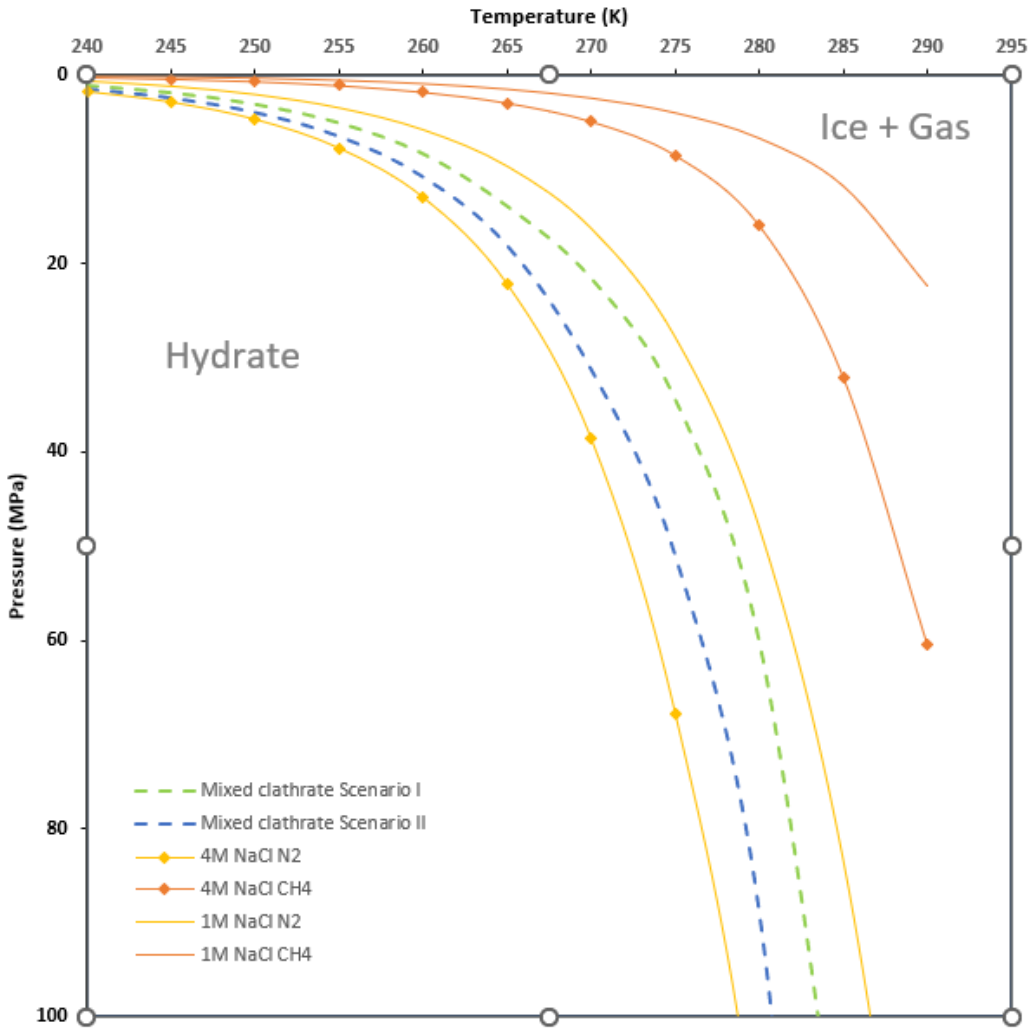

Figure 6.3. Calculated dissociation curves of mixed clathrate hydrate in 10.6 wt% $(NH_4)_2SO_4$-H_2O cryomagma with CH_4 = 6%, N_2 = 94% (Scenario I), and in 40.0 wt% $(NH_4)_2SO_4$-H_2O cryomagma with CH_4 = 6%, N_2 = 94% (Scenario II): dissociation has been calculated at 1M and 4M NaCl molarities respectively. The CURVES component of the CLATHRATES computer package (Bakker, 1997) with the phase equilibria data of Duan et al. (1996) were used to generate the mixed clathrate curves and curves for N_2, and CH_4 for both scenarios.

The equilibrium curves of individual gas clathrates (N_2 and CH_4) were calculated using the CURVES and CLATHRATES programs of Bakker (1996, 1997 and 1998). Figure 6.3 shows the pressure-temperature phase diagram for clathrate stability and decomposition. The phases involved are hydrate (H), ice (I) and gas (G) where H = G + I (after Lu & Keiffer, 2009). The phase equilibria for N_2, CH_4, and mixed gas clathrates are shown at temperatures between 240 K and 295 K.

6.2.1 Fragmentation pressure and depth

The solubilities of CH_4 and N_2 in two cryomagma compositions as a function of pressure were determined using the CH_4 and N_2 components of the CLATHRATES suite of programs (Baker, 1997): 10.6 wt% $(NH_4)_2SO_4$-H_2O at 270.7 K (Scenario I) and 10.6 wt% $(NH_4)_2SO_4$-H_2O (Scenario II) at 253 K (Appendix I). These solubilities were used to model bubble growth and the exsolved fraction as the volatiles entrained in clathrates dissociated in the rising cryomagma.

The extremely low solubility of N_2 in an aqueous cryomagma ensures that the melt becomes supersaturated in N_2 even when dissociation takes place at depth, and N_2 bubbles begin to form (Fortes, 2007). CH_4, which has a much higher solubility, does not contribute to the exsolved gas fraction until the magma is within a few metres of the surface. Fragmentation of the mixed clathrate in the cryomagma occurs at an approximate pressure and depth of 0.21 km and 0.30 MPa for cryomagma composition scenario I (10.6 wt% $(NH_4)_2SO_4$-H_2O) and at a pressure and depth of 0.28 km and 0.40 MPa for cryomagma composition scenario II (40.0 wt% $(NH_4)_2SO_4$-H_2O).

The point at which exsolution starts for each of the clathrate species is shown in table 6.3, showing the calculated depth, pressure, exsolved gas fraction and bulk density of the whole cryomagma plume at that point. Both cryomagma composition scenarios and volatile components modelled, indicate that the most evident difference is in the pressure at which N_2 begins to dissociate: 1.60 MPa in cryomagma composition scenario I (10.6 wt% $(NH_4)_2SO_4$-H_2O) compared to 200 MPa in cryomagma composition scenario II (40 wt% $(NH_4)_2SO_4$-H_2O). The pressures at which CH_4 begin to dissociate are 0.04 MPa and 0.48 MPa for cryomagma compositions scenarios I and II respectively.

The calculated exsolved gas fraction of the cryomagmas as a function of pressure and depth are plotted in figure 6.4, showing the modelled depth and pressure at which exsolution begins for CH_4 clathrate (Scenarios I and II) and N_2 clathrate (Scenario I).

Table 6.3. Modelled depth, pressure, percentage exsolved gas fraction and bulk density at which dissociation begins for each clathrate species in the aqueous cryomagma showing two scenarios where cryomagma composition is 10.6 wt% $(NH_4)_2SO_4$-H_2O (Scenario I) and 40 wt% $(NH_4)_2SO_4$-H_2O (Scenario II). Volatile content is modelled CH_4 = 6%, and N_2 = 94%.

	Scenario I: cryomagma compostion 10.6 wt% $(NH_4)_2SO_4$-H_2O				Scenario II: cryomagma composition 40wt% $(NH_4)_2SO_4$-H_2O			
	Depth (km)	Pressure (MPa)	Exsolved Gas Fraction	Bulk Density (kg m^{-3})	Depth (km)	Pressure (MPa)	Exsolved Gas Fraction	Bulk Density (kg m^{-3})
CH_4	0.03	0.04	0.96	38.60	0.33	0.48	0.71	364.78
N_2	1.11	1.60	0.04	1027.31	138.70	200.00	0.44	1866.21

The calculated bulk magma density of the cryomagmas as a function of pressure is plotted in figure 6.5, showing the modelled depth and pressure at which exsolution begins for CH_4 clathrate (Scenarios I and II) and N_2 clathrate (Scenario I).

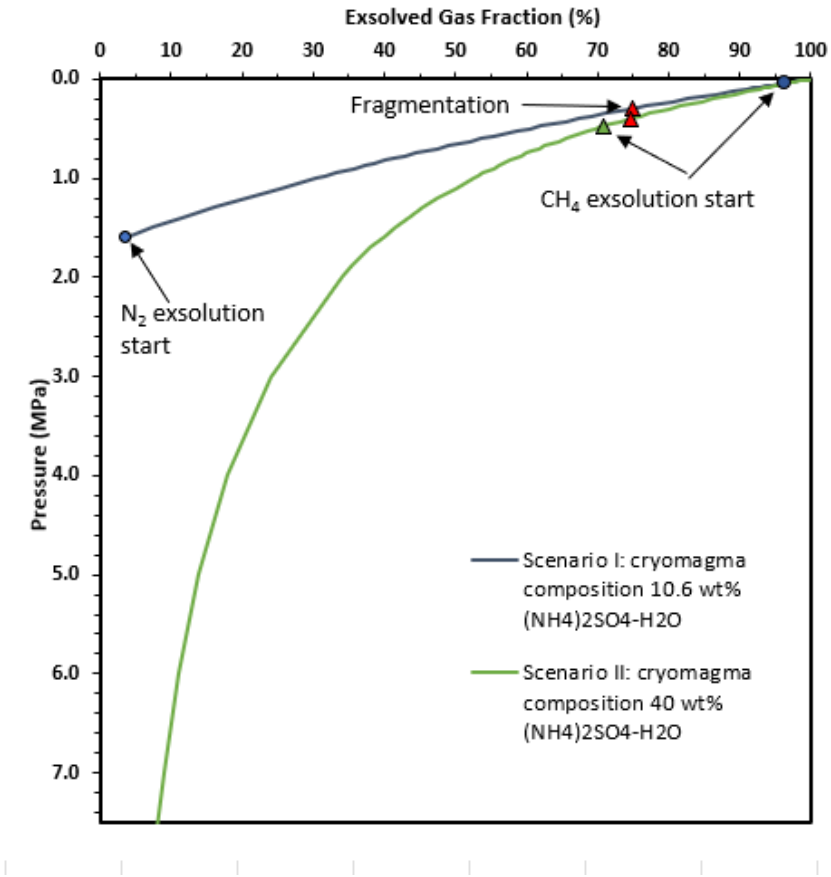

Figure 6.4. The calculated exsolved gas fraction of Titan's cryomagma is plotted as a function of pressure and depth showing cryomagma compositions of 10.6 wt% $(NH_4)_2SO_4$-H_2O (Scenario I) in blue and 40 wt% $(NH_4)_2SO_4$-H_2O (Scenario II) in green. The modelled depth and pressure at which exsolution begins for each clathrate species (N_2, CH_4) is shown as blue dots along the Scenario I curve, and green triangles along the Scenario II cryomagma curve. The approximate point (75% bubble volume fraction) at which fragmentation occurs is shown as red triangle for each curve. The calculated pressure at which N_2 exsolution begins (200 MPa) for scenario II is not shown on the graph.

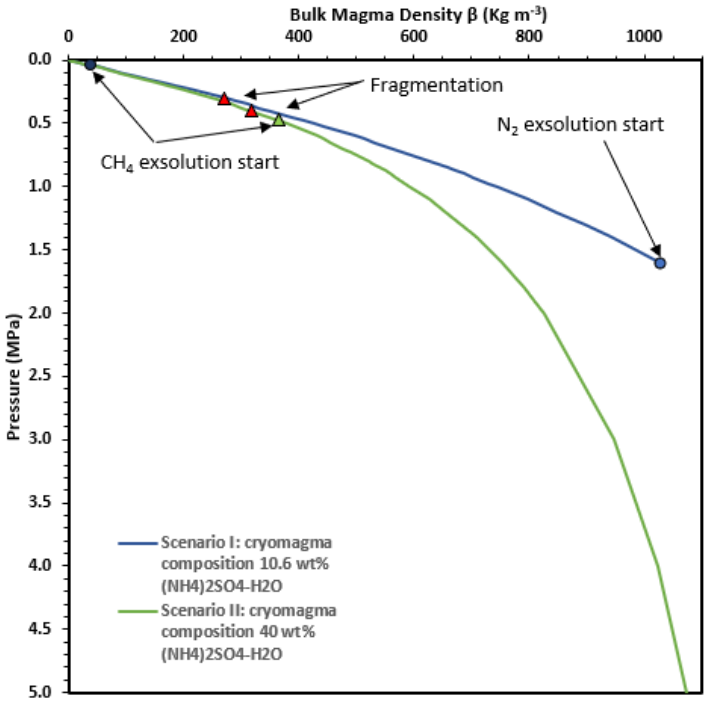

Figure 6.5. The calculated bulk magma density of Titan's cryomagma is plotted as a function of pressure and depth showing cryomagma compositions of 10.6 wt% $(NH_4)_2SO_4$-H_2O (Scenario I) in blue and 40 wt% $(NH_4)_2SO_4$-H_2O (Scenario II) in green. The modelled depth and pressure at which exsolution begins for each clathrate species (N_2, CH_4) is shown as blue dots along the Scenario I curve, and green triangles along the Scenario II cryomagma curve. The approximate point (75% bubble volume fraction) at which fragmentation occurs is shown as red triangle for each curve. The calculated pressure at which N_2 exsolution begins (200 MPa) for scenario II is not shown on the graph.

6.2.2 Cryomagma flow regime

To assess the cryomagma flow regime and plume dynamics, the cryomagma velocity was calculated (equation 3.9), and determined at each point of the pressure and depth set as boundary conditions for the model. Equation 3.11 was used to determine the sound speed, showing the effects of the increase of the gas component in the plume as each of the clathrate species begins, and continues to exsolve. Figure 6.6 shows the calculated sound speed as a function of the exsolved gas fraction, and illustrates that as more gas is exsolved into the plume, the sound speed decreases. This trend is particularly evident in the cryomagma with a composition of 40.0 wt% $(NH_4)_2SO_4$-H_2O at

253.8 K (Scenario II), and less so in the cryomagma with a composition of 10.6 wt% $(NH_4)_2SO_4$-H_2O at 270.7 K (Scenario II). The sound speed in the plume before the entrained clathrate begins to dissociate is unknown for the two cryomagma compositions under investigation. However, using NaCl as an analogue for $(NH_4)_2SO_4$, the sound speed in 1M NaCl (at 270.0 K) and 4M NaCl (at 253.8 K) saline solutions is 1392.91 m s^{-1} and 1286.4 m s^{-1} for cryomagma compositions I and II respectively, before any volatiles have dissociated into the cryomagma. At the point where all the clathrate species have exsolved in Scenario I and II, the calculated sound speeds are 33.3 m s^{-1} and 32.2 m s^{-1} respectively, and have decreased significantly from the gas free cryomagma values mentioned above. As discussed in section 3.3.2, equation 3.11 breaks down if the gas fraction of the exsolving gas is very low. This occurs for the first few data points as N_2 starts to exsolve in scenario II and the sound speed is capped to the gas free sound speed (1286.4 m s^{-1}).

Local cryomagma flow velocities (for cryomagma compositions I and II) were calculated (equation 3.9) at each point of the modelled pressure and depth for the eight estimated conduit geometries (table 6.1). Equation 3.9 incorporates the calculated bulk densities at each pressure point. The results of the calculations to establish local flow velocities at the surface are presented in table 6.4, showing that there is no significant difference between the velocities of each conduit at the surface for each of the two cryomagma compositions, scenarios I and II. The flow velocities of the eight conduit sizes show increasing velocity with decreasing size (figure 6.7). Additionally, the flow velocities of three conduit geometries (C1 = 5 m diameter, C3 = 10 m diameter and C8 = 30 m diameter) were plotted as a function of depth for scenario I (cryomagma composition: 10.6 wt% $(NH_4)_2SO_4$-H_2O) and show the increasing velocity with decreasing size (figure

6.8). Also evident is the increase in velocity with vapour mass flow, for each individual conduit plotted.

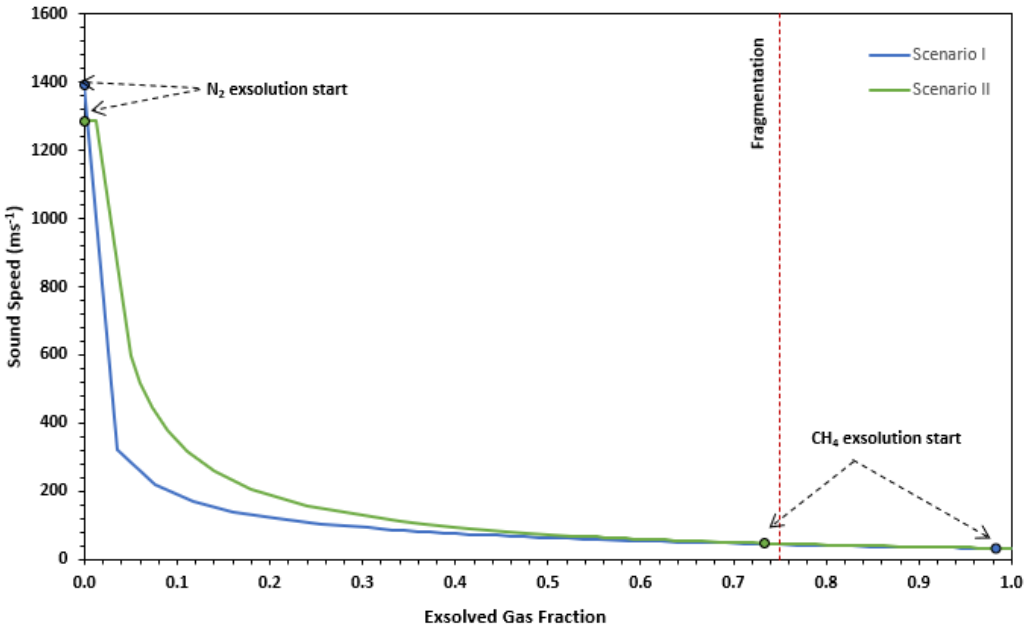

Figure 6.6. Calculated sound speed as a function of the exsolved gas fraction showing cryomagma compositions of 10.6 wt% $(NH_4)_2SO_4$-H_2O at 270.7 K (Scenario I) in blue and 40.0 wt% $(NH_4)_2SO_4$-H_2O at 253.8 K (Scenario II) in green. The volatile components for both scenarios are CH_4 = 5.65% and N_2 = 94.2%. The modelled depth and pressure at which exsolution of CH_4 begins is shown as a blue dot along the Scenario I curve, and a green dot along the Scenario II cryomagma curve. The point at which fragmentation (~75% bubble volume fraction) occurs is shown as a red dotted line although Fortes et al. predict that the total gas bubble volume could be between ~60-85%.

Velocity (m s^{-1}) at surface for mass flow rate of 300 kg s^{-1}		
Conduit	**Cryolava compositon 10.6 wt% $(NH_4)_2SO_4$-H_2O**	**Cryolava compositon 40.0 wt% $(NH_4)_2SO_4$-H_2O**
C1	1917	1786
C2	978	911
C3	479	447
C4	333	310
C5	213	198
C6	120	112
C7	77	71
C8	53	50

Table 6.4. Velocity (m s^{-1}) at the surface for each conduit being investigated, where the cryomagma composition is first modelled as 10.6 wt% $(NH_4)_2SO_4$-H_2O, and secondly, as 40.0 wt% $(NH_4)_2SO_4$-H_2O, at a flow rate of 300 kg s^{-1}.

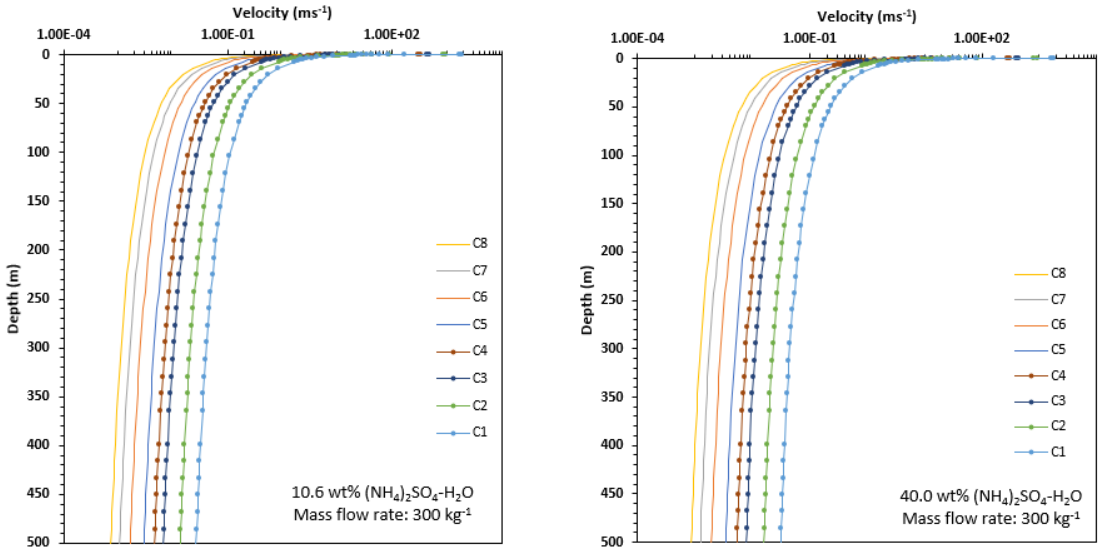

Figure 6.7. Calculated local flow velocities as a function of depth for cryomagma composition: 10.6 wt% $(NH_4)_2SO_4$-H_2O (left) and cryomagma composition: 40.0 wt% $(NH_4)_2SO_4$-H_2O, (right), each with a volatile content of CH_4 = 5.65%, N_2 = 94.2% up to a depth of 500 m for each of the estimated vent diameters where C1 = 5 m, C2 = 7 m, C3 = 10 m, C4 = 12 m, C5 = 15 m diameter, C6 = 25 m diameter, C7 = 30 m diameter and C8 = 30 m diameter.

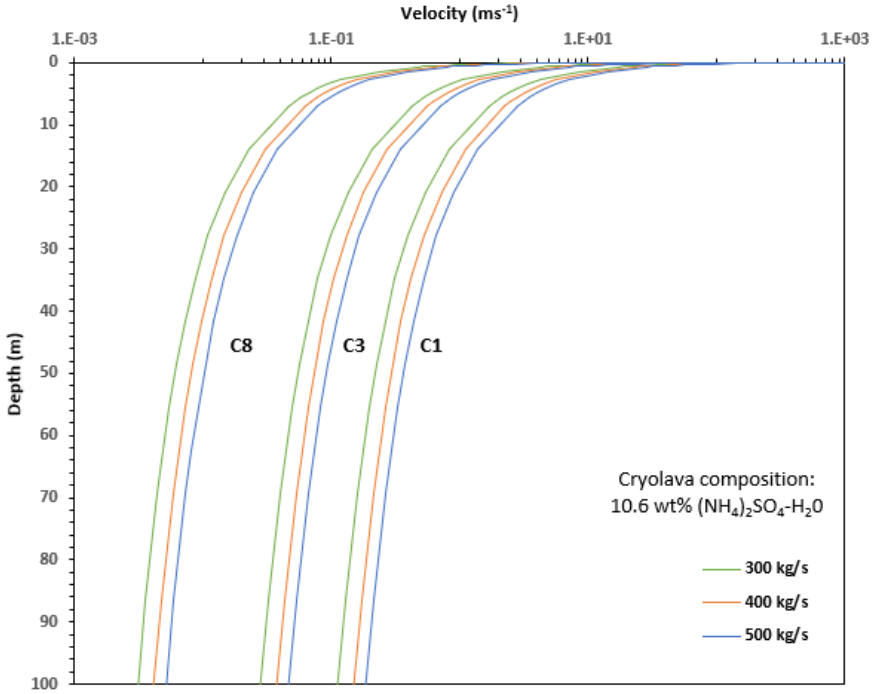

Figure 6.8. Calculated local flow velocities as a function of depth for scenario I (cryomagma composition: 10.6 wt% $(NH_4)_2SO_4$-H_2O) up to a depth of 100 m for each of three of the extrapolated vent geometries where C1 = 5m diameter, C3 = 50m diameter, C6 = 10m diameter and C8 = 30m. Different mass flow rates are shown for each of these vent diameters.

The transition from subsonic to supersonic velocities was determined by calculating the ratio of the local flow velocity to the local sound speed. At the point where the flow velocity is equal to the sound speed, a Mach 1 condition is reached, and subsequent flow is said to be supersonic. The model results show that supersonic flow occurs in all the modelled conduits as seen in figure 6.9, which illustrates the calculated flow velocities and Mach conditions up to a depth of 0.7 m for six of the conduits (C1 to C6)) for a cryolava composition of 10.6 wt% $(NH_4)_2SO_4$-H_2O and mass flow rate of 500 kg s^{-1}.

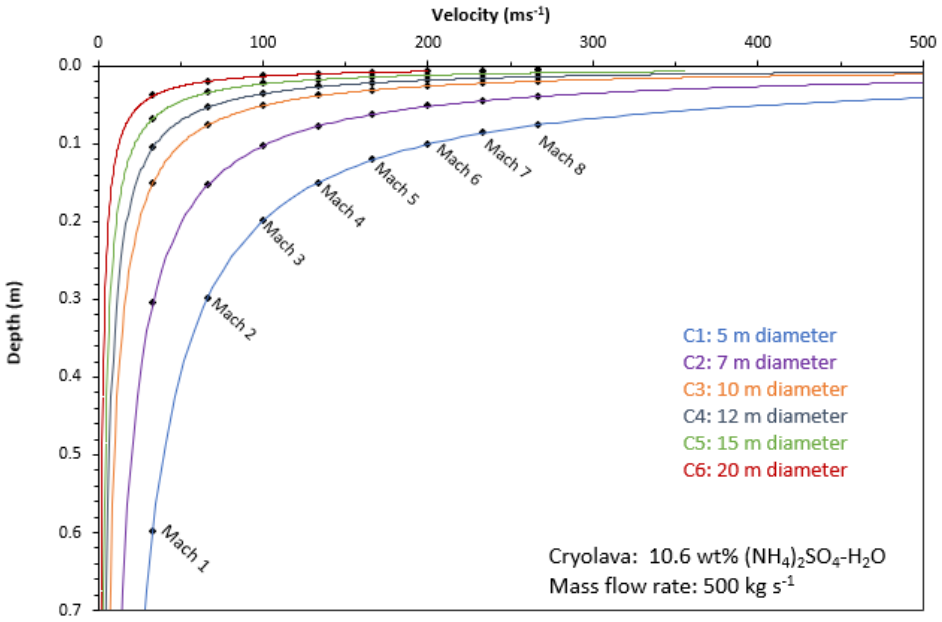

Figure 6.9. Calculated local flow velocities as a function of depth for cryolava composition 10.6 wt% $(NH_4)_2SO_4$-H_2O, mass flow rate 500 kg s^{-1} and volatile content CH_4 = 5.65%, N_2 = 94.2%. Shown are six conduits. Choking conditions (Mach 1) are illustrated for each conduit and well as supersonic flow conditions (up to Mach 8) which occur just before the surface. Each Mach condition is annotated on the graph as a black diamond (method in Appendix II).

The heights of plumes in each of the selected conduits was determined using equation 3.10, which relates the calculated velocity to the surface gravitational acceleration on Titan (1.354 m s^{-2}). The calculated velocities for each conduit (table 6.4) were selected at the surface where the pressure is assumed to be 9.0 Pa. Figure 6.10 shows predicted

plume heights from the candidate conduits at a mass flow rate of 300 kg s^{-1}, for both cryomagma compositions of 10.6 wt% $(NH_4)_2SO_4$-H_2O at 270.7 K (Scenario I) and 40.0 wt% $(NH_4)_2SO_4$-H_2O at 253,8 K (Scenario II). The volatile components for both scenarios are CH_4 = 5365% and N_2 = 94.2%. Figure 6.11 shows the modelled plume heights for a cryomagma composition of 10.6 wt% $(NH_4)_2SO_4$-H_2O, for each conduit at three different mass flow rates.

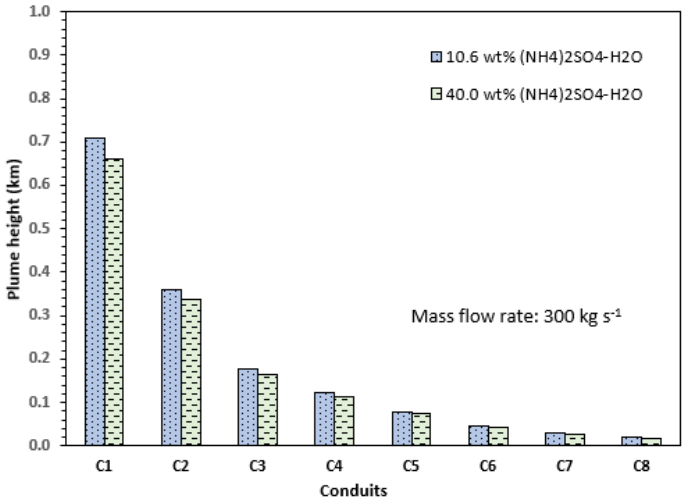

Figure 6.10. Calculated plume heights for the conduits, for cryomagma compositions of 10.6 wt% $(NH_4)_2SO_4$-H_2O at 270.7 K (Scenario I) in blue and 40.0 wt% $(NH_4)_2SO_4$-H_2O at 253,8 K (Scenario II) in green. The volatile components for both scenarios are CH_4 = 5.65% and N_2 = 94.2% and the mass flow rate of 300 kg^{-1}.

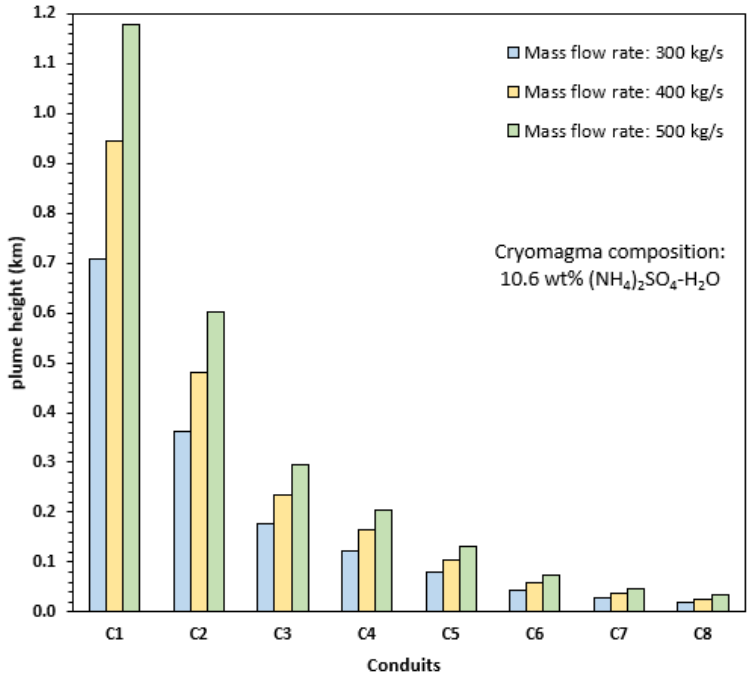

Figure 6.11. Calculated plume heights for the eight conduits, for a cryomagma composition of 10.6 wt% $(NH_4)_2SO_4$-H_2O at 270.7 K at mass flow rates of 300 kg s^{-1} (blue), 400 kg s^{-1} (yellow) and 500 kg s^{-1} (green). The volatile component is CH_4 = 5.65% and N_2 = 94.2%. The estimated diameters of the candidate cryovolcanoes are as follows: C1 = 5 m, C2 = 7 m, C3 = 10 m, C4 = 12 m, C5 = 15 m, C6 = 25, C7 = 30 m and C8 = 30 m.

6.2.3 Viscosity

The viscosities of mixed plumes, for both cryomagma compositions (10.6 wt% $(NH_4)_2SO_4$-H_2O at 270.7 K and 40.0 wt% $(NH_4)_2SO_4$-H_2O at 253.8 K) were calculated where the crystal free cryomagma viscosities, before volatile dissociation begins, were 2160 µPa·s and 6120 µPa·s respectively (after Fortes et al., 2007).

As pressure decreases, clathrates entrained in the plume respond to pressure changes, and exsolve, releasing gas into the plume, impacting the bulk viscosity of the plume. Viscosity is temperature dependent, but since Xenolith II constrains the temperature of the plume to a constant 270.7 K (Scenario I) and 253.8 K (Scenario II), the main impact on the bulk viscosity is the addition of the exsolved gases. The ice and xenolith phases

of the plume are not taken into consideration when determining the viscosity of the mixed component plume. To further constrain the model and estimate the viscosity of the plume, the following assumption has been made: The gas exsolved from the clathrate dissociation process is added to the cryomagma as it erupts, to the liquid phase of the cryomagma, where at the surface, the cryomagma ends up in a ratio of 91 : 8.478 : 0.51 (10.6 wt% $(NH_4)_2SO_4$-H_2O : N_2 : CH_4) for scenario I and 91 : 8.478 : 0.51 (40.0 wt% $(NH_4)_2SO_4$-H_2O : N_2 : CH_4) for scenario II. Before N_2 begins to exsolve, the Xenolith II model assumes that 100% of the plume is liquid cryomagma, and as the clathrates continue to exsolve as the cryomagma rises to the surface, the ratio of liquid to vapour phases of the cryomagma change. The viscosity at each pressure point for scenario I and II is modelled (equation 3:12) with individual gas viscosities (CH_4, N_2) obtained from Haynes, W.M. (Ed.), 2011 (Appendix III). Table 6.5 tabulates the results for cryomagma compositions (scenario I and II) which shows that the viscosity of the mixed cryomagma decreases from the pressure where N_2 exsolution starts at depth, to the surface, by 40.3% and 57.7% for each cryomagma composition (10.6 wt% $(NH_4)_2SO_4$-H_2O and 40.0 wt% $(NH_4)_2SO_4$-H_2O) respectively.

Table 6.5. Modelled pressures and depths at critical points in plume eruption showing the calculated viscosity for the mixed plumes (cryomagma, CH_4, and N_2). The pressures and depths at the start of the exsolution points of CH_4, and N_2 are shown for each selected cryomagma composition where scenario I is 10.6 wt% $(NH_4)_2SO_4$-H_2O and scenario II is 40.0 wt% $(NH_4)_2SO_4$-H_2O. The volatile component of both scenarios is CH_4 = 5.65% and N_2 = 94.2%.

	Scenario I: Cryomagma compositon 10.6 wt% $(NH_4)_2SO_4$-H_2O			Scenario II: Cryomagma compositon 40.4 wt% $(NH_4)_2SO_4$-H_2O		
	Pressure (MPa)	Depth (m)	Viscosity$_{mix}$ µPa·s	Pressure (MPa)	Depth (m)	Viscosity$_{mix}$ µPa·s
0.01 m below surface	0.000009	0.01	1265.67	0.000009	0.01	2576.11
CH_4 exsolution start	0.04	27.74	1608.35	0.475	329.40	2896.81
N_2 exsolution start	1.60	1109.56	2160.00	200.000	138695.29	6120.00

The modelled viscosity of the cryomagma is used to determine the Reynolds number (equation 3.13) for each individual conduit, where viscosity is inversely proportional to the product of the area, density and a factor of 2 (for circular conduits). Table 6.6 shows that as the conduit diameter increases, the Reynolds number decreases, and flow is turbulent under all conditions.

Table 6.6. Modelled Reynolds numbers (Re) at critical depths from the start of N_2 exsolution to the surface are shown for a mass flow rate of 300 kg s^{-1}, where the volatile content is CH_4 = 5.65% and N_2 = 94.2% for both cryomagma compositions (10.6 wt% $(NH_4)_2SO_4$-H_2O and 40.0 wt% $(NH_4)_2SO_4$-H_2O). The flow is turbulent (Re > 4000) from the start of N_2 exsolution for all of the conduits.

	Cryomagma: 10.6 wt% $(NH_4)_2SO_4$-H_2O Mass flow rate: 300 kg s^{-1}				Cryomagma: 40.0 wt% $(NH_4)_2SO_4$-H_2O Mass flow rate: 300 kg s^{-1}			
Conduit	Start of N_2 exsolution 1109.56 m	Fragmentation 208.04 m	Start of CH_4 exsolution 27.74 m	Surface	Start of N_2 exsolution 1109.56 m	Fragmentation 277.39 m	Start of CH_4 exsolution 329.40 m	Surface
C1	35368	42255	47499	59256	12483	26503	26372	29490
C2	25263	30182	33928	42326	8916	18930	18837	21064
C3	17684	21127	23749	29628	6241	13251	13186	14745
C4	14737	17606	19791	24690	5201	11043	10988	12287
C5	11789	14085	15833	19752	4161	8834	8791	9830
C6	8842	10564	11875	14814	3121	6626	6593	7372
C7	7074	8451	9500	11851	2497	5301	5274	5898
C8	5895	7042	7916	9876	2080	4417	4395	4915

6.2.4 Kinetic energy

Using the calculated upward velocity of the plume at each pressure point (equation 3.15), the kinetic energy per unit volume of the cryomagma was determined for each of the circular conduits (C1 to C8) whose diameters are defined in table 6.1. Figure 6.12 illustrates that as clathrate dissociation increases the percentage of gas bubbles in the cryomagma, the kinetic energy increases. The diameters of the conduits are also related to the kinetic energy: the smaller the area of the conduit, the higher the kinetic energy (table 6.7).

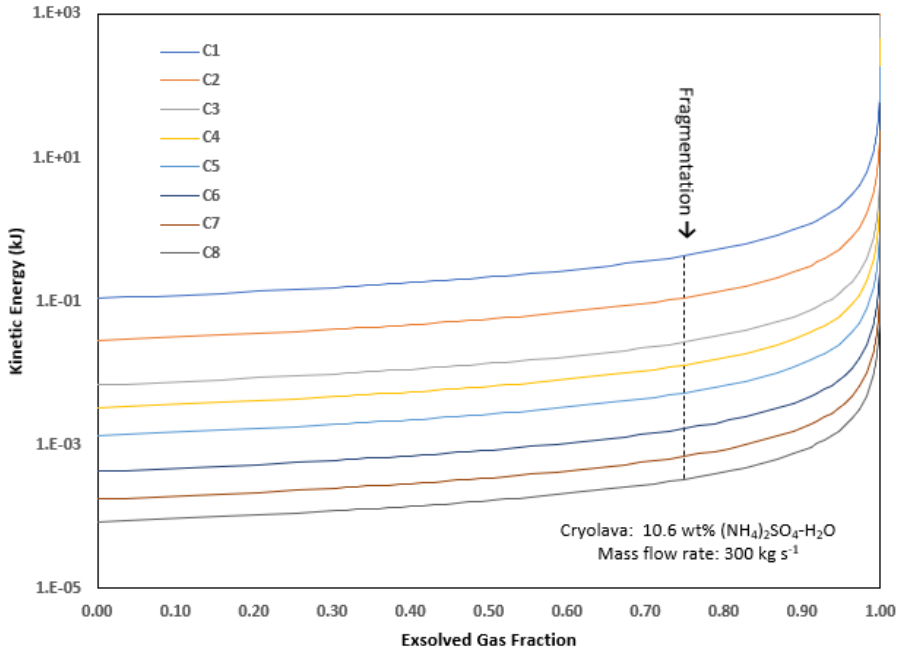

Figure 6.12. Calculated kinetic energy of the cryomagma for each of the estimated conduit diameters (conduits C1 to C8) as a function of bubble volume fraction for a mass flow rate of 300 kg s^{-1}, where the cryomagma composition is 10.6 wt% $(NH_4)_2SO_4$-H_2O. The point at which fragmentation (75% bubble volume fraction) occurs is annotated on the graph.

Table 6.7. Calculated kinetic energy of the cryomagma for each of the estimated conduit diameters (conduits C1 to C8) are shown at the surface for mass flow rates of 300 kg s^{-1}, 400 kg s^{-1} and 500 kg s^{-1} where cryomagma compositions are 10.6 wt% $(NH_4)_2SO_4$-H_2O and 40.0 wt% $(NH_4)_2SO_4$-H_2O.

		Cryolava composition: 10.6 wt% $(NH_4)_2SO_4$-H_2O			Cryolava composition: 40.0 wt% $(NH_4)_2SO_4$-H_2O		
		Mass flow rate (300 kg s^{-1})	Mass flow rate (400 kg s^{-1})	Mass flow rate (500 kg s^{-1})	Mass flow rate (300 kg s^{-1})	Mass flow rate (400 kg s^{-1})	Mass flow rate (500 kg s^{-1})
Conduit	Diameter (m)	Kinetic energy (kJ)	Kinetic energy (kJ)	Kinetic energy (kJ)	Kinetic energy (kJ)	Kinetic energy (kJ)	Kinetic energy (kJ)
C1	5	1.46E+04	2.60E+04	4.07E+04	1.27E+04	2.26E+04	3.53E+04
C2	7	3.81E+03	6.78E+03	1.06E+04	3.31E+03	5.88E+03	9.19E+03
C3	10	9.15E+02	1.41E+03	2.54E+03	7.95E+02	1.41E+03	2.21E+03
C4	12	4.41E+02	7.85E+02	1.23E+03	3.83E+02	6.81E+02	1.06E+03
C5	15	1.81E+02	3.21E+02	5.02E+02	1.57E+02	2.79E+02	4.36E+02
C6	20	5.72E+01	1.02E+02	1.59E+02	4.97E+01	8.83E+01	1.38E+02
C7	25	2.34E+01	4.17E+01	6.51E+01	2.03E+01	3.62E+01	5.65E+01
C8	30	1.13E+01	2.01E+01	3.14E+01	4.97E+01	1.74E+01	2.73E+01

6.2.5 Thermodynamic energy balance

Fortes et al., (2007), calculated that the bulk global heat production on Titan from radiogenic heating of the rock volume of their model of the internal structure to be 240-360 GW (Q_{out} in equation 3.16). In this study, the estimated mass flow rates of a hypothetical plume (m_{out}) are 300 kg s^{-1}, 400 kg s^{-1} and 500 kg s^{-1}: the mass flow rate includes the mass vapour flux and mass particles flux. Without any observational evidence of any current cryovolcanic activity and observed associated mass flow rates, it is assumed that the vapour mass flow rate is 90% of these figures where the modelled xenolith phase is treated as the mass particle flux (10 wt% of the mass flow rate).

Despite the speculatory nature of these assumptions, an attempt has been made to estimate values for the heat required to dissociate clathrates entrained in the plumes, and the sublimation and crystallisation of ice.

Since the molar ratio of the gas mixture (CH_4 and N_2) to the aqueous cryomagma is ~1:10 (Xenolith II model), the mass ratio for the given molar fractions is 1:7 and the vapour flow rate of the gas mixture from clathrate dissociation ($m_{out,g}$) is ~33.8 kg s^{-1} for a mass flow rate of 300 kg s^{-1}, ~45.0 kg s^{-1} for a mass flow rate of 400 kg s^{-1} and ~56.3 kg s^{-1} for a mass flow rate of 500 kg s^{-1}.

The latent heat of dissociation of clathrates is (L_{dis}) is estimated at ≈465 kJ kg^{-1} (kang and Lee, 2001). The mass rate of the sublimated H_2O vapour, $m_{out,v}$, is 350 kg s^{-1}, the latent heat for the sublimation of ice is (L_{sub}) is 2800 kJ kg^{-1} (Lu and Keiffer, 2009) and the latent heat of crystallisation (L_{cry}) is 334 kJ kg^{-1} (Giauque and Stout, 1936) as dissociation will result in a percentage of the liquid cryomagma crystallising (Fortes, 2007). The mass flow rate of the liquid water phase is unknown, and an approximation is made where the mass flow rate is 40% of the total flow rate, 80 kg s^{-1}, since the water vapour to ice

ratio predicted by the Fortes (2007) is ≈60:40. The value for the cryovolcanic conduit pressure (P_r) is taken as the pressure at the surface of Titan (1.5 bars) and the density (ρ_r) is 1065kg m^{-3} (Fortes et al., 2007). Table 6.8 shows the results of the calculated values of the terms in the right hand side of the equation 3.16 where the estimated total heat required to dissociate the mixed clathrate and the sublimation and crystallisation of ice is estimated for the mass flow rates of are 300 kg s^{-1}, 400 kg s^{-1} and 500 kg s^{-1}.

Table 6.8. Estimated values for the heat required to dissociate clathrate, sublimation of ice and crystallisation of ice at different mass flow rates.

Mass flow rate kg s^{-1}	$m_{out,g}H_{dis}$ (GW)	$m_{out,v}L_{sub}$ (GW)	$m_{out}L_{cry}$ (GW)	$m_{out}(P_r/p_r)$ (GW)	Total (GW)
300	5.2	0.098	4.51E-03	5.77E-12	5.30
400	52.3	0.098	6.01E-03	5.77E-12	52.40
500	523.1	0.098	7.52E-03	5.77E-12	523.21

6.3 Evaluation and discussion

There is evidence for past and recent cryovolcanic activity on Titan which has been documented in this chapter's introduction and section 2.3.1, and this has warranted examining the role that clathrate hydrate dissociation may have in explosive cryovolcanism on this moon.

The results of this application of the Xenolith II model to Titan show that the velocity of the cryomagma varies with the size of the conduit, the mass flow rate, the exsolved volatile content (CH_4 and N_2) and cryomagma composition. Once the cryomagma has reached the surface, the dynamics of the plume are related to its upward velocity and

density, relative to the prevailing atmospheric conditions (pressure, density and temperature).

The fragmentation pressure and depth were calculated for the two cryomagma compositions (10.6 wt% $(NH_4)_2SO4$-H_2O and 40.0 wt% $(NH_4)_2SO4$-H_2O), keeping the volatile component (CH_4 = 5.65%, N_2 = 94.2%) and xenolith mass fraction (10 wt%) constant. Comparing these two scenarios in the model resulted in a considerable difference in the start of N_2 exsolution depth and pressure (table 6.3), and less difference for the start of CH_4 exsolution. The four-fold increase in the ammonium sulfate salt component of the cryomagma in the 40.0 wt% $(NH_4)_2SO_4$-H_2O cryomagma composition would be responsible for shifting the dissociation to higher pressures and this is exhibited in these results. Additionally, solubility calculations for CH_4 and N_2 in 1M and 4M NaCl (used as an analogue for $(NH_4)_2SO_4$), show that N_2 has a lower solubility than CH_4 in both 1M and 4M NaCl solutions. The solubility of N_2 in a 4m NaCl solution is ~40% lower than in a 1M NaCl solution.

The conduit sizes selected for investigation were intended to cover a wide range of diameters, from 5 m to 30 m. Results show that the conduit diameter has a major impact on the eruption velocity, for the same cryomagma composition, volatile content and mass flow rate where the smaller caldera diameters have the larger the exit velocities at the surface. From the calculation of Mach numbers (and the transition from subsonic to supersonic speeds) for the flow dynamics of the cryomagma, all the flows in the conduits modelled reached supersonic eruption velocities, near the surface.

The calculated viscosity of the cryomagma is shown to be impacted by the different compositions (10.6 wt% $(NH_4)_2SO_4$-H_2O and 40.0 wt% $(NH_4)_2SO_4$-H_2O) at the same mass flow rate and same gas volatile content (CH_4, N_2), but is independent of vent size, where

the viscosity of the 40.0 wt% $(NH_4)_2SO_4$-H_2O cryomagma was approximately twice that of the 10.6 wt% $(NH_4)_2SO_4$-H_2O cryomagma (table 6.5). The viscosity was also shown to decrease from the pressure and depth at which N_2 exsolution starts.

Reynolds numbers were calculated to determine the nature of the flow (laminar, transitional or turbulent) for each of the candidate cryovolcano conduits and were related to the velocities and viscosities for both cryomagma compositions, at the selected mass flow rates. Results show that all flow from the eight conduits was turbulent from the start of N_2 dissociation.

The eruption column, once it reaches the surface, could exhibit one of several behaviours, depending on its eruption velocity, vent diameter, mass flow rate and mass fraction of volatiles (Wilson et al., 1980, Woods et al., 1995). The mass flow rates are constrained to constant values in the Xenolith II model, as is the mass fraction of volatiles. An erupting column of gas and particles will entrain atmospheric gas, transferring momentum and slowing the plume down. However, the entrained gas could generate buoyancy, forming a convecting plume (Wilson, 2009). The surface pressure on Titan is ~0.15 MPa (approximately 60% greater than that of Earth) and plinian eruption columns should be possible. The modelled results show that it is feasible that the eruptions from the smaller diameter craters erupting at supersonic velocities and relatively low mass flow rates (300 kg s^{-1}) could produce a sufficiently buoyant plume to create a Plinian-like eruption. If the higher mass flow rates selected in this model are insufficient to produce a buoyant column, the upward momentum of the column could be compromised, resulting in collapse and the formation of cryovolcanic flows (Wilson et al., 1980). This is a possible scenario in the north polar region of Titan where some of the relatively small cryovolcanic craters have associated flows (Wood & Radebaugh.,

2020). Based on the results (subject to boundary conditions) of the Xenolith II model, it is shown that clathrate hydrate dissociation in cryovolcanic vents may have a role in explosive cryovolcanism on Titan under certain conditions.

CHAPTER SEVEN

Neutron diffraction experimental study of methane clathrate

7. Neutron diffraction experimental study of methane clathrate

Experiments were carried out at the ISIS facility of the STFC Rutherford Appleton Laboratory near Oxford. ISIS is a pulsed spallation neutron source providing beams of neutrons and muons that allow the investigation of the microscopic structure and dynamics of matter. The neutron diffraction instrument PEARL was selected as it was specifically designed for *in situ* studies of material at high pressures and was used to investigate the behaviour of methane clathrate close to its dissociation point.

The experiments had a number of goals: (1) to provide the first *in-situ* diffraction-based evidence for the phase behaviour of methane clathrate near to its high-pressure dissociation temperature in the 0.6 – 1.6 GPa region; (2) to provide a control measurement at room temperature for comparison with other workers; (3) to obtain Pressure-Volume curves along two isotherms for each of the phases observed (Room Temperature compression).

7.1. Summary of literature on high pressure clathrate hydrate

Much research has been undertaken on hydrates and their equilibrium behaviour in the low-pressure range (~0 - 0.5 GPa) but in recent years the behaviour of hydrates at much higher pressures has been studied and has provided new insights into the structural phase transformations that occur at high pressures. Prior to the late 1990s, researchers had identified that structures sI, sII and sH were the most common clathrate hydrates, forming in a low-pressure range of ~0 – 0.5 GPa. It was also thought that clathrate hydrates decomposed into their component phases at the point where the stability line of the clathrate crossed the ice freezing line, and that methane hydrate sI would dissociate into ice VI plus liquid methane at pressures of >1 GPa and more (Lunine & Stevenson, 1985). Differential thermal analysis (DTA) measurements confirmed the expected behaviour of hydrates at low pressures but found an increasing discrepancy at higher pressures. Results showed a discontinuity in the dissociation curve at 0.62 GPa at ~318 K and there was evidence of a phase boundary in the solid phase. Dyadin et al. (1997) suggested that this indicated a transformation from the low pressure methane hydrate phase I (sI structure), to a higher pressure and a more dense methane hydrate phase. Since 1997, there have been several studies to identify high pressure phases of methane clathrate since Dyadin et al. (1997) first reported the existence of a new methane clathrate high pressure phase at ~500 MPa. Dyadin and co-workers (1997) were able to estimate the density of the expected for sII clathrate, which was not consistent with that expected for cubic sII clathrate, leading them to conclude that a new clathrate structure had formed at the higher pressure. Differential thermal analysis did not reveal the new structure since the investigation did not involve diffraction. The accepted view was that the application of pressure decomposed clathrates into their constituent components; the density of the clathrates became equal to that of the fluid

phase which caused the destabilisation of the hydrate, except for argon hydrate, which was stable up to 3GPa (Dyadin et al., 1997). In addition, before this time, it was considered that a maximum of one guest could occupy a hydrate cage. However, nitrogen was reported to doubly occupy the larger sII hydrate structure (Kuhs et al., 1997). Subsequent studies reported multiple occupancies in sII clathrates for CO_2 (Li et al., 2023; Robustillo et al., 2023), oxygen (Chazallon & Kuhs., 2002), hydrogen (Mao & Duan, 2006), and methane (Hiraga et al., 2020, Robustillo et al., 2023).

Since this period though, and at pressures >1 GPa (at ambient temperature), additional high-pressure clathrate phases have been identified in further studies. Investigations employing neutron, X-ray diffraction, Raman spectroscopy and calorimetric and spectroscopic measurement of a range of clathrate hydrate at pressures approaching 100 GPa have revealed a series of polymorphic phase transitions (Choukroun et al., 2007; Hirai et al., 2000a, 2000b, 2001, 2003, 2004, 2023; Kadobayashi et al., 2018, 2020; Loveday et al., 2001a, 2001b, 2003, 2008; Shimizu et al., 2002; Machida et al., 2006; Noguchi et al., 2021; Ogienko et al., 2006;). Some disagreements remain over the sequence of high pressure phase transitions.

Hirai and co-workers (Hirai et al., 2000a, 2000b) investigated phase changes in a water-methane system using synchrotron X-ray diffraction and diamond-anvil cells in a pressure range from 0.2 to 5.5 GPa at room temperature. They concluded that as pressure was increased gradually from 0.2 GPa the water-methane system containing sI methane clathrate decomposed gradually into ice VII and solid methane at 2.3 GPa.

Using *in-situ* X-ray diffractometry and Raman spectroscopy at room temperature, Hirai et al., (2001) identified three high-pressure phases of methane hydrate; a hexagonal structure (structure A), and two orthorhombic structures (structure B and structure C).

The sI form decomposed into a hexagonal structure (A) and fluid at 0.8 GPa; At 1.6 GPa, this formed an orthorhombic structure (B) and at 2.1 GPa, this changed to structure C (orthorhombic) which survived, maintaining this structure above 7.8 GPa.

The hexagonal and orthorhombic structures, named by the studies of Loveday et al., (2003, 2008) as sII and sIII (methane hydrate structure II and III), were thought to correspond to structure A and structure C respectively, based on the same unit cell parameters, indexing and pressure range of existence. It was concluded that structure B was present as a high pressure structure of methane hydrate (existing in a pressure range from 1.6GPa to 2.1GPa). Subsequent studies by Hirai and co-workers (from 2003) concluded that methane hydrate formed a 'filled ice' structure (sometimes called sIII) which survived up to 42 GPa.

The methane molecule in methane hydrate is close to the cage radius of structure sI, although even small molecules such as N_2 sit in an electrostatic field inside the cages that influence the density of the molecule bond, which in turn subtly shifts the vibrational frequency. Thereby, types of cages and occupancies can be inferred from signatures of trapped molecules using Raman spectroscopy (Sum et al., 1997) as different levels of compression exist between CH_4 molecules in small and large cages. Raman spectra show changes in vibration energy and frequency induced by changes in bond length at equilibrium and in particular, high pressure Raman signatures of methane hydrate is subject to abrupt changes in peak positions when phase transitions occur (Shimizu et al., 2002; Kumazaki et al., 2004; Choukroun et al., 2007).

Choukroun and co-workers (2007) observed and confirmed the formation and structure of methane hydrate sII up to 500 MPa and observed that there are similarities in the peak positions of sI and metastable sII. They suggested that the sII methane hydrate was

formed due to the lower H_2O content and the size of the methane-rich zones in their experiment. It was also observed that on compression, the Raman signature of methane trapped in the sI cages remained the same but increased dramatically in larger cages. The phase transition from sI to sII was observed at ~1GPa (Choukroun et al., 2007) and similar observations were made at similar pressures by other workers (Hirai et al., 2001; Shimizu et al., 2002; Kumazaki et al., 2004).

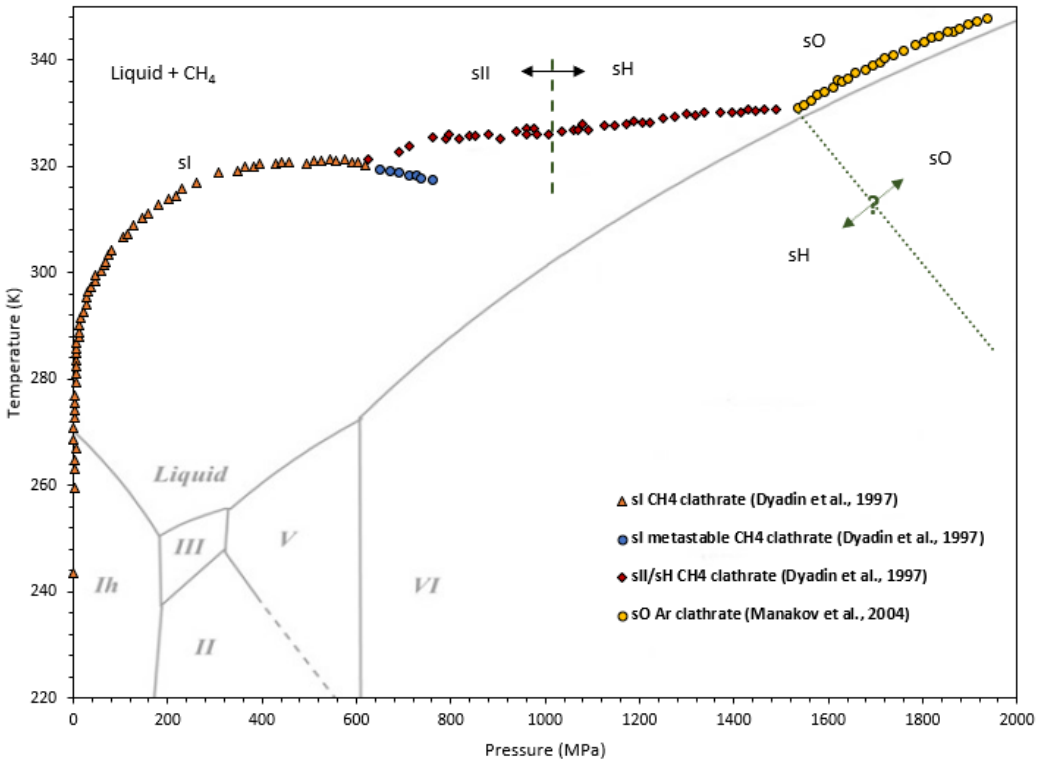

Figure 7.1. The pressure-temperature phase diagram for methane clathrate hydrate, compared with that of H_2O (solid grey lines, from Fortes & Choukroun, 2010 and references therein). The yellow triangles correspond to the dissociation curve of methane clathrate structure sI and the blue dots are a metastable sI phase (Dyadin, et al., 1997). Above 1.5 GPa, the dissociation curve of "filled-ice" sO, is speculative, and based upon that of Ar clathrate hydrate sO polymorph (Manakov et al., 2004). The dashed vertical line indicates the phase transition from sI to sH reported by Loveday et al. (2001a, 2002b), Hirai et al. (2001), Shimizu et al. (2002), Kumazaki et al. (2004), and Choukroun et al. (2007). The dashed green line indicates the suggested transition from methane clathrate sH to sO (Fortes et & Choukroun, 2010).

Thus, the suggested evolution is (shown in Figure 7.1):

$$sI \rightarrow sH$$

Shimizu and workers (2002) observed a second phase transition from sII to sIII at ~1.9GPa. This was confirmed by a later neutron diffraction study (Loveday & Nelmes., 2008) where deuterated methane hydrate transformed on compression first from sI to ice VI and methane hydrate sII, at ~0.9GPa, and then from sII to an sIII structure at ~1.8GPa. The phase transition sequence was:

$$sI \rightarrow sII \rightarrow sIII$$

It was noted by Fortes and Choukroun (2010) that the metastable structure sII detected in the Raman studies observed (Shimizu et al., 2002; Choukroun et al., 2007) was hard to reconcile with the known sII structure, and that a more likely structure would be sH, leading to a favoured transition path of (shown in Figure 7.1):

$$sI \rightarrow sH \rightarrow sO$$

sO is a hydrate compound referred to as 'stuffed' or 'filled' ice where sufficiently small molecules such as H_2, He and Ne can penetrate or dissolve into, the interstices of molecules of ice phase Ih, Ic and II without distorting the structure. The elastic properties of the structures are altered by these occupied cavities, causing them to become stiffer. X-ray and neutron diffraction studies suggest that the following sequence of phase transition may occur for sI clathrates (Fortes & Choukroun, 2010) and this is shown in figure. 7.1:

$$sI \rightarrow sII? \rightarrow sH \rightarrow sO$$

where the '?' indicates uncertainty at the behaviour at relatively high temperatures, nearer dissociation. At ~1.9 GPa and room temperature sI transforms directly to sH

(Loveday et al., 2003). At lower pressures, the following phase transitions have been observed (Dyadin et al., 1997; Loveday et al., 2003; Manakov et al., 2004; Hirai et al., 2004) where sII transforms as follows:

$$sII \rightarrow sH \rightarrow sT \rightarrow sO$$

Structure T (sT) is high pressure structure, a tetragonal single cage type; denoted T', $4^2 5^8 6^4$ (tetrakaidekahedron). Structure T (sT) is shown for illustrative purposes since it is not pertinent to methane hydrate, as only smaller molecules form this type of structure.

7.2. Neutrons and neutron diffraction

Neutrons have no charge, and their electric dipole moment is either zero or too small to be measured by the most sensitive of modern techniques. Neutrons can therefore interact with atoms via nuclear forces which are very short range (a few fermis, where 1 fermi is 10^{-15}m). Because of this, neutrons travel long distances in material without being scattered or absorbed because the sizes of the scattering centres (nuclei) are typically 100,000 smaller than the distances between them. The attenuation, or decrease in intensity of a beam of low-energy neutrons by aluminium for example, is about 1% per millimetre compared with 99% or more for x-rays. On striking a sample, a beam of neutrons can either be absorbed, or emerge in a new direction, with or without a change in energy, and the rest will pass through the sample unaffected. Those that emerge in a new direction are described as 'scattered' neutrons. The effective scattering area of a neutron used for experiments is described in terms of a cross section, σ, barn (1 barn = 10^{-28} m^2), and is the probability of a scattering event when a scattering atom is

exposed to a beam of neutrons. Neutron plane waves[19] have amplitude and phase, and can be scattered, where elastic scattering changes the direction, but not the magnitude of the vector. Inelastic scattering, in which there is an exchange of energy and momentum between the incident neutron and a sample, causes both the direction and the magnitude of the neutron's wave vector to change. The cross section area of a neutron has both coherent and incoherent components. Incoherent scattering changes both the direction and magnitude of the neutron wave vector and involves correlations between the position of an atom at time zero and the same atom at time t. Coherent scattering of an incident neutron wave interacts with all the nuclei in a sample in a coordinated manner whereas in incoherent scattering, an incident neutron wave interacts independently with each nucleus in the sample. Diffraction, or Bragg scattering is the simplest type of coherent neutron scattering. If a beam of neutrons is fired at a lattice (with a fixed position of atoms, as in a crystal), as the incident neutron beam arrives at each atom, the atomic site becomes the centre of a scattered spherical wave. These overlapping waves spread out and overlap with other scattered spherical waves from other atomic sites, causing interference. The waves of scattered neutrons spread out from a regular array of atomic sites and travel in well-defined directions, and these are closely related to the symmetry and spacing (lattice) of the atomic scattering sites. The directions in which incident waves are scattered therefore allows the deductions of both the symmetry of the lattice and the distances between the atoms (diffraction). Bragg's law relates the scattering angle to the interplanar spacing in a crystalline sample.

[19] A plane wave is a constant-frequency wave with infinite parallel planes of constant peak-to-peak amplitude normal to the phase velocity vector as wavefronts.

7.3. Experimental materials and method

Two separate neutron powder diffraction experiments, involving three separate samples, were carried out in 2012 and 2013. Each run involved a loading of the synthesized $CD_4.nD_2O$ specimen into the Paris-Edinburgh (P-E) opposed anvil press and measurements on the PEARL/HiPR beamline. The basic design of the P-E press is shown in figure 7.2. A pair of TiZr gaskets containing the sample in a fine powder form sit between two opposing toroidal tungsten carbide (WC) anvils which are compressed to a high pressure by an integral hydraulic ram. This was used in the first experiment (figure 7.2). Anvils made from zirconia-toughened alumina (ZTA), were used in the second experiment. Different anvils were used in the second experiment since the longer wavelength absorption of WC results in the diffraction data becoming noisy at d-spacings longer than about 3 angstroms. The ZTA anvils are much more transparent in this region, resulting in a lower background, albeit with additional parasitic Bragg peaks from both the zirconia and alumina constituents. The TiZr alloy gaskets are null-scattering, composed of 67.7 mol% titanium and 32.4 mol% zirconium, elements which have negative and positive neutron scattering lengths respectively. In the right proportions, the two scattering lengths cancel to zero such that, even though the material diffracts coherently, the Bragg peaks have zero intensity. The encapsulated shape of the gasket maintains hydrostatic conditions to a much higher pressure than previous designs (Marshall & Francis, 2002). Boron Carbide (B_4C) coatings on the anvils and 5mm boron nitride radial collimators help reduce unwanted scattering from the anvils although small parasitic peaks do appear in sample diffraction patterns. The encapsulated sample is ‘squeezed’ to a high pressure by the 250-ton hydraulic ram

and neutrons entering from the top of the P-E press are scattered from the sample and the anvils. Detectors collect those neutrons emerging at 90° to the incident beam.

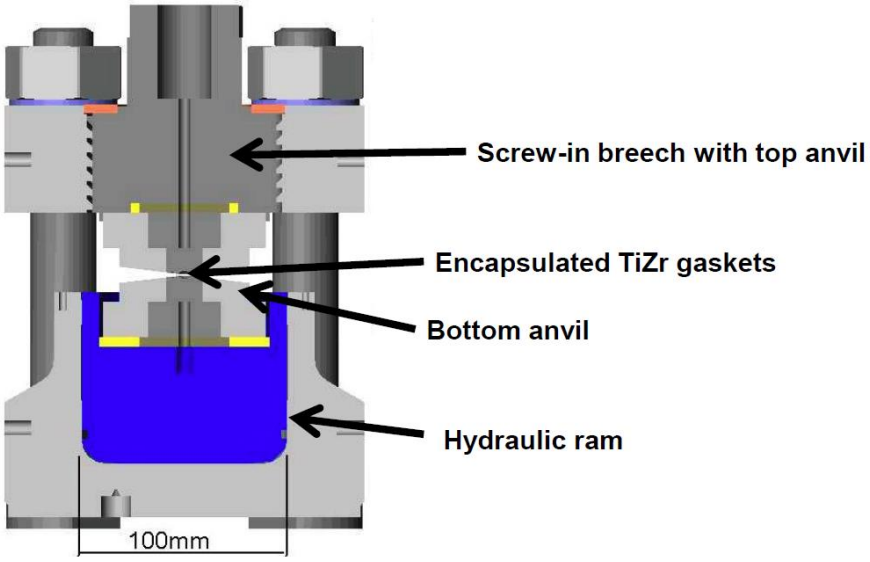

Figure 7.2. Schematic of the Paris-Edinburgh press. TiZr alloy gaskets sit between opposing tungsten carbide anvils which compress the gasket and sample. Neutrons entering the top of the press are scattered from the sample and anvils. (Source: Oxford Summer school of Neutron scattering, September 11th, 2013, Application of neutron diffraction to planetary ices & hydrates)

7.3.1. $CD_4.nH_2O$ synthesis

Deuterated methane clathrate (low-pressure structure sI) was formed in a steel pressure vessel by exposing powdered D_2O ice directly to ~ 123 bar of CD_4 at temperatures of −12°C over a period of five months in the UCL Earth Sciences Cold Rooms (figure 7.3). Deuterium (D or ^2H) is one of two stable isotopes of hydrogen with its nucleus containing one proton and one neutron; unlike the more common hydrogen isotope, protium or ^1H, which has no neutron surrounding the nucleus. Substituting deuterium atoms for hydrogen reduces scattering noise and improves the signal-to-noise ratio in diffraction data sets. The incoherent component of the cross section area of a neutron relates to the background signal and hydrogen (^1H) has a very large component (80.2 x 10^{-24}cm)

compared to that of deuterium (^{2}H), whose small $\sigma_{incoherent}$ of 1.8 x 10^{-24}cm is used in place of hydrogen in creating methane in a laboratory. In neutron scattering experiments, because hydrogen exhibits a large incoherent neutron cross section, a count for shorter times is needed to obtain a given signal to noise ratio for deuterium.

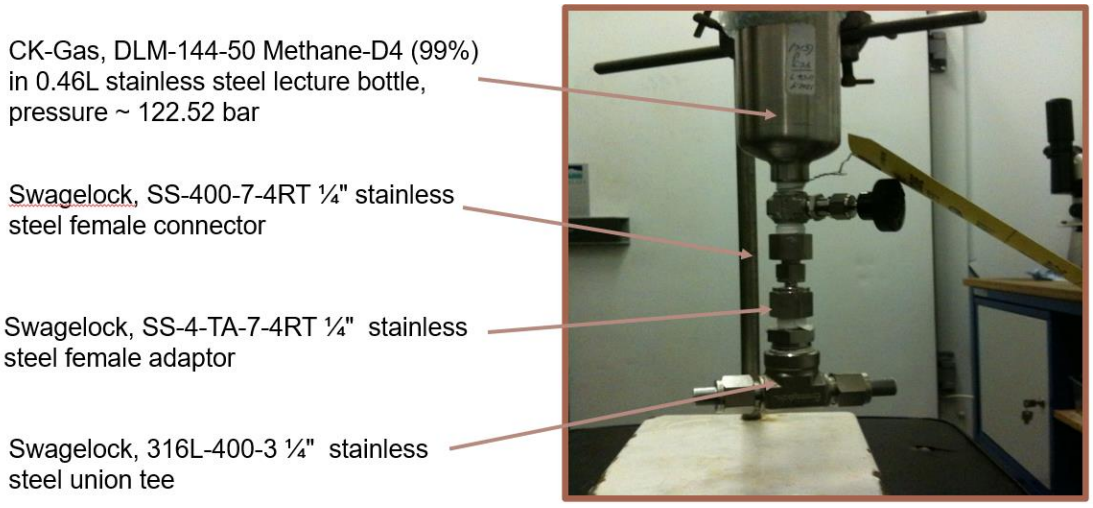

Figure 7.3. Apparatus used to synthesize $CD_4.nD_2O$ by exposing powdered D_2O ice directly to ~ 123 bar of CD4 gas (filled to a custom pressure of 150 bar by CKGas) at a temperature of −12°C over a period of five months in the UCL Earth Sciences Cold Rooms (image courtesy of A.D. Fortes).

On the day prior to each of the experiments, the pressure vessel was isolated from the CD_4 container and immersed in liquid nitrogen. The contents of the pressure vessel, approximately 1 cm^3 of methane clathrate, were then extracted under liquid nitrogen (L-N_2) and ground to a powder for loading into the null-scattering TiZr gaskets of the Paris-Edinburgh (P-E) press (figure 7.4). A portable anvil loading jig was cooled by immersion in liquid nitrogen and used to prepare one satisfactory loading; an attempt to prepare a second loading was not successful. The powdered clathrate was packed, along with approximately 50 mg of lead (Pb) foil to act as a pressure calibrant, into TiZr

encapsulated gaskets and sealed screw-tight between nitrogen-chilled tungsten-carbide anvils. The loading jig was transported in liquid nitrogen to ISIS.

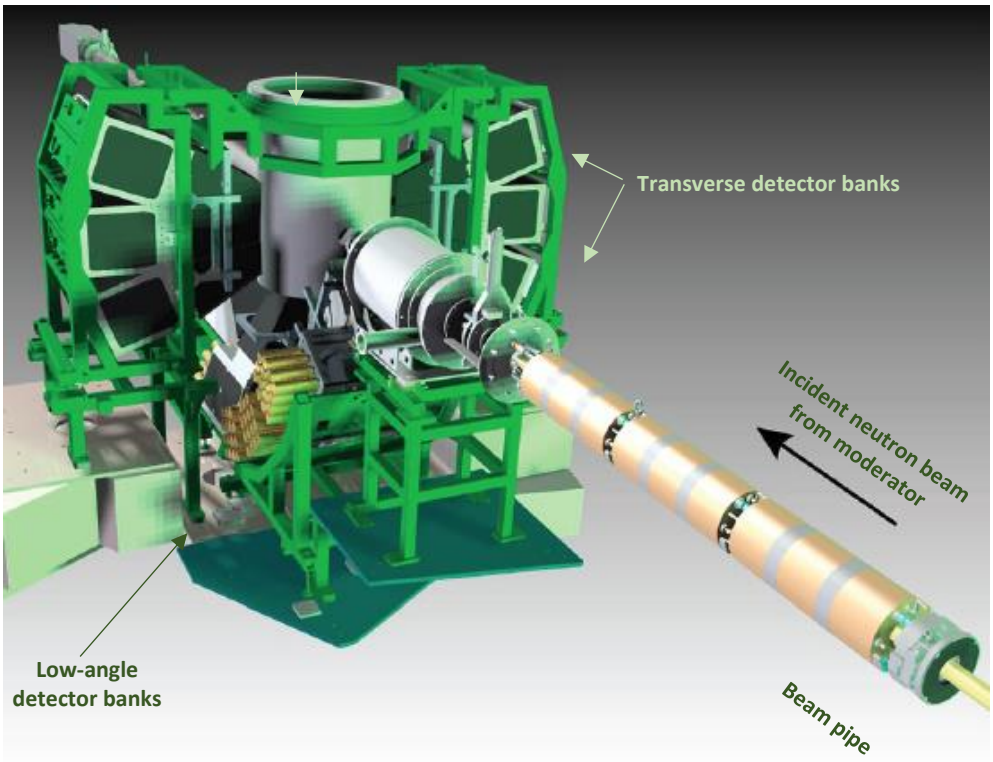

Figure 7.4. Schematic of the geometry of the medium-resolution, high flux PEARL instrument, located on beamline S9 of Target Station 1 at ISIS. The beam pipe, indicated in the schematic, accommodates pairs of movable B_4C jaws which collimate the neutron bean and define the beam size at the sample position. At either side of, and between the sets of jaws are scintillation monitors, composed of alumina-silicate with ^6Li-enriched lithium oxide. A measure of the neutron flux profile as a function of time-of-flight (ToF) is provided by the monitors and provides information used for instrument diagnosis and data reduction normalisation techniques. The ToF path from the moderator to sample is therefore preserved and allows for the correct calibration and comparable d-spacing values throughout an experiment (image used with permission of authors, Bull et al., 2016).

7.3.2. Specimen preparation and loading

The loading jig assembly was mounted into the P-E press at room temperature. The P-E cell was then transferred to its loading cradle and hoisted into position in the PEARL beamline. Images from the experiment show the assembled P-E cell before mounting (figure 7.5) and being lowered into the cradle (figure 7.6).

7.4. Data acquisition and treatment

Calibrated Rh-Fe thermocouples were taped to the anvils with the tips as close as possible to the frames to monitor temperature. Pressure monitoring was achieved by means of using a Pb pressure marker included with the sample. The addition of a pressure calibrant is necessary since the shape of the gasket, the tungsten carbide (WC) anvil geometry of the P-E cell, the porosity of the sample and friction do not allow for the simple calculation of the pressure in the sample space which results from the applied load on the hydraulic ram. Using the cell-parameter of the included Pb pellet, a final accurate value is obtained from a profile refinement; Pb acts as a pressure calibration for the sample.

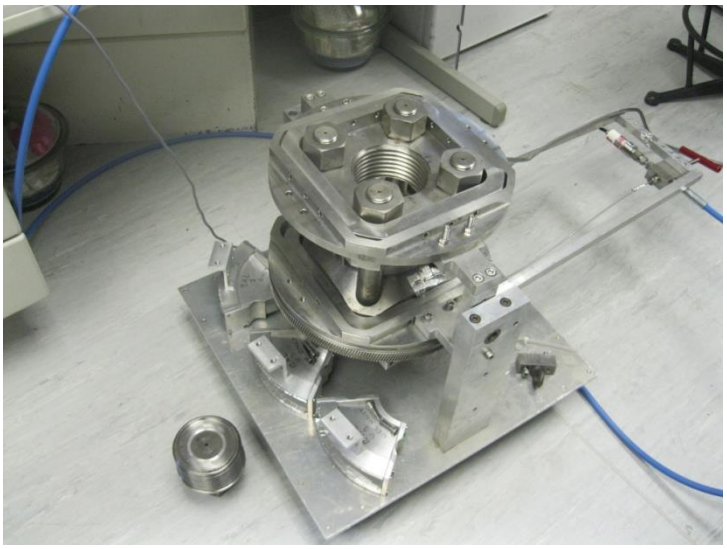

Figure 7.5. Image taken during the 2012 experiment showing assembled P-E cell before mounting in cradle.

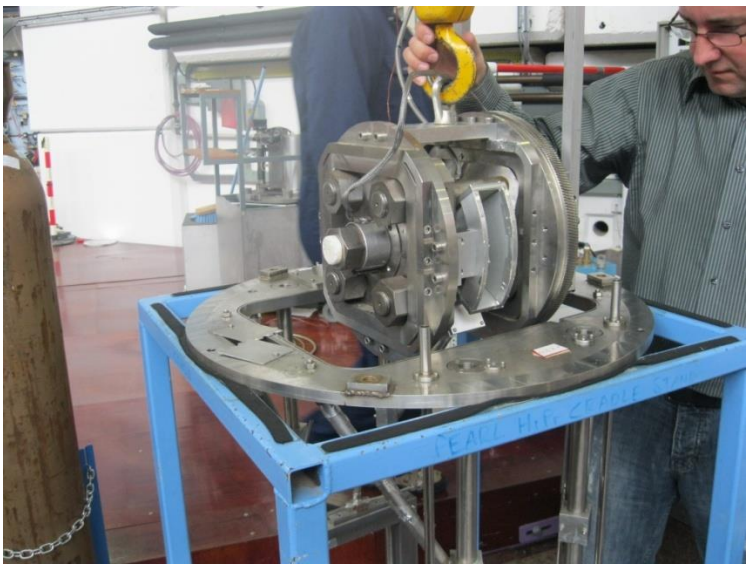

Figure 7.6. Image taken during the 2012 experiment showing the P-E cell being lowered into its cradle.

Lead is both inert and relatively compressible and as such, is suitable as a pressure marker since it is unlikely to react with the sample and the Bragg peaks will undergo measurable shifts even over quite small load increments. The Pb unit-cell dimension is related to the pressure by the Birch-Murnaghan equation of state for Pb, and was parameterized by Fortes et al., (2007b) and used to determine the pressure in these experiments. The equation of state for Pb was derived from a synthesis of literature values for the ambient-pressure thermal expansivity, and ultrasonic determination of the temperature dependence of K_0 and K_0'. The pressure can be determined as follows:

$$P_{V,T} = \frac{3}{2}K_{0,T}\left(x^{7/3} - x^{5/3}\right)\cdot\left[1 + \frac{3}{4}\left(K'_{0,T} - 4\right)\left(x^{2/3} - 1\right)\right] \qquad \text{(Eq. 7.1)}$$

Where $x = V_{0,T}/V_{P,T}$, and the unit cell volume is $V_{0,T}$, the isothermal bulk modulus is $K_{0,T}$, and its first pressure derivative, K_0' , are found from temperature dependent polynomials. The estimated precision of the pressure is ± 0.1 GPa (Fortes et al., 2007b), and references therein). A computer model based on this relationship was devised by

A.D Fortes and used to determine the pressure (GPa) for each run by entering the d-spacing of the strongest Pb peak and the temperature (K).

The diffraction data were normalized to the incident monitor spectrum, corrected for detector efficiency and exported as GSAS-format raw files for analysis. The GSAS system (General Structure Analysis System) contains multiple programs (~50), each with a specific purpose, powder preparation and least squares etc. (Larson & Von Dreele, 2000). The GUI interface, EXPEDT allows the user to edit control data and parameters for calculations, using a common file structure where the experiment name ("experiment.ext") is used throughout, with different file extentions being created during the analysis, depending on file type (e.g., .EXP, .LST, .IPF, .GSS). EXPEDT uses a console screen interface, whereas EXPGUI (Toby, 2001), the graphical interface, works in conjunction with the EXPEDT and accesses features of GSAS.

The height, width and positions of reflections or peaks in intensity, on a diffraction pattern, can be used to determine many aspects of the material's structure. At ISIS, the peak shape is complex because it reflects the time-structure of the moderation process. The typical functional form for time-of-flight involves a combination of Gaussian and Lorentzian components.

Structure refinement is used to characterise crystalline material, analysing profile intensities obtained from neutron diffraction patterns. The Rietveld refinement calculates structure factors using a structural model for the included phases. If there is not an adequate structural model then one uses the LeBail method, where the initial structure factors are all equal and then varied to fit each peak separately. Alternatively, there is a half-way house method called F(calc)-weighted, where the initial structure

factors come from a model, but then subsequent refinement cycles allow the structure factors for each reflection to vary independently.

7.4.1. Experiment 1, Loading 1

The first sample was initially subjected to a load of 10 tonnes at room temperature which it was hoped would generate sufficient pressure on the sample to prevent its dissociation on warming back to room temperature. The data acquisition strategy was to collect diffraction patterns every 60 minutes while raising the pressure in increments of 1 tonne. Initial powder diffraction data were collected for summation and pressures calculated using the Pb equation of state mentioned earlier. These data revealed the presence of sI CD_4 clathrate, however this was observed to melt within two hours of the start of the experiment. The temperature rose a few degrees and it was assumed that the pressure was insufficiently high enough to maintain the stability of the sI clathrate and pushed the sample into liquid D_2O and CD_4 field. Because it was suspected that CD_4 remained trapped in the gaskets, an attempt was made to reform the sI CD_4 clathrate by increasing the load and this proved successful; a phase-pure sample of CD_4 clathrate grew *in situ* under a load of 25 tonnes (later determined to correspond to a pressure of 0.18 GPa) at room temperature. While this was good outcome, it leaves open the possibility that the sample might not have been a very good powder; it may have consisted of a few large crystallites rather than millions of tiny ones. Powder data was acquired for 10 hours in order to carry out a structure refinement of the sI clathrate and thereafter the load was increased in 1 tonne increments, counting for 2 hours per point (figure 7.7). At 27 tonnes, a major power failure at the Rutherford Appleton site halted

the experiment which was abandoned for approximately seven weeks. The sample was left under load for this period.

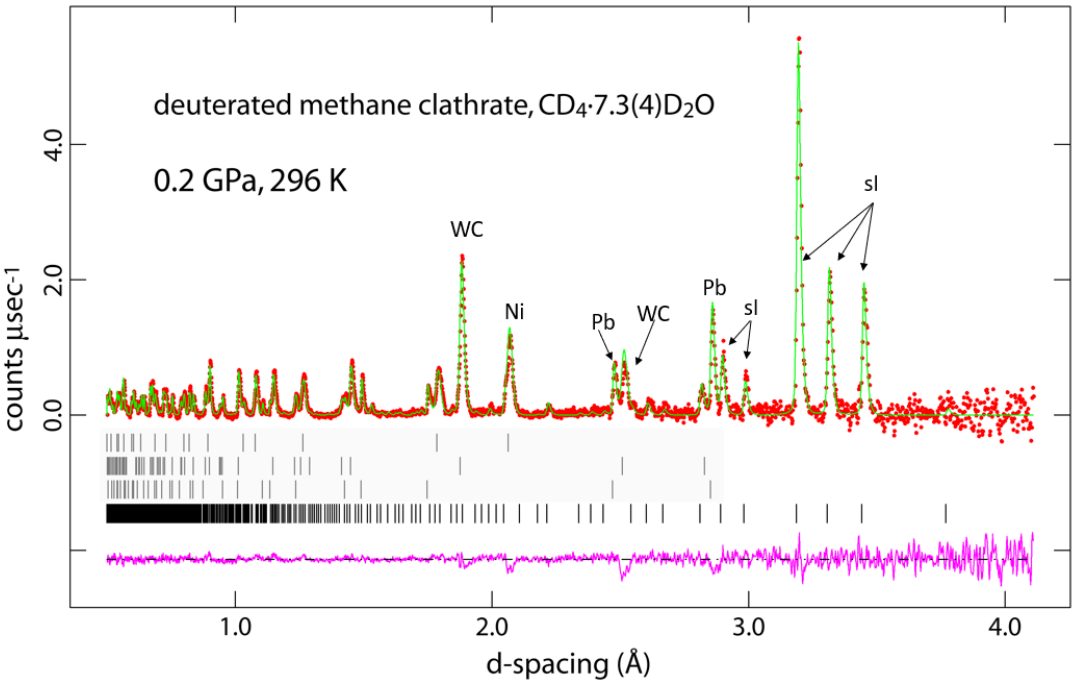

Figure 7.7. GSAS refinement (F(calc) weighted) of the CDH_4 clathrate powder pattern on Run# 75399-75408 (25 tonne load at RT) showing many strong overlapping peaks from the sample environment at short d-spacings. The observed pattern is marked by red dots, the fitted pattern, by the green line, and the difference curve by the purple line underneath. The black tick marks show the positions of the Bragg reflections from each of WC, Ni, Pb and sI methane clathrate. Sharp peaks of tungsten carbide (WC) are marked, which is due to the scattering from the anvils and peaks due to the lead present (Pb). The refinement reveals that the composition is one methane for every 7.3 ± 0.4 water molecules (D_2O) which is not fully occupied (should be 1 to 5.75). No ice is present in the sample.

On re-starting the experiment, a comparison of diffraction patterns of run # 75413-75414 (June) and run # 76155-76157 (July) was made. A slightly more intense diffraction signal was observed (~15%) compared with the previous measurement, probably indicating that further crystallisation had occurred during the 7 weeks the sample had been stored under load (figure 7.8).

Compression was continued in 1 tonne increments, increasing to 2 tonne increments beyond 35 tonnes, counting for 3 hours per point. At 33 tonnes, the onset of a

transformation from clathrate sI to sH was detected. At 34 tonnes this transformation was complete and although there was no sign of ice VI, a broad amorphous feature had appeared (figure 7.9).) indicative of liquid (probably water). Further compression to 37 tonnes resulted in the crystallisation of this water to ice VI (pattern A in figure 7.10). Continuing with compression to 41 tonnes (pattern B in figure 7.10), then rises of 2 tonne increments where at 43 tonnes, sH transformed completely to sO (pattern C in figure 7.10). At 45 tonnes, GSAS refinement was done on a 6 hour soak, and the diffraction pattern shows sO and ice VI (pattern D in figure 7.10).

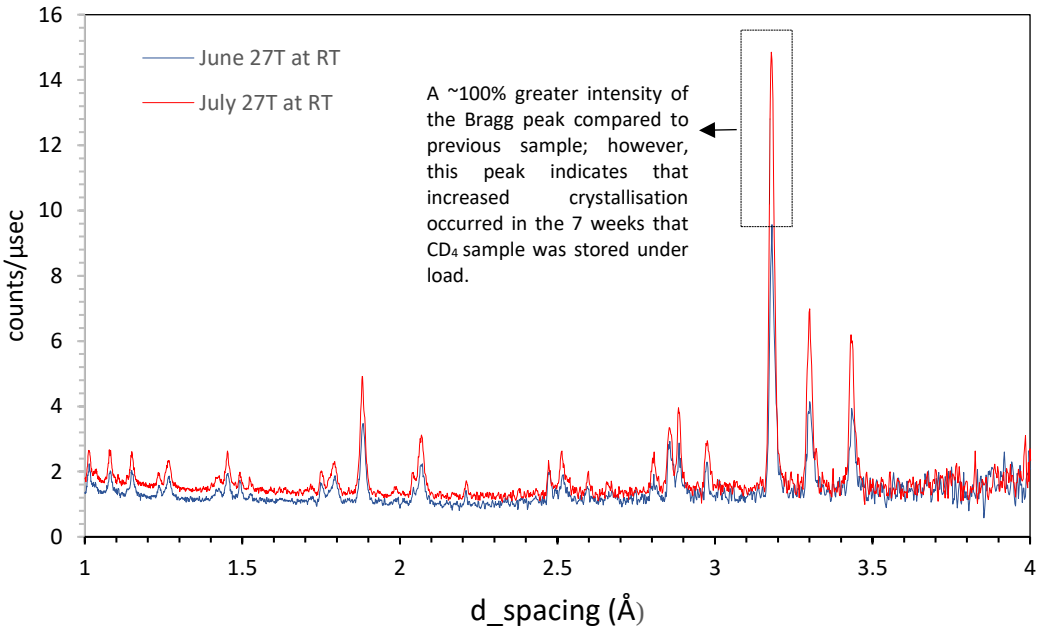

Figure 7 8. Diffraction patterns obtained from a F(calc) weighted refinement of run # 75413-75414 (June) and run # 76155-76157 (July) showing what appears to be a greater intensity of the Bragg peaks, approximately a 100 %, which is probably due to further crystallisation of the specimen during offline storage; both at 27 tonnes and RT. More crystallisation occurred in the sample during the 7 weeks the sample had been stored under load.

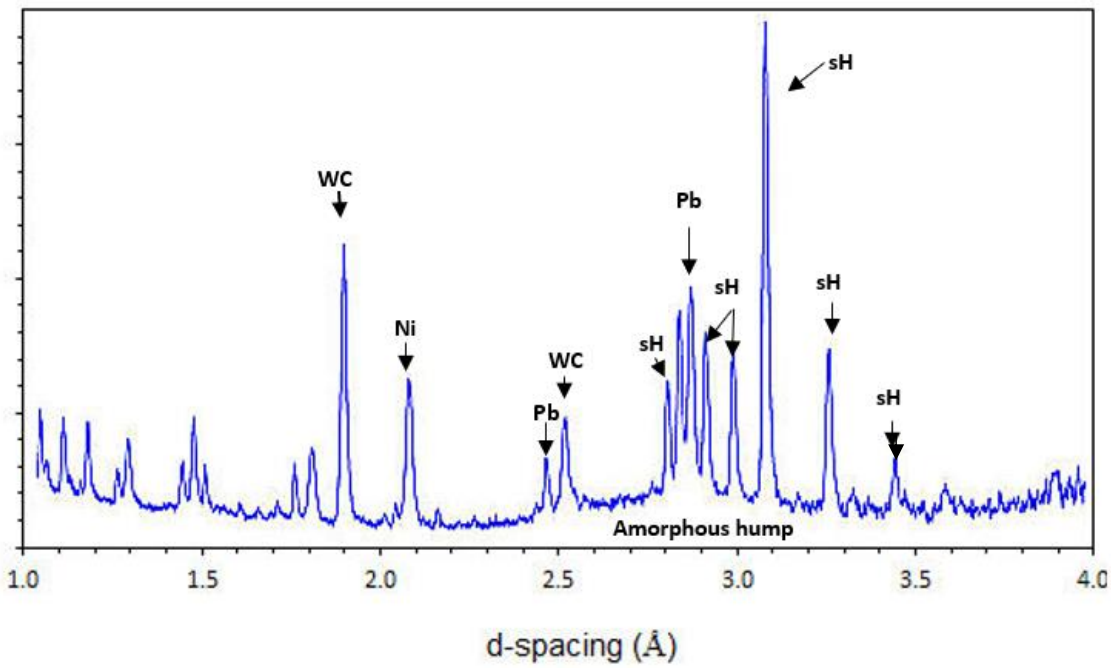

Figure 7.9. Diffraction pattern obtained from a F(calc) weighted refinement, acquired at an applied load of 34 tonnes at RT. The transformation from clathrate sI to sH was complete and although there was no sign of ice VI, an amorphous lump had appeared. There was no sign of ice VI.

The sample was then warmed from room temperature at 45 tonnes (determined to correspond to 2.16 GPa) up to 380 K, and then subsequently decompressed to 10 tonnes in an effort to melt the ice VI part of the specimen leaving only sO clathrate. By 340K all ice VI had transformed to ice VII. It was observed that the solid methane had possibly 'gone' as well; either it had melted or reacted with the ice to form more clathrate. At 360 K, it was observed that ice VII persisted with sO. At 380 K, the ice had failed to melt, so it was decided to reduce the load in ~1 tonne decrements while slowly reducing the temperature to 370K, in the hope that decompression should melt the ice. The goal was to obtain an ice-free diffraction pattern of the sO clathrate. At 10 tonnes, the ice VII was substantially melted, and it was decided to count for 9.5 hours. At the end of this time, only the sO hydrate and liquid were observed.

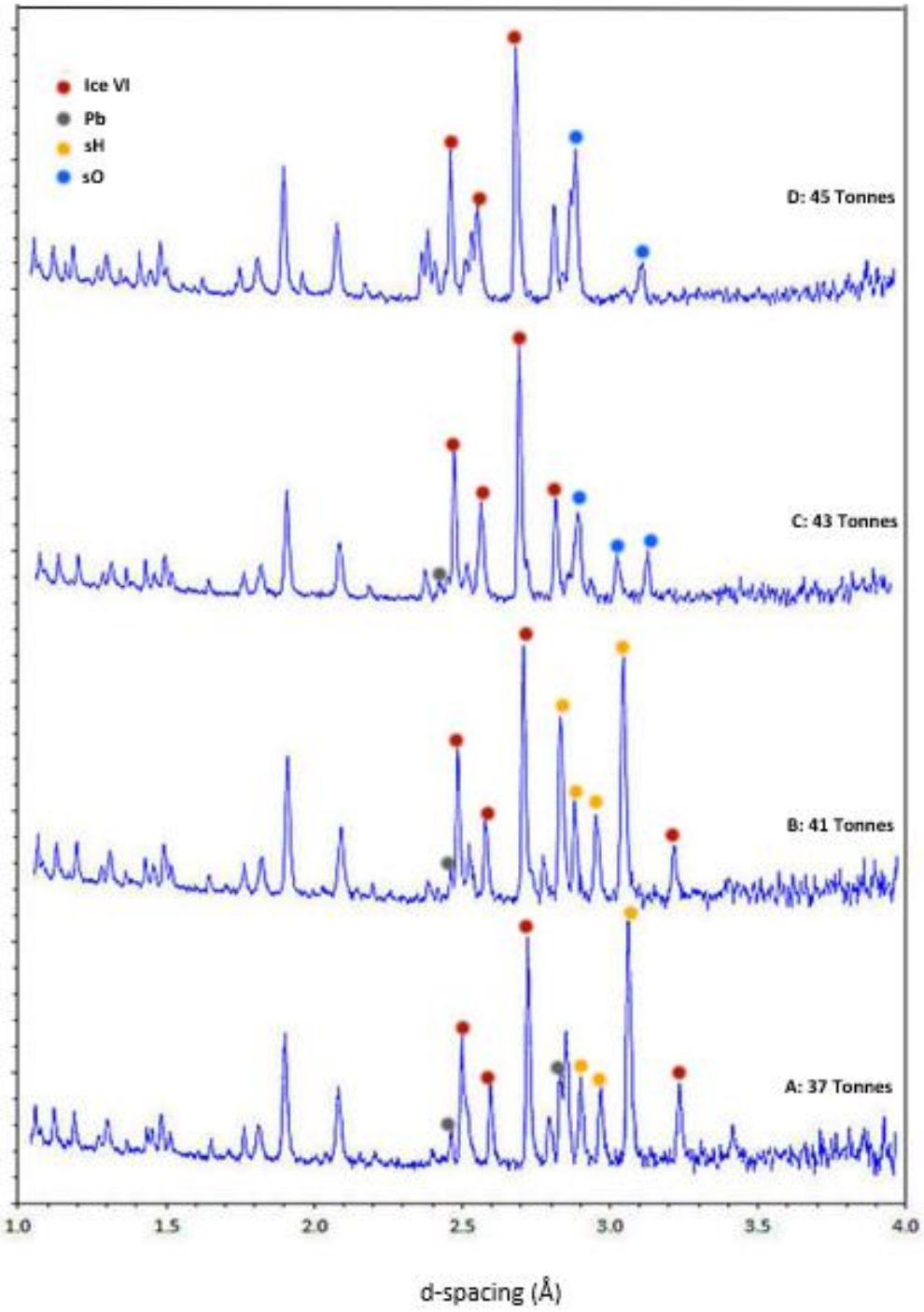

Figure 7.10. Stacked plot showing diffraction patterns obtained from F(calc) weighted refinements where sH is completely transformed to sO under applied loads of 37 to 45 tonnes.

The P-E press was then dismantled, and a hole drilled in the gasket to release the specimen (liquid D_2O and some dissolved CD_4) and the Pb pellet. The press was then re-assembled, and data were collected from the empty press in order to subtract the

sample environment contributions from the powder diffractions patterns. The diffraction pattern of the empty press showed an overall background contribution due to the incoherent scattering, mostly from the TiZr gaskets, and Bragg peaks due to coherent scattering from the tungsten carbide ceramic anvil cores and the nickel binder in the ceramic. These were included as explicit phases during refinement. The empty-press contribution was subtracted and the coherent and incoherent contributions from the anvils and gaskets were removed. The resulting GSAS refinement process allows for the determination of more accurate intensities of clathrate peaks which are used in structure refinements with the removal of the WC and Ni peaks. These structure refinements are used in determining more accurate methane occupancies and position of the methane molecules in the sI and sH clathrates.

7.4.2. Experiment 2, Loading 1#1

The first loading was successful in achieving the initial aims of the first part of the proposed experiment. Figure 7.11 shows the P-T path followed by the first experiment (path 1) and path 2, the P-T path followed in experiment 2. The anvil clamp containing the first sample was loaded in the P-E press at temperature of liquid nitrogen (77.2 K) and loaded offline. At this point a loud popping noise could be heard, the cause of which could have been the presence of water ice, an overfilled gasket, the sample on the gasket, a burst gasket or anvil. Fortunately, as the load was increased, the sample 'settled down' as manual pressure was applied, offset to 20 bars to start. The actual pressure applied was 250 bar.

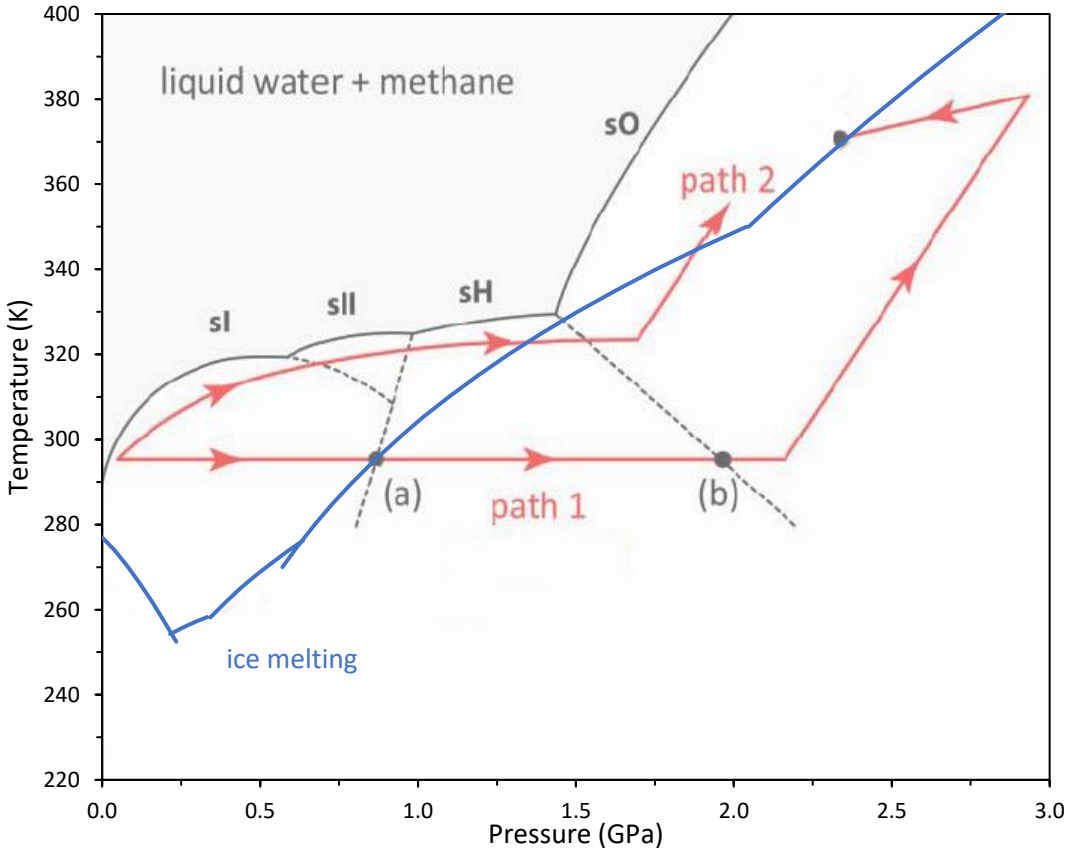

Figure 7.11. Phase diagram of methane clathrate; the solid grey lines indicate the observed dissociation curve and dashed lines are inferred phase boundaries between clathrate polymorphs (Dyadin et al., 1997; Manakov et al., 2004; Loveday et al., 2001a; Loveday et al., 2001b, Hirai et al., 2001; Shimizu et al., 2002; Kumazaki et al., 2004; Choukroun et al., 2007; Fortes & Choukroun, 2010). The blue line shows the melting curve of water ice (Pistorius et al., 1968). P-T path 1, indicated in red (first experiment) shows the proposed sI → sH transition at point (a), and sH → sO, the proposed transition at point (b). Path 2 was the proposed path for experiment 2, loading 2.

The first run of 7 hours duration was carried out under this load of 25 tonnes. The pressure was determined to be 1.56 GPa at 299 K. Figure 7.12 shows ice VI, and methane hydrate structures sH and sO. Thereafter the load was increased in 1 tonne increments. A GSAS refinement was done on the results of each of 25T, 27T, 29T and 31T, and combined in figure 7.13. The results clearly indicate increasing sO being formed, at the expense of sH.

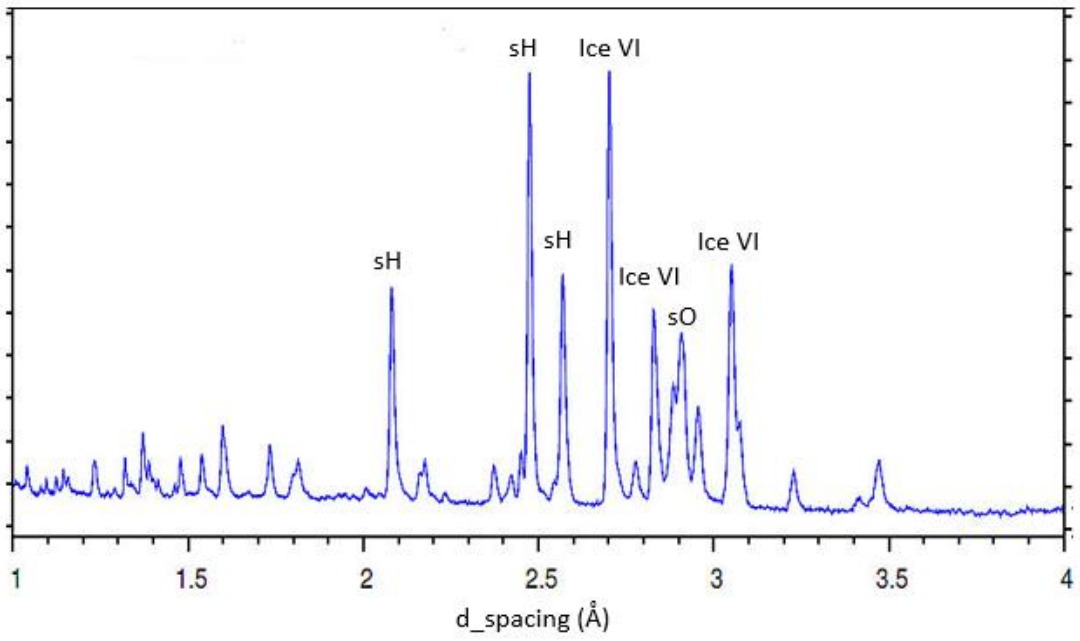

Figure 7.12. Diffraction pattern obtained from a F(calc) weighted refinement, under a 25T load at RT, showing the presence of ice VI, sH and the beginning of sO forming.

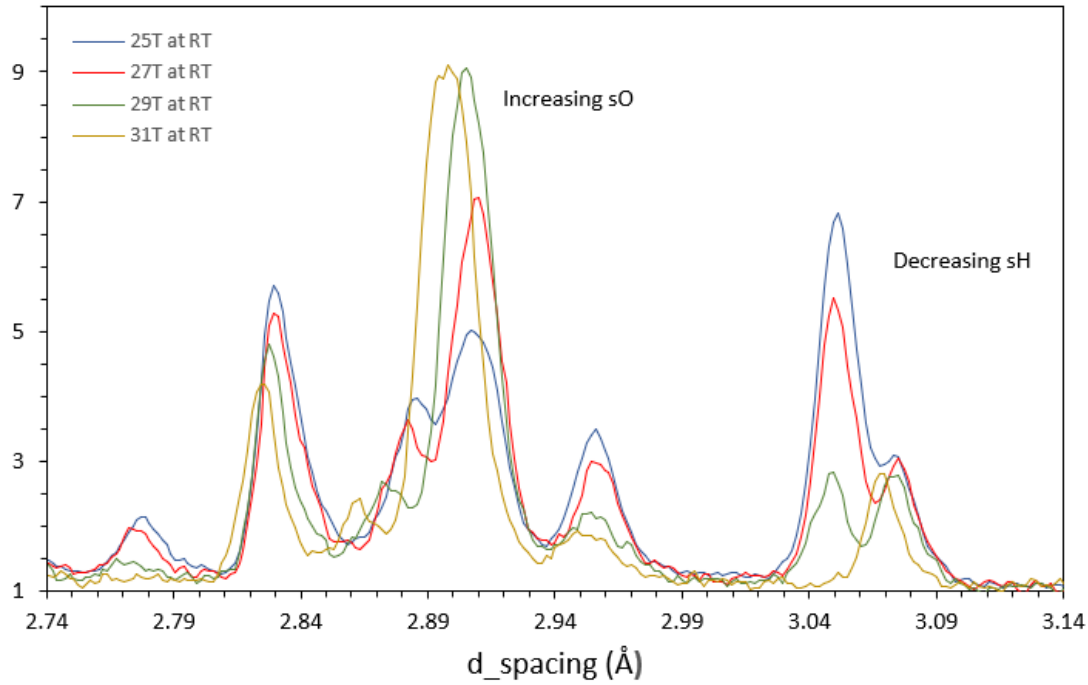

Figure 7.13. Diffraction patterns of four separate runs obtained from F(calc) weighted refinements; 25T, 27T, 29T and 31T loads, at RT. The plots show increasing sO and decreasing sH structures in the sample.

At a load of 35 tonnes, ice VII was starting to form, and ice VI was still present. The load was increased to 37 tonnes; examination of the diffraction patterns showed that the

transition of ice VI → ice VII had not yet completed, and it was decided to increase the load to 39 tonnes and set the sample to run at this load for 10 hours. The runs were combined and a GSAS refinement was performed and showed that ice VI → ice VII transition had completed and there was no ice VI present in the sample (figure 7.14).

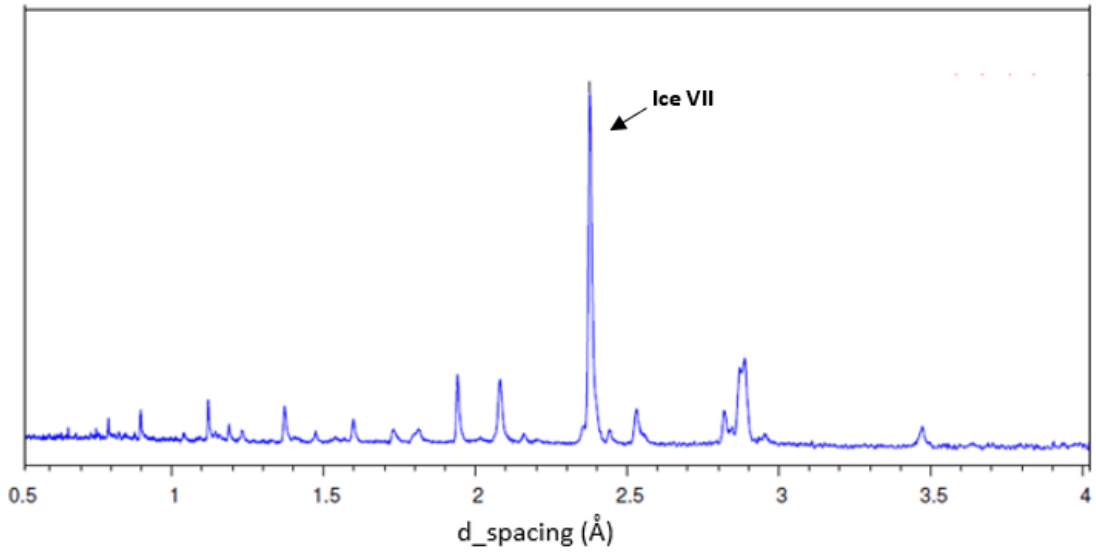

Figure 7.14. Diffraction pattern obtained from F(calc) weighted refinement showing that ice VI → ice VII transition had completed and there was no ice VI present in the sample.

7.4.3. Experiment 2, Loading 2

The anvil clamp containing a second sample being loaded in the P-E press at a temperature of 298.4 K. A load of 15 tonnes was applied, approximately 1 GPa. At the end of the first hour's soak, there was no indication of methane clathrate sO in the sample (not expected at this pressure), and possibly some structure sH. Diffraction patterns showed the presence of ice VI. After the second hour, a mixture of ice VI and methane clathrate sH was detected at ~1.291 GPa. The load was reduced to 11 tonnes, then reduced further to 8 tonnes, because the resulting pressure was insufficient to

maintain ice VI. The temperature was increased to 310 K at a load of 8 tonnes. At this point the ISIS beam went off, and was restored 8 hours later. On resuming, at a load of 10 tonnes, no discernible peak shift had occurred, and the load was increased to 14 tonnes, (0.961 GPa), where no ice VI had formed, although peaks of methane clathrate sH had formed.

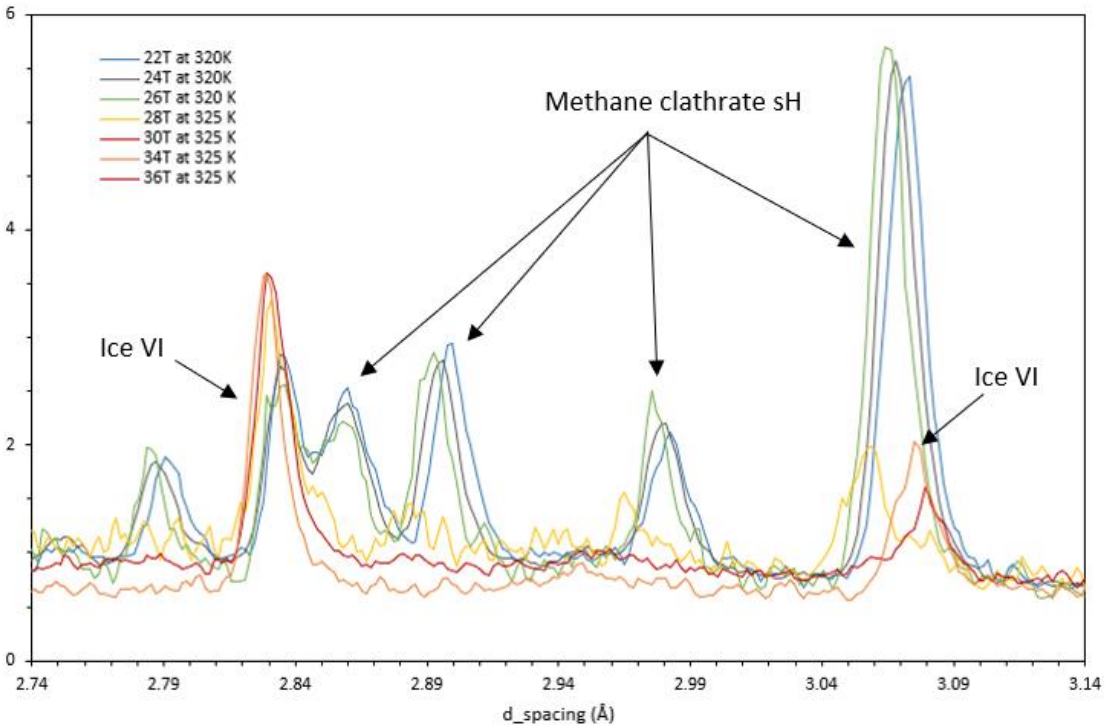

Figure 7.15. Plot of diffraction patterns obtained from F(calc) weighted refinements, showing the effect of increasing the load from 22 tonnes to 34 tonnes, and increasing the temperature from 320 K to 325 K. The prominent peaks of methane clathrate structure sH and ice VI peaks are annotated. Warming from 320-325 K at 1.621 GPa (28 tonnes) results in the decomposition of the clathrates (as seen in the phase diagram, figure 7.11, line b)

The load was increased to 22 tonnes, where ice VI had formed. The sample was warmed to 315 K, and it was noted that the ice VI peaks had diminished in intensity, due to the increased temperature. The sample was further warmed to 320 K and all evidence of ice VI had gone. At increasing loads of 2 tonne increments ice VI started to reform, although at an increased temperature (325 K) ice VI peaks once again diminished,

although methane clathrate sH peaks had formed. The temperature was increased to 325 K, and the load to 32 tonnes over the next two runs. At 34 tonnes and 325 K, ice VI remained and possibly solid CH_4 and liquid. Figure 7.15 shows the results of increasing the pressure and temperature on the sample.

7.4.4. Experiment 2, Loading 1#2

In the final part of experiment two, the anvil clamp containing the first sample, which had been stored in the anvil jig for two days, was loaded in the P-E press at a temperature of 298 K. A load of 39 tonnes was applied.

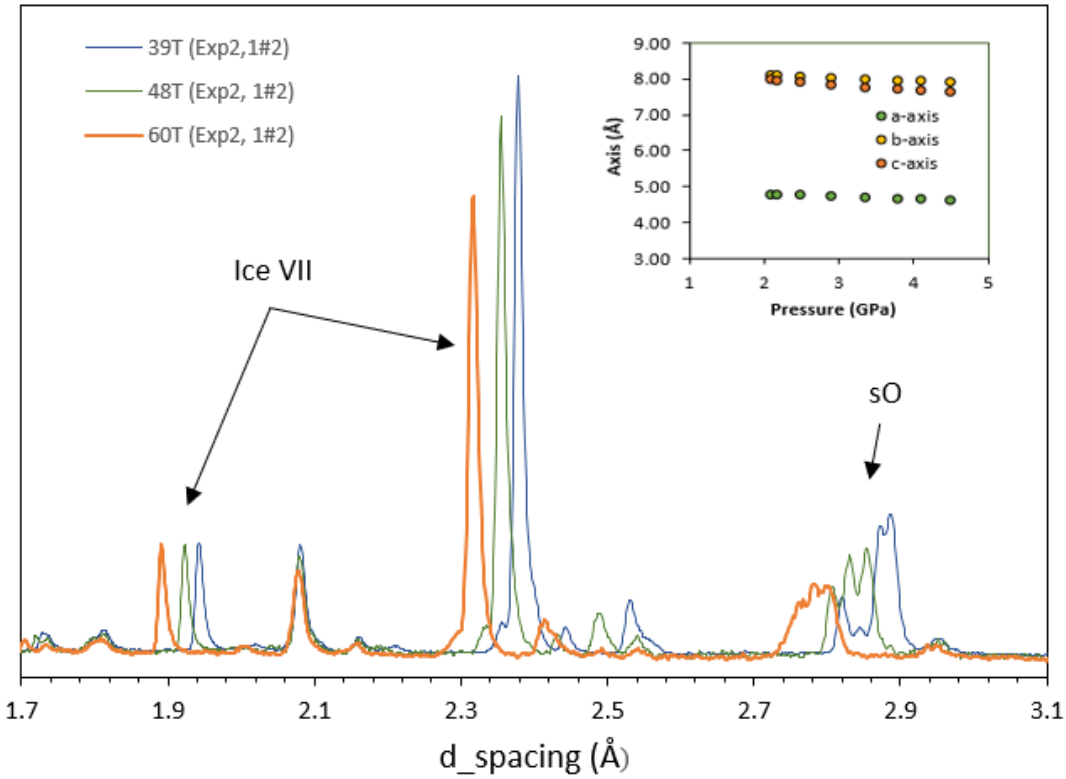

Figure 7.16. Combined diffraction patterns obtained from F(calc) weighted refinements, at room temperature, showing the decrease in intensity of both ice VII and methane clathrate sO peaks. The inset shows the second run of the first loading of experiment two and illustrates the very slight decrease in axial lengths for methane clathrate sO with an increasing load.

A diffraction pattern of this run was compared with the one done at the end of the first part of this experiment (Loading 1), and showed no discernible differences in the peaks of methane clathrate structure sO and ice VII. The load was then increased to 60 tonnes, then increased by 2 tonnes, then in increments of 3 tonnes until a load of 69 tonnes was reached, (figure 7.16) showing ice VII and methane clathrate structure sO Bragg peaks systematically decreasing in intensity, and shifted to shorter d-spacings. The load was then decompressed to 2 tonnes.

7.5. Results

Rietveld powder diffraction statistics showing the unit cell dimensions and volume for $CDH_4.nD_2O$ structure sI, sH and sO, and ices VI and VII, using data collected on PEARL, are presented in Appendix IV (tables I to V). These data represent the results from experiment 1 and experiment 2, (loading 1 and 1#2) at pressures between 0.182 GPa to 4.48 GPa along the room temperature isotherm. The temperature range in experiment 2 (loading 2) was between 299 K and 325 K at pressures between 1.312 to 1.902 GPa.

7.5.1. Bulk and axial compressibility

From the volume-pressure dependence measured in this work, the bulk modulus and its pressure derivatives can be determined by fitting an equation of state to the compression data. The data collected along the RT isotherm during compression on PEARL were fitted with the third-order Birch-Murnaghan isothermal equation of state, BMEOS (Birch, 1952), and parametrized in terms of zero-pressure starting volume (V_0),

zero-pressure isothermal bulk modulus[20] ($K_{T,0}$), and the first pressure derivative of the bulk modulus (K'). The equation of state data is weighted based on difference between observed and calculated values using a least-squares method. The relationship between the volume and pressure is shown where $K_{T,0} = V\partial P/\partial V$:

$$P = \frac{3}{2}K_{T,0}\left[\left(\frac{V_0}{V}\right)^{\frac{7}{3}} - \left(\frac{V_0}{V}\right)^{\frac{5}{3}}\right] \cdot \left[1 + \frac{3}{4}(K' - 4)\left(\frac{V_0}{V}\right)^{2/3} - 1\right] \qquad \text{(Eq. 7.2)}$$

The data set for the sO axial data was combined with results of high pressure studies of methane clathrate using *in situ* x-ray diffraction from Hirai et al., (2003) and Loveday et al. (2001b). These were used to plot the unit-cell volume pressure dependence along the 290K (RT) isotherm in figure 7.17. The plot shows that there is a systematic difference in the compression of sO in the three different studies, and this represents a difference in the pressure calibration between the three different studies. Loveday et al. (2001a, 2001b) report that the fitting parameters K' and K_0 used for their analysis were 4 and 15.2(5) GPa respectively and Hirai et al. (2003) report that the fitting parameters K' and K_0 used for their analysis were 4 and 15.4(5) GPa respectively. The equivalent fitting parameters for this work were 4.0 ± 0.2 (K') and 16.298111 ± 2.0 GPa (K_0) respectively.

Although all three cell parameters a, b and c decrease with increasing pressure, their rates of axial compression are different, as shown in figures 7.18 and 7.19, which are

[20] The isothermal bulk modulus ($K_{T,0}$) determines how a material resists compression at a constant temperature. K' is the slope of the inverse slope of the logarithmic compression curve.

plotted on the same scale: the rate of contraction in axis-c is larger than that of axis-b, which in turn is larger than that of axis-a.

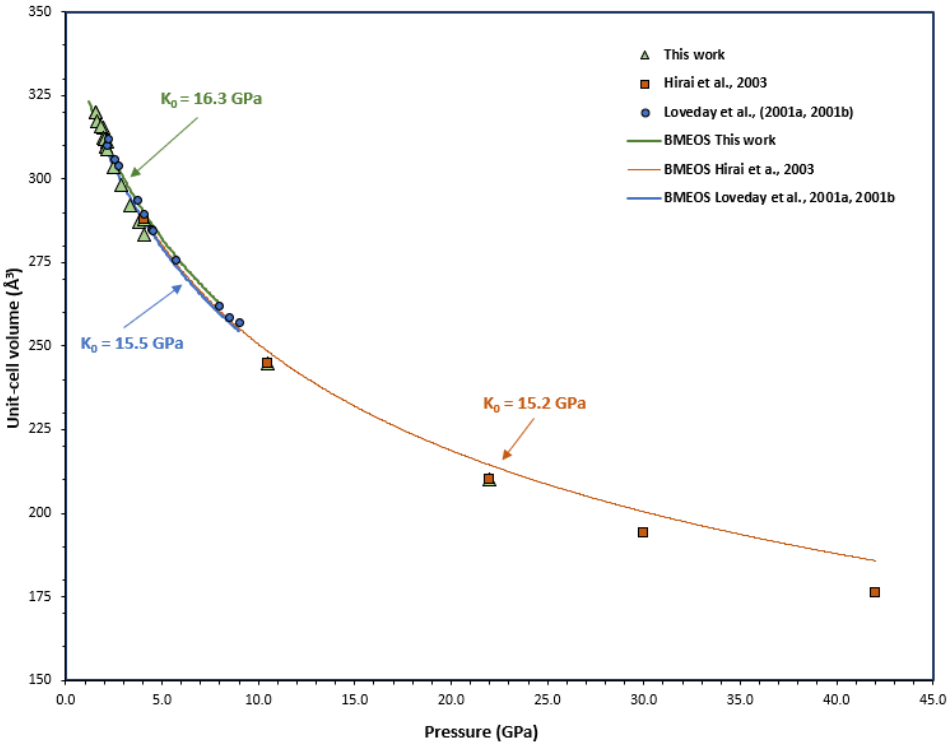

Figure 7.17. Methane clathrate structure sO unit-cell volume pressure dependence along the 290K isotherm (RT) showing this work (data from both experiments combined), and *in situ* x-ray diffraction from Hirai et al. (2003) and Loveday et al. (2001b). The lines are third-order Birch-Murnagham equation of state (BMEOS) fitted to each set of data where the bulk modulus of each (K_0) is indicated (equation 7.2)

The data for each axis are fitted to the linearized version of the 2nd order Birch-Murnaghan equation of state ($P = 1.5K_0[(V_0/V)^{7/3} – (V_0/V)^{5/3}]$) where V is replaced with the relevant axis length cubed (a^3, b^3 or c^3), and V_0 with a_0^3, b_0^3 or c_0^3 respectively (Birch, 1952; Xu et al., 2010). Changes in unit-cell parameters a, b and c axes with pressure for methane clathrate structure sO are shown in figures 7.18 and 7.19 respectively (data from this work).

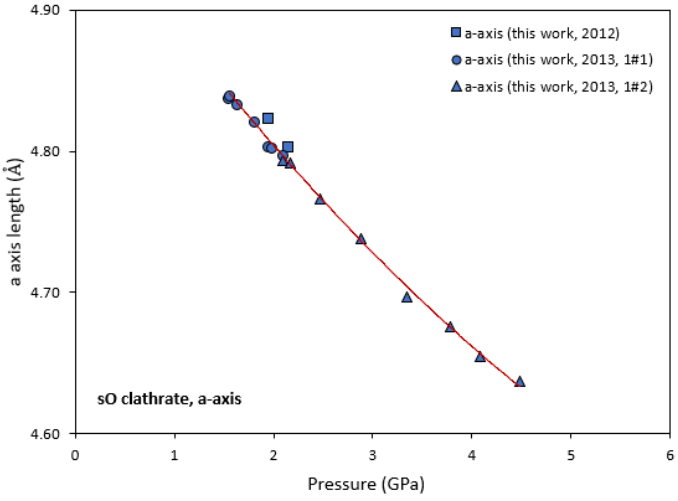

Figure 7.18. Plot of methane clathrate structure sO a-axis lengths (Å) against pressure (GPa) showing data from this work (all results combined). The data are fitted (red line) to the linearized version of the Birch-Murnaghan EOS and yield a_0 = 4.9854 Å and $K_{0,a}$ = 26.57 GPa. Errors reported are smaller than the symbols used in this plot.

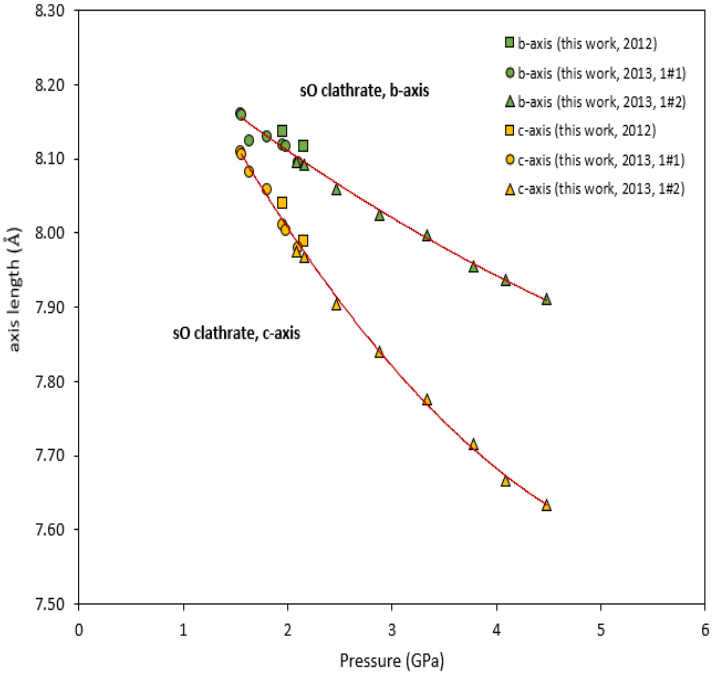

Figure 7.19. Plot of methane clathrate structure sO b-axis and c-axis lengths (Å) against pressure (GPa) showing data from this work (all results combined). The data for axis b and c from this work are fitted (red lines) to the linearized version of the Birch-Murnaghan and yields b_0 = 8.3289 Å, $K_{0,b}$ = 22.627 GPa and c_0 = 8.5278 Å, $K_{0,c}$ = 10.12 GPa, showing that a large elastic anisotropy[21] exists between the b and c axes. Errors reported are smaller than the symbols used in this plot.

[21] Elastic anisotropy occurs when the relationship between stress and strain in a crystal depend on its orientation. The stress is the pressure per unit area and the resultant strain is the deformations that occurs as a result of this stress.

Axial ratios (c/a and b/a) can be indicators of differential thermal expansion or compressibility and may indicate deviations from the most efficient packing of the crystal structure. The pressure evolution of the axial ratios, c/a and b/a, for methane clathrate structure sO is shown in figure 7.20 and the effects of increasing pressure on the c/a ratio of methane clathrate sH can be seen in figure 7.21. Figure 7.22 shows the variation on volume of the three phases of methane hydrate with pressure. Figure 7.23 plots the effects of compression on the specific volumes of the phases of ice (ice VI and ice VII) and methane clathrate (sI, sH and sO).

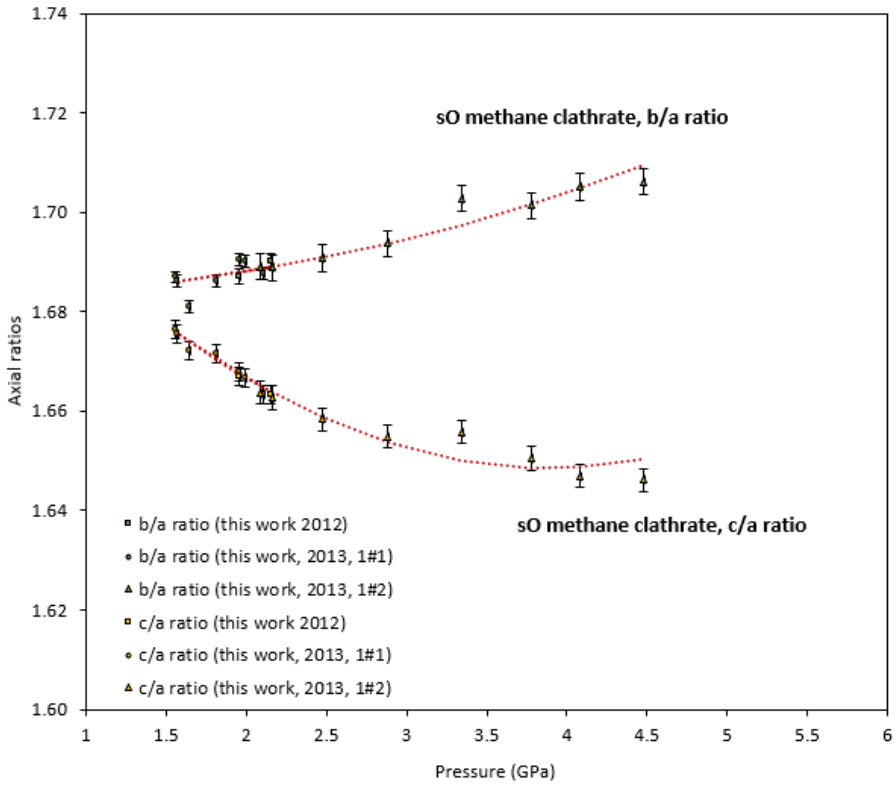

Figure 7.20. Pressure evolution of the axial ratios, b/a and c/a, for methane clathrate structure sO. The linearized version of the Birch-Murnaghan EOS has been fitted to individual lattice parameters and then used to calculate the 'ideal' axial ratios for b/a and c/a (red dotted lines).

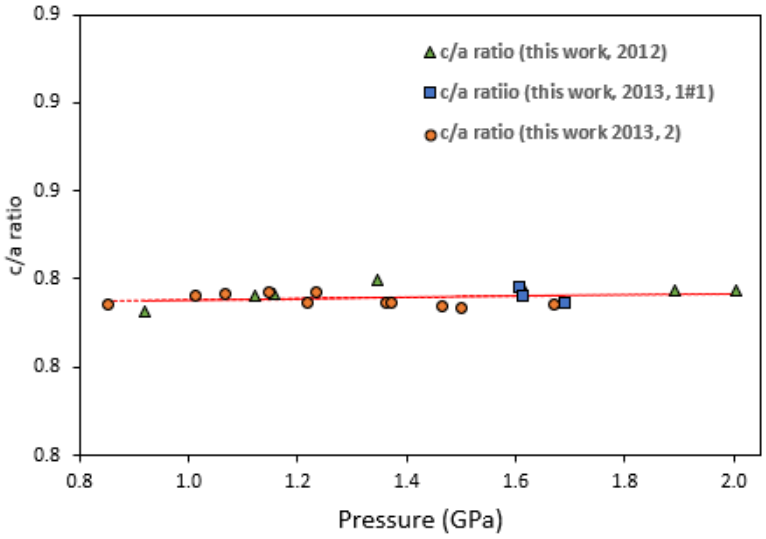

Figure 7.21. Pressure evolution of the axial ratio c/a, for methane clathrate structure sH. The linearized version of the Birch-Murnaghan EOS has been fitted to individual lattice parameters and then used to calculate the 'ideal' axial ratio c/a (red dotted line). This reveals a negligible variation in c/a for sH as a function of P.

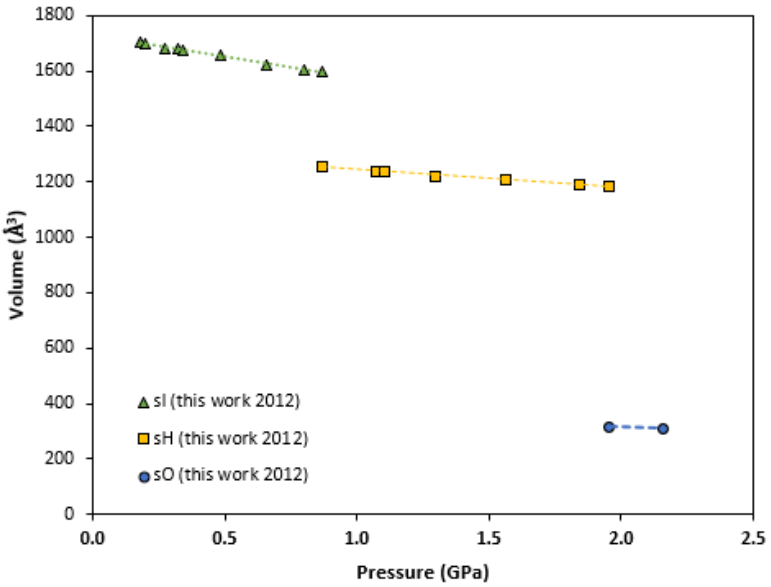

Figure 7.22. Variation of volume with pressure for all three phases of methane clathrate, where the change of compression was observed between 0.2 GPa to 2.2 GPa.

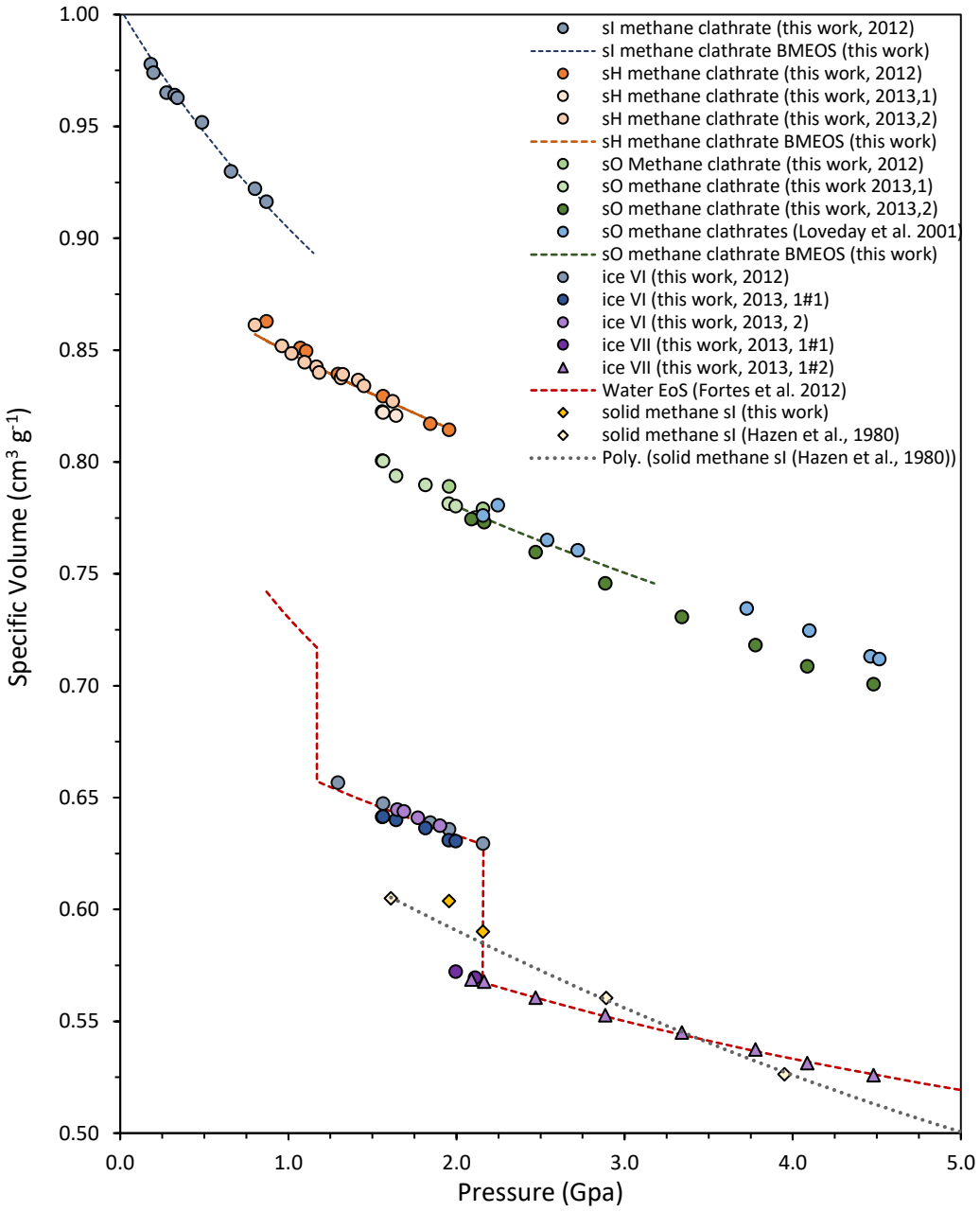

Figure 7.23. Plot showing the effect of compression on the specific volumes of the phases of methane clathrate (sI, sH and sO) and ice VI and VII, observed in these experiments, with the addition of results from Loveday et al. (2001) and Hazen et al. (1980). The water equation of state (Fortes et al., 2012) is indicated by the red dashed line, and the data for methane clathrates structures sI, sH and sO have each been fitted with the Birch-Murnaghan EOS (indicated in the legend).

7.5.2. Observations of phase behaviour

The results obtained from two separate loadings were used to plot the sequence of phase changes of methane hydrate that occurred under compression (figure 7.24).

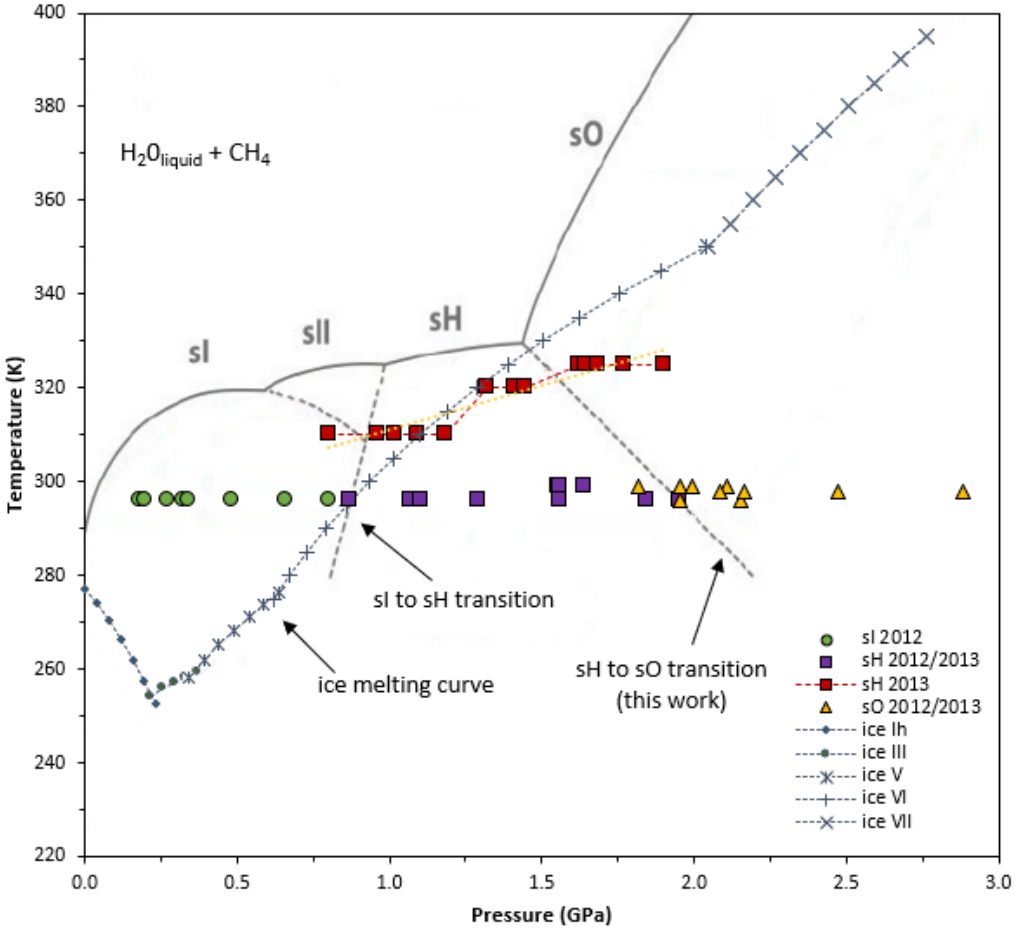

Figure 7.24. Phase diagram of methane clathrate obtained from the results of this experiment; the solid grey lines indicate the observed dissociation curve as discussed in figure 7.1 where the dashed lines are inferred phase boundaries between clathrate polymorphs. The blue line shows the melting curve of water ice.

7.6. Discussion and summary of results

The neutron powder diffraction study described in this chapter has provided *in-situ* diffraction based evidence for the phase behaviour of methane clathrate near to its high-pressure dissociation temperature, and the first direct measurement of the melting point of structure sO methane clathrate.

The sequence of phase changes observed in this work along the 299 K isotherm, showed that upon compression, structure sI methane clathrate (cubic) was stable up to 0.870 GPa, similar to the 0.8 GPa reported by Loveday et al. (2001). Hirai et al. (2003) however reported that the sI structure was stable up to 0.62 GPa. Upon further compression, the methane clathrate in this study was observed to transform into a hexagonal sH structure and remained stable until 1.955 GPa, when it transformed to a filled iced structure phase (orthorhombic), sO (figure 7.24). A similar transformation at 2.0 GPa to sO was reported by Loveday et al. (2001).

The results show that there is a systematic difference in the compression of sO in the three different studies, and this represents a difference in the pressure calibration between the three different studies, where the bulk moduli (K_0) for this study was determined to be 16.3 GPa, compared to 15.2 GPa and 15.5 GPa (Hirai et al., (2003) and Loveday et al. (2001a) respectively (Figure 7.17). Similarly, differences exist in the bulk moduli for sH (this work = 17.9 GPa, Hirai et al., (2002) = 9.8 GPa, Loveday et al. (2001) = 15.2 GPa) and sI (this work = 7.8 GPa, Hirai et al. (2002) = 7.4 GPa).

Figure 7.22 shows the volume change of methane clathrate with pressure where the volume decreased with compression. The variation in volume is small for each clathrate polymorph phase, but as the structure transforms, there is a significant change in the volume. This suggests that under increasing compression, structural changes occur, where cubic sI transforms to hexagonal sH, and continues to transform to orthorhombic sO.

The sI, sII, sH and sO methane hydrates are likely to be major methane-bearing phases in the outer planets and their satellites, and the results obtained in the 0.6 – 1.6 GPa region allowing the characterisation of the phase behaviour of methane clathrate in this

Pressure-Temperature region, thus informing the model processes occurring in the interiors of icy moons containing methane clathrate. This will be discussed in the concluding chapter of this thesis.

CHAPTER EIGHT

Synthesis and conclusions

8. Synthesis and conclusions

This chapter brings together the major findings from the application of the Xenolith II model to Enceladus, Triton and Titan, presenting a critical assessment of the results and methods (8.1). A general synopsis of the results of the model and their implications are presented in section 8.1.1. Implications of the model results and morphological evidence are discussed in section 8.1.2

An appraisal of the model is presented in section 8.1.3, with future work discussed in sections 8.1.4 and 8.1.5. The results obtained from *in situ* high pressure neutron diffraction experiments are correlated with the Xenolith II results, informing the modelling effort (8.2). Finally, a brief conclusion will establish the contribution that Xenolith II makes to our understanding of explosive cryovolcanism on icy planetary bodies.

8.1. Critical assessment of Xenolith II model

The Xenolith II model investigates the role that clathrate dissociation plays in explosive cryovolcanism on Enceladus, Triton and Titan, quantifying the fragmentation depths, flow dynamics, kinetic energy and viscosity of the plumes. The model relates selected conduit sizes to the plume heights, velocity and flow rates, and examines a number of different cryomagma composition scenarios (liquid and volatile content) for each of these, providing a range of outcomes. The model also quantifies the thermodynamic energy balance of the plumes in an attempt to account for the contribution made by clathrate dissociation to the energy radiated by the plumes (latent heats of dissociation, crystallisation and sublimation).

8.1.1. General implications of Xenolith II results

The specific results and implications of each of the model implementations are presented in chapters 4 (Enceladus), 5 (Triton) and 6 (Titan); however, here follows a general discussion of the results and comparisons between the different scenarios for each moon.

The calculated fragmentation depths for each cryomagma composition and volatile content for each moon are summarised in table 8.1 (two scenarios for each). The differences in the fragmentation depths arise for a number of reasons. The different xenolith mass fractions estimated for Enceladus and Triton (16.54 wt%) and Titan (10 wt%) yield different mass fractions for each volatile in the cryomagma, which together with the pressure at each depth modelled, dictate the amount of each volatile present (according to the estimated content at the surface). The depths at which this happens for each clathrate species differ and are related to their solubility in the cryomagma and

the surrounding pressure. As each clathrate species dissociates, it releases gas bubbles into the cryomagma, adding to the total bubble volume fraction, which when reaching ~75%, is considered to cause fragmentation. The bubble volume fraction is also related to the bulk magma density, which in turn is related to the local pressure, cryomagma density, the molecular mass of the gases and the cryomagma temperature. The implications of the results in table 8.1 are that where the volatile content is the same, the fragmentation depth is the same, even where the cryomagma composition differs (Enceladus and Titan). However, in the case of Triton, the volatile content differs for each scenario, resulting in different fragmentation depths. The different pressures and bulk magma densities for the two scenarios for Triton are a result of the different mass fractions of the volatile content in the cryomagma, whereas for Titan, the differences in the pressure and bulk magma density for two scenarios are attributed to the fact that the density and temperature of the cryomagma are different (1065 vs.1235 kg m^{-3} and 270.7 vs. 253.8 K respectively).

Table 8.1. Depth, pressure and bulk magma density at the point of fragmentation for each cryomagma scenario (composition and volatile content)

Model scenarios	Volatle content	Cryomagma composition	Fragmentation depth (km)	Pressure (Pa)	Bulk magma density (kg m^{-3})
Enceladus I	$xCO_2 = 0.364$, $xCH_4 = 0.182$, $xN_2 = 0.454$	Pure H_2O	3.32	375000	256.54
Enceladus II	$xCO_2 = 0.364$, $xCH_4 = 0.182$, $xN_2 = 0.454$	3.5 % NaCl and H_2O	3.32	375000	256.54
Triton I	$xCO_2 = 0.200$, $xCH_4 = 0.110$, $xN_2 = 0.690$	Pure H_2O	0.55	400000	236.76
Triton II	$xCO_2 = 0.100$, $xCH_4 = 0.050$, $xN_2 = 0.850$	Pure H_2O	0.62	450000	237.64
Titan I	$xCH_4 = 0.057$, $N_2 = 0.942$	10.6 wt% $(NH_4)_2SO_4$-H_2O	0.21	300000	270.46
Titan II	$xCH_4 = 0.057$, $N_2 = 0.942$	40.4 wt% $(NH_4)_2SO_4$-H_2O	0.21	400000	316.87

The bulk magma density is calculated where most of the entrained clathrates have exsolved, and the exsolved gas fraction approaches 100%. At this point (very near the surface), the bulk magma density has reduced significantly from the fragmentation depth, and this is shown in table 8.2. The results show that there is very little difference

between each of the scenarios for each moon and that the bulk magma density is very small at the surface. Because the cryomagma is denser than the surrounding ice (table 8.2), buoyancy-driven ascent of the cryomagma should not be possible (negative buoyancy). The addition of exsolved volatiles from the process of clathrate dissociation reduces the density of the aqueous cryomagma, and helps to overcome the negative buoyancy.

Table 8.2. Depth, pressure and bulk magma density at the point where the exsolved gas fraction is 99% for each cryomagma scenario (composition and volatile content), very near the surface

Scenarios for each moon	Depth (m)	Pressure (Pa)	Bulk magma density (kg m^{-3})	Density of crust (kg m^{-3})
Enceladus I	0.09	10	0.0095	1000
Enceladus II	0.09	10	0.0095	1000
Triton I	0.01	10	0.0056	937
Triton II	0.01	10	0.0095	937
Titan I	0.01	10	0.0089	1065
Titan II	0.01	10	0.0095	1235

The velocities at the point where the exsolved gas fraction is 99% is shown in figure 8.1. The velocity of the cryomagma is determined by the conduit size, flow rates and bulk magma density, but since the conduit size is the same for each scenario illustrated in figure 8.1 (using a 5 m diameter for each as a representative example), the different bulk magma densities and flow rates are shown to have an impact on the velocity. On Enceladus, the calculated velocities increase significantly at the surface, where the velocity is related to the bulk magma density. This is in turn is related to the pressure, and at the surface, this is taken to be the vent pressure which is assumed to be comparable to the surface pressure (~ 3×10^{-6} Pa), inferred from modelling of Cassini UVIS occultation data (Hansen et al., 2006). The sudden increase in velocity at the surface is related to the sudden decrease in pressure (and bulk magma density) as the plume erupts. An increase of velocity at the surface is predicted to occur on Triton as

well, where the surface pressure is estimated to be ~1.5 Pa (Brown et al., 1990), with a related drop in bulk magma density. The surface pressure of ~147 Pa (Fulchignoni et al., 2006) is much greater on Titan however, and at the surface, the bulk magma density is predicted to increase, and the velocity to decrease.

The flow rate and bulk magma density are approximately the same for both scenarios for Enceladus, and the outcome of this is that there is no significant difference in the velocities for each scenario. The different flow rates and bulk magmas densities for each of the scenarios for Triton and Titan result in different velocities. However, at the same

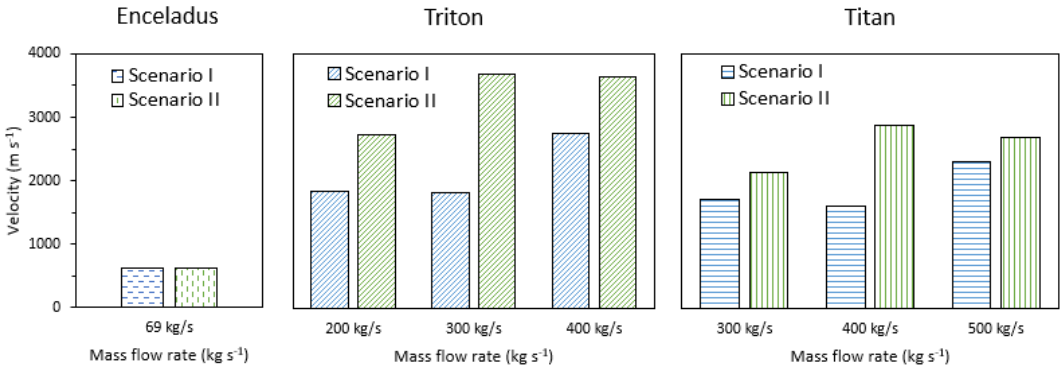

Figure 8.1. Velocity obtained for the estimated flow rates applied to the different volatile content and cryomagma composition scenarios for a circular conduit of 5 m diameter, where the exsolved gas fraction has been determined to be 100%.

pressure, cryomagma density, cryomagma temperature and gases exsolved in the cryomagma (bulk magma density), the velocity increases as the conduit diameter increases, as presented in sections 4.22 (Enceladus), 5.22 (Triton) and 6.22 (Titan*).*

The sound speed is treated independently of the conduit size, and is related to the amount of gases present in the cryomagma, the cryomagma temperature and the pressure. From the results obtained from these calculations, the Mach number can be calculated (by dividing the velocity by the sound speed at each point), allowing for the

determination of whether flow is subsonic (Mach < 1) or supersonic (Mach > 1). Where flow velocity equals the sound speed (Mach = 1), the phenomenon of 'choking' occurs, and this plays a role in the fluid dynamics of the flow because this condition controls the mass flux from depressurizing systems.

Because of the relationship of the velocity to the conduit size, the Mach number has been determined for individual conduits, for each scenario, and for each moon. The depth at which Mach 1 is reached has been plotted for each of these scenarios for a conduit 5 m in diameter (Figure 8.2) and shows that Mach I is reached within the last 1.5 metres (essentially at the surface) for each scenario. Results showing where, and if Mach conditions are reached for all of the other conduits modelled for Enceladus, Triton and Titan are presented in figures 4.8, 5.8 and 6.9 respectively.

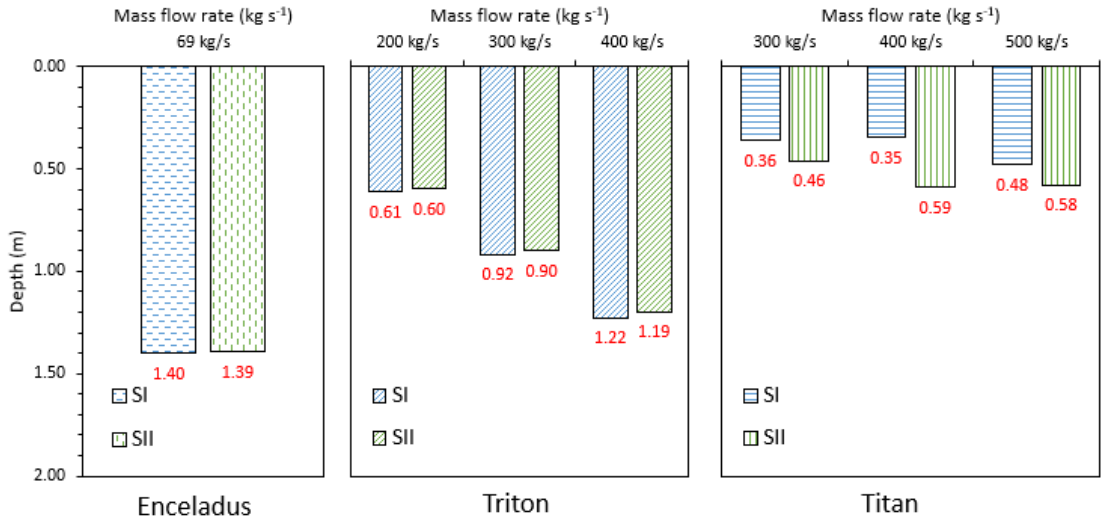

Figure 8.2. Depth (shown in red) at which Mach 1 is reached for selected flow rates for a 5 m diameter conduit. The sound speed where Mach I is achieved is 40 m s^{-1} for both scenario I and II for Enceladus. For Triton, the sound speeds for scenarios I and II are 41 m s^{-1} and 42 m s^{-1} respectively, and for Titan, the sound speeds for scenarios I and II are 33 m s^{-1} and 32 m s^{-1} respectively.

The viscosity of the cryomagma is dependent on the cryomagma composition, volatile content and temperature. However, as a boundary condition for the Xenolith II model,

the temperature is not factored into the calculation for the viscosity (equation 3.13). Generally, high viscosity cryolava flows slowly, typically covering relatively small areas, whereas low viscosity cryomagmas flow more rapidly and form flows that cover much larger areas. The results for Enceladus and Triton show that cryomagma has a very low viscosity at the surface (9.33 µPa·s and 9.48 µPa·s respectively). The results for Titan, however, show that the viscosity of the flow at the surface is very high for each cryomagma composition modelled (1,265.67 µPa·s and 2,576.11 µPa·s). The reason for these significantly higher values relates (equation 3.12) to the different molecular masses of the cryolava on Enceladus and Triton (H_2O) and Titan (Scenario I = 10.6 wt% $(NH_4)2SO_4$-H_2O and Scenario II = 40.0 wt% $(NH_4)2SO_4$-H_2O). The molecular mass of the cryolava for H_2O is 18.016 (Enceladus and Triton), whereas the molecular mass of the two cryolavas modelled on Titan is 1418.694 and 5303.5961 respectively (Scenarios I and II). Additionally, the viscosity of H_2O (liquid) and H_2O (vapour) on Enceladus and Triton is 1791.1 and 8.9458 µPa·s respectively, compared to 2160 and 6120 µPa·s for Scenario I and II on Titan (respectively).

To compare the flow of different cryomagmas on different planetary bodies, Kargel et al. (1991) developed a 'mobility index' where density, viscosity, and the acceleration due to surface gravity are combined in the relation Log_{10} (ρg/µ). According to these authors, liquids with the same mobility index should behave in similar rheological ways and thus a first-order gravity scaling of cryomagmas (Enceladus, Triton and Titan) is compared to gravity-scaled rheological analogs of three terrestrial lavas (Komatiite, Basalt and Rhyolite) and water in figure 8.3. Silicate lava and liquid water are not plausible on icy satellites but are included as a frame of reference. Figure 8.3 illustrates that the mobility

indices of Titan SI and SII cryomagmas are comparable to water on Earth and both are ~3 times 'runnier' than most fluid lava (komatiite) on Earth. The cryomagmas produced on Enceladus and Triton are ~ 5 times more runny than komatiite on Earth and ~2.5 times that of the cryomagmas produced for both scenarios I and II on Titan. Although variations in surface gravity are an important variable factor in determining how fluid a cryomagma is (and the extent to which surface morphologies are formed from flow), the cryolava composition is a far more important factor.

Table 8.1 shows the cryomagma composition and volatile contents for each model scenario. Since the temperature is not considered in the determination of the viscosity, the differences in the cryomagma composition and volatile content are responsible for the variances observed in the result. Enceladus and Triton are modelled with approximately the same cryomagma composition (pure H_2O, or 3.5% NaCl and H_2O), whereas Titan has cryomagma compositions of 10.6%$(NH_4)_2SO_4$-H_2O and 40.0%$(NH_4)_2SO_4$-H_2O, for scenarios I and II respectively. The method for determining the viscosity includes summing the partial viscosities of the components in the cryomagma, which are related to the molecular mass of the cryomagma compositions for Enceladus and Triton, and Titan, which varies considerably since the modelled cryomagma composition is not pure or saline H_2O. Results show a significant difference in the viscosity of the cryolava at the surface for Titan's scenario I and II, where scenario II is more than double that of scenario I. Both viscosities are high though, implying that cryolava flow will be slow, covering a small area. It is also plausible though, that the highly viscous cryolava could block a conduit vent, allowing gas pressure to build up, and result in a powerful eruption. The calculated viscosity is used in determining the Reynolds number (used to predict the transition from laminar to turbulent flow) for each

mass flow rate and conduit size, and incorporates the bulk density of the cryomagma. Tables 4.6 (Enceladus), 5.7 (Triton) and 6.6 (Titan) show the modelled Reynolds numbers at critical deaths from the start of the N_2 exsolution for each modelled scenario, where all the flows are determined to be turbulent at the surface (Reynolds > 4000).

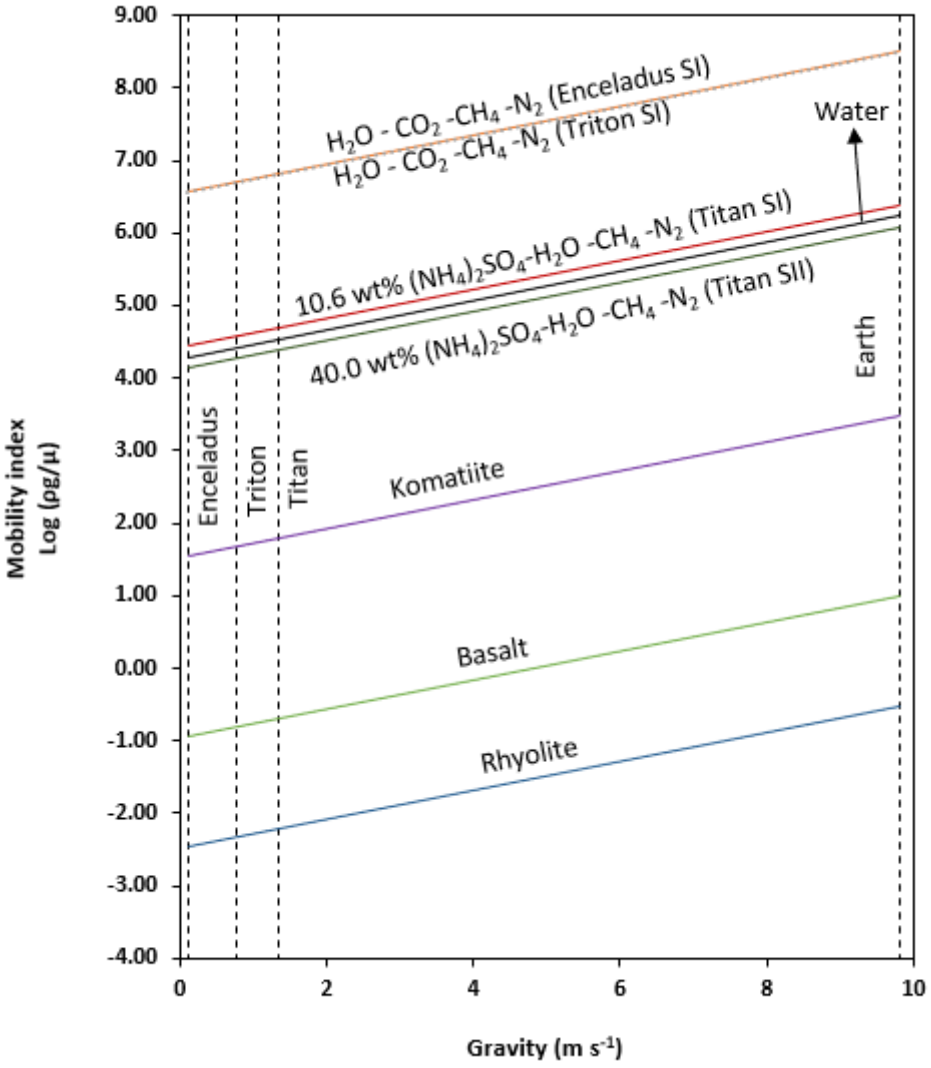

Figure 8.3. Mobility indices of silicate and cryomagma liquids plotted against surface gravity showing the relative differences (after Kargel et al., 1991). The viscosity of Rhyolite = 10^4 Pa. s (Wilson et al., 1980), Basalt = 300 Pa. s (Pinkerton et al., 2002), and Komatiite = 1 Pa. s (Arndt and Lesher, 2016).

The plume height is related to the surface gravity, and eruption velocity for each conduit, although this changes significantly at the point that the eruption column

reaches the surface (as discussed above). However, using a 5 m diameter circular conduit again as an example, with velocities just below the surface, the predicted heights of the plumes for each of the scenarios are tabulated in table 8.3. The calculated velocity of the plumes from the 5 m diameter conduit from Enceladus is at least 2.5 times the escape velocity of 240 m s^{-1} (Teolis et al., 2017). The predicted velocities of all the other conduits (and fissures) exceed the escape velocity at the surface (figure 4.8). These results confirm that the plumes on Enceladus are a plausible source feeding Saturn's E-ring.

Table 8.3. Predicted heights of plumes from a 5 m diameter conduit for each cryomagma composition and volatile content scenario just below the surface, at a pressure of 9 Pa.

Enceladus				Triton				Titan			
Scenario	Mass flow rate (kg s^{-1})	Velocity (m s^{-1})	Height (km)	Scenario	Mass flow rate (kg s^{-1})	Velocity (m s^{-1})	Height (km)	Scenario	Mass flow rate (kg s^{-1})	Velocity (m s^{-1})	Height (km)
I	69	697	2,150	I	200	2,044	1.31	I	300	1917	0.71
-	-	-	-		300	3,065	1.96		400	2556	0.94
-	-	-	-		400	4,087	2.62		500	3195	1.18
II	69	629	2,162	II	200	2,026	1.30	II	300	1786	0.66
-	-	-	-		300	3,039	1.95		400	2382	0.88
-	-	-	-		400	4,052	2.60		500	2977	1.10

The predicted heights on the geysers from a 5 m diameter conduit on Triton do not reach the heights observed by Voyager 2 (~8 km). However, at the surface, where the velocity increases significantly, the plume is predicted to reach and exceed the 8 km observed height of the geysers for both scenarios I and II (see figure 5.9). The hypothetical plumes on Titan, are predicted to be between 0.7 km to 1.2 km in height for a 5 m diameter conduit.

For all scenarios, for both Enceladus and Triton, it has been determined that the flow at the surface is low density, low viscosity, turbulent and supersonic (where Mach is greater than 1). Taking the thin atmospheres and low surface gravity of Enceladus and Triton into consideration (0.113 m s^{-1} and 0.78 m s^{-1} respectively), the predicted heights of the eruptions are plausible when compared to observations from spacecraft missions (see evaluation and discussion sections of chapters 4 and 5) . The flow at the surface for both scenarios for Titan has been determined to be low density, turbulent and supersonic, where the viscosity is high. Despite the high viscosity, dense atmosphere and surface gravity (1.354 m s^{-1}) on Titan, the modelled results predict that if the velocity is sufficiently high, buoyant columns from smaller diameter conduits could result (see evaluation and discussion in chapter 6).

On eruption from a vent, cryomagma decompresses directly into the atmosphere. Since the plume temperature is higher than the ambient temperature, surrounding air will become entrained and should lower the plume density. The plume velocity is predicted to also decelerate due to the force of gravity. Thus, the bulk density of the erupting column will vary with height. The surface air density profile for Titan is determined by first calculating the air pressure (P) using the barometric formula (equation 8.1), using the estimated temperatures shown in the temperature profile in figure 1.2 where a negative temperature gradient exists up to an altitude of ~50km:

$$P = P_0 \; exp\left(\frac{Mg}{RT}h\right) \qquad \text{Eq. 8.1}$$

where P_0 is the air pressure at the surface, g, gravitational acceleration, M the molar mass of air on Titan, h, the altitude, R, the universal gas constant and T, the atmospheric

temperature. From this, the air density can be estimated at different altitudes (and different temperatures) assuming ideal gas behaviour, where ρ = PM/RT, and the mean molar mass of the atmosphere at the surface of Titan is 28.6 g mol^{-1}. This results in air density at the surface of 5.37 kg m^{-3}, and 5.56 kg m^{-3} at 1000 m where the maximum predicted height for a scenario I plume with a mass flow rate of 500 kg s^{-1} is 770 m on Titan. The bulk density (β) of the cryomagma erupting at the surface is estimated as follows (after Woods,1988):

$$\frac{1}{\beta} = (1-n)\frac{1}{\sigma} + \frac{nRT}{P} \qquad \text{Eq. 8.2}$$

where n is the gas mass fraction of the plume at the surface, σ is the density of ice (assuming that any solids in the plume are water ice), R is the specific gas constant, T is the temperature of the plume and P is the atmospheric pressure, as determined using equation 8.1. The density of the plumes and atmospheric density are shown in table 8.4. The densities of the plumes (SI and SII) are both significantly smaller than the atmospheric density at the same height and temperature and are therefore positively buoyant with respect to the atmosphere.

Table 8.4. Density of plumes and atmosphere on Titan (scenarios SI and SII) at increasing altitude up to 1000 m.

Altitude (m)	Air density (kg m-^{3})	Atmospheric Pressure (Pa)	Air Temperature (K)	SI Density (kg m^{-3})	SII Density (kg m^{-3})
0	5.37	146.70	94.00	0.8237	0.8294
100	5.33	145.97	93.77	0.8233	0.8289
200	5.40	145.25	93.54	0.8228	0.8285
300	5.43	144.52	93.31	0.8224	0.8281
400	5.45	143.79	93.08	0.8219	0.8276
500	5.47	143.07	92.85	0.8214	0.8272
600	5.49	142.34	92.62	0.8210	0.8268
700	5.51	141.61	92.39	0.8205	0.8263
800	5.53	140.89	92.16	0.8200	0.8259
900	5.54	140.16	91.93	0.8195	0.8254
1000	5.56	139.43	91.70	0.8191	0.8249

8.1.2 Implications of model results and morphological evidence

The evidence for cryovolcanism on Enceladus, Triton and Titan is discussed in detail in chapter 2 (section 2.3). This includes observations of active plumes erupting on Enceladus and Triton, and morphological evidence on all three moons. Explosive activity could produce a variety of geological landforms and dust (ice crystals) although some of these might be difficult to distinguish from those produced by effusive activities.

High resolution images of the south polar region of Enceladus showed an abundance of icy blocks or boulders littering the surface (Porco et al., 2006) within the south polar terrain, but far fewer outside it. There is no clear preferred distribution of boulders with respect to the locations of the geysers (Landry et al., 2014). Although there is likely no single mechanism (impact cratering, tectonic deformation, distribution of lithospheric ice, seismic disturbance and vapour condensation around icy fumaroles) that can fully account for the presence and distribution of the ice boulder distribution, it is possible

that exceptionally vigorous 'plucking' of the conduit walls could result in entrainment of massive lithic blocks (Fortes, 2007, Martens et al., 2015). Martens et al. (2015) derived a method of estimating the plume velocities that would be required to entrain and suspend ice blocks in the geysers. The minimum velocity (V_{min}) required to suspend a spherical ice block of area A_b in the flow is:

$$V_{min} = \sqrt{\frac{2 m_b g_E}{\rho_V C_D A_b}} \qquad \text{Eq. 8.3}$$

Where g_E is the gravitational acceleration on Enceladus and m_b the Mass of the ice block. The drag coefficient (C_D) is 0.5, which is typical for a spherical object in turbulent flow and ρ_V is the density of the vapour pressure P_V at temperature T, which is computed from the ideal gas law ($\rho_V(T) = \frac{P_V}{RT}$). P_V is estimated as a function of temperature using the ideal-gas version of the Clausius-Clapeyron relationship $P_V(T) = p_0 exp\left[\frac{L}{R}\left(\frac{1}{T_0} - \frac{1}{T}\right)\right]$ where p_0 = 611 Pa, T_0 = 273.15 K, L = 2.83 X 10^6 J kg^{-1} (latent heat of the sublimation of water ice, assumed constant) and R = 461 J K^{-1} kg^{-1} (specific gas constant). The minimum velocity was calculated using equation 8.1 at a temperature of 273.15 K (the model plume temperature) for different spherical blocks of ice between 1.5 m and 3.5 m in diameter and plotted showing the velocities obtained in the application of the Xenolith II model to Enceladus. Figure 8.4 shows the results of this comparison, and it can be seen that the calculated velocities from each of conduits C1 to C4 exceed the minimum velocity required to suspend an ice block in the flow.

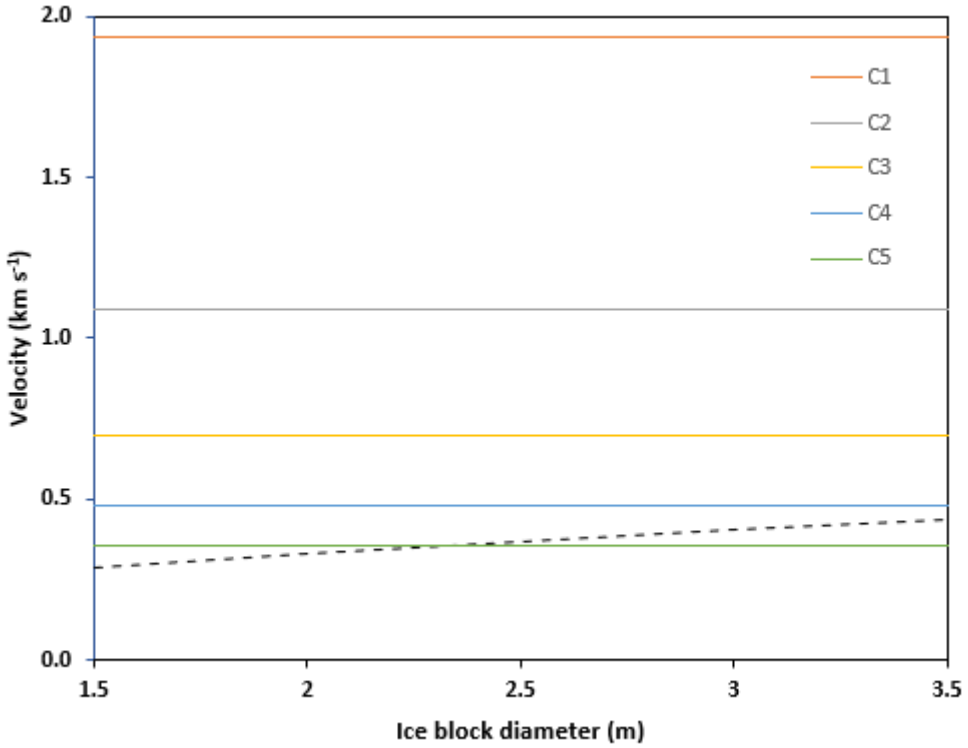

Figure 8.4. The minimum velocity at 273.15 K required to suspend ice blocks of different sizes on Enceladus is shown as a black dashed line. The velocities obtained by the Xenolith II model for conduits C1 to C5 are shown for reference.

Conduit C5 would only be able to suspend blocks smaller than 2.3 m in diameter. It should be noted that some of the sizes of the boulders observed in the SPT of Enceladus approached 180 m in diameter (Landry et al, 2014), and given the diameters of the conduits (between 3 to 7 m) examined in this work, only boulders smaller than modelled conduit diameters were investigated. It is plausible that ejection and ballistic emplacement of smaller ice blocks from the plume eruptions is possible, but as a mechanism for emplacing the largest blocks, other mechanisms would be required.

Analysis of VIMS data in the south polar region of Enceladus indicates that coarse crystalline water ice (order ~100 µm) is most abundant the areas around the tiger

stripes, whereas amorphous ice is more abundant in the south polar regions outside the tiger stripes (Brown et al., 2006; Fortes, 2007). From analysis of Cassini ISS and UVIS data the water vapour to ice ratio in the Enceladus plumes is estimated to be ≈70:30 at altitudes of 15–30 km (Porco et al., 2006; Hansen et al., 2006). It is likely that the plumes become depleted in ice grains at higher altitudes as the larger grains would be ballistically emplaced closest to the vents (Fortes, 2007). Hexagonal ice (Ih) is the most stable form of water below 273.15 K (model plume temperature) so ice in the plume just below the surface would likely be in the crystalline form. Once deposited on the surface, this ice could be amorphized by high energy ions or electrons from Saturn's magnetosphere (Newman et al., 2008). However, in the vicinity of the plumes, the hottest temperatures detected by CIRS were ~145 K or higher (Spencer, 2006), providing strong evidence that crystalline ice would be stable in this region.

The mass flux in the trailing clouds erupted from the plumes on Triton is assumed to consist of fine dark particles suspended in the vapour (Soderblom et al., 1990). It is plausible that the geyser starts out as vapour containing the volatiles (predominantly nitrogen in the Xenolith II model) which condense as it cools and accelerates, since the released latent heat helps to drive the flow. The fraction of the fluid that changes phase is determined by conservation of entropy (Yelle et al., 1991). The dark particles which allow the plume to be visible to observation are likely to be nitrogen and methane frost. Falling back onto the ground, methane frost would over time darken from exposure to radiation, which would explain the numerous observed surface fans. It is also possible the eruptions have sufficient velocity to pick up dust (dark organics on the surface) near the base of the geyser (McKinnon et al 2014). The modelled velocities at the surface are shown in table 5.5 and show that that three of the modelled conduits reach Mach 1 near

the surface, and thus the probability is that an erupting geyser would entrain some particulate matter from the immediate vicinity.

8.1.3. Appraisal of Xenolith II

A number of approximations and estimations were made when constructing the Xenolith II model, and this will inherently result in the accumulation of errors and uncertainty. Although the results of the model implementations have been evaluated according to observations made by spacecraft missions, the outcomes will be only confirmed to a certain degree. Efforts to minimise this this have been made by investigating as wide a range of estimates as possible.

Input parameters and conditions are sourced from the analysis of observations made by space missions, and from these, an attempt has been made to provide an accurate estimate of the physical conditions likely to exist in the interior of Enceladus, Triton and Titan (interior structure, subsurface ocean and cryomagma composition).

Boundary conditions to the model include setting the shape and sizes of the conduits, and treating the cryomagma flow as isothermal. Additionally, the cryomagma and exsolved gases are considered to expand adiabatically, where only the gas phase expands since the liquid phase is considered incompressible.

The current Xenolith II model is constrained by the choices made for volatile content, cryomagma compositions and mass flow rates, which are kept constant. The flow rate is also kept constant in this model, however, at the point that the flow velocity is the same as the sound speed (Mach 1), so-called ‘choking’ occurs, where the flow rate cannot adjust to pressure changes in the conduit. This condition is associated with the development of acoustic shock or discontinuity in gas pressure and density (Bercovici &

Michaut, 2010) which will greatly affect the flow properties (Mitchell, K.L, 2005). The physical phenomena, such as compressibility and nonlinear effects (shock waves for example) should be considered when the flow is supersonic. When the exit velocity is sonic or supersonic, the adjustment to the ambient pressure can be achieved with either an enlargement of the conduit area or through a series of steady shock waves (Giberti & Wilson, 1990). The results show that in most instances of the model implementation, near-surface choking occurs, which would conceivably impact the flow rate.

The model only considers the volatile entrainment of gases exsolved from clathrate dissociation, and does not consider the effects of entrained ice and dust on the plume dynamics, both before erupting at the surface, and after. The rapid transit of low density, low viscosity cryolava containing liquid, vapour and ice crystals up the last few kilometres in a vent will likely generate significant mechanical erosion of the walls, incorporating additional material from the walls into the flow. This process would generate entrained cryoclastic material ranging from small grain sizes to the 'house-sized' blocks as seen in the high resolution images of the south polar region of Enceladus (Porco et al., 2006). The addition of entrained material will also increase the bulk density of the plume which will have an impact on the height of the plume.

Although the mechanism for explosive cryovolcanism is addressed, the calculation of the height of the plumes is simplified and does not take the density of the erupted plume (containing entrained cryoclastic material) into account, nor any other atmospheric conditions into which the plume is erupted (e.g., air density, air temperature, environmental and adiabatic lapse rates). Plume heights are primarily determined by the balance between the thermal energy ejected from the vent and the work done during transport through the atmosphere (Woods, 1998). Pertinent to determining the

thermal energy ejected from the vent are the initial gas content, temperature, velocity and vent radius. The atmospheric density gradient has a strong control on the ascent of the plume since a plume will rise due to buoyancy, except for a region near the vent where the erupted material can be more dense than the atmosphere.

In the case of Enceladus, the volatile component of entrained clathrates was taken to be the same as that of the plume abundances measured by Cassini INMS. Two scenarios were examined though, where the water content of the plume was pure H_2O, and saline (3.5% NaCl).

Voyager 2 could not sample the geysers on Triton, and the ratio of the volatile components of the entrained clathrates in the plumes was therefore assumed to be the same as that of the ratio of volatiles identified on the surface of Triton, although there are conflicting estimates of these in the literature, and thus the model examined two different scenarios.

Similarly, the volatile component of hypothetical cryovolcanic eruptions on Titan was assumed to be the same as the ratio of CH_4 and N_2 detected in the atmosphere near the surface and two separate cryomagma compositions were investigated where (10.6 wt% $(NH_4)_2SO_4$ and 40% wt% $(NH_4)_2SO_4$).

The mass flow rates of the plumes of Enceladus are not well constrained, and even less so on Triton. Cassini data from separate flyby trajectories provided a range of estimates from various workers, and a selection of flow rates was selected and extrapolated from the current literature. Three separate flow rates were estimated for Triton, based on data from current studies. Similarly, three separate flow rates were estimated for Titan. Each of the flow rates selected for each moon were applied to a selection of cryovolcanic

vent sizes and shapes, where circular vents were selected for all, with the addition of fissure shaped vents for Enceladus.

A way of reducing the number of potential model solutions is suggested by a treatment, by Wilson and Head (2017), of explosive eruptions on the Moon in circumstances analogous to those studied here. This method calculates the cryomagma speed, Reynolds number and mass flux for a selection of conduit diameters and does not rely on estimates of different mass flow rates, as is required by the constraints of the Xenolith II model. The Xenolith II model does not include a frictional energy loss term throughout the vertical extent of the conduits modelled, but once a gas phase, rather than a liquid phase, starts to dominate, the term becomes negligible. In a purely liquid phase, the viscosity would dominate in laminar flow, but the results show that there is turbulent flow at all depths, where the friction factor would matter, and this is taken into consideration in the Wilson and Head (2017) method. The Xenolith II model results show that the density and velocity of the cryomagma do not change rapidly with depth for about three quarters of the vertical extent of the conduit. Since the pressure and bulk density in the cryomagma are calculated at all depths in the Xenolith II model, a pressure gradient can be established (after Wilson and Head, 2017), driving the motion of the cryomagma in the deep part of the system, before gas exsolution begins. The pressure gradient driving the fluid upward is due only to the buoyancy of the fluid, proportional to the difference in density between the fluid and the crust. Although this varies with depth, the net differential density is constant since it is assumed that there is no pressure difference between the crust and the cryomagma. The cryomagma speed can be deduced by using a relationship between the pressure gradient, conduit width

and fluid properties, before gas exsolution begins. Appendix V outlines the method used to obtain the pressure gradient in the cryomagma for a circular conduit on Enceladus.

Using the pressure gradient dP/dz, the standard fluid-dynamics equations giving the flow speed, u, in a vertical tube of radius r driven by a pressure gradient dP/dz are

$$u = (r^2 \, \mathrm{d}P/\mathrm{d}z) / (8 \, \eta) \qquad \text{for laminar flow} \qquad \text{Eq. 8.4}$$

and

$$u = [(r \, \mathrm{d}P/\mathrm{d}z) / (f \, r)]^{1/2} \qquad \text{for turbulent flow} \qquad \text{Eq. 8.5}$$

where η is the assumed viscosity of the pure water cryomagma (1.791E-03 Pa·s) and f is a dimensionless friction factor of 0.01, r is the conduit radius and dP/dz is the pressure gradient. The speed is calculated using both equations, for a range of conduit diameters where the smaller speed is adopted (Wilson and Head, 1981). For each speed, the Reynolds number (Re) is calculated:

$$Re = (2 \, r \, u \, \rho) / \eta \qquad \text{Eq. 8.6}$$

where the results of this calculation are checked for consistency: the laminar formula (equation 1) should lead to Re values less than ~1000 and the turbulent formula (equation 2) should lead to values greater than ~1000 (Wilson and Head, 2017). The mass flux is then calculated:

Mass flux = Pi() r^2 u β Eq. 8.7

where r is the conduit radius, u the speed and β, the bulk density. Results of these calculations are tabulated in appendix V, and are shown in figures 8.5 and 8.6.

The Wilson and Head (2017) method can be employed at different depths by varying the viscosity, although the results shown in figures 8.5 and 8.6 are at a depths where the cryomagma is gas free (before exsolution has begun).

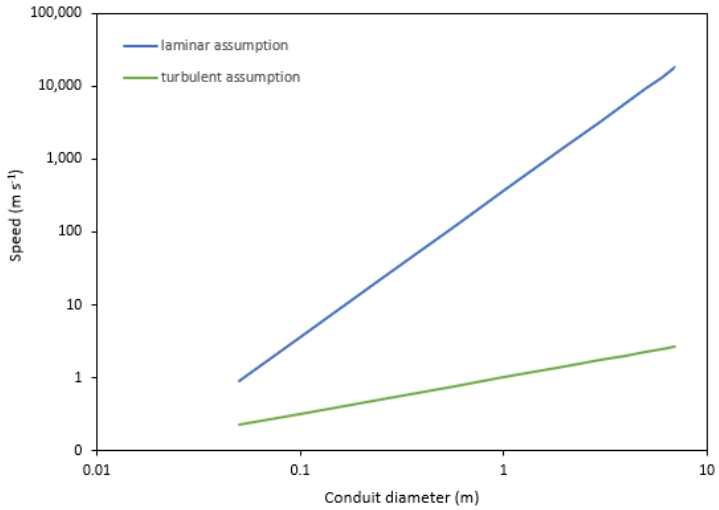

Figure 8.5. Fluid speed in lower conduit as a function of the conduit diameter (after Wilson and Head, 2017) on Enceladus. The pure H_2O cryomagma is assumed to be gas free. The turbulent assumption (equation 8.5) is assumed. Results from the Xenolith II model (for Enceladus) show that all the conduits exhibit turbulent flow after exsolution begins (figure 4.10)

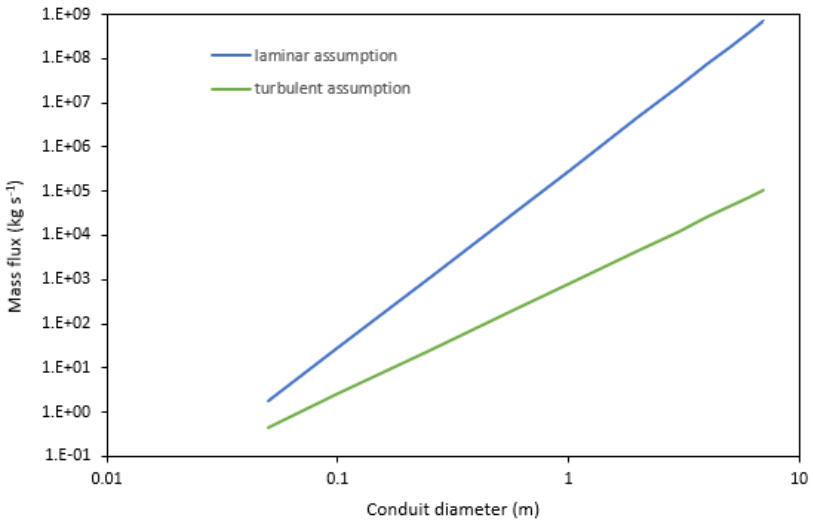

Figure 8.6. Mass flux in lower conduit as a function of the conduit diameter (after Wilson and Head, 2017) on Enceladus. The pure H_2O cryomagma is assumed to be gas free. The turbulent assumption (equation 8.5) is assumed.

8.1.4. Future work

Future work would include adaptations to the current model where possible, addressing some of the issues mentioned in the previous section. The effects of friction from the walls of the cryovolcanic vents would be considered as this would impact the nature of the flow. The effect of and sizes of entrained dust (crystallised particulate matter) in the cryovolcanic plume would be taken into consideration, as would the nature and distance of cryolava flows on the surface.

Although this study was primarily concerned with the mechanism of explosive cryovolcanism, further studies would incorporate the prevailing atmospheric conditions (e.g., density gradient, temperature gradient, environmental and adiabatic lapse rates) and surface conditions (e.g., temperature and pressure) to predict the heights of plumes more accurately. This would be particularly relevant to Titan, which has a dense atmosphere unlike other similarly large planetary bodies, except for Earth and Venus

(Niemann et al., 2005). Titan experiences seasonal changes, with differences in atmospheric temperatures, chemical composition and circular patterns, particularly at the poles (Mitchell et al., 2016; Hörst, 2017; Dhingra et al, 2019). Latitudinal and seasonal variations in temperature profiles and methane mixing ratios were also observed by Cassini on Titan (Hörst, 2017). Triton's atmosphere is layered and has a troposphere, thermosphere and exosphere (Hansen et al., 1990; Ingersoll, 1990) and is thought to experience diurnal, seasonal changes and global warming (e.g., Triton).

The behaviour of cryovolcanic ash clouds in Titan's atmosphere would also be modelled, investigating ash dispersal, the stability of eruption plumes and atmospheric mixing, and whether buoyant plumes could form in cryovolcanic eruptions. This would involve the analysis of Cassini data archived in the NASA Planetary Data System, using the ISIS software package, in order to characterise possible cryovolcanic features on Titan's surface and relate the observations to the modelling effort. Similar modelling has highlighted important difference in the distribution of explosive eruption products between Earth, Venus and Mars. Analysis of flow patterns of cryomagma on the surface would be particularly relevant to Titan, where the determination of the type of eruption (explosive or effusive) might be evaluated from this.

8.1.5. Candidates for future modelling

Candidates for future modelling might include the dwarf planets Ceres and Pluto, and Europa, Jupiter's smallest moon. Evidence has been in found in 2015 by the Dawn mission instruments (framing cameras FC1 and FC2) of possible cryovolcanic activity on Ceres (Occator crater and Ahuna Mons dome). The bright floor material in the basin of Ceres' Occator crater which is estimated to be ~ 6.9 ± 2 million years old, where the

crater itself was formed by an impact event ~ 34 ± 2 million years ago (Nathues et al., 2017). Spectral analysis using the visible and infrared Spectrometer (VIR) onboard Dawn revealed that that the bright spots are predominately carbonates mixed with some dark ammoniated phyllosilicates minerals (Nathues et al., 2017) deposited by cryovolcanic events that occurred some 30 million years after the crater itself formed (figure 8.7). Ahuna Mons is a 4,000 m high mountain on Ceres interpreted as a geologically young cryovolcanic dome (Sori et al., 2017), and marked by numerous bright streaks running down its flank. Spectral analysis has revealed these as being deposits of hydrous minerals, NH_4-phyllosilicates and carbonates (mainly Na-carbonates), left behind from the formation of Ahuna Mons, when plumes of salt water and mud rose and erupted from within Ceres (Zambon et al., 2017). Ceres is thought to be partially differentiated (Park et al., 2016) and possibly contains large amounts of H_2O in the form of an icy mantle and a large liquid reservoir at depth (Castillo-Rogez, 2011). The findings suggest that Ceres has had an active geologic history with cryovolcanic eruptions occurring for an extended period of time (Ruesch et al., 2016; Nathues et al., 2017). Attributing the mechanisms for any cryovolcanic activity to the dissociation of clathrates would require further investigation, but studies of the interior structure by Fu et al. (2017) suggest that the crust of Ceres is composed of at least 30% volume percent of low-density high strength phases consistent with salt and/or clathrate hydrates.

Figure 8.7. Colour mosaic of Occator crater on Ceres in perspective view, obtained at a distance of 1,470 km. The vertical exaggeration of this view is three times. (*image credit: Nathues et al., 2017*).

NASA's New Horizon's mission collected numerous observations of Pluto and several structures on the surface appear to be cryovolcanic in origin (Cruikshank et al., 2021, Singer et al., 2022). Two of these are large mounds with deep central depressions, Wright Mons (~4 km high ~150 km wide, shown in figure 8.8) and Piccard Mons (~6 km high and ~225 km high). Both features have relatively young surfaces with few craters, and it is proposed that some form of cryovolcanism was responsible for building up the crust and creating younger crust (Singer et al., 2016). Pluto is considered to be differentiated with an outer water-ice crust overlaying a rocky core, implying that a level of radiogenic heating could be maintained (Singer et al, 2022). Kamata et al. (2019) have suggested that a thin layer of clathrate hydrates (most likely methane clathrates) at the base of the ice shell acts as a thermal insulator at the top of a subsurface ocean.

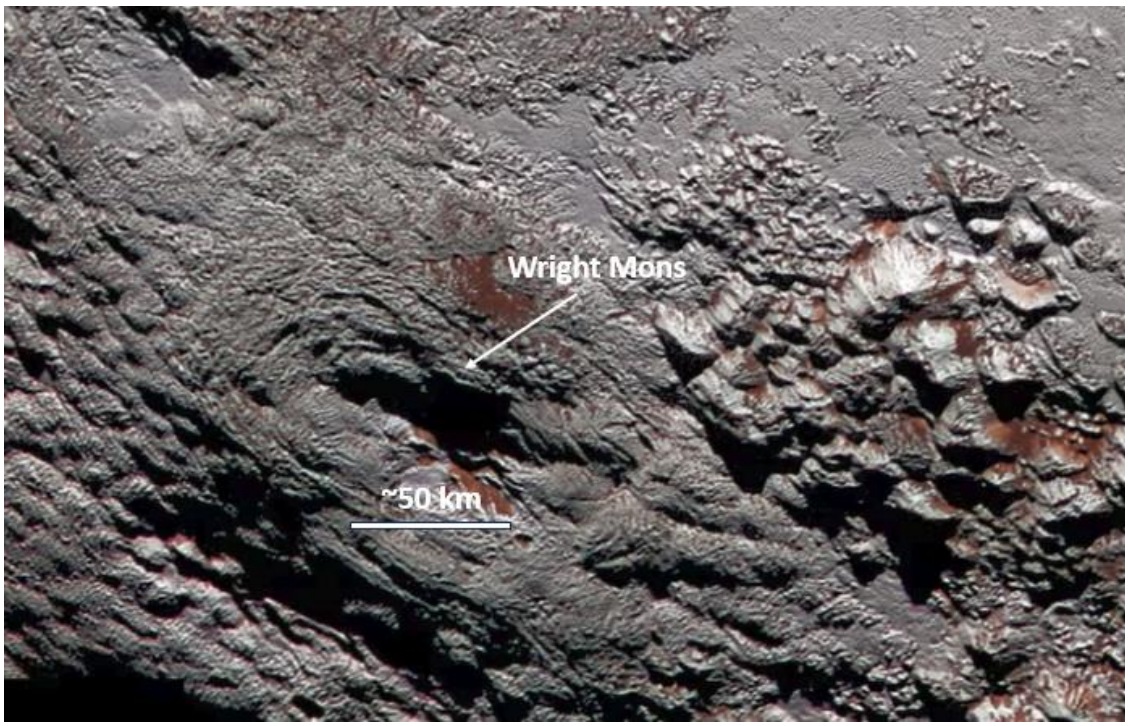

Figure 8.8. Composite image of Wright Mons on Pluto taken by New Horizons (July 2015) from a distance of 48,000 km. (*Image credit: NASA/JHUAPL/SwRI*).

Possible evidence of plumes of water vapour erupting from Europa has previously been found on at least two occasions from observations made by the Hubble Space telescope (figure 8.9). This evidence has been reinforced by thermal anomalies detected by the Galileo Photopolarimeter-radiometer (between 1995 to 2003) seen at the same location of the plumes. This plume activity would indicate that Europa is geologically active in the modern epoch (Sparks et al., 2017). Europa's surface is also considered geologically young (~60-100 Myr) implying that some resurfacing occurs through active cryovolcanism (Hayne et al., 2019). Europa is thought to be differentiated into a metallic core, a silicate mantle and an outer shell of water ice (Jin et al., 2012), and contains a subsurface saltwater ocean (Howell et al., 2020). Prieto-Ballesteros et al. (2005) proposed that clathrates are stable in conditions that exist in the ice shell and subsurface

ocean of Europa. ESA's JUICE mission and NASA's Europa clipper mission will further study these plumes *in-situ* early in 2030 (Huybrighs et al., 2017).

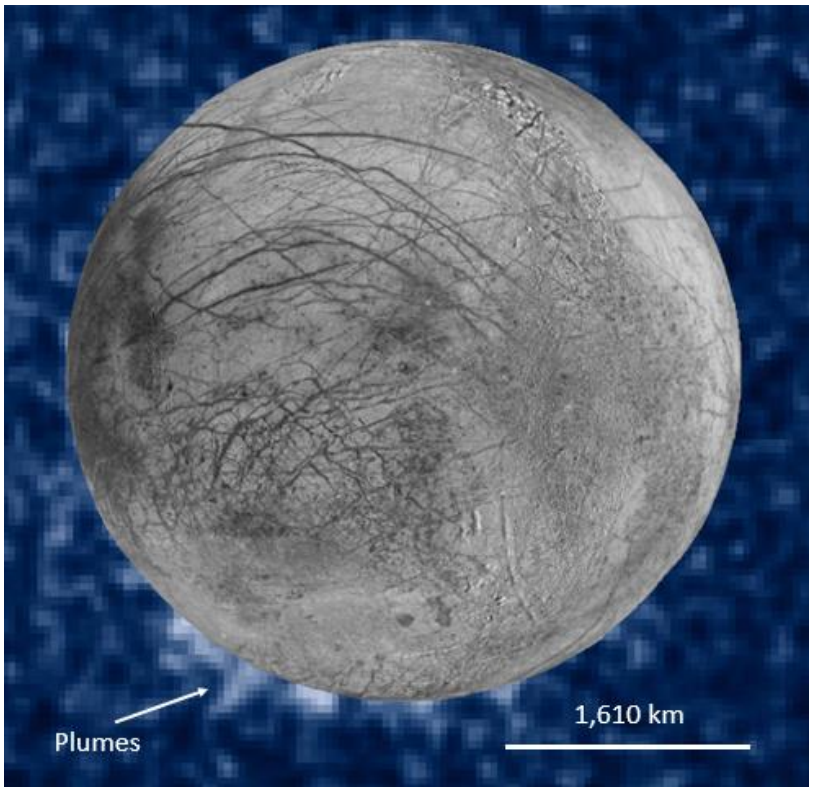

Figure 8.9. Composite image showing suspected plumes of water vapour erupting off the limb of Jupiter's moon Europa. The plumes, photographed by NASA's Hubble's Space Telescope Imaging Spectrograph, were seen in silhouette as the moon passed in front of Jupiter. The image of Europa, superimposed on the Hubble data, is assembled from data from the Galileo and Voyager missions. *(Image credit: NASA/ESA/W. Sparks (STScI)/USGS Astrogeology Science Center).*

8.2. Implications of high pressure methane clathrate phase behaviour

The evidence obtained from high pressure studies of methane clathrate from this work and others (Loveday et al., 2001a, 2001b, 2003; Hirai et al., 2000b, 2001, 2003, 2004) have had important implications for the modelling of Titan. Prior to these high pressure studies, it was thought that methane accreted into Titan's core during its formation, and would have outgassed and risen rapidly to the surface, forming part of the early atmosphere. However, methane persists in Titan's atmosphere and is constantly

replenished despite being lost over a relatively short period through photolysis. High pressure studies have established that methane clathrate can remain stable at high pressure in the sH and sO phases. This implies that Titan's primordial methane reservoir may not have been outgassed early in the satellite's history and is still a plausible source of the continuing replenishment of methane in Titan's atmosphere, despite the irreversible loss of atmospheric methane to photolysis over a relatively short period of time.

By correlating the predictions from interior models of Enceladus, Triton and Titan (chapters 4, 5 and 6) with the outputs obtained from the Xenolith II model, and the results of the high pressure study of methane clathrate in chapter 7, it is possible to obtain the hypothetical depths at which the three methane clathrate structures (sI, sH and sO) could form on each moon. These depths were determined by fitting the third-order Birch-Murnaghan isothermal equation of state (equation 7.2) to the compression data collected along the room temperature isotherm (shown in table 8.5).

Table 8.5. Modelled depths at which clathrates structures sI, sH and sO could form, based on experimentally obtained results.

Experiment observation		Modelled depth at which clathrate structure would form (km)		
CH_4 clathrate structure	Pressure GPa (start)	Enceladus depth (km)	Triton depth (km)	Titan depth (km)
sI	0.182	1,611	249	126
sH	0.87	7,699	1,190	603
sO	1.955	17,301	2,675	1,356

Assuming that clathrates could form in the shells of the Enceladus, Triton and Titan, the pressure (GPa) at the bottom of each shell has been calculated and presented in table 8.6. The predicted depth of each shell is obtained from the interior models of the three

moons (chapters 4, 5 and 6), and the pressure calculated from the Xenolith II model at each depth.

Table 8.6. Table showing the calculated pressures from the Xenolith II model at the bottom of each ice shell where Enceladus is predicted to have a single ice I shell, and Triton, two ice shells (ice I and ice II/III). Titan is predicted to have an ice I shell and an ice VI shell.

	Ice I Shell depth (km)	Pressure (GPa)	Ice II/III Shell depth (km)	Pressure (GPa)	Ice VI shell depth (km)	Pressure (GPa)
Enceladus	82	0.20	-	-	-	-
Triton	252	0.19	402	0.29	-	-
Titan	123	0.18	-	-	524	0.75

From the experimental results (tables 8.4 and 8.5), it is possible to postulate where the different clathrate structures will be stable within each shell, on each moon. In the ice I shell of Enceladus, structure sI would be stable from a hypothetical depth of 1,611 km to the surface, which is clearly not feasible, given that the diameter of the moon is ~504 km and the shell depth is only 83 km. Therefore, the model data and experimental data show that the only likely methane clathrate structure on Enceladus is sI, and that sH and sO phases are unlikely to persist. Similarly, the ice I shell on Triton is likely to contain only structure sI clathrates. Triton's ice II/II shell would also contain methane clathrate sI, where structure sH would only be stable from a depth of ~1,190 km, below the lower depth of the predicted ice II/III shell (where Triton's radius is 1,353 km). Structure sI would be in the stable phase in Titan's ice I shell, and structure sH would be stable in the ice VI shell. This phase would persist until a depth of 1,256 km, where sH would transform to structure sO. This depth is below the estimated lower depth of the ice VI shell as predicted in the Fortes et al (2007) model (figure 6.1) of the internal structure

of Titan. This reinforces the current thinking that Titan's methane is from a primordial source and continues to be a source of replenishment of methane in Titan's atmosphere. It is important to note as well, that the depth limits imposed on the shells are predictions from models. Additionally, temperature is also a factor in the stability of methane hydrate and the Xenolith II model constrains the temperature of the plume to a constant 273.15 K whereas the experiment results were obtained at room temperature (293 K).

The depth and pressure at which dissociation of entrained methane clathrate in the cryomagma begins has been calculated in the application of the Xenolith II model to Enceladus, Triton and Titan. The model examined two separate scenarios for each moon, each with a different volatile content scenarios. This resulted in different depths and pressure at which CH_4 was calculated to begin dissociation within the rising cryomagma (table 8.7). At these depths, methane clathrate phase would be stable as structure sI, before dissociating to gas and ice.

Table 8.7. Results from Xenolith II model showing the depth and pressure at which methane clathrate began dissociation, for each of the modelled cryomagma content scenarios.

	Scenario I		Scenario II		
	Depth (km)	Pressure (GPa)	Depth (Km)	Pressure (GPa)	Source (this work)
Enceladus	8.85	1.0^{-3}	11.50	1.3^{-3}	table 4.4
Triton	0.86	6.3^{-4}	0.38	2.8^{-4}	table 5.4
Titan	0.03	4.0^{-5}	0.33	4.8^{-4}	table 6.3

8.3. Conclusion

Clathrates are thought to be abundant in the outer solar system, where they are likely to be an important constituent in the interiors of icy satellites. During planetary accretion, clathrates may have trapped large quantities of gas directly into protoplanetary condensates and methane clathrate is thought to have been the predominant methane containing phase in the nebula from which Saturn, Uranus, Neptune and their moons formed. For these reasons, and the plausible evidence for active (Enceladus, Triton) and past (and possible current) cryovolcanism (Titan), clathrate dissociation is investigated as a mechanism for driving explosive cryovolcanism on Enceladus, Triton and Titan. The prerequisites for explosive cryovolcanism on icy planetary bodies include the persistence of a subsurface ocean or localized liquid source in the icy mantle, a heat source, a mechanism for bringing cryolava to the surface, a volatile inventory and a mechanism for the opening of a vent to allow for the movement of cryolava to the surface. The extent to which each of the moons examined in this study provide evidence that these prerequisites have been met is discussed in chapters 4, 5 and 6 where the case is made for a subsurface ocean, the volatile inventory and a heat sources for each.

Cassini's instruments have revealed that Enceladus hosts a subsurface ocean, and data from a number of flybys have helped to constrain the composition and the structure of the plumes at low altitudes, as well as making key geophysical measurements over the south polar terrain (including observation of hot spots). It is thought that the vents from which the plumes erupt are able to open and close due to tidal forcing. Although the mass flow rates were estimated in the Xenolith II model, the volatile component of entrained clathrates was taken to be the same as that of the plume abundances

measured by Cassini INMS. It has been proposed that the only way to incorporate these gases in the plume is by the dissociation of clathrate hydrates (Keffer et al., 2006; Fortes et al., 2007). Thus, there is a compelling argument that the decompression dissociation of clathrate hydrates entrained in xenoliths provides a mechanism for generating the explosive icy plumes in the south pole of Enceladus and the results from the Xenolith II model strongly match with the observational data from Cassini. Further mission concepts have been proposed by Spiers et al. (2021) and other workers, designed to constrain the habitability of Enceladus and further investigate the nature of the subsurface ocean.

Voyager 2 did not carry a spectrometer capable of determining Triton's surface composition and although Voyager 2 images provide some observational evidence for the exchange processes between the surface and subsurface, the existence of a subsurface ocean needs to be confirmed as well as a comprehensive spectral mapping of Triton's surface undertaken. The Trident space concept mission, proposed in 2019 would have included instruments to perform magnetic induction measurements to assess the potential existence of an internal ocean (Prockter et al., 2019) and the Neptune Odyssey planetary mission concept (Rymer et al., 2020) proposed a broader and more in depth investigation of Triton. Although neither mission concept was accepted by NASA, there continues to be questions that need answering; whether Triton has a subsurface ocean which is exchanging material with the surface and the compositional nature of the surface. The results of the model as applied to Triton are ambiguous without further data being obtained from future missions to constrain the model inputs. However, dissociation of clathrate hydrates presents a possible explanation for the explosive plumes on Triton, since the some of the results obtained

from a range of different scenarios match the observational evidence of Voyager 2 images.

The nature and existence of candidate cryovolcanic terrains on Titan has been the subject of some controversy which is unlikely to be resolved by Cassini data, mainly due to imagery and spatial coverage limitations. Interpretations are based on morphology in some cases, differences in composition from surrounding terrains as well as temporal variations. Hot spots and thermal activity have not been detected (which could indicate active cryovolcanism), although this in itself does not discount the possibility, since Cassini instruments would need to be observing the right locations at the right time. Current models predict that an aqueous ammonia-rich ocean several tens of kilometres thick exists under the ice shell and the primary heat source supplying thermal energy for cryovolcanic activity is radiogenic heating. The volatile component of the entrained clathrates in the Xenolith II model was assumed to be the same as what was detected in the atmosphere near the surface of the Huygens lander. NASA's Dragonfly mission to Titan (part of the New Frontiers Program), whose robotic rotocraft is slated to arrive in 2034, will take advantage of the dense nitrogen-based atmosphere, and will sample and examine promising sites during its 32 month baseline mission. The primary goal of the mission is to search for chemical biosignatures, investigate the moon's active methane cycle and explore the prebiotic chemistry taken place in the atmosphere and on the surface (Barnes et al., 2021). Although Cassini orbited Saturn for 13 years, the thick atmosphere on Titan made it challenging to reliably identify the materials on its surface. While Cassini's radar was able to penetrate the atmosphere and identify morphologic structures, including potential cryovolcanic terrains and flows, the data could not reveal their composition. Dragonfly will be the first mission to explore the surface of Titan and

identify the detailed composition of its surface, interactions with the surface and atmosphere, and possible material originating from the interior. Since explosive activity becomes possible if cryomagma contains volatile species, and produces craters (calderas), ash cones and ash flows, a future mission to Titan will need to characterize these features in adequate detail, investigating the small-scale morphology of flow units (particularly possible small ash cones and spatter deposits deposits), as well as their composition. These data would constrain the Xenolith II model inputs, and create a more accurate prediction of whether the dissociation of clathrate hydrates provides a mechanism for generating the explosive eruptions. Nevertheless, based on the model parameters selected, the Xenolith II model results suggest that explosive activity could occur as a result of the decompression dissociation of clathrates in cryovolcanic vents on Titan, producing some of the cryovolcanic terrains observed by Cassini radar and acting as a source of the replenishment of methane in the atmosphere.

Modelling of this process has provided further insights into what is likely to occur on all three of these planetary bodies, providing an improvement and extension of the current models by developing a more complete physical model of the process of the clathrate dissociation mechanism that may be involved in explosive cryovolcanism. Together with the high pressure neutron diffraction studies of methane clathrate, a parameter space in which explosive activity can occur on icy moons has been established in this thesis, thus contributing to a firm physical basis for future modelling and observation.

REFERENCES

Abramov, O., Spencer, J.R. (2007). South polar thermal anomaly on Enceladus, modelling and observations. Lunar and Planetary Science, XXXVIII, Abstract 2343.

Adeyemo, A., Kumar, R., Linga, P., Ripmeester, J., Englezos, P. (2010). Capture of carbon dioxide from flue or fuel gas mixtures by clathrate crystallization in a silica gel column. International Journal of Greenhouse Gas Control, 4, 478–485

Agnor, C.B., Hamilton, D.P. (2006). Neptune's capture of its moon Triton in a binary–planet gravitational encounter. Nature Vol 441, 192-194.

Anderson, S.E., Mousis, O., Ronnet, T. (2021). Formation Conditions of Titan's and Enceladus's Building Blocks in Saturn's Circumplanetary Disk. The Planetary Science Journal, 2:50.

Archinal, B. A., Acton, C. H., A'Hearn, M. F., Conrad, A., Consolmagno, G. J., Duxbury, T., Hestroffer, D., Hilton, J. L., Kirk, R. L., Klioner, S. A., McCarthy, D., Meech, K., Oberst, J., Ping, J., Seidelmann, P. K., Tholen, D. J., Thomas, P. C., Williams, I. P. (2018). Report of the IAU Working Group on Cartographic Coordinates and Rotational Elements: 2015. Celestial Mechanics and Dynamical Astronomy volume 130 : 22.

Arndt, N.T, Lesher, C.M. (2016). Igneous Rocks, Komatiite. Reference Module in Earth Systems and Environmental Sciences. ScienceDirect.

Atreya, S.K., Adams, E.Y., Niemann, H.B., Demick-Montelara, J.E., Owen, T.C., Fulchignoni, M., Ferri, F., Wilson, E.H. (2006). Titan's methane cycle. Planetary and Space Science 54, 1177-1187.

Bakker, R.J., Dubessy, J., Cathelineau, M. (1996). Improvements in clathrate modelling I: the H_2O-CO_2 system with various salts. Geochimica Cosmochimica Acta, v. 60, 1657-1681.

Bakker, R.J. (1997). Clathrates: Computer programs to calculate fluid inclusion V-X properties using clathrate melting temperatures. Computers and Geosciences, 23, 1, 1-18.

Bakker, R.J. (1998) Improvements in clathrate modelling II: The H_2O-CO_2-CH_4-N_2-C_2H_6 fluid system. In: Henriet, J.-P. & Mienert, J. (eds) Gas Hydrates: Relevance to World Margin Stability and Climate Change. Geological Society, London, Special Publications, v. 137, 75-105.

Baland, R., Tobie, G., Lefevre, A., Van Hoolst, T. (2014). Titan's internal structure inferred from its gravity field, shape, and rotation state. Icarus, 237, 29–41.

Barnes, J.W., Brown, R.H., Radebaugh, J., Buratti, B.J., Sotin, C., Le Mouelic, S., Rodriguez, S., Turtle, E.P., Perry, J., Clark, R., Baines, K.H., Nicholson, P.D. (2006). Cassini observations of flow-like features in western Tui Regio, Titan. Geophysical Research Letters, VOL. 33, L16204.

Barnes, J.W., Turtle, E.P., Trainer, M.G., Lorenz, R,D., MacKenzie, S.M., Brinckerhoff, W.B., Cable, M.L., Ernst, C.M., Freissinet, C., Hand, K.P., Hayes, A.G., Hörst, S.M., Johnso, J.R., Karkoschka, E., Lawrence, D.J., Le Gall, A., Lora, J.M., McKay, C.P., Miller, R.S., Murchie, S.L., Neish, C.D., Newman, C.E., Núñez, J., Panning, M.P., Parsons, A.M., Peplowski, P.N., Quick, L.C., Radebaugh, J., Rafkin, S.C.R., Shiraishi, H., Soderblom, J.M., Sotzen, K.S., Stickle, A.M., Stofan, E.R., Szopa, C., Tokano, T., Wagner, T., Wilson, C., Yingst, R.A. Zacny, K., Stähler, S.C. (2021). Science Goals and Objectives for the Dragonfly Titan Rotorcraft Relocatable Lander. The Planetary Science Journal, 2:130.

Bauer J.M., Buratti, B.J., Li, J., Mosher, J.A., Hicks, M.D., Schmidt, B.E., Goguen, J.D. (2010). Direct Detection of Seasonal Changes on Triton with Hubble Space Telescope. The Astrophysical Journal Letters, 723: L49-L52.

Bennington, S.M. (2004). The use of neutron scattering in the study of ceramics. Journal of Materials Science. November 2004.

Bercovici, D., Michaut, C. (2010). Two-phase dynamics of volcanic eruptions: compaction, compression and the conditions for choking. Geophys. J. Int. 182, 843–864.

Birch, F. (1952). Elasticity and Constitution of the Earth's Interior. Journal of Geophysical Research, 57, 2, 227-286.

Birch, S.P.D., Hayes, A.G., Dietrich, W.E., Howard, A.D., Bristow, C.S., Malaska, M.J., Moore, J.M., Mastrogiuseppe, M., Hofgartner, J.D., Williams, D.A., White, O.L.,

Soderblom, J.M., Barnes, J.W., Turtle, E.P., Lunine, J.I., Wood, C.A., Neish, C.D., Kirk, R.L., Stofan, E.R., Lorenz, R.D., Lopes, R.M.C. (2017). Geomorphologic mapping of titan's polar terrains: Constraining surface processes and landscape evolution. Icarus 282 214–236.

Birch, S.P.D., Hayes, A.G., Hofgartner, J.D., Lunine, J.I., Malaska, M.J., Wall, S., Lopes, R.M.C., White, O. (2019). Geophysical Research Letters. 46, 5846–5854.

Bouchafaa W., Dalmazzone' D. (2011). Thermodynamic equilibrium data for mixed hydrates of CO_2-N_2, CO_2-CH_4 and CO_2-H_2 in pure water and TBAB solutions. Proceedings of the 7th International Conference on Gas Hydrates (ICGH 2011).

Brilliantov, N.V., Schmidt, J., Spahn, F. (2008). Geysers of Enceladus: Quantitative analysis of qualitative models. Planetary and Space Science, 56, 1596–1606.

Broadfoot A.L., Atreya, S.K., Bertaux, J.L., Blamont, J.E., Dessler, A.J., Donahue, T.M., Forrester, W.T., Hall, D.T., Herbert, F., Holberg, J.B., Hunten, D.M., Krasnopolsky, V.A., Linick, S., Lunine, J.I., McConnell, J.C., Moos, H.W., Sandel, B.R., Schneider, N.M., Shemansky, D.E., Smith, G.R., Strobel, D.F., Yelle, R.V. (1989). Ultraviolet Spectrometer Observations of Neptune and Triton. Science, 246, 1459-1466.

Brown R.H., Kirk, R.L., Johnson, T.V., Soderblom, L.A. (1990). Energy Sources for Triton's Geyser-Like Plumes. Science, New Series, 250, 4979, 431-435

Brown R.H., Cruikshank, D.P. (1997). Determination of the Composition and State of Icy Surfaces in the Outer Solar System. Annual Review of Earth and Planetary Sciences, 25: 243-277.

Brown R.H., Clark, R.N., Buratti, B.J., Cruikshank, D.P., Barnes, J.W., Mastrapa, R.M.E., Bauer, J., Newman, S., Momary, T., Baines, K. H., Bellucci, G., Capaccioni, F., Cerroni, P., Combes, M., Coradini, A., Drossart, P., Formisano, V., Jaumann, R., Langevin, Y., Matson, D.L., McCord, T.B., Nelson, R.M., Nicholson, P.D., Sicardy, B., Sotin, C. (2006). Composition and Physical Properties of Enceladus' Surface. Science, 311, 1425-1428.

Bruusgaard, H., Beltrán, J.G., Servio, P. (2008). Vapor-Liquid Water-Hydrate Equilibrium Data for the System N_2 + CO_2 + H_2O. Journal of Chemical Engineering Data, 53, 2594- 2597.

Bull, C.L., Funnell, N.P., Tucker, M.G., Hull, S., Francis, D.J., Marshall, W.G. (2016). PEARL: the high pressure neutron powder diffractometer at ISIS. HIGH PRESSURE RESEARCH, 36, 4, 493-511.

Buratti, B.J., Bauer, J.M., Hicks, M.D., Mosher, J.A., Filacchione, G., Momary, T., Baines, K.H., Brown, R.H., Clark, R.N., Nicholson, P.D. (2010). Cassini spectra and photometry 0.25-5.1 μm of the small inner satellites of Saturn. Icarus 206, 524-536.

Buratti, B.J., Bauer, J.M., Hicks, M.D., Hillier, J.K., Verbiscer, A., Hammel, H., Schmidt, B., Cobb, B., Herbert, B., Garsky, M., Ward, J., Foust, J. (2011). Photometry of Triton 1992-2004: Surface volatile transport and discovery of a remarkable opposition surge. Icarus, 212, 835-847.

Burgdorf, M., Cruikshank, D. P., Dalle Ore, C. M., Sekiguchi, T., Nakamura, R., Orton, G., Quirico, E., Schmitt, B. (2010). A Tentative Identification of JCN Ice on Triton. The Astrophysical Journal Letters, 718, L53-L57.

Burger M.H., Sittler Jr, E.C., Johnson, R.E., Smith, H.T., Tucker, O.J., Shematovich, V.I. (2007). Understanding the escape water from Enceladus. Journal of Geophysical Research, 112, A06219.

Castillo-Rogez, J.C. (2011). Ceres – Neither a porous nor salty ball. Icarus 215 599–602.

Chazallon, B., Kuhs, W.F. (2002). *In situ* structural properties of and air-clathrates by neutron diffraction. J. Chem. Phys. 117, 308–320

Choblet G., Tobie G., Sotin C., Běhounková M., Čadek O., Postberg F. and Souček O. (2017). Powering prolonged hydrothermal activity inside Enceladus. Nat Astron 1, 841–847.

Choukroun, M., Morizet, Y., Grasset, O. (2007). Raman study of methane clathrate hydrates under pressure: new evidence for the metastability of structure II. Journal of Raman Spectroscopy, 38, 440-451.

Conrath, B., Flasar, F.M., Hanel, R., Kunde, V., Maguire, W., Pearl, J., Pirraglia, J., Samuelson, R., Gierasch, P., Weir, A., Bezard, B., Gautier, D., Cruikshank, D., Horn, L., Springer, R., Shaffer, W. (1989). Infrared Observations of the Neptunian System. Science, New Series, 246, 4936, 1454-1459.

Coradini A., Magni, G., Turrini, D. (2010). From Gas to Satellitesimals: Disk Formation. Space Science Review. 153, 411-429.

Coustenis, A. (2005). Formation and Evolution of Titan's Atmosphere. Space Science Reviews 116: 171–184.

Coustenis, A., Taylor, F.W. (2008). Titan: Exploring an Earthlike World (2nd Edition). World Scientific Publishing, Singapore.

Cruikshank D.P., Brown, R.H., Clark, R.N. (1984). Nitrogen on Triton. Icarus, 58, 293-305.

Cruikshank D.P., Apt, J. (1984). Methane on Triton: Physical State and Distribution. Icarus, 58, 306-311.

Cruikshank D.P., Brown, R.H., Tokunaga, A.T., Smith, R.G., Piscitelli, J.R. (1988). Volatiles on Triton: The Infrared Spectral Evidence, 2.0-2.5/μm. Icarus, 74, 413-423.

Cruikshank D.P., Roush, T.L., Owen, T.C., Geballe, T.R., de Bergh, C., Schmitt, B., Brown, R.H., Bartholomew, M.J. (1993). Ices on the Surface of Triton. Science, 261, 742-745.

Cruikshank D.P., Schmitt, B., Roush, T.L., Owen, T.C., Quirico, E., Geballe, T.R., de Bergh, C., Bartholomew, M.J., Dalle Ore, C.M., Douté, S., Meier, R. (2000). Water Ice on Triton. Icarus 147, 309-316.

Cruikshank, D.P. (2005). Triton, Pluto, Centaurs and Trans-Neptunian Bodies. Space Science Reviews, 116, 421-439.

Cruikshank, D.P., Dalle Ore, C.M., Scipioni, F., Beyer, R.A., White, O.L., Moore, J.M., Grundy, W.M., Schmitt, B., Runyon, K.D., Keane, J.T., Robbins, S.J., Stern, S.A., Bertrand, T., Beddingfield, C.B., Olkin, C.B., Young, L.A.,Weaver, H.A., Ennico, K. (2021). Cryovolcanic flooding in Viking Terra on Pluto. Icarus 356, 1-9

Czechowski L., Kossacki, K. (2009). Thermal convection in the porous methane-soaked regolith of Titan: Investigation of stability. Icarus 202, 599-606.

Dalton J.B. (2010). Spectroscopy of Icy Moon Surface Materials. Space Science Review, 153, 219-241. Davidson, T.A. (1993). A Simple and Accurate Method for Calculating Viscosity of Gaseous Mixtures. United States Bureau of Mines, Report of Investigations 9456.

DeMeo, F.E., Dumas, C., de Bergh, C., Protopapa, S., Cruikshank, D.P., Geballe, T.R., Alvarez-Candal, A., Merlin, F., Barucci, M. (2010). A search for ethane on Pluton and Triton. Icarus, 208, 412-424.

Dhingra, R.D., Barnes, J.W., Brown, R.H., Burrati, B.J., Sotin, C., Nicholson, P.D., Baines, K.H., Clark, R.N., Soderblom, J.M., Jauman, R., Rodriguez, S., Le Mouélic, S., Turtle, E.P., Perry, J.E., Cottini, V., Jennings, D.E. (2019). Observational Evidence for Summer Rainfall at Titan's North Pole. Geophysical Research Letters, 46, 1205–1212.

Dong Y., Hill, T.W., Teolis, B.D., Magee, B.A., Waite, J.H. (2011). The water vapor plumes of Enceladus. Journal of Geophysical Research, 116, A10204.

Dougherty, M.K., Khurana, K.K., Neubauer, F.M., Russell, C.T., Saur, J., Leisner, J.S., Burton, M.E. (2006). Identification of a Dynamic Atmosphere at Enceladus with the Cassini Magnetometer. Science. Vol 311.

Dougherty, M.K., Waite, J.H., Esposito, L.W., Helfenstein, P., Ingersoll, A.P., Jaumann, R., McKay, C.P., Nimmo, F. (2009). Saturn from Cassini-Huygens (eds). Chapter 21, Enceladus: An Active Cryovolcanic Satellite. DOI 10.1007/978-1-4020-9217-6_21.

Dorofeeva, V. A., Ruskol, E. L. (2010). On the Thermal History of Saturn's Satellites Titan and Enceladus. Solar System Research, Vol. 44, No. 3, pp. 192–201.

Duan, Z., Møller, N., Weare, J.H. (1996). A general equation of state for supercritical fluid mixtures and molecular dynamics simulation of mixture PVTX properties. Geochimica et Cosmochimica Acta, Vol. 60, No. 7, pp. 1209-1216.

Duan, Z.H., Sun, R. (2003). An improved model calculating CO_2 solubility in pure water and aqueous NaCl solutions from 273 to 533 K and from 0 to 2000 bar. Chemical Geology. 193, 257-271.

Duan, Z., Mao, S. (2006). A thermodynamic model for calculating methane solubility, density and gas phase composition of methane-bearing aqueous fluids from 273 to 523 K and from 1 to 2000 bar. Geochimica et Cosmochimica Acta, 70, 3369-3386.

Duxbury, N.S., Brown, R.H. (1997). The Role of Internal Heat Source for the Eruptive Plumes of Triton. Icarus, 125, 83-93.

Dyadin, Y.A., Aladko, E Y., Larionov, E.G. (1997). Decomposition of methane hydrates up to 15 kbar. Mendeleev Communications, 7(1), 34-35.

Elachi, C., Wall, S., Allison, M., Anderson, Y., Boehmer, R., Callahan, R., Encrenaz, P., Flamini, E., Franceschetti, G., Gim, Y., Hamilton, G., Hensley, S., Janssen, M., Johnson, W., Kelleher, K., Kirk, R., Lopes, R., Lorenz, R., Lunine, J., Muhleman, D., Ostro, S., Paganelli, F., Picardi, G., Posa, F., Roth, L., Seu, R., Shaffer, S., Soderblom, L., Stiles, B., Stofan, E., Vetrella, S., West, R., Wood, C., Wye, L., Zebker, H. (2005). Cassini Radar Views the Surface of Titan. Science, 308, 970-974.

Elliot, J.L., Hammel, H.B., Wasserman, L.H., Franz, O.G., McDonald, S.W., Person, M.J., Olkin, C.B., Dunham, E.W., Spencer, J.R., Stansberry, J.A., Buie, M.W., Pasachoff, J.M., Babcock, B.A., McConnochie, T.H. (1998). Global warming on Triton. Nature, 393, 765-767.

Elliot, J.L., Strobel. D.F., Zhu, X., Stansberry, J.A., Wasserman, L.H., Franz, O.G. (2000). The Thermal Structure of Triton's Middle Atmosphere. Icarus, 143, 425-428.

Eslamimanesh, A., Babaee, S., Gharagheizi, F., Javanmardi, J., Mohammadi, A.H., Richon, D. (2013). Assessment of clathrate hydrate phase equilibrium data for CO2 + CH4/N2 + water system. Fluid Phase Equilibria, 349, 71– 82

Fortes A.D. (2007). Metasomatic clathrate xenoliths as a possible source for south polar plumes of Enceladus. Icarus 191, 743-748.

Fortes A.D., Wood, I. G., Alfredsson, M., Vočadlo, L., Knight, K. S., Marshall, W. G., Tucker, M. G., Fernandez-Alonso, F. (2007b). The high-pressure phase diagram of ammonia dihydrate. High Pressure Research, 27 (2), 201-212.

Fortes, A.D., Grindrod, P.M., Trickett, S.K., Vočadlo, L. (2007). Ammonium sulphate on Titan: Possible origin and role in cryovolcanism. Icarus 188, 139-153.

Fortes, A.D., Choukroun, M. (2010). Phase behaviour of Ices and Hydrates. Space Science Review, 153, 185-218.

Fortes, A.D. (2012). Titan's internal structure and the evolutionary consequences. Planetary and Space Science 60, 10–17.

Fu, R.R., Ermakov, A.I., Marchi, S., Castillo-Rogez, J.C., Raymond, C.A., Hager, B.H., Zuber, M.T., King, S.D., Bland, M.T., De Sanctis, M.C., Preusker, F., Park, R.S., Russell, C.T., (2017). The interior structure of Ceres as revealed by surface topography. Earth and Planetary Science Letters 476, 153–164.

Fulchignoni, M., Ferri, F., Angrilli, F., Ball, A. J., Bar-Nun, A., Barucci, M.A., Bettanini, C., Bianchini, G., Borucki, W., Colombatti, G., Coradini, M., Coustenis, A., Debei, S., Falkner, P., Fanti, G., Flamini, E., Gaborit, V., Grard, R., M. Hamelin, M., Harri, A.M., Hathi, B., Jernej, I., Leese, M.R., Lehto, A., Lion Stoppato, P.F., López-Moreno, J.J., Mäkinen, T., McDonnell, J.A.M., McKay, C.P., Molina-Cuberos, G., Neubauer, F.M., Pirronello, V., Rodrigo, R., Saggin, B., Schwingenschuh, K., Seiff, A., Simões, F., Svedhem, H., Tokano, T., Towner, M.C., Trautner, R., Withers, P., Zarnecki, J.C. (2006). In situ measurements of the physical characteristics of Titan's environment. Nature 04314.

Gaeman, J., Hier-Majumder, S., Roberts, J.H. (2012). Sustainability of a subsurface ocean within Triton's interior. Icarus 220, 339–347.

Gautier, D., Hersant., F. (2005). FORMATION AND COMPOSITION OF PLANETESIMALS. Space Science Reviews 116: 25–52.

Geissler, P. (2015). Encyclopedia of Volcanoes: Cryovolcanism in the Outer solar System. Elsevier Inc. Chapter 44, 763-776.

Giauque, W.F., Stout, J.W. (1936). The Entropy of Water and the Third Law of Thermodynamics. The Heat Capacity of Ice from 15 to 273 K. Chemical Laboratory of the University of California, Vol 58, 1145 – 1150.

Giberti, G. & Wilson, L. (1990) The influence of geometry on the ascent of magma in open fissures. Bulletin of Volcanology 52 (7), 515-521.

Glein, C.R., Baross, J.A., Waite Jr., J.H. (2015). The pH of Enceladus' ocean. Geochimica et Cosmochimica Acta, 162,202-219.

Glein, C.R., Waite Jr., J.H. (2020). The carbonate geochemistry of Enceladus' ocean. Geophysical Research Letters, *47*, e2019GL085885

Goguen, J.D., Buratti, B.J., Brown, R.H., Clark, R.N., Nicholson, P.D., Hedman, M.M., Howell, R.R., Sotin, C., Cruikshank, D.P., Baines, K.H., Lawrence, K.J., Spencer, J.R., Blackburn, D.G. (2013). The temperature and width of an active fissure on

Enceladus measured with Cassini VIMS during the 14 April 2012 South Pole flyover. Icarus, 226, 1128-1137.

Goldstein, D.B., Hedman, M., Manga, M., Perry, M., Spitale, J., Teolis, B. (2018). Enceladus Plume Dynamics: From Surface to Space. In Enceladus and the Icy Moons of Saturn (P. M. Schenk et al., eds.), 175–194.

Gonnermann, H.M. (2015). Magma Fragmentation. Annu. Rev. Earth Planet. Sci., 43:431–58

Grasset, O., Sotin, C. (1996). The Cooling Rate of a Liquid Shell in Titan's Interior. Icarus, 123, 101–112.

Grasset, O., Sotin, C., Deschamps, F. (2000). On the internal structure and dynamics of Titan. Planetary and Space Science 48 617-636.

Gordon, S., McBride, B.J. (1994). Computer Program for the Calculation of Complex Chemical Equilibrium Compositions with Applications; I. Analysis. NASA Reference Publication 1311.

Grindrod, P.M., Fortes, A.D., Nimmo, F., Feltham, D.L., Brodholt, J.P., Vočadlo, L. (2008). The long-term stability of a possible aqueous ammonium sulfate ocean inside Titan. Icarus, 197, 137–151.

Grundy, W.M., Young, L.A., Stansberry, J.A., Buie, M.W., Olkin, C.B., Young, E.F. (2010). Near-infrared spectral monitoring of Triton with IRTF/SpeX II: Spatial distribution and evolution of ices. Icarus, 2005, 594-604.

Halevy I., Stewart, S.T. (2008a). A Non-equilibrium hydrate dissociation model and applications to Enceladus' plume. Lunar Planetary Science XXXIX. Abstract 1174.

Halevy I., Stewart, S.T. (2008b). Is Enceladus' plume tidally controlled? Geophysical Research Letters, VOL. 35, L12203,

Hammond, N.P., Parmentier, E.M., Mlinar., A.B. (2018). Compaction and Melt Transport in Ammonia-Rich Ice Shells: Implications for the Evolution of Triton: ICE AMMONIA OCEAN EVOLUTION. The Journal of Geophysical Research Planets. 123(7090).

Hansen, C.J., McEwan, A.S., Ingersoll, A.P., Terrile, R.J. (1990). Surface and Airborne Evidence for Plumes and Winds on Triton. Science, 250, 4979, 421-424.

Hansen, C. J., Esposito, L., Stewart, A.I.F., Colwell, J., Hendrix, A., Pryor, W., Shemansky, D., West, R. (2006). Enceladus' water vapour plume. Science 311, 1422-1425.

Hansen, C. J., Shemansky, D.E., Esposito, L.W., Stewart, A.I.F., Lewis, B.R., Colwell, J.E., Hendrix, A.R., West, R.A., Waite Jr., J.H., Teolis, B., Magee, B.A. (2011). The composition and structure of the Enceladus plume. Geophysical Research Letters, 38, L11202, 1-5.

Hansen, C.J. , Castillo-Rogez, J., Grundy, W., Hofgartner, J.D., Martin, E.S., Mitchell, K., F. Nimmo, F., Nordheim, T. A., Paty, C., Quick, L. C., Roberts, J. H. , Runyon, K., Schenk, P., Stern, A., Umran, O. (2021). Triton: Fascinating Moon, Likely Ocean World, Compelling Destination! The Planetary Science Journal, 2:137, 1-12.

Hay, H.C.F.C., Matsuyama, I. (2017). Numerically modelling tidal dissipation with bottom drag in the oceans of Titan and Enceladus. Icarus, 281, 342 – 356.

Hayes, A.G. (2016). The Lakes and Seas of Titan. Annu. Rev. Earth Planet. Sci. 44:57–83. 10.1146/annurev-earth-060115-012247

Haynes, W.M. (Ed.), 2011. CRC Handbook of Chemistry and Physics. 92nd ed. CRC Press/Taylor & Francis Group, Boca Raton.

Hayne, P.O. (2019). Modeling Thermal Signatures of Active Regions and Plumes on Europa. EPSC Abstracts Vol. 13, EPSC-DPS2019-1186-2,

Hazen, R.M., Mao, H.K., Finger, L.W., Bell, P.M. (1980). Structure and compression of crystalline methane at high pressure and room temperature. Applied Physics Letters, 37, 288-289.

Head, J.W., Wilson, L. (2003). Deep submarine pyroclastic eruptions: Theory and predicted landforms and deposits. Journal of Volcanology and Geothermal Research, 121, 155-193.

Hedman, M.M., Gosmeyer, C.M., Nicholson, P.D., Sotin, C., Brown, R.H., Clark, R.N., Baines, K.H., Buratti, B.J., Showalter, M.R. (2013). An observed correlation between plume activity and tidal stresses on Enceladus. Nature, 500, 182-184.

Helfenstein, P., Porco, C.C. (2015). Enceladus' geysers: relation to geological features. The Astronomical Journal, 150, 96, 1-33.

Herning, E., Zipperer, L. (1936). Calculation of the Viscosity of Technical Gas Mixtures from the Viscosity of the Individual Gases. Gas-und Wasserfach, v. 79, 69-73.

Hillier, J., Helfenstein, P., Verbiscer, A., Veverka, J., Brown, R.H., Goguen, J., Johnson, T.V. (1990). Voyager Disk-Integrated Photometry of Triton. Science, 250, 4979, 419-421.

Hiraga, Y., Sasagawa, T., Yamamoto, S., Komatsu, H., Ota., M., Tsukada. T., Smith. R.L. (2020). A precise deconvolution method to derive methane hydrate cage occupancy ratios using Raman spectroscopy. Chemical Engineering Science, 214, 115361

Hirai, H., Hasegawa, H., Yagi, T., Yamamoto, Y., Nagashima, K., Sakashita, M., Aoki, K., Kikegawa, T., (2000a). Methane hydrate, amoeba or a sponge made of water molecules. Chemical Physics Letters, 325, 490-498.

Hirai, H., Kondo, T., Hasegawa, M., Yagi, T., Yamamoto, Y., Komai, T., Nagashima, K., Sakashita, M., Fujihisa, H., Aoki, K. (2000b). Methane Hydrate Behavior under High Pressure. Journal of Physical Chemistry B, 104, 1429-1433.

Hirai, H., Uchihara, Y., Fujihisa, H., Sakashita, M., Katoh, E., K. Aoki, K., Nagashima, K., Yamamoto, Y., Yagi, T. (2001). High-pressure structures of methane hydrate observed up to 8 GPa at room temperature. Journal of Chemical Physics, 115 (15), 7066-7070.

Hirai, H., Tanaka, T., Kawamura, T., Yamamoto, Y., Yagi, T. (2003). Retention of filled ice structure of methane hydrate up to 42 GPa. Physical Review B, 68, 172102, 1-4.

Hirai, H., Tanaka, T., Kawamura, T., Yamamoto, Y., Yagi, T. (2004). Structural changes in gas hydrates and existence of a filled ice structure of methane hydrate above 40 GPa. Journal of Physics and Chemistry of Solids, 65, 1555-1559.

Hirai, H., Kadobayashi, H. (2023). Significance of the high-pressure properties and structural evolution of gas hydrates for inferring the interior of icy bodies. Progress in Earth and Planetary Science, 10:3.

Hofgartner, J.D., Birch, S.P.D., Castillo, J., Grundy, W.M., Hansen, C. J., Hayes, A.G., Howett, C.J.A., Hurford, T.A., Martin, E.S., Mitchell, K.L., Nordheim, T.A., Poston, M.J., Prockter, L.M., Quick, L.C., Schenk, P., Schindhelm, R.N., Umurhan, O.M. (2022). Hypotheses for Triton's plumes: New analyses and future remote sensing tests. Icarus, 375, 114835.

Hogenboom, D.L., Kargel, J.S., Consolmagno, G.J., Holden, T.C., Lee, L., Buyyounouski, M. (1997). The Ammonia–Water System and the Chemical Differentiation of Icy Satellites. Icarus, 128, 171–180.

Hörst, S.M. (2017). Titan's atmosphere and climate. J. Geophys. Res. Planets, 122, 432–482.

Howell, S.M., Pappalardo, R.T. (2020). NASA's Europa Clipper—a mission to a potentially habitable ocean world. Nature Communications 11:1311.

Howett, C.J.A., Spencer, J.R., Pearl, J., Segura, M. (2011). High heat flow from Enceladus' south polar region measured using 10–600 cm−1 Cassini/CIRS data. Journal of Geophysical Research, VOL. 116, E03003,

Hsu, H., Postberg, F., Sekine, Y., Shibuya, T., Kempf, S., Horányi, M., Juhász, A., Altobelli, N., Suzuki, K., Masaki, Y., Kuwatani, T., Tachibana, S., Sirono, S., Moragas-Klostermeyer, G., Srama, R. (2015). Ongoing hydrothermal activities within Enceladus. Nature, 519, 207-209.

Hu, H.X.S., Van der Wal, W., Vermeersen, L.L.A. (2019). Rotational dynamics of tidally deformed planetary bodies and validity of fluid limit and quasi-fluid approximation. Icarus, Volume 321, 583-592.

Huybrighs, H.L.F., Roussos, E., Krupp, N., Fraenz, M., Futaana, Y., Barabash S., Glassmeier, K. (2017). Are there signatures of active Europa plumes in Galileo in situ data? Vol. 11, EPSC2017-452, European Planetary Science Congress 2017

Hurford, T.A., Helfenstein, P., Hoppa, G.V., Greenberg, R., Bills, B.G. (2007). Eruptions arising from tidally controlled periodic openings of rifts on Enceladus. Nature, 447, 292-294.

Hussmann H., Sohl, F., Spohn, T. (2006). Subsurface oceans and deep interiors of medium-sized outer planet satellites and large trans-neptunian objects. Icarus, 185, 258-273.

Iess, L., Stevenson, D.J., Parisi, M., Hemingway, D., Jacobson, R.A., Lunine, J.I., Nimmo, F., Armstrong, J.W., Asmar, S.W., Ducci, M., Tortora, P. (2014). The Gravity Field and Interior Structure of Enceladus. Science, 344, 78-80.

Ingersoll, A.P. (1990). Dynamics of Triton's atmosphere. Nature, 344, 315-317.

Ingersoll, A.P., Tryka, K.A. (1990). Triton's Plumes: The Dust Devil Hypothesis. Science, 250, 4979, 435-437.

Ingersoll, A.P., Pankine, A.A. (2010). Subsurface heat transfer on Enceladus: Conditions under which melting occurs. Icarus, 206, 594-607.

Jacobson, R.A. (2009). The Orbits of the Neptunian Satellites and the Orientation of the Pole of Neptune. The Astronomical Journal, 137, 4322-4329.

Jin, S., Ji, J.H. (2012). The internal structure models of Europa. Sci China-Phys Mech Astron, 55: 156–161,

Johnson, T.V. (2005). Geology of the Icy Satellites. Space Science Reviews, 116, 401-420.

Kadobayashi, H., Hirai, H., Ohfuji, H., Ohtake, M., Yamamoto. Y. (2018). *In situ* Raman and X-ray diffraction studies on the high pressure and temperature stability of methane hydrate up to 55 GPa. J. Chem. Phys. 148, 164503

Kadobayashi, H., Hirai, H., Machita. K., Ohfuji, H., Muraoka. M., Yoshida. S., Yamamoto, Y. (2020). High-pressure phase transition of methane hydrate in water–methane–ammonia system. Journal of Physics: Conference Series, 1609, 012006.

Kamata, S., Nimmo, F., Sekine, Y., Kuramoto, K., Noguchi, N., Kimura., J., Tani, A. (2019). Pluto's ocean is capped and insulated by gas hydrates. Nature Geoscience. 12(6), 407-410.

Kang, S.P., Lee, H. (2001). Enthalpies of dissociation of clathrate hydrates of carbon dioxide, nitrogen, (carbon dioxide + nitrogen), and (carbon dioxide + nitrogen + tetrahydrofuran). J. Chem. Thermodynamics, 33, 513–521.

Kargel, J.S., Croft, S.K. Lunine, J.I. Lewis, J.S. (1991). Rheological Properties of Ammonia-Water Liquids and Crystal-Liquid Slurries Planetological Applications. Icarus, 89, 93-112.

Kargel, J.S. (1995). Cryovolcanism on the Icy Satellites. Earth, Moon and Planets, 67:101-113.

Kavanagh, J.L., Engwell, S.L., Martin, S.A. (2018). A review of laboratory and numerical modelling in volcanology. Solid Earth, 9, 531–571.

Keiffer, S.W. (1977). Sound Speed in Liquid-Gas Mixtures' Water-Air and Water-Steam. Journal of Geophysical Research, 82, 2895-2904.

Kieffer S.W., Lu, X., Bethke, C.M., Spencer, J.R., Marshak, S., Navrotsky, A. (2006). A clathrate reservoir hypothesis for Enceladus' south polar plume. Science 314, 1764-1766.

Kirk, R.L. (1990). Thermal models of insolation-driven Nitrogen geysers on Triton. Abstracts of the Lunar and Planetary Science Conference, volume 21, page 633.

Kirk, R. L., Howington-Kraus, E., Barnes, J. W., Hayes, A. G., Lopes, R. M., Lorenz, R. D., Lunine, J. I., Mitchell, K. L., Stofan, E. R., Wall, S. D. (2010). La Sotra y las otras: Topographic evidence for (and against) cryovolcanism on Titan. American Geophysical Union, Fall Meeting 2010, abstract id.P22A-03

Klauda, J.B., Sandler, S.I. (2003). Phase behavior of clathrate hydrates: a model for single and multiple gas component hydrates. Chemical Engineering Science, 58, 27-41.

Koh, C.A., Sum, A.K., Sloan, E.D. (2009). Gas hydrates: Unlocking the energy from icy cages. Journal of Applied Physics, 106, 061101, 1-14.

Kuhs, W.F., Chazallom, B., Radaelli, P.G., Pauer, F. (1997). Cage Occupancy and Compressibility of Deuterated N_2-Clathrate Hydrate by Neutron Diffraction. Journal of Inclusion Phenomena and Molecular Recognition in Chemistry, 29, 65-77.

Kumazaki, T., Kito, Y., Sasaki, S., Kume, T., Shimizu, H. (2004). Single-crystal growth of the high-pressure phase II of methane hydrate and its Raman scattering study. Chemical Physics Letters, 388, 18-22.

Kvorka, J., Čadek, O., (2022). A numerical model of convective heat transfer in Titan's subsurface ocean. Icarus, 376, 114853.

Kwon, T., Kneafsey, T. J., Rees, E.V.L. (2011). Thermal Dissociation Behavior and Dissociation Enthalpies of Methane-Carbon Dioxide Mixed Hydrates. Journal of Physical Chemistry B, 115, 8169-8175.

Landry, B.C., Munsill, L.C., Collins, G.C., Mitchell, K.L. (2014). Observations About Boulders On The South Polar Terrain Of Enceladus. 45th Lunar and Planetary Science Conference, 2317.

Larson, A. C., Von Dreele, R.B. (2000). General Structure Analysis System (GSAS). Los Alamos National Laboratory Report No. LAUR 86–748, Los Alamos, New Mexico, 2000. (http://www.ncnr.nist.gov/xtal/software/gsas.html).

Lavvas, P., Yelle, R.V., Vuitton, V. (2009). The detached haze layer in Titan's mesosphere. Icarus, 201, 626-633.

Le Corre, L., Le Mouélic, S., Sotin, C., Combe, J.P., Rodriguez, S., Barnes, J.W., Brown, R.H., Buratti, B.J., Jaumann, R., Soderblom, J., Soderblom, L.A., Clark, R., Baines, K.H., Nicholson, P.D. (2009). Analysis of a cryolava flow-like feature on Titan. Planetary and Space Science 57, 870–879

Le Mouélic, S., Cornet, T., Rodriguez, S., Sotin, C., Barnes, J.W., Baines, K.H., Brown, R.H., Lefèvre, A., Buratti, B.J., Clark, R.N., Nicholson, P.D. (2012). Global mapping of Titan's surface using an empirical processing method for the atmospheric and photometric correction of Cassini/VIMS images. Planetary and Space Science 73, 178–190.

Li, M., Chen, B., Li, K., Song, Y., Yang. M. (2023). Stability and structure of multiply occupied sII CO_2 clathrate hydrates: A possibility for carbon capturing. Journal of Molecular Liquids, 380, 121746.

Liu, X., Bara, J.E., Turner, C.H. (2021). Understanding Gas Solubility of Pure Component and Binary Mixtures within Multivalent Ionic Liquids from Molecular Simulations. Phys. Chem. B, 125, 29, 8165–8174.

Lopes, R.M.C., Mitchell, K.L., Stofan, E.R., Lunine, J.I., Lorenz, R., Paganelli, F., Kirk, R.L., Wood, C.A., Wall. C.A., S.D., Robshaw, L.E., Fortes, A.D., Neish, C.D., Radebaugh, J., Reffet, E., Ostro, S.J., Elachi, C., Allison, M.D., Anderson, Y., Boehmer, R., Boubin, G., Callahan, P., Encrenaz, P., Flamini, E., Francescetti, G., Gim, Y., Hamilton, G., Hensley, S., Janssen, M.A., Johnson, W.T.K., Kelleher, K., Muhleman, D.O., Ori, G., Orosei, R., Picardi, G., Posa, F., Roth, L.E., Seu, R., Shaffer, S., Soderblom, L.A., Stiles, B., Vetrella, S., West, R.D., Wye, L., Zebker,

H.A. (2007). Cryovolcanic features on Titan's surface as revealed by the Cassini Titan Radar Mapper. Icarus, 186, 395-412.

Lopes, R.M.C., Stofan, E.R., Peckyno, R., Radebaugh, J., Mitchell, K.L., Mitri, G., Wood, C.A., Kirk, R.L., Wall, S.D., Lunine, J.I., Hayes, A., Lorenz, R., Farr, T., Wye, L., Craig, J., Ollerenshaw, R.J., Janssen, M., LeGall, A., Paganelli, F., West, R., Stiles, B., Callahan, P., Anderson, Y., Valora, P., Soderblom, L., Cassini RADAR Team. (2010). Distribution and interplay of geologic processes on Titan from Cassini radar data. Icarus, 205, 540-558.

Lopes, R.M.C., Kirk, R.L., Mitchell, K.L., LeGall, A., Barnes, J.W., Hayes, A., Kargel, J., Wye, L., Radebaugh, J., Stofan, E.R., Janssen, M.A., Neish, C.D., Wall, S.D., Wood, C.A., Lunine, J.I., Malaska, M.J. (2013). Cryovolcanism on Titan: New results from Cassini RADAR and VIMS. Journal of Geophysical Research: Planets, 118, 416-435.

Lopes, R.M.C., Malaska, M.J., Solomonidou, A., Le Gall, A., M.A. Janssen, M.A., Neish, C.D., Turtle, E.P., Birch, S.P.D., Hayes, A.G., Radebaugh, J., Coustenis, A., Schoenfeld, A., Stiles, B.W., Kirk, R.L., Mitchell, K.L., Stofan, E.R., Lawrence, K.J., the Cassini RADAR Team (2016). Nature, distribution, and origin of Titan's Undifferentiated Plains. Icarus 270, 162–182.

Lopes, R.M.C., Wall, S. D., Elachi, C., Birch, S., Corlies, P., Coustenis, A., Hayes, A., Hofgartner, J., Janssen, M., Kirk, R., LeGall, A., Lorenz, R., Lunine, J., Malaska, M., Mastroguiseppe, M., Mitri, G., Neish, C., Notarnicola, C., Paganelli, F., Paillou, P., Poggiali, V., Radebaugh, J., Rodriguez, S., Schoenfeld, A., Soderblom, J., Solomonidou, A., Stofan, E., Stiles1, B., Tosi, F., Turtle, E., West, R., Wood, C., Zebker, H., Barnes, J., Casarano, D., Encrenaz, P., Farr, T., Grima, C., Hemingway, D., Karatekin, O., Luca, A., Mitchell, K., Ori, G., Orosei, R., Ries, P., Riccio, D., Soderblom, L., Zhang, Z. (2019). Titan as Revealed by the Cassini Radar. Space Science Reviews, 215(4).

Lorenz, R.D. (2002). Thermodynamics of Geysers: Application to Titan. Icarus, 156, 176-183.

Lorenz, R.D., Stiles, B.W., Kirk, R.L., Allison, M.D., Persi del Marmo, P., Iess, L., Lunine, J.I., Ostro, S.J., Hensley, S. (2008). Titan's Rotation Reveals an Internal Ocean and Changing Zonal Winds. Science, Vol 319, 1649 - 1651.

Loveday, J.S., Nelmes, R.J., Guthrie, M., Belmonte, S.A., Allan, D.R., Klug, D.D., Tse, J.S., Handa, Y.P. (2001a). Stable methane hydrate above 2 GPa and the source of Titan's atmospheric methane. Nature, 410, 661-663.

Loveday, J.S., Nelmes, R.J., Guthrie, M., Klug, D.D., Tse, J.S. (2001b). Transition from Cage Clathrate to Filled Ice: The Structure of Methane Hydrate III. Physical Review Letters. 87, 21, 215501-1-4.

Loveday, J.S., Nelmes, R.J., Klug, D.D., Tse, J.S., Desgreniers. S. (2003). Structural systematics in the clathrate hydrates under pressure. Canadian Journal of Physics. 81, 539-544.

Loveday, J.S., Nelmes, R.J. (2008). High-pressure gas hydrates. Physical Chemistry Chemical Physics, 10, 913-1068.

Lu, X., Keiffer, S.W. (2009). Thermodynamics and Mass Transport in Multicomponent, Multiphase H_2O Systems of Planetary Interest. Annual Review of Earth and Planetary Sciences, 37,449-477.

Lunine, J.I., Stevenson, D.J. (1985). Thermodynamics of clathrate hydrate at low and high pressures with application to the outer solar system. The Astrophysical Journal Supplement Series. 58, 493-531.

Machida, S., Hirai, H., Kawamura, T., Yamamoto, Y., Yagi, T. (2006). A new high-pressure structure of methane hydrate surviving to 86 GPa and its implications for the interiors of giant icy planets. Physics of the Earth and Planetary Interiors, 155, 170-176.

Makogan, Y.F. (2010). Natural gas hydrates – a promising source of energy. Journal of Natural Gas Science and Engineering 2, 49-59.

Manakov, A. Y., Voronin, V.I., Kurnosov, A.V., Teplykh, A.E., Komorov, V.Y., Dyadin, Y.A. (2004). Structural Investigations of Argon Hydrates at Pressures up to 10 kbar. Journal of Inclusion Phenomena and Macrocyclic Chemistry, 48**,** 11-18.

Manga, M., Wang, C.Y. (2007). Pressurised oceans and the eruption of liquid water on Europa and Enceladus. Geophysical Research Letters, 34, L07202, 1-5.

Marshall, W.G., Francis, D.J. (2002). Attainment of near-hydrostatic compression conditions using the Paris-Edinburgh cell. Journal of Applied Crystallography, 35, 122-125.

Mathews, C.N., Minard, R.D., (2006). Hydrogen cyanide polymers, comets and the origin of life. Faraday Discussion, 133, 393-401.

Mao, S., Duan, Z. (2006). A thermodynamic model for calculating nitrogen solubility, gas phase composition and density of the N_2–H_2O–NaCl system. Fluid Phase Equilibria 248 (2), 103-114.

Martens, H.R., Ingersoll, A.P., Ewald, S.P., Helfenstein, P., Giese, B. (2015). Spatial distribution of ice blocks on Enceladus and implications for their origin and emplacement. Icarus, 245, 162-176.

Marvin, K. (2010). Understanding the Clathrate Hydrate. K-12 teacher Outreach, Janda Labs.

Masters, A., Achilleos, N., Agnor, C.B., Campagnola, S., Charnoz, S., Christophe, B., Coates, A.J. Fletcher, L.N., Jones, G.H., Lamy, L., Marzari, F., Nettelmann, N., Ruizm, J., Ambrosi, R., Andre, N., Bhardwaj, A., Fortney, J.J., Hansen, C.J., Helled, R., Moragas-Klostermeyer, G., Orton, G., Ray, L., Reynaud, S., Sergis, N., Srama, R., Volwerk, M. (2014). Neptune and Triton: Essential pieces of the Solar System puzzle. Planetary and Space Science, 104,108–121.

Mauersberger, K., Krankowsky, D. (2003). Vapour pressure above ice at temperatures below 170 K. Geophysical Research Letters, 30, 3, 21, 1-3.

McKay, P., Pollack, J.B., Zent, A.P., Cruikshank, D.P. (1989). The Thermal Structure of Triton's Atmosphere: Pre-Voyager Models. Geophysical Research Letters, 16, 8, 973-976.

McKay, C.P., Pollack, J.B., Courtin, R. (1991). The Greenhouse and Antigreenhouse Effects on Titan. Science 253:1118-1121.

McKinnon, W.B., Kirk, R.L. (2014). Encyclopedia of the Solar System: Triton. Elsevier Inc. Chapter 40, 861-881.

Meriggiola, R., Iess, L., Stiles, B.E., Lunine, J.L., Mitri. (2016). The rotational dynamics of Titan from Cassini RADAR images. Icarus, 275, 183–192.

Mitchell, K.L. (2005). Coupled conduit flow and shape in explosive volcanic eruptions. Journal of Volcanology and Geothermal Research 143,187-302.

Mitchell, J.L., Lora, J.M. (2016). The Climate of Titan. Annu. Rev. Earth Planet. Sci. 44:353–80

Mitri, G., Showman, A.P., Lunine, J.J., Lopes. R,M.C. (2008). Resurfacing of Titan by ammonia-water cryomagma. Icarus 196, 216–224.

Mitri, G., Showman, A.P. (2008). Thermal convection in ice-I shells of Titan and Enceladus. Icarus 193, 387-396.

Mousis, O., Lunine, J.I., Waite Jr., J.H., Magee, B., Lewis, W.S., Mandt, K.E., Marquer, D., Cordier, D. (2009a). Formation conditions of Enceladus and origin of its methane reservoir. The Astrophysical Journal, 701, L39-L42.

Mousis, O., Lunine, J.I., Pasek, M., Cordier, D., Waite Jr., J.H., Mandt, K.E., Lewis, W.S., Nguyen, M. (2009b). A primordial origin for the atmospheric methane of Saturn's moon Titan. Icarus 204, 749-751.

Mousis, O., Chassefière, E., Holm, N.G., Bouquet, A., Waite, J.H., Geppert, W.D., Picaud, S., Aikawa, Y., Ali-Dib, M., Charlou, J., Rousselot, P. (2015). Methane clathrates in the solar system. Astrobiology, 15(4), 308-26.

Nathues, A., Platz, T., Thangjam, G., Hoffmann, M., Mengel, K., Cloutis, E.A., Le Corre, L., Reddy, V., Kallisch, J., Crown, D.A. (2017). Evolution of Occator Crater on Ceres**.** The Astronomical Journal, 153, 112, 1-12.

Nelson, R.M., Kamp, L.W., Lopes, R.M.C., Matson, D.L., Kirk, R.L., Hapke, B.W., Wall, S.D., Boryta, M.D., Leader, F.E., Smythe, W.D., Mitchell, K.L., Baines, K.H., Jaumann, R., Sotin, C., Clark, R.N., Cruikshank, D.P., Drossart, P., Lunine, J.I., Combes, M., Bellucci, G., Bibring, J., Capaccioni, F., Cerroni, P., Coradini, A., Formisano, V., Filacchione, G., Langevin, Y., McCord, T.B., Mennella, V., Nicholson, P.D., Sicardy, B., Irwin, P.G.J., Pearl. J.C. (2009). Photometric changes on Saturn's Titan: Evidence for active volcanism. Geophysical Research Letters, 36, L04202, 1-5.

Newman, S.F., Buratti, B.J., Brown, R.H., Jaumann, J., Bauer, J., Momary, T. (2008). Photometric and spectral analysis of the distribution of crystalline and amorphous ices on Enceladus as seen by Cassini. Icarus, 193, 397 – 406.

Niemann, S.K., Atreya, S.K., Bauer, S. J., Carignan, G. R., Demick, J. E., Frost, R. L., Gautier, D., Haberman, J. A., D. N. Harpold, D. N., Hunten, D. M., Israel, G., Lunine, J. I., Kasprzak, W.T., Owen, T,C., Paulkovich, M., Raulin, F., Raaen, E., Way, S.H. (2005). The abundances of constituents of Titan's atmosphere from the GCMS instrument on the Huygens probe. NATURE, Vol 438.

Niemann, S.K., Atreya, S.K., Demick, J.E., Gautier, D., Haberman, J.A., Harpold, D.N., Kasprzak, W.T., Lunine, J.I., Owen, T,C., Raulin, F. (2010). Composition of Titan's lower atmosphere and simple surface volatiles as measured by the Cassini-Huygens probe gas chromatograph mass spectrometer experiment. Journal of Geophysical Research, 115, E12006, 1-22.

Nimmo, F., Spencer, J.R., Pappalardo, R.T., Mullen, M.E, (2007). Shear heating as the origin of the plumes and heat flux on Enceladus. Nature 447, 289-291.

Nimmo. F., Spencer, J.R. (2015). Powering Triton's recent geological activity by obliquity tides: Implications for Pluto geology. Icarus, 246, 2-10.

Noguchi. N., Yonezawa, T., Yokoi, Y., Tokunaga, T., Moriwaki, T., Ikemoto, Y., Okamura, H. (2021). Infrared and Raman Spectroscopic Study of Methane Clathrate Hydrates at Low Temperatures and High Pressures: Dynamics and Cage Occupancy of Methane. J. Phys. Chem. C, 125, 189−200.

Ogienko, A.G., Kurnosov, A.V., Manakov, A.Y., Larionov, E.G., Ancharov, A.I., Sheromov, M.A., Nesterov, A.N. (2006). Gas Hydrates of Argon and Methane Synthesized at High Pressures: Composition, Thermal Expansion, and Self-Preservation. Journal of Physical Chemistry B, 110, 2840-2846.

Oreskes, N., Shrader-Frechette, K., Belitz, K. (1994). Verification, Validation, and Confirmation of Numerical Models in the Earth Science. Science, New Series, 263, 5147, 641-646.

Park, R,S., Konopliv, A. S., Bills, B. G., Rambaux, N., Castillo-Rogez, J. C., Raymond, C. A., Vaughan, A. T., Ermakov, A. I., Zuber, M. T., Fu, R. R., Toplis, M. J., Russell, C. T., Nathues, A., Preusker, F., (2016). A partially differentiated interior for (1) Ceres deduced from its gravity field and shape. Nature, Vol. 537

Pistorius, C.W.F.T., Rapoport, E., Clark, J.B. (1968). Phase Diagrams of H_2O and D_2O at High Pressures. J Chem Phys 48(12), 5509-5514.

Pinkerton, H., Wilson, L., MacDonald, R. (2002). The transport and eruption of magma from volcanoes: A review. Contemporary Physics, 43 (3), 197-210.

Porco, C.C., Helfenstein, P., Thomas, P.C., Ingersoll, A.P., Wisdom, J., West, R., Neukum, G., Denk, T., Wagner, R., Roatsch, T., Kieffer, S., Turtle, E., McEwen, A., Johnson, T.V., Rathbun, J., Veverka, J., Wilson, D., Perry, J., Spitale, J., Brahic, A., Burns, J.A., DelGenio, A.D., Dones, L., Murray, C.D., Squyres, S. (2006). Cassini Observes the Active South Pole of Enceladus. Science, 311, 1393-1401.

Porco, C., DiNino, D., Nimmo, F. (2014). How the geysers, tidal stresses, and thermal emission across the south polar terrain of Enceladus are related. The Astronomical Journal, 148, 45, 1-24.

Portyankina, G., Esposito, L.W., Aye, K-M., Hansen, C.J., Ali, A. (2020); Modeling the complete set of Cassini's UVIS occultation observations of Enceladus' plume. Preprint submitted to Icarus. arXiv:2004.02663v1 [astro-ph.EP] 6 Apr 2020

Postberg, F., Kempf, S., Schmidt, J., Brilliantov, N., Beinsen, A., Abel, B., Buck, U., Strama, R. (2009). Sodium salts in E-ring ice grains from an ocean below the surface of Enceladus. Nature, 459, 1098-1101.

Postberg, F., Schmidt, J., Hillier, J., Kempf, S., Strama, R. (2011). A salt-water reservoir as the source of a compositionally stratified plume on Enceladus. Nature, 474, 620-622.

Prieto-Ballesteros, O., Kargel, J.S., Fernández-Sampedro, M., Selsis, F., Martínez, E.S., Hogenboom, D.L. (2005). Evaluation of the possible presence of clathrate hydrates in Europa's icy shell or seafloor. Icarus 177, 491–505.

Prinn, R.G., Fegley, Jr., B. (1981). Kinetic inhibitions of CO and N_2 reduction in circumplanetary nebulae – Implications for satellite composition. Astrophysics Journal, 249, 308-317.

Prockter, L.M., Lopes, R.M.C., Giese, B., Jaumann, R., Lorenz, R.D., Pappalardo, R.T., Patterson, G.W., Thomas, P.C., Turtle, E.P., Wagner, R.J. (2010). Characteristics of Icy Surfaces. Space Science Review, 153, 63-111.

Prockter, L. M., Mitchell, K. L., Howett, C. J. A., Smythe, W. D., Sutin, B. M., Bearden, D. A., Frazier, W. E. (2019). Exploring Triton with Trident: A discovery-class mission. 50th Lunar and Planetary Science Conference 2019 (LPI Contrib. No. 2132) 3188

Quirico, E., Douté, S., Scmitt, B., deBergh, C., Cruikshank, D.P., Owen, T.C., Geballe, T.R., Roush, T.L. (1999). Composition, Physical State, and Distribution of Ices at the Surface of Triton. Icarus, 139, 159-178.

Rages, K., Pollack, J.B. (1992). Voyager Imaging of Triton's Clouds and Hazes. Icarus, 99, 289-301.

Robustillo, M.D., Sanches de Menezes, D. É., de Alcántara Pessôa Filho, P. (2023). Phase equilibrium of double-guest clathrates of methane and CO_2, ethane, or propane as measured by high-pressure microcalorimetry. Journal of Molecular Liquids, 387, 122609.

Rowell, C.R., Jellinek, A.M., Hajimirza, S., Aubry, T.J. (2022) External Surface Water Influence on Explosive Eruption Dynamics, With Implications for Stratospheric Sulfur Delivery and Volcano-Climate Feedback. Front. Earth Sci., Vol 10.

Rubincam, D.P. (2003). Polar wander on Triton and Pluto due to volatile migration. Icarus, 163, 469-478.

Rufu, R., Robin M. Canup, R.M. (2017). Triton's Evolution with a Primordial Neptunian Satellite System. The Astronomical Journal, 154:208.

Ruesch, O., Platz, T., Schenk, P., McFadden, L.A., Castillo-Rogez, J.C., Quick, L.C., Byrne, S., Preusker, F., O'Brien, D.P., Schmedemann, N., Williams, D.A., Li, J.-Y., Bland, M.T., Hiesinger, H., Kneissl, T., Neesemann, A., Schaefer, M., Pasckert, J.H., Schmidt, B.E., Buczkowski, D.L., Sykes, M.V., Nathues, A., Roatsch, T., Hoffmann, M., Raymond, C.A., Russell, C.T. (2016). Cryovolcanism on Ceres. Science, Vol. 353, Issue 6303.

Ruiz, J. (2003). Heat flow and depth to a possible internal ocean on Triton. Icarus, 166, 436-439.

Rymer, A. M., Clyde, B., & Runyon, K. (2020). NASA Strategic Planning Planetary Missions Concept Studies Reports, https://science.nasa.gov/ files/science-red/s3fs-public/atoms/files/Neptune%20Odyssey.pdf

Saur, J., Schilling, N., Neubauer, F.M., Strobel, D.F., Simon, S., Dougherty, M.K., Russell, C.T., Pappalardo, R.T. (2008). Evidence for temporal variability of Enceladus' gas jets: Modeling of Cassini observations. Geophysical Research Letters, 35, L20105, 1-5.

Schenk, P., Sobieszczyk, S. (1999). Cratering asymmetries on Ganymede and Triton: from the sublime to the ridiculous. Bull. Am. Astron. Soc. 31 (4). Abstract 70.02.

Schmidt, J., Brilliantov, N., Spahn, F., Kempf, S. (2008). Slow dust in Enceladus' plume from condensation and wall collisions in tiger stripe fractures. Nature, 451, 685-688.

Schneider, N.M, Burger, M.H., Schaller, E.L., Brown, M.E., Johnson, R.E., Kargel, J.S., Dougherty, M.K., Achilleos, N.A. (2009). No sodium in the vapour plumes of Enceladus. Nature, 459, 1102-1104.

Schubert, G., Anderson, J.D., Travis, B.J., Palguta, J. (2007). Enceladus: Present internal structure and differentiation by early and long-term radiogenic heating. Icarus, 188, 345-355.

Schulz, F., Maillard, J., Kaiser, K., Schmitz-Afonso, I., Gautier, T., Afonso, C., Carrasco, N.,

Gross, L. (2021), Imaging Titan's Organic Haze at Atomic Scale. The Astrophysical Journal Letters, 908:L13.

Shimizu, H., Kumazaki, T., Kume, T., Sasaki, S. (2002). In Situ Observations of High-Pressure Phase Transformations in a Synthetic Methane Hydrate. Journal of Physical Chemistry B, 106, 30-33.

Showman, A.P., Mosqueira, I., Head III, J.W. (2004). On the resurfacing of Ganymede by liquid–water volcanism. Icarus 172, 625-640.

Singer, K. N., White, O. L., Schenk, P. M., Moore, J. M., McKinnon, W. B., Howard, A. D., Spencer, J. R., Stern, S. A., Cook, J. C., Grundy, W. M., Cruikshank, D. P., Beyer, R. A., Nimmo, F., Umurhan, O., Howett, C. J. A., Parker, A. H., Protopapa, S., Lauer, T. R., Weaver, H. A., Young, L. A., Olkin, C. B., Ennico, K. (2016). PLUTO'S PUTATIVE CYROVOLCANIC CONSTRUCTS. 47th Lunar and Planetary Science Conference (2276)

Singer, K.N., White, O'L., Schmitt, B., Rader, E.L., Protopapa, S., Grundy 5, W.M., Cruikshank, D.P., Bertrand, T., Schenk, P.M., McKinnon, W.B., Stern, S.A., Dhingra, R.D., Runyon, K.D., Beyer, R.A., Bray, V.J., Ore, C.D., Spencer, J.R., Moore, J.M., Nimmo, F., Keane, J.T., Young, L.A., Olkin, C.B., Lauer, T.R., Weaver, H.A., Ennico-Smith, K. (2022). Large-scale cryovolcanic resurfacing on Pluto. NATURE COMMUNICATIONS, 13:1542.

Sloan, E.D. and Koh, C.A. (2008). Clathrate Hydrates of Natural Gases, Third Edition (Chemical Industries). CRC Press.

Sloan, E.D., Fleyfel, F. (1992). Hydrate dissociation enthalpy and guest size. Fluid Phase Equilibria, 76, 123-140.

Soderblom, L.A., Kieffer, S.W., Becker, T.L., Brown, R.H., Cook II, A.F., Hansen, C.J., Johnson, T.V., Kirk, R.L., Shoemaker, E.M. (1990). Triton's Geyser-like Plumes: Discovery and Basic Characterization. Science, 250, 4979, 410-415.

Soderblom, L.A., Brown, R.H., Soderblom, J.M., Barnes, J.W., Kirk, R.L., Sotin, C., Jaumann, R., Mackinnon, D.J., Mackowski, D.W., Baines, K.H., Buratti, B.J., Clark, R.N., Nicholson, P.D. (2009). The geology of Hotei Regio, Titan: Correlation of Cassini VIMS and RADAR. Icarus 204, 610–618.

Sohl, F., Sears, W.D., Lorenz. R.D. (1995). Tidal Dissipation on Titan. Icarus, 115, 278-96.

Sohl, F. (2010). Revealing Titan's Interior. Science, 327, 1338.

Sori, M.M., Byrne, S., Bland, M.T., Bramson, A.M., Ermakov, A.I., Hamilton, C.W., Otto, K.A., Ruesch, O., Russell, C.T. (2017). The vanishing cryovolcanoes of Ceres. Geophys. Res. Lett., 44, 1243–1250,

Sotin, C., Jaumann, R., Buratti, B. J., Brown, R. H., Clark, R. N., Soderblom, L. A., Baines, K. H., Bellucci, G., Bibring, J.-P., Capaccioni, F., Cerroni, P., Combes, M., Coradini, A., Cruikshank, D. P., Drossart, P., Formisano, V., Langevin, Y., Matson, D. L., McCord, T. B., Nelson, R. M., Nicholson, P. D., Sicardy, B., LeMouelic, S., Rodriguez, S., Stephan, K., Scholz, C. K. (2005). Release of volatiles from a possible cryovolcano from near-infrared imaging of Titan. Nature, Vol 435,

Sotin, C., Tobie., G. (2008). Titan's Hidden Ocean. Science, Vol 319, 1629 – 1630.

Solomonidou, A., Hirtzig, M., Coustenis, A., Bratsolis, E., Le Mouélic, S., Rodriguez, S., Stephan, K., Drossart, P., Sotin, C., Jaumann, R., Brown, R.H., Kyriakopoulos, K., Lopes, R.M.C., Bampasidis, G., Stamatelopoulou-Seymour, K., Moussas, X. (2014). Surface albedo spectral properties of geologically interesting areas on Titan. J. Geophys. Res. Planets, 119, 1729–1747,

Sparks, R.S.J. (1978) The dynamics of bubble formation in magmas: a review and analysis. Journal of Volcanology and Geothermal Research, 3, 1-37.

Sparks, W. B., Schmidt, B. E., McGrath, M. A., Hand, K. P., Spencer, J. R., Cracraft, M., Deustua, S. E. (2017). Active Cryovolcanism on Europa? The Astrophysical Journal Letters, 839:L18.

Spencer, J.R., Pearl, J.C., Segura, M., Flasar, F.M., Mamoutkine, A., Romani, P., Buratti, B.J., Hendrix, A.R., Spilker, L.J., Lopes, R.M.C. (2006). Cassini encounters Enceladus: Background and the discovery of a south polar hot spot. Science 311, 1401–1405.

Spencer, J. (2009). Enceladus with a grain of salt. Nature, 459, 1067-1068.

Spencer, J.R., Howett, C.J.A., Verbiscer, A., Hurford, T.A., Segura, M., Spencer, D.C. (2013). Enceladus Heat Flow from High Spatial Resolution Thermal Emission Observations. EPSC Abstracts, Vol. 8, EPSC2013-840-1

Spiers, E.M., Weber, J.M., Venigall, C., Annex, A.M., Chen, C.P., Lee, C., Gray, P.C., McIntyre, K.J., Berdis, J.R., Mogan, S.R.C., Pereira, P.V., Kumar, S., O'Neil, W., Czajka, E.A., Johnson, P.E., Pascuzzo, A., Tallapragada, S., Phillips, D., Mitchell, K., Nash, A., Scully, J., Lowes, L. (2021). Tiger: Concept Study for a New Frontiers Enceladus Habitability Mission. The Planetary Science Journal, 2:195.

Spitale, J.N., Porco, C.C. (2007). Association of the jets of Enceladus with the warmest regions on its south-polar fractures. Nature, 449, 695-697.

Spitale, J.N., Hurford, T.A., Rhoden, A.R., Berkson, E.E., Platts, S.S. (2015). Curtain eruptions from Enceladus' south-polar Terrain. Nature, 521, 57-60.

Smith, B.A., Soderblom, L.A., Banfield, D., Barnet, C., Basilevksy, A.T., Beebe, R.F., Bollinger, K., Boyce, J.M., Brahic, A., Briggs, G.A., Brown, R.H., Chyba, C., Collins, S.A., Colvin, T., Cook, A.F., Crisp, D., Croft, S.K., Cruikshank, D., Cuzzi, J.N.,

Danielson, G.E., Davies, M.E., De Jong, E., Dones, L., Godfrey, D., Goguen, J., Grenier, I., Haemmerle, V.R., Hammel, H., Hansen, C.J., Helfenstein, C.P., Howell, C., Hunt, G.E., Ingersoll, A.P., Johnson, T.V., Kargel, J., Kirk, R., Kuehn, D.I., Limaye, S., Masursky, H., McEwen, A., Morrison, D., Owen, T., Owen, W., Pollack, J.B., Porco, C.C., Rages, K., Rogers, P., Rudy, D., Sagan, C., Schwartz, J., Shoemaker, E.M., Showalter, M., Sicardy, B., Simonelli, D., Spencer, J., Sromovsky, L.A., Stoker, C., Strom, R.G., Suomi, V.E., Synott, S.P., Terrile, R.J., Thomas, P., Thompson, W.R., Verbiscer, A, Veverka, J. (1989). Voyager 2 at Neptune: Imaging Science Results. Science, New Series,246, 1422-1449.

Smith H.T., Johnson, R.E., Perry, M.E., Mitchel, D.G., McNutt, R.L., Young, D.T. (2010). Enceladus plume variability and the neutral gas densities in Saturn's magnetosphere. Journal of Geophysical Research, 115, A10252, 1-11.

Stern, S.A., McKinnon, W.B. (1999). Triton's surface age and impactor population revisited (evidence for an internal ocean). In: Proc. Lunar Planet. Sci. Conf. 30th. Abstract 1766.

Stone, E.C., Miner, E.D. (1989). The Voyager 2 Encounter with the Neptune System. Science, 246, 4936, 1417-1421.

Sum, A. K., Burrus, R.C., Sloan, Jr., E.D. (1997). Measurement of Clathrate Hydrates via Raman Spectroscopy. Journal of Physical Chemistry B, 101, 7371-7377.

Sum, A. K., Koh, A.A., Sloan, E.D. (2009). Clathrate Hydrates: From Laboratory Science to Engineering Practice. Industrial and Engineering Chemistry Research, 48, 7457-7465.

Sun, Y., Li, S., Zhang, G., Guo, W., Zhu, Y. (2017). Hydrate Phase Equilibrium of CH_4+N_2+CO_2 Gas Mixtures and Cage Occupancy Behaviours. Industrial and Engineering Chemistry Research, 56, 8133-8142.

Szulágyi, J., Cilibrasi, M., Mayer, L. (2018). In Situ Formation of Icy Moons of Uranus and Neptune. The Astrophysical Journal Letters, 868:L13.

Taheri, Z., Shabani, M.R., Nazari, K., Mehdizaheh, A. (2014). Natural gas transportation and storage by hydrate technology: Iran case study. Journal of Natural Gas Science and Engineering, 21, 846-849.

Tenishev, V., Combi, M.R., Teolis, B.D., Waite, J.H. (2010). An approach to numerical simulation of the gas distribution in the atmosphere of Enceladus. Journal of Geophysical Research, 115, A09302, 1-8.

Tenishev, V. (2014). Effect of the Tiger Stripes on the water vapor distribution in Enceladus' exosphere. Journal of Geophysical Research: Planets, 119, 1-10.

Teolis, B.D., Perry, M.E., Hansen, C.J., Waite, J.H., Porco, C.C., Spencer, J.R., Howett, C.J.A. (2017). Enceladus Plume Structure and Time Variability: Comparison of Cassini Observations. ASTROBIOLOGY Volume 17, Number 9.

Thomas P. C., Tajeddine R., Tiscareno M. S., Burns J. A., Joseph J., Loredo T. J., Helfenstein P. and Porco C. (2016). Enceladus's measured physical libration requires a global subsurface ocean. Icarus 264, 37–47.

Tian, F. (2007). Monte Carlo simulations of the water vapour plumes on Enceladus. Icarus 188, 154.

Tobie, G., Grasset, O., Lunine, J.I., Mocquet, A., Sotin, C. (2005). Titan's internal structure inferred from a coupled thermal-orbital model. Icarus 175, 496–502

Tobie, G., Lunine, J.I., Sotin, C. (2006). Episodic outgassing as the origin of atmospheric methane on Titan. Nature, Vol 440.

Tobie, G., Giese, B., Hurford, T.A., Lopes, R.M., Nimmo, F., Postberg, F., Retherford, K.D., Schmidt, J., Spencer, J.R., Tokano, T., Turtle, E.P. (2010). Surface, Subsurface and Atmospheric Exchanges on the Satellites of the Outer Solar System. Space Science Review, 153, 375-410.

Tobie, G. (2015). Enceladus' hot springs. Nature , Vol 519, 162-163.

Toby, B.H. (2001). EXPGUI, a graphical user interface for GSAS. J. Appl. Cryst. 34, 210–213

Tokano, T. (2009). The Dynamics of Titan's Troposphere. Phil. Trans. R. Soc. A 367, 633-648.

Tomasko, M.G., Bézard, B., Doose, L., Engel, S., Karkoschka, E., Vinatier, S. (2008). Heat balance in Titan's atmosphere. Planetary and Space Science 56, 648–659.

Travis, B.J., Schubert, G. (2015). Keeping Enceladus warm. Icarus, 250, 32–42.

Trafton, L. (1984). Large Seasonal Variations in Triton's Atmosphere. Icarus, 58, 312-324.

Tucker, O.J., Combi, M.R., Tenishev, V.M. (2015). 2D models of gas flow and ice grain acceleration in Enceladus' vents using DSMC methods. Icarus 257, 362-376.

Tyler, G.L., Sweetnam, D.N., Anderson, J.D., Borutzki, S.E., Campbell, J.K., Eshleman, V.R., Gresh, D.L., Gurrola, E.M., Hinson, D.P., Kawashima, N., Kursinski, E.R., Levy, G.S., Lindal, G.F., Lyons, J.R., Marouf, E.A., Rosen, P.A., Simpson, R.A., Wood, G.E. (1989). Voyager Radio Science Observations of Neptune and Triton. Science, 246, 1466-1473.

van der Waals, J. H., and Platteeuw, J. C. (1958). Clathrate Solutions. Advances in Chemical Physics, Vol II, 1-57 (John Wiley & Sons, Inc.).

Villanueva, G. L., Hammel, H. B., Milam, S. N., Kofman, V., Faggi, S., Glein, C. R., Cartwright, R., Roth, L., Hand, K. P., Paganini, L., Spencer, J., Stansberry, J., Holler, B., Rowe-Gurney, N., Protopapa, S., Strazzulla, G., Liuzzi, G., Cruz-Mermy, G. El Moutamid, M. Hedman, M., Denny, K. (2023). JWST molecular mapping and characterization of Enceladus' water plume feeding its torus. Nature Astronomy volume 7, pages 1056–1062.

Waite Jr., J.H., Combi, M.R., Ip, W.-H., Cravens, T.E., McNutt Jr., R.L., Kasprzak, W., Yelle, R., Luhmann, J., Niemann, H., Gell, D., Magee, B., Fletcher, G., Lunine, J., Tseng, W. (2006). Cassini Ion and Neutral Mass Spectrometer: Enceladus plume composition and structure. Science 311, 1419-1422.

Waite Jr., J.H., Lewis, W.S., Magee, B.A., Lunine, J.I., McKinnon, W.B., Glein, C.R., Mousis, O., Young, D.T., Brockwell, T., Westlake, J., Nguyen, M.-J., Teolis, B.D., Niemann, H.B., McNutt Jr., R.L., Perry, M., Ip, W.-H. (2009). Liquid water on Enceladus from observations of ammonia and ^{40}Ar in the plume. Nature, 460, 487-490.

Waite, J.H., Glein, C.R., Perryman, R.S., Teolis, B.D., Magee, B.A., Miller, G., Grimes, J., Perry, M.E., Miller, K.E., Bouquet, A., Lunine, J.L., Brockwell, T., Bolton, S.J. (2017). Cassini finds molecular hydrogen in the Enceladus plume: Evidence for hydrothermal processes. Science 356, 155–159

Wall, S. D., Lopes, R. M., Stofan, E. R., Wood, C. A., Radebaugh, J. L., Hörst, S. M., Stiles, B. W., Nelson, R. M., Kamp, L. W., Janssen, M. A., Lorenz, R. D., Lunine, J. I., Farr, T. G., Mitri, G., Paillou, P., Paganelli, F., Mitchell, K. L. (2009). Cassini RADAR

images at Hotei Arcus and western Xanadu, Titan: Evidence for geologically recent cryovolcanic activity. GEOPHYSICAL RESEARCH LETTERS, VOL. 36, L04203.

West, R.A., Balloch, J., Dumont, P., Lavvas, P., Lorenz, R., Rannou, P., Ray, T., Turtle, E.P. The evolution of Titan's detached haze layer near equinox in 2009. (2011). GEOPHYSICAL RESEARCH LETTERS, VOL. 38, L06204.

Wilson, L. (1980). Relationship between pressure, volatile content and Ejecta velocity in three types of volcanic explosion. Journal of Volcanology and Geothermal Research, 8. 297-313.

Wilson. L., Sparks, R.S J., Walker, G. P.L. (1980). Explosive volcanic eruptions - IV. The control of magma properties and conduit geometry on eruption column behaviour. Geophys. J. R. astr. Soc. 63,117-148

Wilson, L., Head III, J.W. (1981). Ascent and eruption of basaltic magma on Earth and Moon. Journal of Geophysical Research, 86. 2971-3001.

Wilson, L. (2009). Volcanism in the Solar System. Nature Geoscience, 2, 389-397. Woods, A.W. (1988). The fluid dynamics and thermodynamics of eruption columns. Bull Volcanology, 50:I69 193

Wilson, L., Head., J.W. (2017). Generation, ascent and eruption of magma on the Moon: New insights into source depths, magma supply, intrusions and effusive/explosive eruptions (Part 1: Theory). Icarus, 283, 146-175.

Wood, C. A., Radebaugh, J. (2020). Morphologic evidence for volcanic craters near Titan's north polar region. Journal of Geophysical Research: Planets, 125.

Woods, A.W. (1988). The fluid dynamics and thermodynamics of eruption columns. Bull Volcanology, 50, 169 -193.

Woods, A.W. (1995), The dynamics of explosive volcanic eruptions. Reviews in Geophysics 33, 4, 495-530.

Woods, A.W., Bower, S.M., Bursik, M.I. (1995). Models of explosive volcanism. Nonlinear processes in Geophysics, 2: 2690279.

Xu, H., Zhao, Y., Zhang, J., Wang, Y., Hickmott, D.D., Daemen, L.L., Hartl, M.A., Wang, L. (2010). Anisotropic elasticity of jarosite: A high-*P* synchrotron XRD study. American Mineralogist, Volume 95, pages 19–23.

Yelle, R.V., Lunine, J.I., Hunten, D.M. (1991). Energy Balance and Plume Dynamics in Triton's Lower Atmosphere. Icarus, 89, 347-358.

Yeoh, S.K., Chapman, T.A., Goldstein, D.B., Varghese, P.L., Trafton, L.M. (2015). On understanding the physics of the Enceladus south polar plume via numerical simulation. Icarus 253, 205-222.

Yeoh, S. K., Li, Z., Goldstein, D.B., Varghese, P.L., Levin, D.A., Trafton, L.M. (2017). Constraining the Enceladus plume using numerical simulation and Cassini data. Icarus, 281, 357-378.

Yumoto, K., Yuichiro, C., Koyaguchi, T., Sugita, S. (2023). Dynamics of gas-driven eruption on Ceres as a probe to its interior. Icarus, 400, 115533.

Zambon, F., Raponi, A., Tosi, F., De Sanctis, M. C., McFadden, L. A., Carrozzo, F. G., Longobardo, A., Ciarniello, M., Kroh, K., Stephan, K., Palomba, E., Pieters, C. M., Ammannito, E., Russell, C. T., Raymond, C. A. (2017). Spectral analysis of Ahuna Mons from Dawn mission's visible-infrared spectrometer. Geophys. Res. Lett., 44, 97–104.

Zolotov, M.Y. (2007). An oceanic composition on early and today's Enceladus. Geophysical Research Letters, 34, L23203, 1-5.

APPENDIX I – Solubility fits

Solubility Fits – pure H_2O at 273.15K

P(bar)	P(MPa)	mCH_4 (mol/kg)	mass fraction CH_4	mN_2 (mol/kg)	mass fraction N_2	mCO_2 (mol/kg)	mass fraction CO_2
1	0.1	0.00247	0.0003952	0.00104	0.0002912	0.07500	0.0330000
2	0.2	0.00494	0.0007904	0.00209	0.0005852	0.14930	0.0656920
3	0.3	0.00739	0.0011824	0.00312	0.0008736	0.22240	0.0978560
4	0.4	0.00982	0.0015712	0.00416	0.0011648	0.29420	0.1294480
5	0.5	0.01223	0.0019568	0.00519	0.0014532	0.36480	0.1605120
6	0.6	0.01462	0.0023392	0.00621	0.0017388	0.43420	0.1910480
7	0.7	0.01699	0.0027184	0.00724	0.0020272	0.50250	0.2211000
8	0.8	0.01934	0.0030944	0.00825	0.0023100	0.56950	0.2505800
9	0.9	0.02167	0.0034672	0.00927	0.0025956	0.63530	0.2795320
10	1.0	0.02398	0.0038368	0.01027	0.0028756	0.70000	0.3080000
15	1.5	0.03525	0.0056400	0.01525	0.0042700	-	-
20	2.0	0.04605	0.0073680	0.02013	0.0056364	-	-
25	2.5	0.05640	0.0090240	0.02490	0.0069720	-	-
30	3.0			0.02957	0.0082796	-	-
35	3.5			0.03415	0.0095620	-	-
40	4.0			0.03864	0.0108192	-	-
50	5.0			0.04733	0.0132524	-	-

The solubilities of CO_2, CH_4, and N_2 in pure water as a function of pressure at 273.15 K. CO_2 hydrate - after 13bar, input pressure greater than the equilibrium pressure, so values after 10bar not valid (Duan and Sun, 2003; Duan and Mao, 2006; Mao and Duan, 2006). Calculated from the CLATHRATE suite of programs (CH_4 solubility, CO_2 solubility, N_2 solubility) of Bakker et al., 1996, Bakker, 1997 and Bakker, 1998

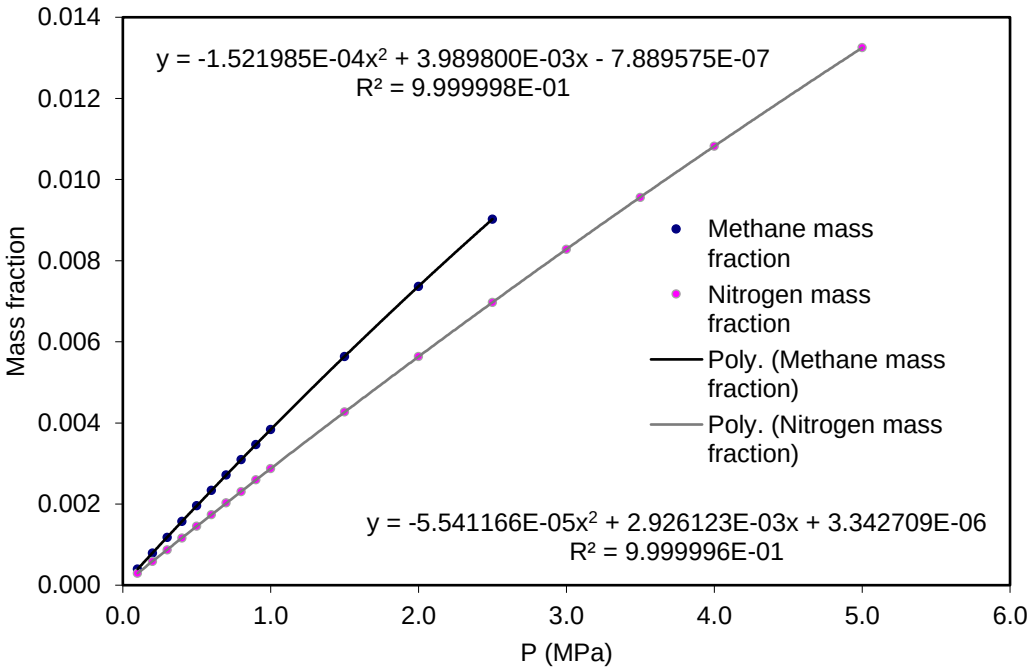
y = -1.521985E-04x² + 3.989800E-03x - 7.889575E-07
R² = 9.999998E-01
Methane mass fraction
Nitrogen mass fraction
Poly. (Methane mass fraction)
Poly. (Nitrogen mass fraction)
y = -5.541166E-05x² + 2.926123E-03x + 3.342709E-06
R² = 9.999996E-01
Mass fraction
P (MPa)
0.000
0.002
0.004
0.006
0.008
0.010
0.012
0.014
0.0
1.0
2.0
3.0
4.0
5.0
6.0

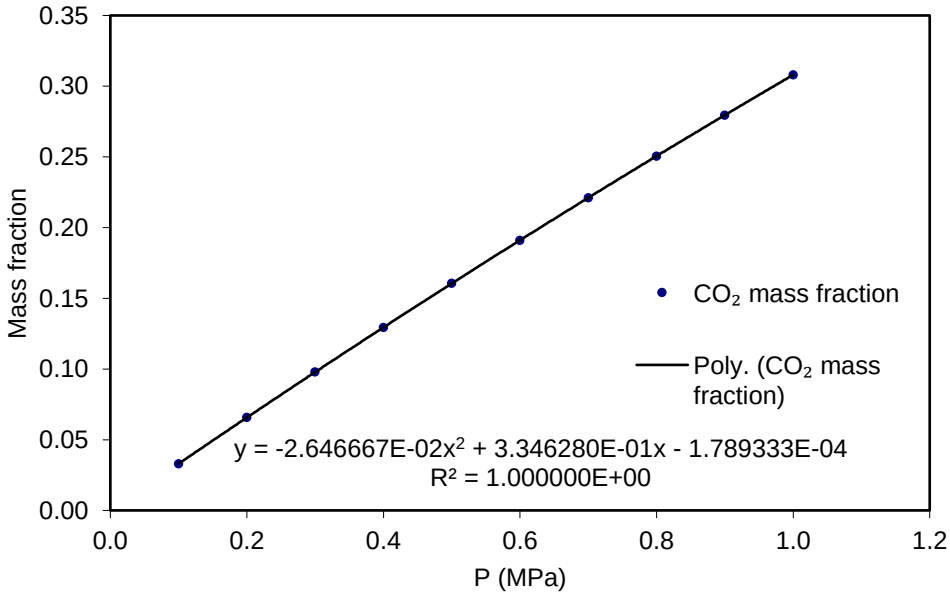
CO₂ mass fraction
Poly. (CO₂ mass fraction)
y = -2.646667E-02x² + 3.346280E-01x - 1.789333E-04
R² = 1.000000E+00
Mass fraction
P (MPa)
0.00
0.05
0.10
0.15
0.20
0.25
0.30
0.35
0.0
0.2
0.4
0.6
0.8
1.0
1.2

Solubility Fits – 3.5% (0.5989 mol/kg) NaCl and H_2O at 273.15K

P(bar)	P(MPa)	mCH_4 (mol/kg)	mass fraction CH_4	mN_2 (mol/kg)	mass fraction N_2	mCO_2 (mol/kg)	mass fraction CO_2
1	0.1	0.00202	0.0003232	0.00083	0.0002324	0.0658	0.0289520
2	0.2	0.00404	0.0006464	0.00167	0.0004676	0.13040	0.0573760
3	0.3	0.00604	0.0009664	0.00250	0.0007000	0.19390	0.0853160
4	0.4	0.00802	0.0012832	0.00333	0.0009324	0.25620	0.1127280
5	0.5	0.00999	0.0015984	0.00415	0.0011620	0.31740	0.1396560
6	0.6	0.01194	0.0019104	0.00497	0.0013916	0.37750	0.1661000
7	0.7	0.01391	0.0022256	0.00579	0.0016212	0.43660	0.1921040
8	0.8	0.01579	0.0025264	0.00661	0.0018508	0.49450	0.2175800
9	0.9	0.01769	0.0028304	0.00742	0.0020776	0.55140	0.2426160
10	1.0	0.01958	0.0031328	0.00822	0.0023016	0.60730	0.2672120
15	1.5	0.02877	0.0046032	0.01221	0.0034188	-	-
20	2.0	0.03757	0.0060112	0.01611	0.0045108	-	-
25	2.5	0.04600	0.0073600	0.01994	0.0055832	-	-
30	3.0	0.05406	0.0086496	0.02368	0.0066304	-	-
35	3.5	0.06178	0.0098848	0.02735	0.0076580	-	-
40	4.0	0.06915	0.0110640	0.03094	0.0086632	-	-
50	5.0	0.08292	0.0132672	0.03791	0.0106148	-	-

The solubilities of CO_2, CH_4, and N_2 in 3.5% NaCl as a function of pressure at 273.15 K. CO_2 hydrate - after 13bar, input pressure greater than the equilibrium pressure, so values after 10bar not valid(Duan & Sun, 2003; Duan and Mao, 2006; Mao and Duan, 2006). Calculated from the CLATHRATE suite of programs (CH_4 solubility, CO_2 solubility, N_2 solubility) of Bakker et al., 1996, Bakker, 1997 and Bakker, 1998.

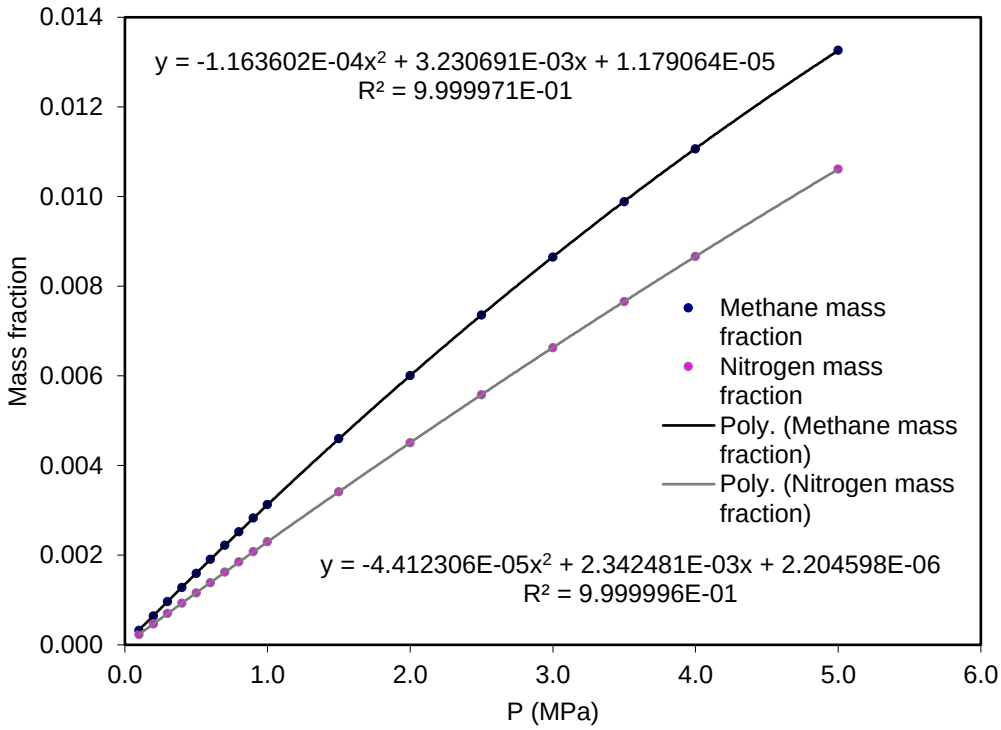
y = -1.163602E-04x² + 3.230691E-03x + 1.179064E-05
R² = 9.999971E-01
y = -4.412306E-05x² + 2.342481E-03x + 2.204598E-06
R² = 9.999996E-01
Methane mass fraction
Nitrogen mass fraction
Poly. (Methane mass fraction)
Poly. (Nitrogen mass fraction)
Mass fraction
P (MPa)
0.000
0.002
0.004
0.006
0.008
0.010
0.012
0.014
0.0
1.0
2.0
3.0
4.0
5.0
6.0

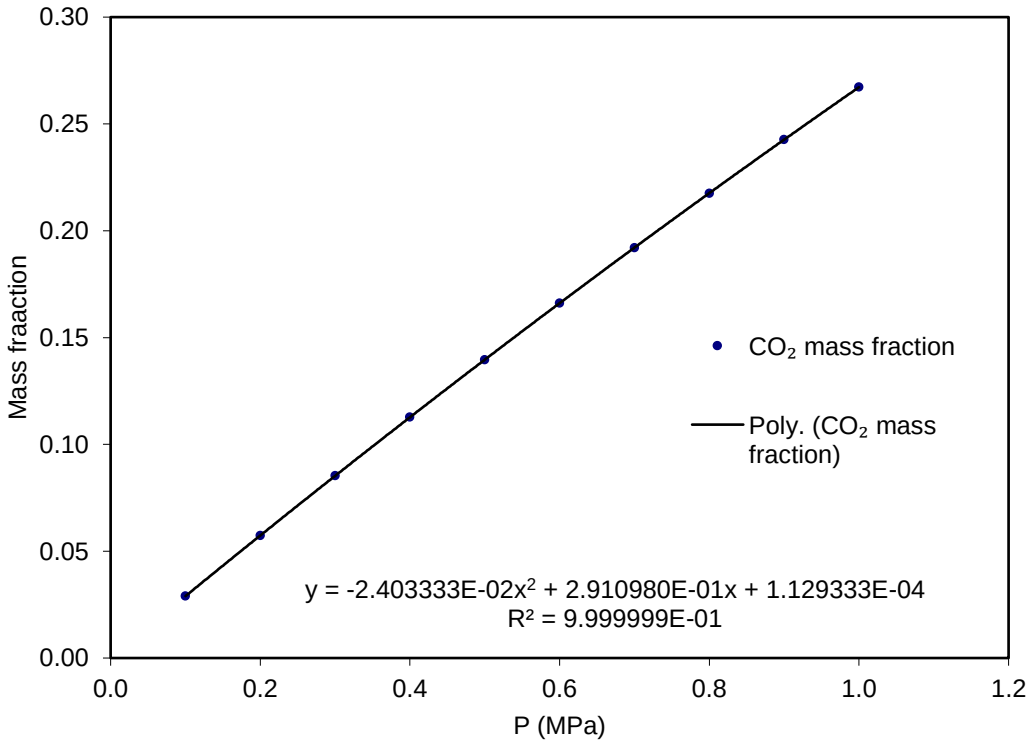
y = -2.403333E-02x² + 2.910980E-01x + 1.129333E-04
R² = 9.999999E-01
CO2 mass fraction
Poly. (CO2 mass fraction)
Mass fraaction
P (MPa)
0.00
0.05
0.10
0.15
0.20
0.25
0.30
0.0
0.2
0.4
0.6
0.8
1.0
1.2

Solubility Fits – 4 mol/kg NaCl and H_2O at 253.8 K

P(bar)	P(MPa)	mCH_4 (mol/kg)	mass fraction CH_4	mN_2 (mol/kg)	mass fraction N_2
1	0.1	0.00100	0.0001600	0.00030	0.0000840
2	0.2	0.00199	0.0003184	0.00061	0.0001708
3	0.3	0.00297	0.0004752	0.00091	0.0002548
4	0.4	0.00394	0.0006304	0.00121	0.0003388
5	0.5	0.00490	0.0007840	0.00151	0.0004228
6	0.6	0.00585	0.0009360	0.00181	0.0005068
7	0.7	0.00678	0.0010848	0.00210	0.0005880
8	0.8	0.00771	0.0012336	0.00240	0.0006720
9	0.9	0.00863	0.0013808	0.00269	0.0007532
10	1.0	0.00954	0.0015264	0.00298	0.0008344
15	1.5	0.01393	0.0022288	0.00442	0.0012376
20	2.0	0.01808	0.0028928	0.00582	0.0016296
25	2.5	0.02200	0.0035200	0.00719	0.0020132
30	3.0	0.02569	0.0041104	0.00852	0.0023856
35	3.5	0.02918	0.0046688	0.00982	0.0027496
40	4.0	0.03245	0.0051920	0.01110	0.0031080
50	5.0	0.03842	0.0061472	0.01355	0.0037940

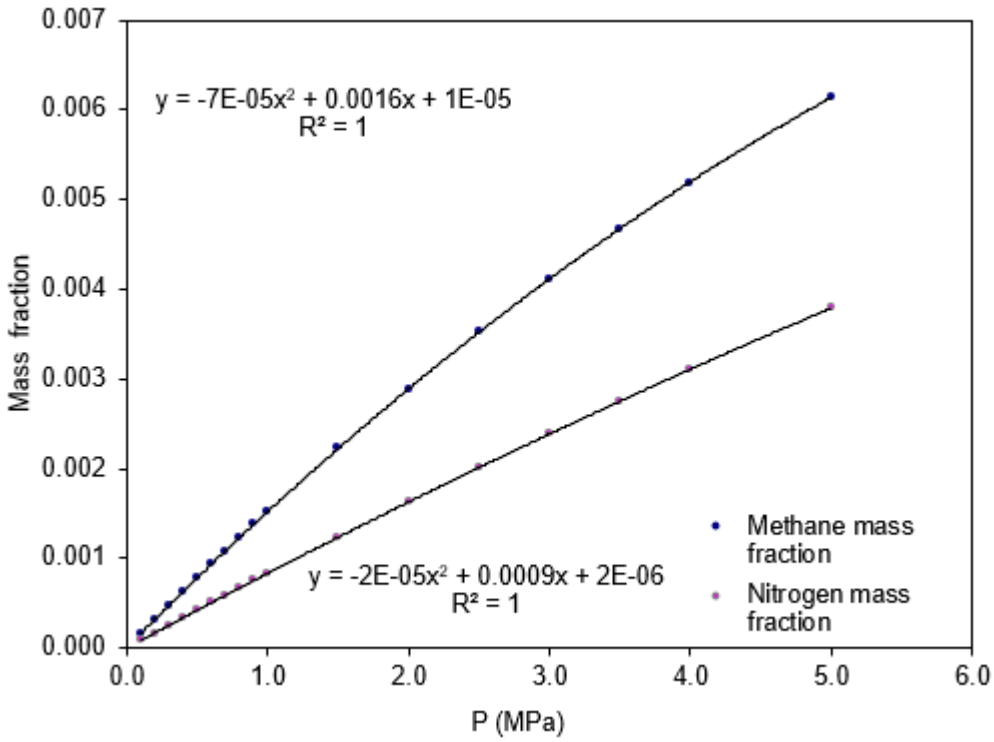

Solubility Fits – 1 mol/kg NaCl and H_2O at 270.7K

P(bar)	P(MPa)	mCH_4 (mol/kg)	mass fraction CH_4	mN_2 (mol/kg)	mass fraction N_2
1	0.1	0.00188	0.0003008	0.00076	0.0002128
2	0.2	0.00376	0.0006016	0.00152	0.0004256
3	0.3	0.00562	0.0008992	0.00230	0.0006440
4	0.4	0.00747	0.0011952	0.00303	0.0008484
5	0.5	0.00930	0.0014880	0.00378	0.0010584
6	0.6	0.01111	0.0017776	0.00452	0.0012656
7	0.7	0.01291	0.0020656	0.00527	0.0014756
8	0.8	0.01470	0.0023520	0.00601	0.0016828
9	0.9	0.01646	0.0026336	0.00675	0.0018900
10	1.0	0.01822	0.0029152	0.00748	0.0020944
15	1.5	0.02675	0.0042800	0.01110	0.0031080
20	2.0	0.03491	0.0055856	0.01465	0.0041020
25	2.5	0.04271	0.0068336	0.01812	0.0050736
30	3.0	0.05017	0.0080272	0.02152	0.0060256
35	3.5	0.05728	0.0091648	0.02484	0.0069552
40	4.0	0.06408	0.0102528	0.02810	0.0078680
50	5.0	0.07672	0.0122752	0.03442	0.0096376

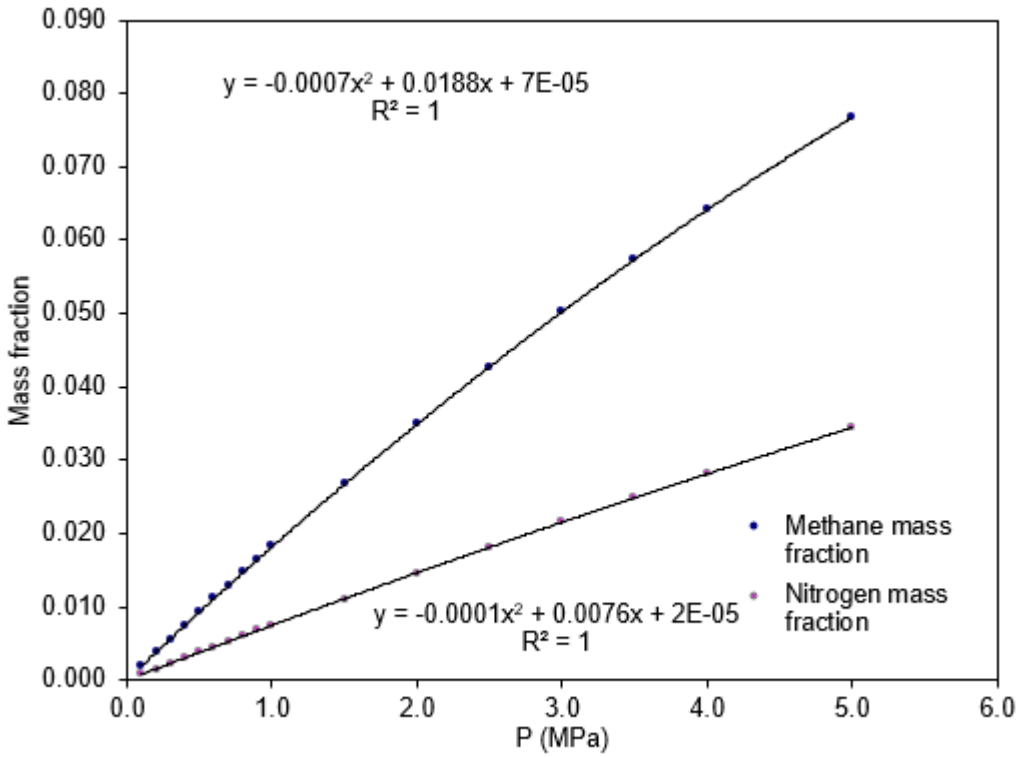

APPENDIX II – Methods

Method for plotting velocity vs depth showing Mach numbers: Enceladus example.

1. Plot calculated values for Mach (x) against velocity (y) for each conduit.

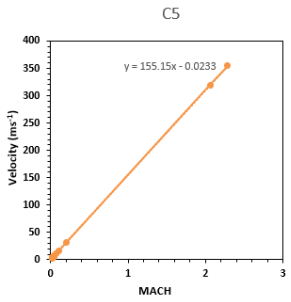

2. Generate linear trendline for each conduit (R^2 = 1 for each), and use graph equations to get exact velocity of each Mach point:

Pure H_2O	trendline (linear)
C1	y = 155.15x - 0.1275
C2	y = 155.15x - 0.0716
C3	y = 155.15x - 0.0458
C4	y = 155.15x - 0.0318
C5	y = 155.15x - 0.0233

3.5% NaCl	trendline (linear)
C1	y = 155.42x - 0.1556
C2	y = 155.42x - 0.0875
C3	y = 155.42x - 0.0555
C4	y = 155.42x - 0.0385
C5	y = 155.42x - 0.0282

Pure H_2O	C1	C2	C3	C4	C5
Mach #	Velocity (ms^{-1})				
1	155.02	155.48	155.50	155.52	155.53
2	310.17	311.03	311.05	311.07	311.08
3	465.32	466.58	466.60	466.62	466.63
4	620.47	622.13	622.15	622.17	622.18
5	775.62	777.68	777.70	777.72	777.73
6	930.77	933.23	933.25	933.27	933.28
7	1085.92	1088.78	1088.80	1088.82	1088.83
8	1241.07	1244.33	1244.35	1244.37	1244.38
9	1396.22	1399.88	1399.90	1399.92	1399.93
10	1551.37	1555.43	1555.45	1555.47	1555.48
11	1706.52	1710.98	1711.00	1711.02	1711.03
12	1861.67	1866.53	1866.55	1866.57	1866.58

3.5% NaCl	C1	C2	C3	C4	C5
Mach #	Velocity (ms^{-1})				
1	155.26	155.33	155.36	155.38	155.39
2	310.68	310.75	310.78	310.80	310.81
3	466.10	466.17	466.20	466.22	466.23
4	621.52	621.59	621.62	621.64	621.65
5	776.94	777.01	777.04	777.06	777.07
6	932.36	932.43	932.46	932.48	932.49
7	1087.78	1087.85	1087.88	1087.90	1087.91
8	1243.20	1243.27	1243.30	1243.32	1243.33
9	1398.62	1398.69	1398.72	1398.74	1398.75
10	1554.04	1554.11	1554.14	1554.16	1554.17
11	1709.46	1709.53	1709.56	1709.58	1709.59
12	1864.88	1864.95	1864.98	1865.00	1865.01

3. Plot velocity (x) against depth (y) for each conduit, and generate best fit trendline (highest R^2) – in this instance, power trendline. Use trendline equation to get depth at which specific Mach number occurs for each conduit. Example:

	R^2	x	y	line eq.
C1-Mach 1	0.8638	155.02	0.91	$y = 1101.5x^{-1.408}$
C2-Mach 1	0.8638	155.48	0.40	$y = 489.52x^{-1.408}$
C3-Mach 1	0.8638	155.50	0.21	$y = 260.83x^{-1.408}$
C4-Mach 1	0.8638	155.52	0.13	$y = 155.86x^{-1.408}$
C5-Mach 1	0.7827	155.53	0.09	$y = 165.13x^{-1.496}$

APPENDIX III – Viscosity data

Method for getting viscosity data at 273.15 K from CRC data.

Viscosity data (μPa·s) from CRC Handbook of Chemistry and Physics (Haynes, 2011)											
CO_2				CH_4				N_2			
T (K)	0.1 Mpa	1 MPa	10 MPa	T (K)	0.1 Mpa	1 MPa	10 MPa	T (K)	0.1 Mpa	1 MPa	10 MPa
220	11.06	242.80	260.20	220	8.42	8.56	19.37	220	13.97	14.16	17.74
240	12.07	12.20	189.40	240	9.12	9.26	14.89	240	15.00	15.17	18.13
260	13.06	13.18	139.50	260	9.80	9.94	13.80	260	15.99	16.14	18.67
280	14.05	14.15	102.20	280	10.47	10.60	13.61	280	16.96	17.09	19.29
300	15.02	15.11	71.03	300	11.13	11.25	13.75	300	17.89	18.01	19.96
320	15.98	16.07	32.39	320	11.77	11.89	14.04	320	18.80	18.91	20.66
340	16.93	17.01	22.80	340	12.39	12.51	14.41	340	19.68	19.79	21.37
360	17.87	17.94	21.83	360	13.00	13.11	14.82	360	20.55	20.64	22.08

1. Plot temperature against pressure for each pressure point (0.1 MPa, 1 MPa, 10 MPa). Using 2nd order polynomial trendline, obtain value for viscosity at 273.15K – example:

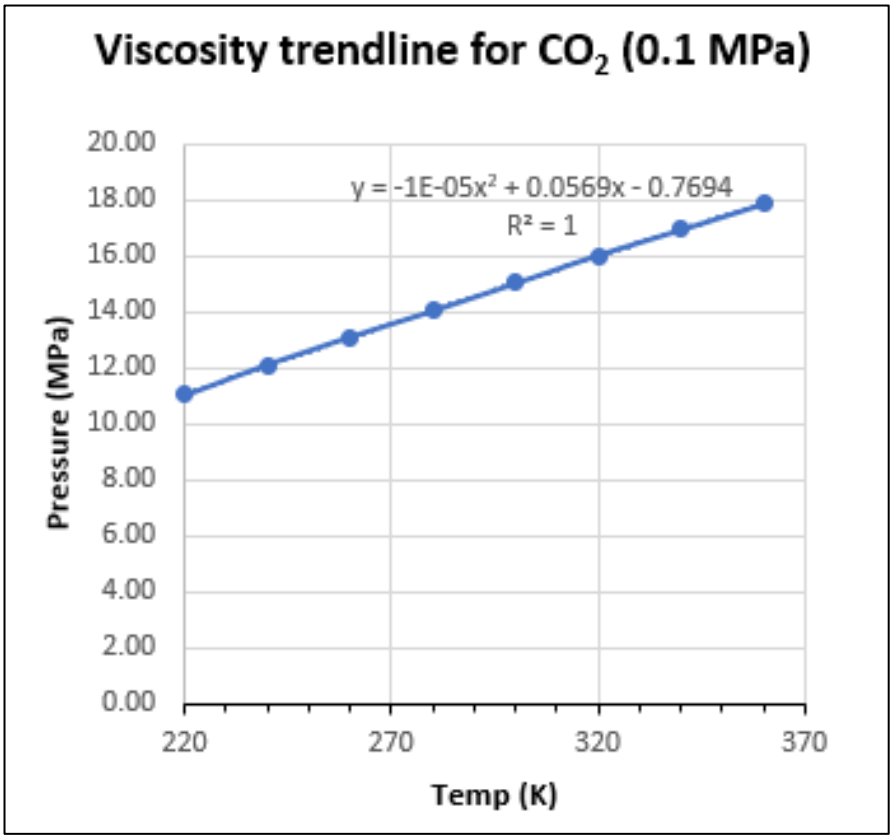

Resulting calculations (Enceladus and Triton):

CO_2	MPa	µPa·s
273.15	0.1	14.03
273.15	1	13.96
273.15	10	114.98

CH_4	MPa	µPa·s
273.15	0.1	10.22
273.15	1	10.29
273.15	10	13.68

N_2	MPa	µPa·s
273.15	0.1	16.82
273.15	1	16.73
273.15	10	19.08

Resulting calculations (Titan):

CH_4	MPa	µPa·s
270.7	0.1	10.14
270.7	1	10.21
270.7	10	13.70

N_2	MPa	µPa·s
270.7	0.1	16.70
270.7	1	16.62
270.7	10	19.00

CH_4	MPa	µPa·s
253.8	0.1	9.57
253.8	1	9.66
253.8	10	13.86

N_2	MPa	µPa·s
253.8	0.1	15.85
253.8	1	15.82
253.8	10	18.48

2. Using these data plot pressure against viscosity, and use the 2nd order polynomial trendline to calculate viscosity at different pressures – example:

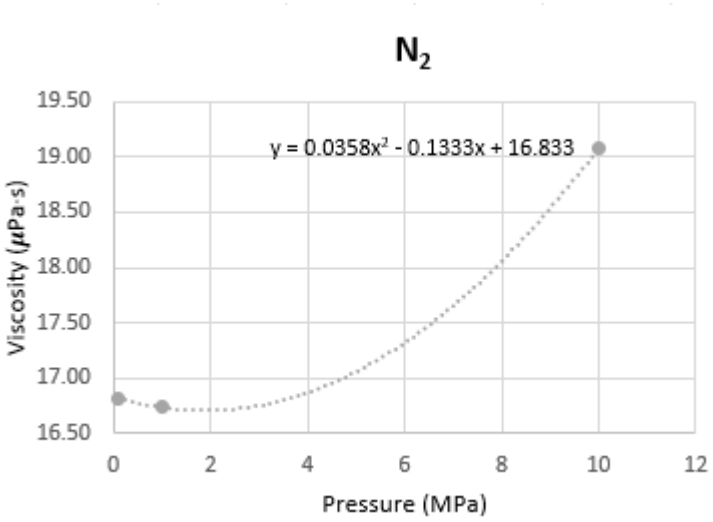

Resultant equations :

Enceladus and Triton @ 273.15 K

$y = 1.138x^2 - 1.2944x + 14.118$	CO_2
$y = 0.0299x^2 + 0.0474x + 10.214$	CH_4
$y = 0.0358x^2 - 0.1333x + 16.833$	N_2

Titan @ 279.7 K

$y = 0.0308x^2 + 0.0482x + 10.132$	CH_4
$y = 0.0356x^2 - 0.1265x + 16.711$	N_2

Titan @ 253.8 K

$y = 0.0376x^2 + 0.054x + 9.5636$	CH_4
$y = 0.0342x^2 - 0.0799x + 15.862$	N_2

APPENDIX IV - Neutron diffraction experiment results

Table I. Results of refinement (LeBail or F(calc)-weighted) showing unit cell dimensions for $CD_4.nD_2O$ structure sI using data collected on PEARL at pressures between 0.182 GPa to 0.870 GPa at RT

Run number	Load (t)	*P* (GPa)	*T* (K)	*a-axis* (Å)	*Volume* (Å³)	Specific volume[1] ($cm^3\ g^{-1}$)
2012 data set (Experiment RB1110043)						
75399_75408	25	0.182	296	11.9376(3)	1701.2(1)	0.9779
75410-75412	26	0.197	296	11.9225(5)	1694.2(2)	0.9741
75413-75414	27	0.274	296	11.8857(5)	1694.7(2)	0.9651
76155-76157	27	0.323	296	11.8814(4)	1677.2(2)	0.9641
76162-76164	28	0.340	296	11.8764(4)	1675.1(2)	0.9629
76165-76167	29	0.486	296	11.8313(3)	1656.1(2)	0.9520
76168-76170	31	0.659	296	11.7395(4)	1617.9(2)	0.9300
76171-76173	32	0.801	296	11.7067(4)	1604.4(2)	0.9222
76174-76176	33	0.870	296	11.6825(4)	1594.4(1)	0.9165[2]

[1] This value is calculated on the basis of an assumed composition. For sI it comes from the actual Rietveld refinement of the 25t soak and for sH and sO from an assumed stoichiometry of 3.5:1 and 2:1 respectively.

[2] Phase boundary at 0.870 GPa, sI co-exists with sH

Table II. Results of refinement (LeBail or F(calc)-weighted) showing unit cell dimensions for $CD_4.nD_2O$ structure sH, using data collected on PEARL over three sets of loadings.

Run number	Load (t)	*P* (GPa)	*T* (K)	*a-axis* (Å)	*c-axis* (Å)	*Volume* (Å³)	Specific volume ($cm^3\ g^{-1}$)	c/a
2012 data set (Experiment RB1110043)								
76174-76176	33	0.870	296	12.028(7)	10.0167(13)	1255.1(2)	0.8629	0.8328(1)
76177-16200	34	1.071	296	11.957(3)	9.9967(4)	1237.8(1)	0.8511	0.8360(0)[3]
76201-76203	35	1.106	296	11.948(7)	9.9967(9)	1235.8(1)	0.8497	0.8367(1)
76204-76206	37	1.295	296	11.8849(6)	9.9803(9)	1220.8(1)	0.8394	0.8397(1)[4]
76207-76209	39	1.563	296	11.8457(7)	9.9274(9)	1206.4(1)	0.8295	0.8381(1)
76210-76212	41	1.843	296	11.7903(9)	9.8727(11)	1188.6(1)	0.8172	0.8374(1)
76213-76215	43	1.955	296	11.7777(14)	9.8607(21)	1184.6(2)	0.8145	0.8372(2)[5]
2013 data set (Experiment RB1310031 - Loading 1)								
80921-80928	25	1.557	299	11.8122(4)	9.9009(5)	1196.4(1)	0.8226	0.8382(1)
80929-80931	27	1.563	299	11.8202(7)	9.8827(8)	1195.8(1)	0.8222	0.8361(1)
80932-80933	29	1.640	299	11.8217(5)	9.8648(15)	1193.9(2)	0.8209	0.8345(1)

[3] sH and liquid H_2O

[4] H_2O crystallises to ice VI

[5] Phase boundary at 1.955 GPa, sH co-exists with sO and some solid methane (phase I, Fd-3m)

Table II continued.

Run number	Load (t)	*P* (GPa)	*T* (K)	*a-axis* (Å)	*c-axis* (Å)	*Volume* (Å³)	Specific volume (cm³ g⁻¹)	c/a
2013 data set (Experiment RB1310031 - Loading 2)								
80953-80954	15	1.312	299	11.9005(5)	9.9319(6)	1218.3(1)	0.8376	0.8346(1)
80956-80957	8	1.167	299	11.9246(6)	9.9527(7)	1225.6(1)	0.8427	0.8346(1)
80958-80967	8	0.801	310	12.0140(5)	10.0213(7)	1252.6(1)	0.8613	0.8341(1)
80970-80971	14	0.961	310	11.9613(6)	10.0009(9)	1239.2(1)	0.8520	0.8361(1)
80972-80973	16	1.018	310	11.9427(6)	9.9922(10)	1234.3(1)	0.8486	0.8367(1)
80974-80975	18	1.096	310	11.9237(6)	9.9784(9)	1228.6(1)	0.8447	0.8369(1)
80976-80978	20	1.183	310	11.9012(5)	9.9609(9)	1221.8(1)	0.8401	0.8370(1)
80989-80991	22	1.323	320	11.9082(4)	9.9395(7)	1220.6(1)	0.8393	0.8347(1)
80992-81002	24	1.415	320	11.9004(3)	9.9226(5)	1217.0(1)	0.8367	0.8338(0)
81003	26	1.449	320	11.8892(7)	9.9108(8)	1213.2(1)	0.8342	0.8336(1)
81008	28	1.621	325	11.8537(16)	9.8869(25)	1203.1(3)	0.8272	0.8341(2)

Table III. Results of refinement (LeBail or F(calc)-weighted) showing unit cell dimensions for $CD_4.nD_2O$ structure sO, using data collected on PEARL over three sets of loadings.

Run number	Load (t)	*P* (GPa)	*T* (K)	*a-axis* (Å)	*b-axis* (Å)	*c-axis* (Å)	*Volume* (Å³)	Specific volume ($cm^3\ g^{-1}$)	b/a	c/a
2012 data set (Experiment RB1110043)										
76213-76215	43	1.955	296	4.8221(7)	8.1356(13)	8.0386(14)	315.4(1)	0.7892	1.6871(4)	1.6670(4)
76216-76221	45	2.156	296	4.8022(5)	8.1161(9)	7.9880(6)	311.3(0)	0.7791	1.6901(3)	1.6634(2)
76235-76237	45	2.916	380	4.8142(6)	8.1562(8)	7.9525(15)	312.3(1)	0.7814	1.6942(3)	1.6519(4)
76260-76278	10	2.324	370	4.8149(10)	8.1226(16)	7.9960(9)	312.7(1)	0.7826	1.6870(5)	1.6607(4)
2013 data set (Experiment RB1310031 - Loading 1)										
80921-80928	25	1.557	299	4.8364(4)	8.1589(10)	8.1082(4)	319.9(0)	0.8007	1.6870(2)	1.6765(1)
80929-80931	27	1.563	299	4.8380(4)	8.1578(14)	8.1057(5)	319.9(0)	0.8006	1.6862(3)	1.6754(2)
80932-80933	29	1.640	299	4.8324(4)	8.1237(8)	8.0807(10)	317.2(0)	0.7939	1.6811(2)	1.6722(2)
80934-80936	31	1.815	299	4.8201(4)	8.1277(9)	8.0571(6)	315.6(0)	0.7899	1.6862(2)	1.6716(2)
80937-80938	33	1.953	299	4.8023(4)	8.1181(7)	8.0098(7)	312.3(0)	0.7814	1.6905(2)	1.6679(2)
80939-80940	35	1.995	299	4.8017(5)	8.1156(8)	8.0028(7)	311.9(0)	0.7804	1.6901(2)	1.6667(2)
80942-80952	39	2.110	299	4.7964(3)	8.0944(5)	7.9784(3)	309.8(0)	0.7752	1.6876(2)	1.6634(1)

Table III continued.

Run number	Load (t)	*P* (GPa)	*T* (K)	*a-axis* (Å)	*b-axis* (Å)	*c-axis* (Å)	*Volume* (Å³)	Specific volume ($cm^3 g^{-1}$)	b/a	c/a
2013 data set (Experiment RB1310031 - Loading 1#2)										
81050	39	2.088	298	4.7935(4)	8.0961(6)	7.9751(4)	309.5(0)	0.7745	1.6890(2)	1.6637(2)
81051	42	2.164	298	4.7918(4)	8.0924(6)	7.9673(4)	308.9(0)	0.7731	1.6888(2)	1.6627(2)
81052-81053	45	2.471	298	4.7663(5)	8.0586(7)	7.9040(5)	303.6(0)	0.7597	1.6908(2)	1.6583(2)
81054	48	2.884	298	4.7377(6)	8.0241(8)	7.8402(6)	298.0(0)	0.7459	1.6937(3)	1.6549(2)
81055-81056	51	3.34	298	4.6964(5)	7.9971(6)	7.7762(5)	292.0(0)	0.7309	1.7028(2)	1.6558(2)
81057-81058	54	3.777	298	4.6755(5)	7.9546(7)	7.7166(5)	287.0(0)	0.7182	1.7013(2)	1.6504(2)
81059	57	4.085	298	4.6549(7)	7.9370(8)	7.6664(7)	283.2(0)	0.7088	1.7051(3)	1.6470(3)
81060	60	4.48	298	4.6390(8)	7.9114(10)	7.6332(9)	280.0(0)	0.7008	1.7062(4)	1.6462(3)

Table IV. Results of refinement (LeBail or F(calc)-weighted) showing unit cell dimensions for ice VI, using data collected on PEARL over three sets of loadings.

Run number	Load (t)	*P* (GPa)	*T* (K)	*a-axis* (Å)	*c-axis* (Å)	*Volume* (Å^3)	Specific volume (cm^3 g^{-1})
2012 data set (Experiment RB1110043)							
76204-76206	37	1.295	296	6.1883(3)	5.7041(6)	218.4(0)	0.6568
76207-76209	39	1.563	296	6.1604(4)	5.6737(6)	215.3(0)	0.6475
76210-76212	41	1.843	296	6.1357(4)	5.6435(7)	212.5(0)	0.6388
76213-76215	43	1.955	296	6.1274(2)	5.6330(4)	211.5(0)	0.6359
76216-76221	45	2.156	296	6.1091(2)	5.6100(4)	209.4(0)	0.6296
2013 data set (Experiment RB1310031 - Loading 1)							
80921-80928	25	1.557	299	6.1445(1)	5.6501(2)	213.3(0)	0.6414
80929-80931	27	1.563	299	6.1449(1)	5.6503(3)	213.4(0)	0.6415
80932-80933	29	1.640	299	6.1398(11)	5.6467(2)	212.9(0)	0.6401
80934-80936	31	1.815	299	6.1286(1)	5.6348(3)	211.6(0)	0.6364
80937-80938	33	1.953	299	6.1136(1)	5.6153(2)	209.9(0)	0.6311
80939-80940	35	1.995	299	6.1121(2)	5.6142(3)	209.7(0)	0.6307
2013 data set (Experiment RB1310031 - loading 2)							
80953-80954	15	1.312	299	6.1697(2)	5.6811(3)	216.3(0)	0.6503
80956-80957	8	1.167	299	6.1825(2)	5.6986(5)	217.8(0)	0.6550
81009-81011	30	1.647	325	6.1507(3)	5.6678(10)	214.4(0)	0.6447
81012	32	1.686	325	6.1504(3)	5.6608(5)	214.1(0)	0.6439
81013-81014	34	1.769	325	6.1427(2)	5.6504(2)	213.2(0)	0.6411
81015-81016	36	1.902	325	6.1318(2)	5.6504(2)	212.0(0)	0.6375

Table V. Results of refinement (LeBail or F(calc)-weighted) showing unit cell dimensions for ice VII, using data collected on PEARL over three sets of loadings.

Run number	Load (t)	*P* (GPa)	*T* (K)	*a-axis* (Å)	*Volume* (Å^3)	Specific volume (cm^3 g^{-1})
2012 data set (Experiment RB1110043 – Loading 1)						
76216-76221	45	2.156	296	3.3617(2)	38.0(0)	0.5712
2013 data set (Experiment RB1310031 - Loading 1)						
80939-80940	35	1.995	299	3.3639(1)	38.0(0)	0.5723
80942-80952	39	2.110	299	3.3585(0)	37.9(0)	0.5695
2013 data set (Experiment RB1310031 - loading 1#2)						
81050	39	2.088	298	3.3569(0)	37.8(0)	0.5687
81051	42	2.164	298	3.3549(0)	37.8(0)	0.5678
81052-81053	45	2.471	298	3.3408(0)	37.3(0)	0.5606
81054	48	2.884	298	3.3252(0)	36.8(0)	0.5528
81055-81056	51	3.34	298	3.3097(0)	36.3(0)	0.5451
81057-81058	54	3.777	298	3.2944(0)	35.8(0)	0.5375
81059	57	4.085	298	3.2818(0)	35.0(0)	0.5314
81060	60	4.48	298	3.2705(0)	35.0(0)	0.5259

APPENDIX V – Cryomagma flow using pressure gradient

1. Plot graph of bulk density (kg m^{-3}) as a function of depth in km, fitting a 3rd order (cubic) polynomial:

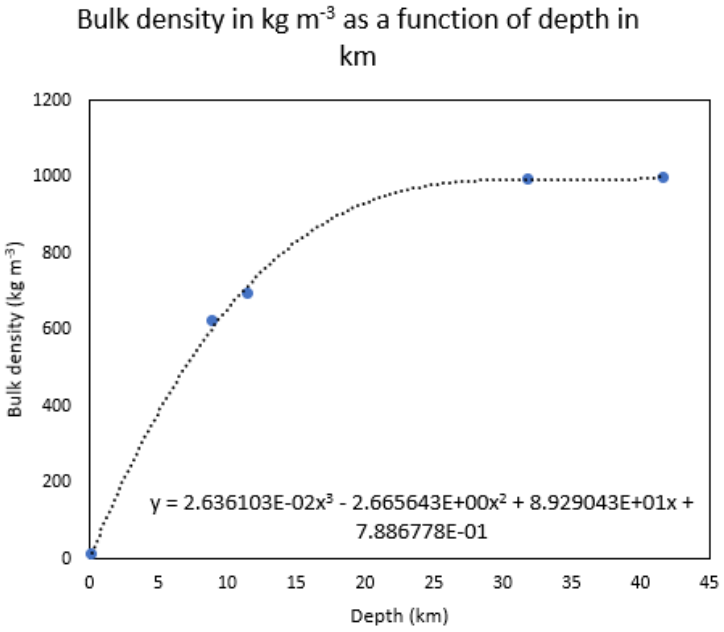

2. Calculate the cryomagma bulk density for a range of depths using the polynomial equation, and the difference, delta-rho, between the cryomagma bulk density and the host ice crust density (1000 kg m^{-3}). The average values of delta-rho multiplied by the acceleration due to gravity on Enceladus gives an estimate of the pressure gradient dP/dz driving the cryomagma upward (19.14 Pa m^{-1}). The pressure at each depth due to the weight of the overlying cryomagma is shown in the 4th column in the table below. The cryomagma pressure (3.8346E+06 Pa) at 42.5 km depth was then compared with the crust pressure at the same depth (4.8025E+06 Pa) resulting in difference of 9.6788E+06 Pa. This difference was then divided by the 42.5 km depth (arbitrarily selected at a point before gas exsolution begins), resulting in a second estimate of pressure gradient (dP/dz) of 22.77 Pa m^{-1}. The two values for dP/dz differ because of the coarseness of the depth increments in the first column in the table, and an average of these is taken, ~21 Pa m^{-1}.

depth (km)	bulk density (kg m^{-3})	delta-rho (kg m^{-3})	magma weight (kg m^{-3})
0	0.7886778	999.21132	0
2.5	207.766375	792.23362	2.9458E+04
4.5	351.018491	648.98151	9.2601E+04
6.5	475.792454	524.20755	1.8603E+05
8.5	583.353594	416.64641	3.0571E+05
10.5	674.967239	325.03276	4.4790E+05
12.5	751.898721	248.10128	6.0914E+05
14.5	815.413367	184.58663	7.8625E+05
16.5	866.776508	133.22349	9.7633E+05
18.5	907.253473	92.74653	1.1768E+06
20.5	938.109591	61.89041	1.3853E+06
22.5	960.610191	39.38981	1.5999E+06
24.5	976.020604	23.97940	1.8187E+06
26.5	985.606159	14.39384	2.0404E+06
28.5	990.632185	9.36782	2.2637E+06
30.5	992.364011	7.63599	2.4878E+06
32.5	992.066967	7.93303	2.7120E+06
34.5	991.006383	8.99362	2.9361E+06
36.5	990.447587	9.55241	3.1600E+06
38.5	991.65591	8.34409	3.3840E+06
40.5	995.89668	4.10332	3.6086E+06
42.5	1004.43523	-4.43523	3.8346E+06
	average =	169.37658 k m^{-3}	
	dP/dz	19.13955 Pa m^{-1}	

3. Using the following parameters, calculate speed (eq. 8.4 for laminar flow and eq. 8.5 for turbulent flow) , Reynolds number (eq. 8.6) and mass flux (eq. 8.7):

Parameters	Value	
Gas free cryomagma	1.791E-03	Pa s
Cryomagma density	1000	kg m^{-3}
Wall friction factor	0.01	(dimensionless)
Pressure gradient (d*P* /dz)	21	Pa m^{-1}

for a selection of conduit diameters:

	Laminar assumption			Turbulent assumption		
Conduit diameter (m)	**Speed (m s^{-1})**	**Reynolds number (Re)**	**Mass flux (kg s^{-1})**	**Speed (m s^{-1})**	**Reynolds number (Re)**	**Mass flux (kg s^{-1})**
0.05	0.916	2.56E+04	1.80E+00	0.229	6.40E+03	4.50E-01
0.1	3.664	2.05E+05	2.88E+01	0.324	1.81E+04	2.54E+00
0.25	22.901	3.20E+06	1.12E+03	0.512	7.15E+04	2.51E+01
0.573*	120.305	3.85E+07	3.10E+04	0.776	2.48E+05	2.00E+02
1	366.415	366.4154	2.88E+05	1.025	5.72E+05	8.05E+02
2	1465.662	1.64E+09	4.60E+06	1.449	1.62E+06	4.55E+03
3	3297.739	5.52E+09	2.33E+07	1.775	2.97E+06	1.25E+04
4	5862.647	1.31E+10	7.37E+07	2.049	4.58E+06	2.58E+04
5	9160.385	2.56E+10	1.80E+08	2.291	6.40E+06	4.50E+04
6	13190.955	4.42E+10	3.73E+08	2.510	8.41E+06	7.10E+04
7	17954.355	7.02E+10	6.91E+08	2.711	1.06E+07	1.04E+05